

AMERICAN UNIVERSITY OF BEIRUT

ON THE MODELING OF GRAIN FRAGMENTATION IN  
METALLIC STRUCTURES USING THE CONTINUUM  
DISLOCATION DYNAMICS APPROACH

by

ALI AL-HADI IBRAHIM KOBAlSSY

A dissertation  
submitted in partial fulfillment of the requirements  
for the degree of Doctor of Philosophy  
to the Department of Mechanical Engineering  
of the Maroun Semaan Faculty of Engineering and Architecture  
at the American University of Beirut

Beirut, Lebanon  
January 2022

# AMERICAN UNIVERSITY OF BEIRUT

## ON THE MODELING OF GRAIN FRAGMENTATION IN METALLIC STRUCTURES USING THE CONTINUUM DISLOCATION DYNAMICS APPROACH

by

ALI AL-HADI IBRAHIM KOBAlSSY

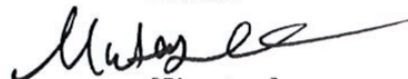
Approved by:

[Signature]

---

Dr. Mu'tasem Shehadeh, Associate Professor  
Department of Mechanical Engineering  
American University of Beirut, Lebanon

Advisor



[Signature]

---

Dr. Georges Ayoub, Assitant Professor  
Department of Industrial and Manufacturing Systems Engineering  
University of Michigan-Dearborn, Michigan, USA

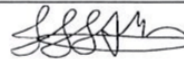
Advisor



[Signature]

---

Dr. Issam Lakkis, Professor  
Department of Mechanical Engineering  
American University of Beirut, Lebanon



Chair of Committee

[Signature]

---

Dr. Samir Mustapha, Associate Professor  
Department of Mechanical Engineering  
American University of Beirut, Lebanon

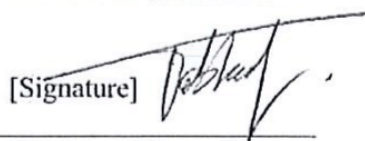
Co-Advisor

[Signature] *Samir mustapha*

---

Dr. Malek Tabbal, Professor  
Department of Physics  
American University of Beirut, Lebanon

Member of Committee



[Signature]

---

Dr. Laszlo Toth, Professor  
Laboratory of Excellence on Design of Alloy Metals for low-mAss Structures (DAMAS)  
Université de Lorraine, Metz, France

Member of Committee

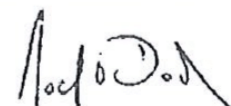
[Signature]



---

Dr. Noel O'Dowd, Professor  
School of Engineering, Bernal Institute  
University of Limerick, Ireland

Member of Committee



Date of dissertation defense: January 5, 2022



## ACKNOWLEDGEMENTS

In the name of Allah, the Most Gracious and the Most Merciful

All praises to God, Allah, for His blessing, kindness, and inspiration in helping me to accomplish my thesis. I would like to express my gratitude to Him for lending me the spirit to reach this stage of writing my final words in my Ph.D. thesis. Without your guidance and divine care, I am nothing. Thank You, my Lord, for every blessing You've offered to me, and for every iniquity You've pushed away from me. In addition, may peace and salutation be given to Prophet Mohammad and his Righteous Family (peace be upon them all) who have taken humanity from the darkness to the lightness.

First and foremost, I would like to express my deepest appreciation to my dear advisors Dr. Mu'tasem Shehadeh and Dr. Georges Ayoub for all their support and guidance throughout the years of my PhD journey. I am sincerely honored and grateful for their unwavering encouragement and inspiration without which I could never have made it this far. You have always backed me up in all sorts of academic and research support. Thank you!

My special thanks go to Dr. Laszlo Toth for his help and support during my visit to Metz, France where I gained vast experience in my research life. Your encouraging notes, valuable comments and fruitful discussions made my research more advanced and developed. Thanks for your motivation! I would also like to thank Dr. Samir Mustapha for being my co-advisor and for his support and encouragement.

I am also thankful to Dr. Issam Lakkis, Dr. Samir Mustapha, Dr. Noel O'Dowd, Dr. Laszlo Toth, and Dr. Malek Tabbal for accepting being part of my PhD committee. Your comments and suggestions while defending my proposal have given me a great push to enhance my research topic.

To Dr. Hussein Zbib, I would like to express my deepest sorrow for his pass away. I have enjoyed the scientific discussions with him in Qatar and Japan which solved a critical issue in my thesis. May your soul rest in peace. I dedicate this thesis to his soul.

To the American University of Beirut, thanks for accepting me as a member of your community. Thanks for leveling up my academic skills and for improving my critical thinking. Thanks for all workshops and seminars that shaped my professional personality. Special acknowledgements for the faculty and staff members of the Maroun Semaan Faculty of Engineering and Architecture at AUB and in specific the Department of Mechanical Engineering, to the Chairman Dr. Issam Lakkis, and to the Dean of the Faculty, Dr. Alan Shihadeh. Thanks for your financial support during my PhD.

Recognition and gratitude are addressed to the National Council for Scientific Research of Lebanon (CNRS-L) for granting me a 3-year doctoral scholarship, to the Qatar foundation for funding my visit to Qatar, and to the University of Lorraine for funding my stay in Metz, France.

Special thanks are delivered to my beloved friends I met at AUB and abroad. Thanks for the amazing times we have spent together and for the difficulties we have shared to overcome these tough years.

Finally, words can't describe how thankful I am for my lovely family. My parents, mom and dad, you are my most precious treasure, I know that nothing could emulate your sacrifice, but I hope you accept this modest work as a dedication to you. Without your infinite support and love, this thesis could not come out to the light. My gorgeous wife Fatima, you are my God's gift in my life. Thanks for being the heaven in all hard moments and thanks for helping me crossing all difficult paths. My brothers, Mohamad and Mostafa, and my sisters, Fatima, Nour, Doha, and Malak, your presence in my life provided me happiness and encouragement. Thanks for the beautiful memories we have lived together. My parents-in-law and siblings-in-law, Ali, Mahdi, Malika and Zeinab, I have seen the unconditional care to me and to my wife as if you are my great loving parents. Your love and support were endless.

Thank you all!

# ABSTRACT OF THE DISSERTATION OF

Ali Al-Hadi Ibrahim Kobaissy

for Doctor of Philosophy  
Major: Mechanical Engineering

Title: On the Modeling of Grain Fragmentation in Metallic Structures Using the Continuum Dislocation Dynamics Approach

Predicting the mechanical properties and the microstructural features of metals subjected to severe thermo-plastic deformation processes is of supreme importance in designing novel or enhanced materials. The objective of this research is to investigate these properties using a hybrid physically based multiscale modelling approach. A grain fragmentation model is proposed and implemented into the continuum dislocation dynamics model coupled with a crystal plasticity framework to predict the texture, grain size, yield strength, and dislocation densities. The proposed model is also used to understand the deformation mechanisms that influence the distinct mechanical behaviors of metals. In this study, the grain fragmentation approach was based on the grain-grain interaction where the formation and accumulation of the geometrically necessary dislocations at the grain boundaries restrict the free deformation of the grain. A misorientation difference arises between the core of the grain and its boundaries. The grain fragmentation process is triggered when the misorientation reaches a threshold value leading to the formation of new grains. The model was first applied to the face centered cubic metallic structures such as copper and aluminum subjected to equal channel angular pressing process (ECAP). Prior to the prediction of the ECAP and post-ECAP properties, model parameters have to be calibrated by a simple mechanical testing for the as-received material such as tension, compression, or shear. ECAP predictions have shown good reliability and predictability for both materials. The proposed model was then upgraded and developed to include additional deformation mechanisms such as twinning to be able to mimic the behavior of hexagonal closed packed metallic structures such as magnesium. The microstructural features and mechanical properties of the processed materials via ECAP were in good accordance with the experiments. Mechanical properties of the pre-ECAP, during ECAP, and post ECAP are studied and analyzed by the power of the proposed model.

# TABLE OF CONTENTS

ACKNOWLEDGEMENTS .....	1
ABSTRACT .....	3
ILLUSTRATIONS .....	8
TABLES .....	12
ABBREVIATIONS .....	13
1. INTRODUCTION .....	16
1.1 Dislocations .....	16
1.2 Dislocation Generation and Movement .....	17
1.3 Micro-Plasticity (Deformation Mechanisms) .....	19
1.3.1 Slip Mechanism .....	19
1.3.2 Twinning Mechanism .....	21
1.3.3 Size Effect.....	24
1.4 Plasticity Theory .....	24
1.5 Theoretical Background on Grain Fragmentation Mechanism.....	25
1.5.1 Grain Fragmentation in FCC Materials .....	26
1.5.2 Grain Fragmentation in BCC Materials.....	29
1.5.3 Grain Fragmentation in HCP Materials .....	30
1.6 Thesis Overview .....	33
1.6.1 Motivations and Objectives .....	33
1.6.2 Chapter Summaries.....	34

<b>2. CONTINUUM DISLOCATION DYNAMICS-BASED GRAIN FRAGMENTATION MODELING .....</b>	<b>37</b>
2.1 Introduction.....	37
2.2 Methodology .....	44
2.2.1 Summary of the Modeling Framework.....	46
2.2.2 CDD Model.....	48
2.2.3 Geometrically Necessary Dislocations .....	52
2.2.4 Grain Fragmentation Model.....	54
2.2.5 Numerical Implementation .....	60
2.3 Results and Discussions.....	62
2.3.1 Experiments and Model Parameters Identification.....	63
2.3.2 ECAP Predictions and Experimental Validation .....	67
2.3.2.1 Texture Prediction.....	68
2.3.2.2 Grain Size .....	70
2.3.2.3 Grain Distribution.....	71
2.3.2.4 Dislocation Density Evolution.....	72
2.4 Conclusions.....	74
 <b>3. MODELING OF THE ECAP INDUCED STRAIN HARDENING BEHAVIOR IN FCC METALS .....</b>	 <b>76</b>
3.1 Introduction.....	76
3.2 Experimental Procedure and Results .....	83
3.2.1 Equal Channel Angular Pressing (ECAP) .....	83
3.2.2 Electron Back Scatter Diffraction (ESBD) .....	83
3.2.3 Experimental Results .....	84
3.3 Modeling Methodology .....	92
3.3.1 Summary of the CP-CDD Approach .....	92
3.3.2 Grain Fragmentation Modeling .....	95



3.4 Results and Discussions.....	98
3.4.1 Calibration of Model Parameters.....	99
3.4.2 Predictions of ECAP.....	102
3.4.2.1 Texture.....	102
3.4.2.2 Strain-Hardening Behavior.....	105
3.4.2.3 Slip Activity.....	109
3.4.2.4 Grain Size.....	112
3.4.3 Post-ECAP.....	113
3.5 Conclusions.....	117
<b>4. ON THE MODELING OF THE ANISOTROPIC BEHAVIOR OF MAGNESIUM AZ31 ALLOY SUBJECTED TO ECAP.....</b>	<b>120</b>
4.1 Introduction.....	120
4.2 Modeling approach.....	128
4.2.1 Texture development.....	128
4.2.1.1 Texture representation in Euler space.....	128
4.2.1.2 Crystallographic Rotations associated with ECAP passes.....	130
4.2.2 Summary of grain refinement modeling.....	132
4.2.3 Strain hardening model (Theoretical framework).....	135
4.3 Results and discussions.....	141
4.3.1 Pre-ECAP Model Parameters Calibration.....	142
4.3.2 ECAP Model Predictions.....	146
4.3.2.1 Microstructural and texture predictions.....	146
4.3.2.2 Microstructural behavior.....	149
4.3.3 Post-ECAP mechanical behavior.....	153
4.4 Conclusions.....	157
<b>5. CONCLUSIONS and RECOMMENDATIONS.....</b>	<b>161</b>

5.1 Summary and Conclusions .....	161
5.2 Recommendations for Future Work .....	162
5.2.1 Grain Boundary Sliding (GBS) model.....	162
5.2.2 Effect of neighboring grains .....	163
LIST OF PUBLICATIONS.....	164
BIBLIOGRAPHY .....	165

## ILLUSTRATIONS

1. Schematic representation of a dislocation line that has an edge (E), screw (S), and mixed (M) character (Figure from William Callister, Jr., Materials science and engineering, John Wiley and sons, Inc, 2010). .....	17
2. Cross-slip mechanism where a screw dislocation can move from one slip plane to another. (Figure from W.F. Hosford, Mechanical Behavior of Materials (Second Edition), 2010) .....	18
3. Frank-Read source mechanism .....	19
4. Slip elements (slip direction and slip plane normal) in uniaxial tension [8]. ....	21
5. Twinning elements ( $K1, K2, \eta1, \eta2$ ). (Figure from A. Kelly, K.M. Knowles, Crystallography and Crystal Defects (Second Edition), 1970).....	22
6. (a) Type I twin. (b) Type II twin. (Figure from A. Kelly, K.M. Knowles, Crystallography and Crystal Defects (Second Edition), 1970).....	23
7. (a) Nonlinear elasticity and (b) elasto-plasticity .....	25
8. Illustration of grain fragmentation mechanism for the Cu-30wt%Zn alloy processed by high pressure torsion [64]. .....	29
9. TEM micrographs of (a) HPT processing of a polycrystalline iron up to an equivalent strain of $\sim 210$ [91]; (b) ECAP+ rolling processing of polycrystalline W at high temperatures [90]. Dislocation walls are indicated by the white arrows while sub-grains boundaries are indicated by red arrows.....	30
10. TEM images of a Ti sample processed by ECAP (channel angle= $120^\circ$ ) through (a) 2 passes, (b) 6 passes and (c) 8 passes at room temperature [100]. .....	32
11. Schematic of the ECAP mechanism .....	38
12. (a) Processing billets through different ECAP die angles and the ideal orientations of the ECAP textures for FCC metals in a $\{111\}$ pole figure, (b) ECAP routes: A, Ba, Bc, and C. Route A: re-insert the billet without rotation around ED but only 90 around TD. Route Ba: re-insert with rotation 90 alternatively around ED and 90 around TD after each pass. Route Bc: re-insert with rotation 90 clockwise around ED and 90 around TD after each pass. Route C: rotate 180 around ED and 90 around TD between passes . .....	39
13. Schematic representation of EBSD maps of the ECAP-processed samples subjected to (a) 1 pass, (b) 4 passes, and (c) 8 passes (based on the results presented by Reihanian et al. (2008) [137]) .....	45
14. (a) Schematic representation of the polycrystal, (b) different crystal orientations, (c) grid representing the grain positions .....	46
15. (a) Strain state without the effect of neighboring grains, (b) strain state accounting for grain-grain interaction effect, (c) misorientation evolution	

between the center and the boundary of the grain, (d) effect of GND on the rotation of the grain boundary. ....	59
16. Example of fragmentation for several grains after reaching a certain strain level. ....	60
17. Flowchart of the Taylor crystal plasticity model in the Fortran program.....	62
18. Initial texture of the copper represented by (a) (111) pole figure, (b) ODFs at $\varphi_2 = 0$ and $45^\circ$ sections.....	63
19. Comparison of the stress-strain behavior of copper between experimental [183] and crystal plasticity modeling at different initial dislocation densities.....	65
20. ODF $\varphi_2 = 0, 45^\circ$ sections for (a) ideal orientations, (b) and (d) experimental textures, (c) and (e) Taylor-Lin CP-CDD model .....	66
21. (a) (111) Ideal orientations of FCC metal texture subjected to one pass ECAP with die angle=90, (b) measured (111) pole figure (PF) after 1A [147], (c) predicted (111) PF texture by Taylor visco-plastic model after 1A [147], and (d) predicted (111) PF texture by Taylor-Lin CP-CDD model after 1A. Isolevels: 0.7, 1, 1.2, 1.4, 1.6, 2, 2.5, 3, 3.5, 4 .....	69
22. (111) pole figures for the (a) measured texture [147], (b) predicted textures by Taylor-Lin CP-CDD model, and (c) predicted textures by Taylor VP model of ECAP 2Bc [147]. Isolevels: 0.7, 1, 1.2, 1.4, 1.6, 2, 2.5, 3, 3.5, 4.....	70
23. Evolution of grain size after two passes of ECAP.....	71
24. Grain refinement at different strains during ECAP 1A .....	72
25. Prediction of dislocation densities evolution after two ECAP passes .....	74
26. (a) Simple schematic of the ECAP process, (b) reinsertion of the billet in route A with no rotations between passes, (c) reinsertion of the billet in route B <sub>a</sub> with a rotation of 90° in alternative directions between consecutive passes, (d) reinsertion of the billet in route B <sub>c</sub> with a rotation of 90° in the same sense between each pass, (e) reinsertion of the billet in route C with a rotation of 180° between passes.....	78
27. Pole figures representing the initial texture of Aluminum alloy AA-1100. ....	84
28. Measured stress-strain response of the as-received Al-1100 alloy at two strain rates, $10^{-2} \text{ s}^{-1}$ and $10^{-4} \text{ s}^{-1}$ . ....	86
29. Measured textures of the tensile as-received samples at two strain rates. ....	87
30. (111) pole figures of the measured textures after 1 (a), 2 (b), and 4 (c) passes of ECAP via route C. ....	88
31. Experimental tensile behavior data (yield strength (YS), ultimate tensile strength (UTS) and elongation) of the as-received sample (0 pass) and the ECAPed	

samples after 1, 2, and 4 passes via route C at two strain rates. Data values for only the ED tests are shown.....	89
32. Engineering stress vs. engineering strain plots for the ECAPed Al-1100 alloy at two different strain rates and along two directions for routes (a) 1A, (b) 2C, and (c) 4C. (ED: extrusion direction and FD: flow direction).....	91
33. (a) Subdivision of grain into 9x9x9 subgrains, and (b) schematic representation of the polycrystal. ....	97
34. Experimental and simulated true stress-true strain behaviors at two different strain rates $10^{-2} \text{ s}^{-1}$ and $10^{-4} \text{ s}^{-1}$ . ....	99
35. Comparison of the measured and the simulated textures of the tensiled as-received samples at two strain rates. Note the experimental results are repeated here for the sake of visual comparison. ....	101
36. (111) key pole figure representing the ideal orientations after one pass of ECAP. ....	103
37. (111) pole figures of the measured and predicted textures after 1, 2, and 4 passes of ECAP via route C. Note the experimental results are repeated here for the sake of visual comparison. ....	105
38. Predicted hardening behavior of aluminum alloy during four passes of ECAP	107
39. Dislocation density evolution during the four passes of ECAP.....	108
40. Relative slip system activities during ECAP. ....	109
41. Predicted volume fraction of grains with at maximum three, four, five, six, seven or eight active slip system during four ECAP passes. ....	110
42. Predictions of the stress-strain behavior of the ECAPed sample after one pass at two strain rates and along two directions (ED: extrusion direction and FD: flow direction).....	114
43. Predictions of the stress-strain behavior of the ECAPed sample after second pass at two strain rates and along two directions (ED: extrusion direction and FD: flow direction).....	116
44. Predictions of the stress-strain behavior of the ECAPed sample after fourth pass at two strain rates and along two directions (ED: extrusion direction and FD: flow direction).....	117
45. Euler angle rotation representation in space .....	129
46. The shear planes observed on the X, Y, and Z planes for 4A and 4K processing routes.....	131
47. Example of the projection of the three cross-sections viewed on X, Y and Z planes .....	132

48. (a) Schematic representation of the decomposition of the deformation gradient accounting only for slip, (b) schematic representation of the decomposition of the deformation gradient accounting for both slip and twinning mechanisms [278].	136
49. (a) Initial texture of the as-received magnesium AZ31 material, (b) Schematic of as-received material of magnesium showing the tensile directions along ND and TD.	142
50. Stress strain responses of the as-received material tensile tested along normal (ND) and transverse (TD) directions at (a) room temperature and (b) 200 C.	143
51. Slip/twin systems activities of the tensiled as-received material.	143
52. Measured (experimental) textures compared with the simulated ones for four passes of route A and route K.	149
53. Schematic of ECAPed samples showing the tensile loading under the extrusion direction (ED) and the flow direction (FD)	152
54. Relative activity of slip systems as function of strain for four passes of route A and route K.	152
55. Dislocation density evolution along slip systems for route A and route K	153
56. Mechanical responses of the ECAP-samples loaded along extrusion and flow directions.	156
57. Predictions of slip/twin activities of the tensiled samples after four passes of ECAP	156
58. Predicted dislocation density evolution of the tensiled samples after four passes of ECAP	157

## TABLES

### Table

1. Slip system families for FCC, BCC and HCP metals [1,7] .....	20
2. Twinning element of different crystal structures [8] .....	24
3. Estimated CRSS (MPa) for five common deformation systems in Mg and Ti. (CRSS data for Mg and Ti were obtained for the temperature ranges of 500–600 K and 200–600 K, respectively) .....	31
4. Model parameters of copper .....	66
5. List of properties and calibrated model parameters of aluminum alloy. ....	100
6. Main ideal orientations, represented by their Euler angles and Miller indices, of FCC crystals in ECAP with die angle $\Phi=90^\circ$ . ....	102
7. Distorted planes projected on X, Y and Z planes for routes A and K up to four passes .....	132
8. Burgers vector magnitude at different slip/twin systems.....	139
9. List of model parameters calibrated at two temperatures $T=25^\circ\text{C}$ and $T=200^\circ\text{C}$ . .....	145

## ABBREVIATIONS

<b>FCC</b>	Face centered cubic
<b>BCC</b>	Body centered cubic
<b>HCP</b>	Hexagonal close-packed
<b>CP</b>	Crystal plasticity
<b>CDD</b>	Continuum dislocation dynamics
<b>DDD</b>	Discrete dislocation dynamics
<b>EPSC</b>	Elasto-plastic self-consistent
<b>VPSC</b>	Visco-plastic self-consistent
<b>SPD</b>	Severe plastic deformation
<b>ECAP</b>	Equal channel angular pressing
<b>HPT</b>	High pressure torsion
<b>ARB</b>	Accumulative roll bonding
<b>TE</b>	Twist extrusion
<b>CEC</b>	Cyclic extrusion and compression
<b>CRSS</b>	Critical resolved shear stress
<b>SSD</b>	Statistically stored dislocations
<b>GND</b>	Geometrically necessary dislocations
<b>GBS</b>	Grain boundary sliding
<b>GNB</b>	Geometrically necessary boundaries
<b>EBSD</b>	Electron back-scattered diffraction
<b>LAGB</b>	Low angle grain boundary
<b>HAGB</b>	High angle grain boundary



<b>SFE</b>	Stacking fault energy
<b>TB</b>	Twin Boundary
<b>RT</b>	Room temperature
<b>GB</b>	Grain boundary
<b>RVE</b>	Reference volume element
<b>ODF</b>	Orientation distribution function
<b>VM</b>	Von Mises
<b>YS</b>	Yield strength
<b>UTS</b>	Ultimate tensile strength
<b>TD</b>	Transverse direction
<b>RD</b>	Rolling direction
<b>ND</b>	Normal direction
<b>ED</b>	Extrusion direction
<b>FD</b>	Flow direction

To my most loving and most lovely family...

# CHAPTER 1

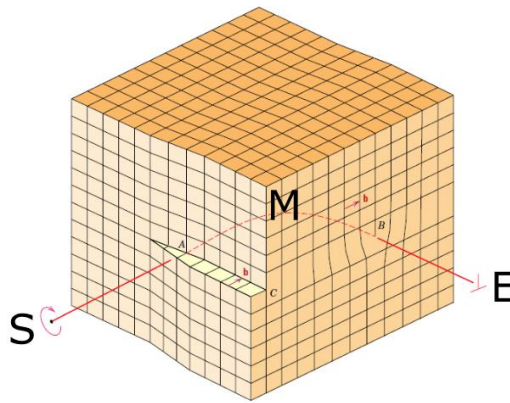
## INTRODUCTION

Solid materials, such as metals, polymers, ceramics, etc., can be classified according to their atomic arrangements. All metals exhibit crystalline structures under normal conditions where they are composed of a large number of single crystals. Each crystal is composed of a large number of atoms sorted in a periodic pattern to form cubic, hexagonal or other structures. There are several crystal structures that metals can form, the most common structures are: FCC (face-centered cubic), BCC (body-centered cubic), and HCP (hexagonal close-packed). However, most crystalline metals do not exist in their perfect form, several imperfections can be present. Those imperfections include point defects such as vacancies and self-interstitial atoms, linear defects (mainly dislocations), surface defects such as grain boundaries and finally volume defects such as cracks, pores or foreign inclusions. Dislocations are the most important crystal defects in crystalline materials amongst the others since they initiate, through their movement, plastic deformation [1]. The concept of dislocations was first developed mathematically by Volterra in the early 1900s. However, in the 1930s, Orowan, Polanyi, and Taylor published almost simultaneous work connecting the plastic deformation to the motion of dislocations [2].

### 1.1 Dislocations

Dislocations are one-dimensional linear defects in which a half plane of atoms is added or removed from the crystal. Dislocations can exist in two types, edge and screw; they are defined by their dislocation line and Burgers vector  $\mathbf{b}$  (Figure 1.1). The burgers

vector is defined as one interatomic spacing and is given as a function of the lattice parameter  $a$  ( $\mathbf{b}(\text{FCC})=\frac{a}{2}\langle 110\rangle$ ,  $\mathbf{b}(\text{BCC})=\frac{a}{2}\langle 111\rangle$ ,  $\mathbf{b}(\text{HCP})=\frac{a}{3}\langle 11\bar{2}0\rangle$ ) [1]. Edge dislocation moves parallel to the applied shear stress where the dislocation line and burgers vector are perpendicular. On the other hand, screw dislocations move perpendicular to the applied shear stress causing a spiral ramp within the crystal in which the dislocation line and the burgers vector are parallel. In most crystalline materials, dislocations are neither pure edge nor pure screw, but mixed dislocations where the dislocation line and the burgers vector are neither parallel nor perpendicular.

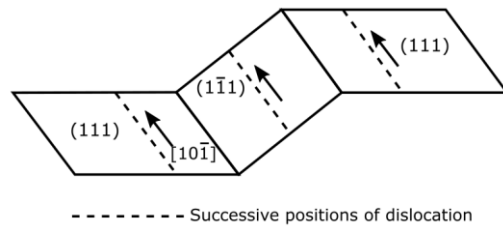


**Figure 1.1** Schematic representation of a dislocation line that has an edge (E), screw (S), and mixed (M) character (Figure from William Callister, Jr., Materials science and engineering, John Wiley and sons, Inc, 2010).

## 1.2 Dislocation Generation and Movement

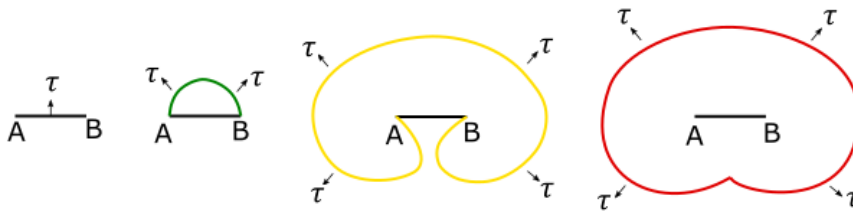
In general, dislocations move either by glide or by climb. Dislocations lying on their slip planes can exist in two forms, glissile or sessile. Glissile occurs when the dislocation moves in a surface containing both its dislocation line and its Burgers vector, while the dislocation which is not able to move in this manner is called sessile. Climb motion can occur when an edge dislocation moves out of its slip plane; this happens mostly at high temperatures [3]. Another mechanism occurs by the movement of a screw dislocation from one slip plane to another plane containing the Burgers vector, is known

as cross-slip (Figure 1.2). However, if the screw dislocation is dissociated into two partials connected by a stacking fault, it cannot cross-slip, since both partials will not be screws. They must recombine to a screw dislocation before they cross-slip and then dissociate again on the second plane.



**Figure 1.2 Cross-slip mechanism where a screw dislocation can move from one slip plane to another. (Figure from W.F. Hosford, Mechanical Behavior of Materials (Second Edition), 2010)**

Generation of dislocations could occur by several mechanisms. The simplest mechanism is the Frank-Read source mechanism, suggested by Frank and Read where a dislocation is generated and multiplied from an existing source called the Frank-Read sources [4]. A Frank-Read source is conceived as a dislocation line pinned at two points A and B (Figure 1.3) which may be formed from dislocation immobilization or dislocation interactions with other point defects or precipitates. In Figure 1.3, a shear stress  $\tau$ , acting on a plane containing the dislocation segment AB, cause the dislocation to bow out. As the shear stress increases, the dislocation continues to bow out until it forms a dislocation loop that can expand under the stress. This bowing out is resisted by a force called the line tension of the dislocation which results in the restored segment AB between the pinning points. Many loops can be produced from the same dislocation segment by repeating the same process.



**Figure 1.3 Frank-Read source mechanism**

### 1.3 Micro-Plasticity (Deformation Mechanisms)

During elastic deformation, the inter-atomic bond only stretches and then returns to its initial position after releasing the load, while during plastic deformation, several deformation mechanisms could occur, such as slip and twinning [5].

#### 1.3.1 Slip Mechanism

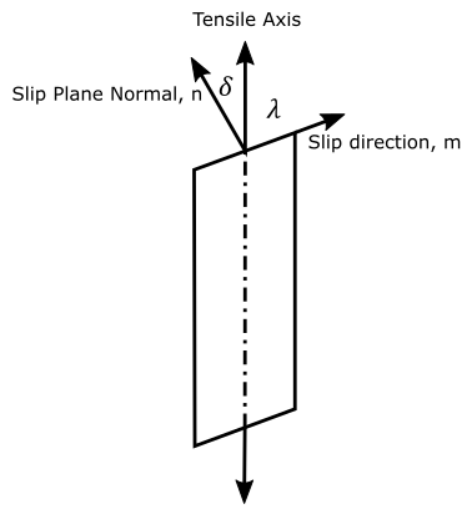
Slip or glide process is produced by the motion of dislocations during plastic deformation. This process requires the breaking-up and reforming of the interatomic bonds, where it involves shearing of crystals on certain crystallographic planes (slip planes) and certain crystallographic directions (slip directions) [6]. The slip plane is defined as the plane that has the most dense atomic packing and is represented by the unit vector of its normal direction  $n$ . The slip direction corresponds to the direction that has the most closely packed atoms within the slip plane and is represented by its unit vector  $m$  (Figure 1.4). The combination of the slip direction and the slip plane forms the so-called slip systems [1]. For FCC crystal structure, dislocations can glide on 12 individual slip systems along  $\langle 110 \rangle$  directions within the  $\{111\}$  planes (or can be written as  $\langle 110 \rangle \{111\}$  systems). In BCC crystals, slip can occur along the  $\langle 111 \rangle$  direction on the  $\{110\}$ ,  $\{112\}$  or  $\{123\}$  plane families where it can reach 48 slip systems. In HCP metals, slip can take place on basal  $\{0001\}$ , prismatic  $\langle a \rangle \{10\bar{1}0\}$ , or pyramidal  $\langle a \rangle \{10\bar{1}1\}$

planes along the common slip direction  $\langle 11\bar{2}0 \rangle$  direction. Another slip may take place on the pyramidal  $\langle c + a \rangle \{11\bar{2}2\}\langle\bar{1}\bar{1}23\rangle$  [5]. The slip planes and directions are summarized in Table 1-1.

**Table 1-1 Slip system families for FCC, BCC and HCP metals [1,7]**

Crystal structure	Slip plane	Slip direction	Number of slip systems
FCC	{111}	$\langle 1\bar{1}0 \rangle$	12
	{110}	$\langle \bar{1}11 \rangle$	12
BCC	{211}	$\langle \bar{1}11 \rangle$	12
	{321}	$\langle \bar{1}11 \rangle$	24
HCP	{0001}	$\langle 11\bar{2}0 \rangle$	3
	{10 $\bar{1}$ 0}	$\langle 11\bar{2}0 \rangle$	3
	{10 $\bar{1}$ 1}	$\langle 11\bar{2}0 \rangle$	6
	{11 $\bar{2}$ 2}	$\langle \bar{1}\bar{1}23 \rangle$	6

In order to initiate slip, a critical value of the shear stress known as the critical resolved shear stress (CRSS), should be reached on a particular slip plane. The resolved shear stress can be written as:  $\tau_R = \sigma \cos \delta \cos \lambda$ , where  $\sigma$  is the applied stress,  $\delta$  is defined as the angle between the slip plane normal and the applied stress direction, and  $\lambda$  is defined as the angle between the slip direction and the tensile axis [1] (Figure 1.4).

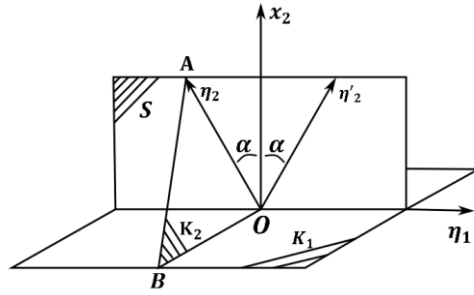


**Figure 1.4 Slip elements (slip direction and slip plane normal) in uniaxial tension [8].**

### ***1.3.2 Twinning Mechanism***

Twinning is a common deformation mechanism in most crystalline materials at low temperatures and high strain rates [9,10]. Twinning dominates slip in HCP metals since slip systems are not easily activated at low temperatures [8]. Mechanical twinning affects the lattice orientation where a part of the crystal becomes the mirror image of the other part of the crystal. The boundary of the twinned crystals occurs at a crystallographic plane called the twinning plane. Twinning, unlike slip, involves a shear displacement of a fraction of an interatomic distance where it reorients the lattice abruptly [5]. In addition, twinning shear is directional-dependent, thus reversing the shear direction could exhibit different effect on the lattice. For instance, in FCC crystals, twinning occurs by shearing along the  $[11\bar{2}]$  direction on the (111) plane and not along  $[\bar{1}\bar{1}2]$  direction for the same plane [8].





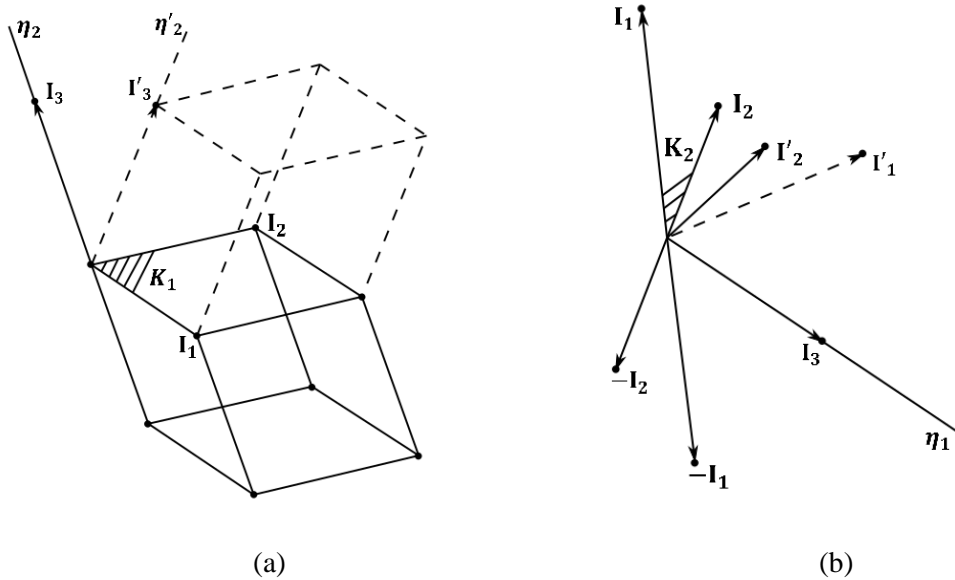
**Figure 1.5** Twinning elements ( $K_1, K_2, \eta_1, \eta_2$ ). (Figure from A. Kelly, K.M. Knowles, *Crystallography and Crystal Defects (Second Edition)*, 1970)

To illustrate more how twinning occurs, the simple shear geometry is shown in Figure 1.5. After twinning, two material planes remain undistorted. The first undistorted plane is the twinning plane  $K_1$  (i.e. the mirror plane), and the second one is denoted by plane  $K_2$ . All atoms on the upper side of the plane  $K_1$ , which is also an unrotated plane, are displaced in the shear direction  $\eta_1$ . The plane where the atoms are displaced is called the shear plane  $S$ , defined by two vectors,  $\eta_1$  and the normal to  $K_1$ . Plane  $K_2$  is a rotated, but undistorted, plane which is a result of the twinning operation. Similarly,  $\eta_2$  is a rotated, but undistorted, direction lying in both planes  $S$  and  $K_2$ .  $\eta_2$  rotates to a new position  $\eta'_2$ , by the means of the simple shear, by an angle  $2\alpha$  where  $\alpha$  is defined as the angle between the normal of plane  $K_1$  and  $\eta_2$  direction [11].

Twinning can reproduce the lattice in two types, type I and type II. Each type depends on the rationality of the twinning elements  $K_1, K_2, \eta_1$ , and  $\eta_2$ . The rationality signifies whether the elements pass through the set of points of the Bravais lattice or not.

In type I,  $K_1$  and  $\eta_2$  are rational. Therefore,  $I_1$  and  $I_2$  can be considered, as shown in Figure 1.6(a), as the unaffected vectors by shear. However, the lattice vector  $I_3$  (parallel to  $\eta_2$ ) is rotated to  $I'_3$  (parallel to  $\eta'_2$ ) after shearing. So, the new basis vectors of the twinned unit cell (dotted cell) become  $(I_1, I_2, I'_3)$  which reflects the un-twinned unit cell

(solid cell)  $(I_1, I_2, -I_3)$ . This type of twinning (type I) is also called the reflection twin type where  $K_1$  and  $\eta_2$  are rational while  $K_2$  and  $\eta_1$  are irrational.



**Figure 1.6 (a) Type I twin. (b) Type II twin. (Figure from A. Kelly, K.M. Knowles, Crystallography and Crystal Defects (Second Edition), 1970)**

Type II is shown in Figure 1.6(b). In this type,  $K_2$  and  $\eta_1$  are rational while  $\eta_2$  and  $K_1$  are irrational. The lattice vector  $I_3$  is chosen to be in the rational direction  $\eta_1$  and the two lattice vectors  $I_1$  and  $I_2$  are chosen in the  $K_2$  plane.  $I_1$ ,  $I_2$  and  $I_3$  define the basis vectors before the shear has taken place. After shearing,  $I_3$  is unchanged while  $I_1$  and  $I_2$  are rotated to a new position  $I'_1$  and  $I'_2$ , respectively. Thus, the new basis of the sheared unit cell is  $(I'_1, I'_2, I_3)$ . This type of twinning is called the rotation type [11]. In most metals, the four twinning elements can be rational, so the two types can merge. In this case, the twin is called compound-type which is usually found in the symmetrical crystal lattices. For example, in cubic structures, the only possible type of twinning is the compound type (the full argument can be found in Ref. [11]). The set of twinning elements (twinning planes and directions) are tabulated in Table 1-2 for different crystal structures:

**Table 1-2 Twinning element of different crystal structures [8]**

Structure	$K_1$	$\eta_1$	$K_2$	$\eta_2$
FCC	{111}	$\langle 11\bar{2} \rangle$	{11 $\bar{1}$ }	$\langle 112 \rangle$
BCC	{112}	$\langle 11\bar{1} \rangle$	{11 $\bar{2}$ }	$\langle 111 \rangle$
HCP	{10 $\bar{1}2$ }	$\langle 10\bar{1}1 \rangle$	{ $\bar{1}012$ }	$\langle \bar{1}011 \rangle$

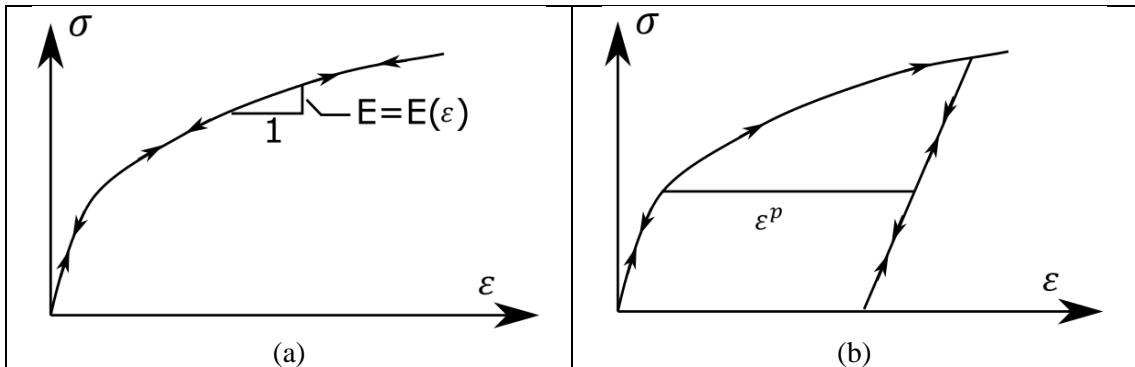
### 1.3.3 Size Effect

Ultra-fine and nano-crystalline materials are revealed to exhibit stronger mechanical properties compared to the coarse crystalline structures of the same material. Microstructural features such as grain size and dislocations are not considered in the classical plasticity theories, thus the size effect could not be predicted. By incorporating the material length scale in modeling framework, size effect is then possible to be predicted. Size effect can be either categorized intrinsically due to microstructural constraints such as grain boundaries, dislocations, and grain sizes, or extrinsically due to the dimensional constraints of the sample size such as micropillars or thin films materials where dislocation motion could be affected by the materials surface [12].

### 1.4 Plasticity Theory

Structural mechanics analysis can be classified into linear static or nonlinear analyses. In linear analysis, displacements are assumed to be infinitesimal, and Hooke's law is assumed applicable. On the other hand, nonlinearity could arise from the high load application which results in significant geometrical changes in the material. Although loading of a nonlinear material within its elastic regime exhibit a nonlinear stress-strain relation, the material follows a linear elastic behavior while unloading since the material

returns to its initial configuration (Figure 1.7(a)). However, in the nonlinear plasticity, permanent irreversible plastic strain arises (Figure 1.7(b)).



**Figure 1.7 (a) Nonlinear elasticity and (b) elasto-plasticity**

When the material reaches its yield strength, the process is called yielding. As the applied stress exceeds the yield strength, the material then flows, this process is called plasticity. Plasticity theory can be explained by several fundamental concepts such as the yield criterion and the flow rule in which stresses are described in function of strain for the plasticized material. Subjecting material to a specific type of loading (eg., tension, compression, torsion, ...etc) results in elastic strain. As the load increases, plastic strain is then developed. The total strain in the material is the sum of the elastic and plastic strains at any instant of loading [13].

### 1.5 Theoretical Background on Grain Fragmentation Mechanism

Severe plastic deformation (SPD) processes induce extreme microstructure refinement by achieving large strain levels. These processes have played an essential role in designing novel metallic and non-metallic materials [14–19]. Various SPD techniques were developed in the past decades to achieve uniform grain refinement that resulted in superior mechanical properties [20–23]. Examples of SPD processes are equal channel angular pressing (ECAP) [22], high pressure torsion (HPT) [19,23], accumulated roll

bonding (ARB) [24,25], twist extrusion (TE) [26], cyclic extrusion and compression (CEC) [27], and repetitive corrugation and straightening (RCS) [28]. Detailed description, principles, and major structural features of these processes can be found in previous comprehensive reviews [22,23,29,30]. All these techniques rely on imposing high hydrostatic pressure and applying severe shear deformation to the bulk material. As a result of the high strain level attained, dislocation slip, and deformation twinning are the major deformation mechanisms that induce plastic deformation [31]. Each of these deformation modes can be activated differently depending on the crystalline structure and the stacking fault energy (SFE) of the material. Recent studies showed that SPD-processed materials with different SFE exhibit different grain refinement processes [32–36].

### ***1.5.1 Grain Fragmentation in FCC Materials***

For FCC materials, three types of SFEs can be distinguished; high, medium and low SFE materials; since different deformation mechanisms could be activated. Experimental observations on high stacking fault energy materials (SFM), such as Al, showed that the grain refinement is mainly affected by the dislocation slip mechanism [37–42]. Subgrains are rapidly formed at the initial stage of plastic deformation demarcated by dislocation walls, named geometrically necessary boundaries (GNBs). As plastic strain increases, cell walls, formed from the mutual and the statistically trapped dislocations, divide the parent grain into cell blocks. A misorientation resulting from the difference in the lattice rotation between the cell blocks increases, prompted by the movement of GNB trapped dislocations on different slip systems of the neighboring cell blocks [43]. In addition, driven by the reorientation of the cell blocks during deformation,

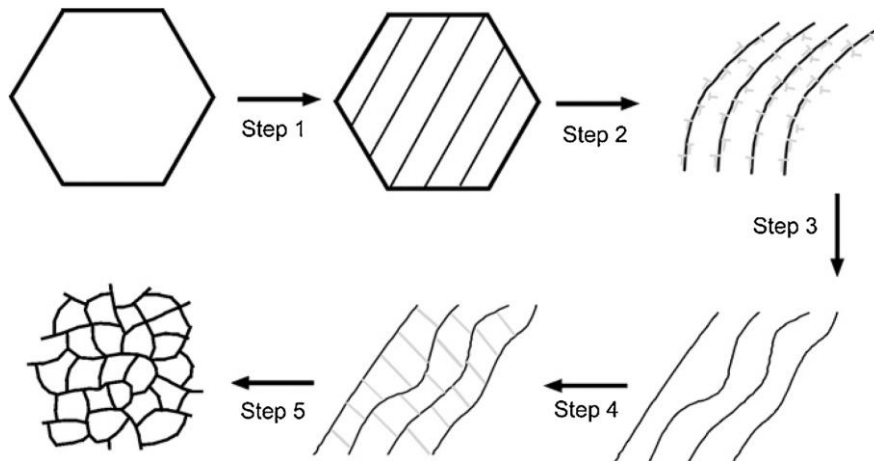
some of the low angle grain boundaries are transformed into high angle grain boundaries [44–47]. Continuous increase of the plastic deformation lead to the increase of the misorientation between cell blocks; thus, lamellar subgrains around interconnecting boundaries are formed [39,45,47–49]. Furthermore, equiaxed grains start to form leading to finer microstructure [41,50,51]. Finally, the plastic deformation reaches a steady state when the multiplication and generation of dislocations are balanced by dynamic recovery mechanisms leading to ultrafine equiaxed grain microstructure [46,52–56].

Materials with medium SFEs, such as Cu, behave similarly to the high SFEs materials when processed under low hydrostatic pressure, low strain rate, and at room temperature where dislocation slip is the major deformation mechanism and deformation twinning is negligible. However, their microstructural evolution differs under different deformation conditions. Unlike high SFE materials, increasing the hydrostatic pressure during SPD processing (e.g., HPT) for the medium SFE microstructures induces more grain refinement. For instance, processing a UFG copper sample by HPT under a pressure of 7 GPa lead to the subdivision of the ultrafine grains into nanodomains [57]. The internal region of these nanodomains contains a high density of nano-twins rather than dislocations that are located mainly at the nanodomains boundaries. At this scale, deformation twinning mechanism dominates the dislocation slip mechanism due to the formation of the nanodomains as suggested in ref. [57]. This observation was contradicted by other studies in which deformation twinning is difficult to occur in the refined microstructures of the course-grained materials [20,58].

Evidently, deformation twinning is the major deformation mechanism that induces effective grain refinement in the SPD-processed FCC materials having low SFEs. Activation of twinning can be affected significantly by the processing conditions such as

strain rate [59,60], temperature [61,62], and stress [63]. Microstructural evolution for low SFE (eg. Cu-30wt% Zn alloy) has been studied by processing the material by HPT for 5 revolutions under a hydrostatic pressure of 5 GPa [64]. The grain refinement process for this alloy is represented schematically in Figure 1.8. Twin lamellae are formed in the ultrafine grains accompanied by an increase in the twins and the dislocations densities since twin boundaries (TBs) act as obstacles for dislocation slip (step 1). The accumulation of dislocations at the TBs transforms the flat coherent TBs into incoherent TBs by gradual bending (step 2). Further shear straining leads to the complete transformation of the incoherent TBs into high-angle grain boundaries (HAGBs) due to the interaction between TBs and dislocations (step 3). This interaction generates new dislocation sources at the GBs that result in the emission of partial dislocations from the new GBs with further deformation in addition to the formation of secondary twins. The intersection between the new GBs and the secondary TBs subdivides the lamellar grains into rhombic domains (step 4). Finally, the secondary TBs are transformed into HAGBs leading to the formation of newly refined microstructure (step 5) [64]. It is worth mentioning here that the aforementioned grain refinement process is very common for all FCC metals with low SFEs [60,65].

As illustrated above, grain refinement can be significantly affected for FCC materials with different SFEs. In general, materials with lower SFEs exhibit enhanced grain refinement since deformation twinning are activated and twin boundary spacings are reduced.



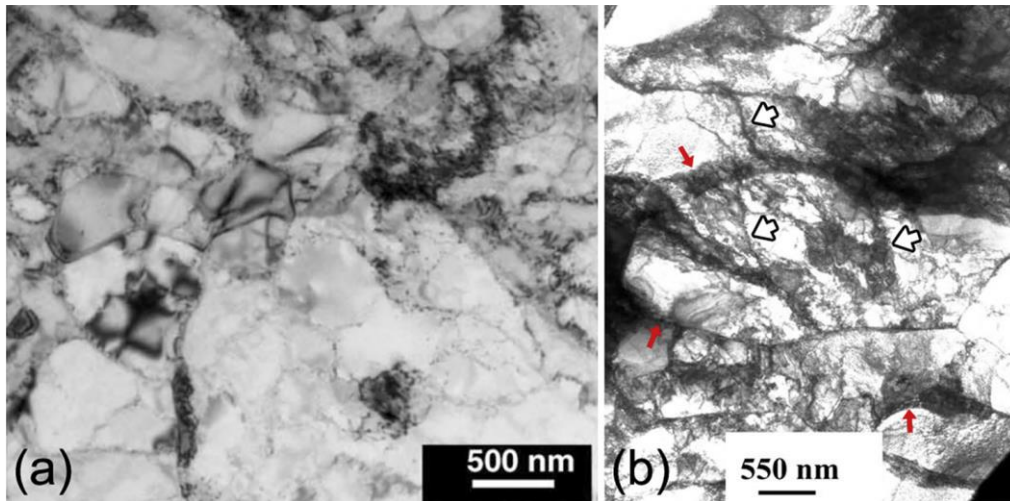
**Figure 1.8 Illustration of grain fragmentation mechanism for the Cu-30wt%Zn alloy processed by high pressure torsion [64].**

### ***1.5.2 Grain Fragmentation in BCC Materials***

Although literatures on SPD-processed BCC materials are not extensive as FCC materials [31], research on some materials can be found including Tantalum (Ta) [66,67], Tungsten (W) [68–70], Molybdenum (Mo) [71,72], Iron (Fe) [73–75] and other materials [76,77]. Dislocation slip in bulk BCC materials has a major effect in inducing plastic deformation while deformation twinning is less common observed [69,76,78,79]. Slip in BCC materials is observed to occur on  $\{110\}$ ,  $\{112\}$ , and  $\{123\}$  slip planes along the  $\langle 111 \rangle$  slip directions [80,81]. Grain refinement process of BCC materials processed by SPD techniques is nearly similar to that illustrated for FCC materials with high SFEs [82–89]. By subjecting the material to high shear strain, dislocation structures develop such that GNBs are formed by trapping dislocations at the subgrain boundaries. Figure 1.9 shows the presence of dislocation walls and subgrain boundaries in Fe processed by HPT (Figure 1.9(a)) and W processed by ECAP then rolling at high temperature (Figure 1.9(b)). As the shear strain increases, similar features observed in SPD-induced FCC materials such as the formation of lamellar dislocation structures and interconnecting boundaries are observed in BCC materials [90,91]. High dislocation densities ( $>$



$10^{16}m^{-2}$ ) can be easily reached due to the dislocation multiplication and interactions while processing by SPD. By attaining sufficiently high shear strains, BCC microstructure reaches a steady-state in which no more grain refinement can occur [76,92,93].



**Figure 1.9** TEM micrographs of (a) HPT processing of a polycrystalline iron up to an equivalent strain of  $\sim 210$  [91]; (b) ECAP+ rolling processing of polycrystalline W at high temperatures [90]. Dislocation walls are indicated by the white arrows while sub-grains boundaries are indicated by red arrows.

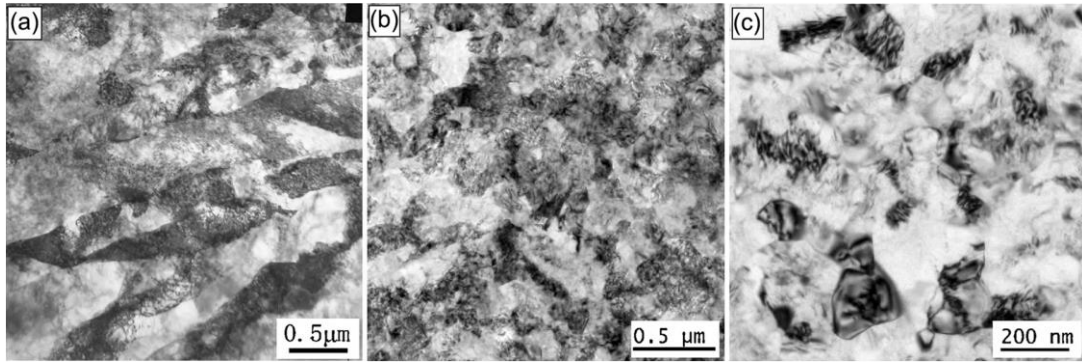
### *1.5.3 Grain Fragmentation in HCP Materials*

In contrast to the cubic materials, both dislocation slip and deformation twinning play an essential role in inducing plastic deformation for HCP materials. HCP materials possess low crystallographic symmetry where slip systems can be categorized as easy slip systems (basal and prismatic) and hard slip systems (pyramidal). Activity for the slip/twinning systems depends on the critical resolved shear stress (CRSS) (Table 1-3) and the  $c/a$  ratio. For HCP structures having  $c/a$  ratio above 1.6 (eg. Mg), dislocations prefer to slip along the  $\langle a \rangle$  basal slip systems while for those having  $c/a$  ratio below 1.6, dislocations prefer to slip along the prismatic  $\langle a \rangle$  slip systems. In addition, activation of pyramidal  $\langle a \rangle$  slip systems could also occur in some HCP materials [94]. Since slip

systems with  $\langle a \rangle$  Burgers vectors do not exhibit more than four independent slip systems, dislocations moving along the  $\langle a \rangle$  slip systems are insufficient to fulfill the von Mises criterion which requires at least five independent slip systems to achieve strain compatibility [94,95]. Therefore, activation of  $\langle c+a \rangle$  pyramidal slip systems and/or deformation twinning systems are required to obtain homogeneous deformation of HCP metals. According to the abovementioned features, SPD-induced HCP microstructures affected by both dislocation slip and deformation twinning will behave differently from FCC and BCC microstructures. Dislocation slip is a dominant deformation mechanism that induces grain refinement of HCP materials [96–99]. TEM images of a commercially Ti material processed by ECAP showed that grain refinement occurs in several stages. First, after the first pass, parallel and complex shear bands containing high densities of dislocations are formed [100]. Then, the ECAPed Ti sample processed for 2 passes (strain =1.2) (Figure 1.10(a)) showed that grains with interconnecting boundaries are formed. With further straining (Figure 1.10(b)) (up to 6 ECAP passes, strain = 3.6), the microstructure is transformed into an ultrafine grained microstructure with indefinite GBs. After 8 ECAP passes, Ti microstructure becomes evident with sharp GBs and the average grain size saturates at 200 nm [100] (Figure 1.10(c)).

**Table 1-3 Estimated CRSS (MPa) for five common deformation systems in Mg and Ti. (CRSS data for Mg and Ti were obtained for the temperature ranges of 500–600 K and 200–600 K, respectively)**

Materials	Basal $\langle a \rangle$ slip	Prismatic $\langle a \rangle$ slip	Pyramidal $\langle c+a \rangle$ slip	$\{10\bar{1}2\}\langle\bar{1}011\rangle$ extension twinning	$\{10\bar{1}1\}\langle10\bar{1}2\rangle$ Contraction twinning
Mg [101–103]	2.7-13	12-20	24-45	10-18	100
Ti [95,104–108]	49-150	37-98	120-224	125-213	N/A



**Figure 1.10** TEM images of a Ti sample processed by ECAP (channel angle=120°) through (a) 2 passes, (b) 6 passes and (c) 8 passes at room temperature [100].

In addition to dislocation slip, grain refinement of the SPD-induced HCP materials is influenced significantly by deformation twinning required for shear strain accommodation along the *c*-axis [10,101]. Unless the material is not oriented intentionally to favor the  $\langle a \rangle$  slip, deformation twinning competes for dislocation slip vigorously in the coarse-grained HCP materials [109–112]. Several conditions such as temperature [112,113], stress state [101,114], strain rate [115] and *c/a* ratio [95,116] have revealed the formation of different types of deformation twins with various thicknesses. For example, ECAP processing of Ti samples has shown the formation of deformation twins with thicknesses varying between 80 nm and 500 nm [117,118]. In addition, for the same type of twin (eg. extension twin  $\{10\bar{1}2\}\langle\bar{1}011\rangle$ ), several crystallographic systems could be active leading to twinning intersections that expedite the grain refinement process [115,119]. Similar to the FCC materials with low SFEs, activation of deformation twinning is influenced significantly by the grain size of the HCP materials in which microstructures with smaller grain sizes impedes the deformation twinning occurrence [120–123].

## **1.6 Thesis Overview**

### ***1.6.1 Motivations and Objectives***

Understanding the scientific principles of severe plastic deformation induced by SPD processes has revealed a great importance in developing technological needs. Tracing the past century, Bridgman was found to be the first one who noticed the increase of material compressive strength subjected to twisting [124]. Bridgman works then focused on studying the mechanical behavior of bulk metals under very high pressures where he invented an apparatus to produce extreme pressures and was awarded a Nobel Prize in Physics for this work [19]. Research in material strengthening field continued where numerous SPD processing techniques have emerged and developed (refer to section 1.5). These techniques have revealed high efficiency in producing ultrafine grained materials which exhibit superior mechanical properties. One of these attractive techniques is the equal channel angular pressing process due to several reasons. ECAP can be applied to wide range of materials with various crystal structures, performed on both small- and large-scale billets to be used in structural applications, and can achieve reasonable homogeneity for billets pressed to very high strains. In addition, ECAP process may be developed and scaled-up accordingly for use in metal-processing within the commercial sectors [22]. These various attractive features have attracted many corporations and laboratories to invest in developing ECAP process over the last decades. The strength-to-ductility relationship in ultrafine grained materials produced by ECAP has attracted material scientists to investigate the hidden power behind this process. Thus, numerous experimental studies were performed to investigate the grain refinement mechanism induced by ECAP. In spite of the importance of the experimental work, modeling of such mechanisms has gained significant interest due to its time-efficiency and low-cost

compared to the experiments. Thus, several modeling approaches were proposed and developed to mimic and predict the experimental results. However, despite the various studies that focused on modeling grain refinement of metallic materials, some of the fundamental issues about modeling this mechanism still remain unclear in literature. Some examples include the grain-grain interaction effect, the strain hardening effect on grain refinement, and the influence of dislocation density on grain size reduction and slip/twin activity during equal channel angular pressing. To illustrate these effects on various metallic structures such as FCC and HCP structures, a hybrid multiscale model that describes the main deformation mechanisms during severe plastic deformation processes is proposed.

The main objectives of the following research are as follows:

- Implement the continuum dislocation dynamics model into the crystal plasticity scheme using Fortran language to mimic the deformation mechanisms induced by plastic deformation.
- Develop a novel grain refinement approach to predict the evolution of grain size reduction during the severe plastic deformation process.
- Analyze and investigate the texture and microstructural features of ECAPed materials under different routes.
- Predict the mechanical properties of the processed metallic materials.

### ***1.6.2 Chapter Summaries***

This dissertation comprises a total of five chapters starting from the current chapter. The rest four chapters' descriptions are as follows:

In chapter 2, a grain fragmentation modeling approach that couples continuum dislocation dynamics analysis with a crystal-plasticity framework is proposed. The

proposed model investigates the microstructural features of FCC metals subjected to severe plastic deformation (SPD) processes and in particular equal channel angular pressing (ECAP). Several aspects of the deformation process are considered in this model, including texture evolution, statistically stored dislocations (SSDs) and geometrically necessary dislocations (GNDs) densities evolution, and grains fragmentation and its effect on the overall mechanical response. The proposed model is applied to a reference volume element (RVE) in which the grains are distributed and assigned an initial position. Within the model, each grain has the ability to split into 1024 new smaller grains, which subsequently leads to strain hardening and grain refinement. The model parameters are calibrated using torsion tests of pure copper material. The simulation results give reliable predictions of the crystallographic texture, the evolution of dislocation density, and the final grain size based on available experimental data.

The proposed multiscale model is upgraded in chapter 3 in which each grain is allowed to split into nine subgrains instead of four subgrains. An Al-1100 billet, with rolling texture, is ECAP processed under Route C for different numbers of passes. Mechanical, microstructure, and texture characterization is achieved for the received and ECAPed materials. The proposed model parameters are calibrated using the tensile true-stress true-strain curves of the unprocessed material at two strain rates. The ECAP-processed aluminum microstructure, texture and dislocation densities and then the mechanical properties are predicted.

In chapter 4, we investigate and analyze the microstructural evolution of an equal channel angular pressed (ECAPed) Mg-3Al-1Zn rolled billet, processed at 200°C. The model parameters are first calibrated on the tensile behavior of the highly anisotropic as-received material along two different loading axes and two different temperatures. The

ECAP-processing of the Mg-3Al-1Zn induced a large reduction of the average grain size from 20  $\mu\text{m}$  into 2~4  $\mu\text{m}$  after four ECAP passes. The proposed model accurately captured the ECAP resulting textures, the average grain size as well as the dislocation density evolution and slip/twin activities post-mechanical properties under different routes and number of passes. Additionally, dislocation density evolution and slip/twin activities are predicted and analyzed by the proposed model anisotropic behavior of the ECAPed samples is predicted and analyzed based on slip/twin activity and dislocation density evolution.

The dissertation is closed in chapter 5 with a final summary and recommendations for future work.

## CHAPTER 2

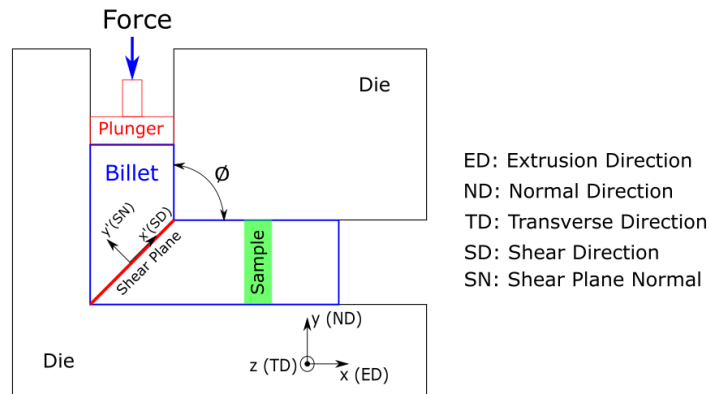
# CONTINUUM DISLOCATION DYNAMICS-BASED GRAIN FRAGMENTATION MODELING

### 2.1 Introduction

Metallic materials subjected to severe plastic deformation (SPD) develop improved mechanical properties, mainly induced by grain refinement and increasing dislocation density. SPD materials exhibit extremely refined grains of sub-micron size. There are different manufacturing processes by which SPD grain refinement can be achieved, such as equal-channel angular pressing, high-pressure torsion, and accumulated roll bonding [125].

Equal-channel angular pressing (ECAP) has now become a conventional technique to enhance the mechanical properties of metals. ECAP is a thermomechanical process in which the material is subjected to severe plastic deformation leading to a drastic increase in the dislocation density. The internal energy associated with the dislocation microstructure reaches high levels, and as a result, the material undergoes grain fragmentation as a relief mechanism. Numerous studies were conducted to uncover the grain refinement mechanisms and their effects on the texture and the microstructure of metals [21,22,29,126–131]. ECAP was studied extensively due to its advantage of achieving large strains while preserving the cross-sectional area of the sample [132]. Figure 2.1 shows a schematic of the ECAP process, in which a plunger presses a billet through a die. The die consists of two channels with equal cross-sections intersecting at an angle  $\phi$ . Repeating the pressing of the sample leads to a high level of strain and significant grain refinement [22,29,30].

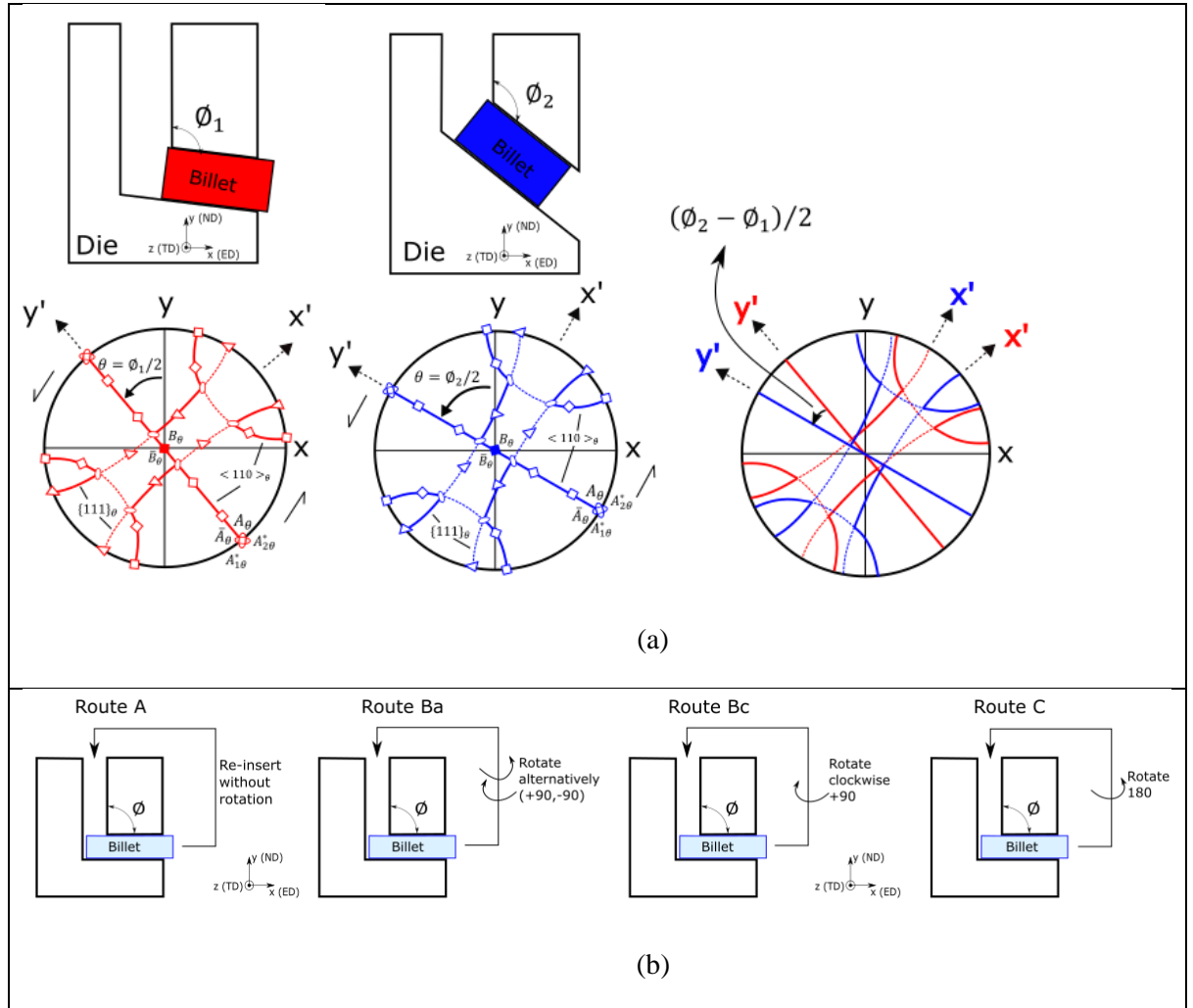




**Figure 2.1 Schematic of the ECAP mechanism**

The combination of several ECAP process parameters, such as the die geometry (i.e., die angle), the number of passes, the deformation routes, and the back pressure, yields to a wide range of texture and microstructure features within the material [129]. The die angle  $\phi$  influences the texture evolution in two ways, first by deviating the texture from the ideal orientations resulting from simple shear. For instance, if two identical textures are pressed using the same route through two dies with different angles ( $\phi_1$ ,  $\phi_2$ ), the expected difference in the resulting texture is a rotation of  $(\phi_1 - \phi_2)/2$  about the transverse direction (TD) (Figure 2.2(a)) [30]. Second, the die angle  $\phi$  impacts the texture evolution, which is directly related to the level of induced shear deformation, i.e., by decreasing  $\phi$  the induced shear deformation increases, leading to the formation of a stronger texture. Furthermore, ECAP routes (Figure 2.2(b)) and pass numbers significantly affect the texture evolution. In both routes A and C, texture symmetry can be achieved by rotating the sample around the TD axis only. Therefore, the TD axis is called the “texture symmetry axis,” where the monoclinic symmetry is lost by any rotation around the other axes. However, in routes  $B_a$  and  $B_c$ , the initially monoclinic symmetry is lost after the first pass since the texture is rotated between passes around a non-symmetric axis [133]. Gholinia et al. (2000) evaluated the strain in different routes and

demonstrated that the highest strain levels are achieved by maintaining an identical route throughout the process. Furthermore, routes  $B_a$  and  $B_c$  are found to induce the highest levels of grain fragmentation [134].



**Figure 2.2 (a) Processing billets through different ECAP die angles and the ideal orientations of the ECAP textures for FCC metals in a  $\{111\}$  pole figure, (b) ECAP routes: A, Ba, Bc, and C. Route A: re-insert the billet without rotation around ED but only 90 around TD. Route Ba: re-insert with rotation 90 alternatively around ED and 90 around TD after each pass. Route Bc: re-insert with rotation 90 clockwise around ED and 90 around TD after each pass. Route C: rotate 180 around ED and 90 around TD between passes .**

Numerous investigations on the texture and the microstructural development in ECAP-processed FCC metals have been conducted over the past years. Sun et al. (2003) showed that using different deformation routes does not only affect the grains' shape, but

also affects the grain refinement rate [17]. Suwas et al. (2006) reported that for copper samples pressed via route A, texture showed very strong components in the first two passes [135]. Weakening of texture components follows when additional passes are applied. Moreover, the strong and weak texture components of the three materials were shifted from their ideal positions as the deformation increased. Lapovok et al. (2008) processed AA6111 aluminum alloy sheets used by the automotive industry through ECAP. They reported that the average grain size was refined, the as-rolled texture components were reduced, and an acceptable level of bi-axial ductility was achieved [136]. In order to study the effect of a high number of ECAP passes, Alexander and Beyerlein (2005) ECAP-processed high-purity copper up to four passes via route C. The mechanical properties were determined after each pass, and the results were compared to the ones reported on the same material ECAP-processed via route  $B_c$ . It was observed that both compression-yield stresses and flow stresses were greater than those in tension. Moreover, similar compression-flow stresses were measured for copper ECAP-processed in routes  $B_c$  and C after the same number of passes [137]. Although the ECAP process enhances the mechanical response of pure aluminum, Reihanian et al. (2008) found that the material's strength starts to decrease after a threshold number of passes [138]. In addition, Vega et al. (2015) reported that there is no significant change in terms of strength for an aluminum sample when processed by ECAP alone or by ECAP followed by rolling. However, essential consequences were observed on the microstructural level. During ECAP, high angle grain boundaries (HAGB) were aligned with the shear direction, while during rolling HAGB were re-aligned in the rolling direction, forming a lamellar structure [139]. In spite of all the experimental and theoretical advancements in the area of SPD-induced microstructure and mechanical properties, understanding the

mechanisms of grain refinement is still lacking.

Over the past years, significant attempts for predicting grain refinement and texture evolution of ECAP-processed materials using either phenomenological- or crystal-plasticity-based models have been reported [109,140–150]. Beygelzimer (2005) proposed a phenomenological modeling approach for describing the grain refinement mechanism. The grain refinement mechanism was considered to be active when sufficient pressure and strain were reached. The model assumed the self-similarity of the grain refinement process [140]. A quantitative approach, proposed by Petryk and Stupkiewicz (2007), accounted for the grain fragmentation process. The model described explicitly the microstructural changes of FCC metals and predicted the major features of grain refinement and strain hardening during SPD. This model predicted the yield stress, grain size, and HAGB (high angle grain boundary) distribution; however, it neglects the texture [143].

Crystal plasticity-based approaches were used to model grain fragmentation. Beyerlein et al. (2003) used a visco-plastic self-consistent (VPSC) based model [144] to study the texture development and microstructural evolution and to account for grain fragmentation in FCC materials [141]. While the proposed model takes into consideration the influence of the grain shape in the subdivision criteria, it neglects the intragranular microstructure. Several researchers have studied grain refinement by combining a VPSC model with a disclination modeling approach [145,146]. The grain fragmentation mechanism was activated only when a grain was deforming more slowly than the surrounding medium. Therefore, the grain fragmentation (each grain is allowed to split into two) occurred when the crystals were oriented favorably with respect to the applied strain. Frydrych and Kowalczyk-Gajewska (2016) combined a grain refinement criterion

with a crystal plasticity framework by assuming that each grain is initially subdivided into several subdomains. Each subdomain is slightly misoriented with respect to the nominal orientation of its parent grain. As strain increases, an evolving misorientation angle for each subdomain is calculated with respect to the mean orientation of the parent grain. When the misorientation angle between subdomains reaches a threshold value, the grain fragmentation mechanisms are activated [147].

As stated earlier, grain refinement is induced during an ECAP pass; the average grain size can drop below the micron level for some cases, and thus enhancement in the material's strength is reported [151–154]. This size-dependent strengthening behavior, the so-called Hall-Petch effect, can be explained by the pile-up of dislocations on the grain boundaries that hinders the dislocation motion. The classical plasticity approach cannot be used to explain the size effect since it does not take into consideration an internal length scale. For this reason, plasticity theories that involve strain gradients have been developed to capture the size effect more precisely [152–154]. Within these models, dislocations are considered to be the main attribute for material hardening and they are divided into two types, the statistically stored dislocations (SSDs) and the geometrically necessary dislocations (GNDs). The SSDs refer to randomly trapped dislocations that arise as a result of plastic strain. However, the GNDs refer to dislocations accompanied by a plastic strain gradient. GNDs are formed in order to accommodate the lattice curvature during the non-uniform plastic deformations, as introduced by Nye [155] and then expanded by Ashby [156]. In order to incorporate the GNDs' effect in the model, Ohashi (2005) and Ohashi et al. (2007) proposed an approach by accounting for the effective dislocation mean free path [157,158]. In this context, the GNDs are incorporated within a multiscale model that couples continuum dislocation dynamics (CDD) with a

crystal plasticity (CP) framework [159].

Inspired by the strain gradient theory, a physically based model accounting for grain fragmentation incorporated into a crystal plasticity framework was presented by Toth et al. [148]. The authors assumed that grain rotation is impeded near the grain boundaries, inducing the development of a lattice curvature. The development of lattice curvature resulted in an increasing internal grain misorientation and consequently led to grain fragmentation. On that basis, a grain fragmentation scheme was integrated into a Taylor crystal plasticity model. The authors assumed that each subgrain can be reoriented depending on the encountered strain level; therefore, if the misorientation angle between subgrains exceeds a threshold value, the subgrain is then considered as a new grain. The model was validated by comparing the predicted and experimental textures and the final average grain size of pure copper ECAP processed in two  $B_C$  passes [148].

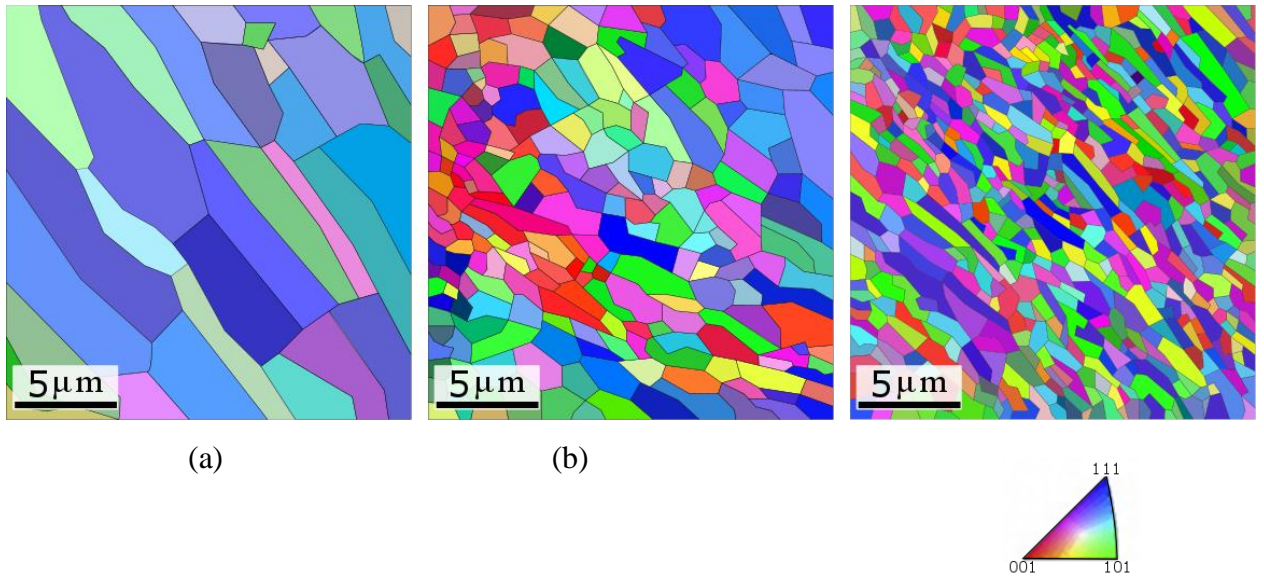
Some research has been done on modeling grain refinement during ECAP processes; however, to the best of our knowledge, no studies have considered the influence of the neighboring grains and the position of the grain in the microstructure. The current work proposes an efficient predictive model to simulate the behavior of ECAP-processed materials using continuum dislocation dynamics coupled with a crystal plasticity model. The grain fragmentation hypothesis used in this work is based on the Toth et al. [148] lattice curvature assumption, which assumes that the orientation of a single crystal undergoes changes induced by a higher accumulation of dislocations near the grain boundary. The grain fragmentation process is considered by accounting for the accumulation of GNDs at the grain boundary (GB) resulting in increasing lattice curvature. As a result, a misorientation will develop within a grain that will activate the refinement process when a threshold value of misorientation is reached. This paper is

organized as follows: in section 2.2, the grain fragmentation criterion and the constitutive equations coupling the continuum dislocation dynamics with the crystal plasticity models are described. In section 2.3, the experimental data of torsion and ECAP on copper samples are presented. Discussions and comparisons between the experimental and modeling results are presented in section 2.3. Finally, concluding remarks are given in section 2.4.

## **2.2 Methodology**

Polycrystalline ECAP-processed metals undergo severe plastic deformation that induces grain size refinement, texture evolution, and consequently an increase of the dislocation density. The grain fragmentation rate was demonstrated by Reihanian et al. (2008) to increase as the number of ECAP passes increases [138]. A schematic representation of the EBSD map (Figure 2.3), based on the Reihanian et al. (2008) results, illustrates the fragmentation process of Al samples subjected to 1, 4, and 8 ECAP passes, respectively. After the first pass (Figure 2.3(a)), mainly elongated grains with low angle misorientation grain boundaries constitute the microstructure, with an average grain size of 1.6  $\mu\text{m}$ . After 4 ECAP passes, equiaxed and elongated grains with some high-angle-misorientation grain boundaries are formed, with an average grain size of 0.56  $\mu\text{m}$  (Figure 2.3(b)). The average grain size reaches 0.37  $\mu\text{m}$  after 8 ECAP passes, and the microstructure is constituted mainly of equiaxed and high-angle-misorientation grain boundaries (Figure 2.3(c)). The transformation of low-angle grain boundaries into high-angle misorientations is a clear indication that the grain refinement mechanism results from increasing the misorientation between subgrains. Consequently, the materials will release the accumulated energy by splitting the grains once a threshold value of

misorientation is attained.

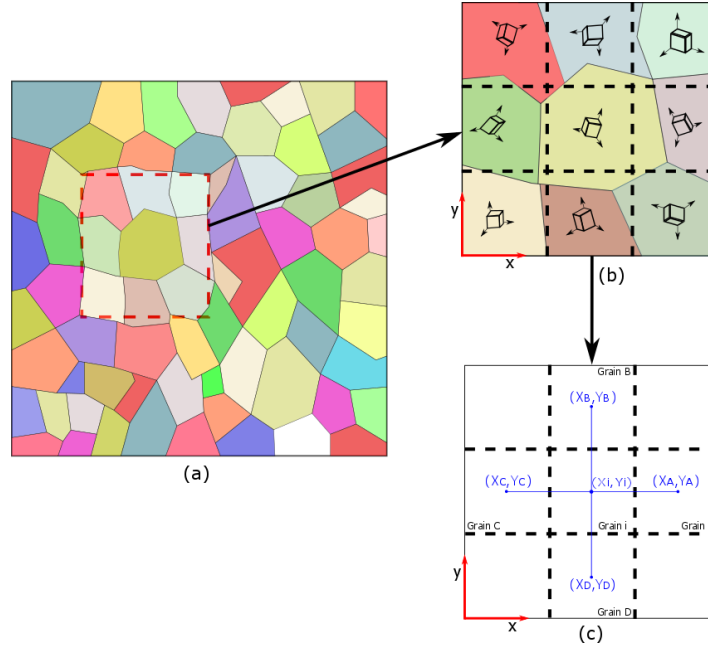


**Figure 2.3 Schematic representation of EBSD maps of the ECAP-processed samples subjected to (a) 1 pass, (b) 4 passes, and (c) 8 passes (based on the results presented by Reihanian et al. (2008) [138])**

In order to simplify our analysis, the initial microstructure of the material is assumed to have equiaxed grains similar to the one presented in Figure 2.4(a). The domain is discretized into a uniform mesh of square elements. Each element represents a single grain surrounded by 8 neighboring grains, and each grain is assigned a position and orientation as presented in Figure 2.4(c). In our simulations, the grains keep a constant square shape; however, the square size evolves depending on the fragmentation rate. The stress and strains on each grain and the average stress on all the grains are computed using the single crystal plasticity and Taylor Linn polycrystalline approach following Kalidindi et al. (1992) [160]. The grid is used for the calculation of the geometrically necessary dislocations and to illustrating the grain fragmentation.

In this work, tensors and vectors are denoted by bold-face symbols.





**Figure 2.4 (a) Schematic representation of the polycrystal, (b) different crystal orientations, (c) grid representing the grain positions**

### 2.2.1 Summary of the Modeling Framework

Crystal plasticity is used to capture the behavior of each crystal. The overall response of the polycrystal is captured using a Taylor-Lin homogenization scheme [161–163]. In this scheme, all grains are assumed to have equal grain size, and the deformation gradient associated with each grain is assumed to be identical to the macroscopic deformation gradient as proposed by Asaro and Needleman (1985) [164]. The overall stress of the structure can be written as follows:  $\mathbf{T} = \frac{1}{N} \sum_{k=1}^N w^{(k)} \mathbf{T}^{(k)}$  where  $N$  is the total number of crystals and  $\mathbf{T}^{(k)}$  and  $w^{(k)}$  correspond to the Cauchy stress and the weight factor of the  $k^{th}$  grain, respectively. In this work, Kalidindi et al. (1992) mathematical framework of the single crystal plasticity model is adopted. The crystal plasticity model accounts for slip in FCC materials. In this work, the plastic shear rate is described by the continuum dislocation dynamics (CDD) approach [159,165].

In a metallic single crystal, the elastic portion of the deformation is small

compared to the plastic portion [160]. Therefore, the stress in each grain is taken to be the second Piola-Kirchhoff stress tensor, and the constitutive equation is expressed as follows:

$$\mathbf{T}^* = \mathcal{L} \cdot \mathbf{E}^e \quad (2.1)$$

The Cauchy stress is determined from the second Piola-Kirchhoff stress by the following relation:  $\mathbf{T}^{(k)} = \frac{1}{\det \mathbf{F}^e} \mathbf{F}^e \mathbf{T}^* \mathbf{F}^{e-T}$ . Where  $\mathbf{E}^e = \frac{1}{2}(\mathbf{F}^{eT} \mathbf{F}^e - \mathbf{I})$  is the elastic Green-Lagrange strain tensor,  $\mathbf{I}$  is the identity tensor and  $\mathcal{L}$  is the fourth-order stiffness tensor. The deformation gradient  $\mathbf{F}$  can be decomposed into elastic part  $\mathbf{F}^e$  and plastic distortion part  $\mathbf{F}^p$ . The elastic part is associated with the elastic stretching and rotation of the lattice, while the plastic part is associated to the distortion of the crystal lattice due to the formation of dislocations. The deformation gradient can be written as  $\mathbf{F} = \mathbf{F}^e \mathbf{F}^p$ , as proposed by Lee (1969) [166]. In this work, the superscript “e” and “p” denotes the elastic and plastic parts, respectively. The time derivative of the deformation gradient is written as  $\dot{\mathbf{F}} = \mathbf{L} \mathbf{F}$ , where  $\mathbf{L}$  is the velocity gradient. The velocity gradient may be decomposed, according to Lee (1969) [166], multiplicatively and additively as  $\mathbf{L} = \dot{\mathbf{F}} \mathbf{F}^{-1}$  and  $\mathbf{L} = \mathbf{D} + \mathbf{W}$ , respectively, where  $\mathbf{D} = 1/2 (\mathbf{L} + \mathbf{L}^T)$  is the stretching tensor rate and  $\mathbf{W} = 1/2 (\mathbf{L} - \mathbf{L}^T)$  is the spin tensor. Alternative decomposition for the velocity gradient can be done as follows:  $\mathbf{L} = \mathbf{L}^e + \mathbf{L}^p = \dot{\mathbf{F}}^e \mathbf{F}^{e-1} + \mathbf{F}^e \dot{\mathbf{F}}^p \mathbf{F}^{p-1} \mathbf{F}^{e-1}$ , with  $\mathbf{L}^e = \mathbf{D}^e + \mathbf{W}^e$  and  $\mathbf{L}^p = \mathbf{D}^p + \mathbf{W}^p$ , where  $\mathbf{D}^e$  and  $\mathbf{D}^p$  are the elastic and plastic stretching tensors, respectively, and  $\mathbf{W}^e$  and  $\mathbf{W}^p$  are the elastic and plastic spins, respectively. The plastic deformation gradient can be determined from  $\dot{\mathbf{F}}^p = \mathbf{L}^p \mathbf{F}^p$ , expressed as a function of the plastic velocity and deformation gradients. The plastic velocity gradient is expressed as the sum over the “s” slip systems of the product identity tensor with the plastic distortion as:

$$\mathbf{L}^p = \sum_s^{N_s} \dot{\gamma}^s \mathbf{S}^s \quad (2.2)$$

where  $\dot{\gamma}^s$  is the slip shear rate on the ‘s’ slip system,  $N_s$  is the total number of slip systems and  $\mathbf{S}^s = \mathbf{m}_0^s \otimes \mathbf{n}_0^s$  is the Schmid tensor.  $\mathbf{m}_0^s$  and  $\mathbf{n}_0^s$  are unit vectors defining, in the initial configuration, the slip direction and the slip-plane normal of the ‘s’ slip system, respectively. The evolution of the slip systems’ direction and normal is determined as follows:  $\mathbf{m}^s = \mathbf{F}^e \cdot \mathbf{m}_0^s$  and  $\mathbf{n}^s = \mathbf{n}_0^s \cdot \mathbf{F}^{e-1}$ , respectively [160].

### 2.2.2 CDD Model

This study developed a hybrid continuum-dislocation-dynamic model coupled with a Taylor-Lin polycrystalline plasticity approach. This hybrid model can predict experimental severe plastic deformation in polycrystalline FCC materials. In this approach, the dislocation density evolution rates of the mobile and immobile dislocations are used to compute the shearing rate in each grain. The plastic shear rate  $\dot{\gamma}^s$  can be described by a phenomenological power law as proposed by Needleman et al. (1985) [167] and Anand (1992) [168] or alternatively by the continuum dislocation dynamics (CDD) approach, where  $\dot{\gamma}^s$  and the hardening behavior is calculated by considering the dislocation velocities and dislocation reactions [159,165]. In this framework, the plastic shear rate  $\dot{\gamma}^s$  in the slip system “s” is determined by the Orowan relationship [169]:

$$\dot{\gamma}^s = \rho_m^s b v_g^s \quad (2.3)$$

where  $\rho_m^s$  is the mobile dislocation density in slip system “s”,  $b$  is the magnitude of the Burger vector, and  $v_g^s$  is the dislocation glide velocity on system “s”, which takes the power law form:

$$\begin{cases} v_g^s = v_0 \left| \frac{\tau^s}{\tau_{th}^s} \right|^{1/\eta} \text{sign}(\tau^s) & \text{for } \tau^s \geq \tau_{th}^s \\ v_g^s = 0 & \text{for } \tau^s < \tau_{th}^s \end{cases} \quad (2.4)$$

where  $v_0$  is the reference velocity,  $\eta$  is the strain rate sensitivity factor,  $\tau^s$  is the resolved shear stress on slip system “s” and  $\tau_{th}^s$  is the threshold stress of slip system “s”. The resolved shear stress on each slip/twinning system identified in the current configuration is written as  $\tau^s = \mathbf{T}^* : \mathbf{S}^s$ . The threshold stress can be decomposed as follows:

$$\tau_{th}^s = \tau_0 + \tau_{HP}^s + \tau_H^s \quad (2.5)$$

where  $\tau_0$  is the initial critical resolved shear resisting the movement of dislocations,  $\tau_{HP}^s$  is the Hall-Petch stress which captures the energy required for glide and pileup dislocations to overcome the boundary obstacle, and  $\tau_H^s$  is the shear stress resulting from the long-range interactions between dislocations. The Hall-Petch stress is inversely proportional to the square root of the average grain size D (D is experimentally measured) and expressed as  $\tau_{HP}^s = K^s D^{-0.5}$ , where  $K^s$  is the Hall-Petch parameter. The dislocation long-range interaction term can be determined using the Bailey-Hirsh [158] relation such that:

$$\tau_H^s = \sum_{r=1}^{N_{si}} \Omega^{sr} \alpha_{BH} \mu b \sqrt{\rho_{TS}^r} \quad (2.6)$$

where  $\alpha_{BH}$  is the Bailey-Hirsh coefficient in the order of 0.1,  $\mu$  is the shear modulus,  $N_{si}$  is the number of slip systems that interact with the slip system “s”,  $\rho_{TS}^r$  is the total statistically stored dislocation density representing the sum of mobile ( $\rho_m^r$ ) and immobile ( $\rho_i^r$ ) dislocation densities in the slip system “r” ( $\rho_{TS}^r = \rho_m^r + \rho_i^r$ ), and  $\Omega^{sr}$  is the interaction

matrix that describes the self and the latent hardening contributions among the slip systems. The hardening matrix  $\Omega^{sr}$ , for fcc crystals, is a 12x12 matrix.  $\Omega^{sr}$  can be written as follows:

$$\Omega^{sr} = \begin{Bmatrix} A & qA & qA & qA \\ qA & A & qA & qA \\ qA & qA & A & qA \\ qA & qA & qA & A \end{Bmatrix} \quad (2.7)$$

where A is a 3x3 matrix fully filled by ones, and q is the ratio of the latent hardening rate to the self hardening rate .

In CDD modeling, the dislocation densities evolve according to the six rate equations. These rate equations account for the physical contribution of the mobile and immobile dislocations to the hardening behavior of the material [170]. The different rate equations can be identified by discrete dislocation dynamic (DDD) simulations [171,172].

The first rate equation captures the multiplication and generation of mobile dislocations due to the propagation of the resident dislocations and the production of Frank-Read source dislocations:

$$\dot{\rho}_{m1}^s = \alpha_1 \rho_m^s v_g^s / \bar{l} \quad (2.8)$$

where  $\alpha_1$  is the dislocation multiplication coefficient,  $\rho_m^s$  is the mobile dislocation density in slip system “s”, and  $\bar{l}$  is the mean free path of dislocations. The second rate equation describes the annihilation of two mobile dislocations of either the edge or the screw dislocation type having opposite signs in slip system “s”:

$$\dot{\rho}_{m2}^s = -2\alpha_2 R_c (\rho_m^s)^2 v_g^s \quad (2.9)$$

where  $\alpha_2$  is the dislocation annihilation coefficient and  $R_c$  is the critical radius for the dislocation annihilation event (two mobile dislocations of opposite polarities can

mutually annihilate while moving along the same slip plane and once they reach a critical distance between each other).  $R_c$  is set to be 15 times the burgers vector for all slip systems. The third rate equation accounts for the immobilization of mobile dislocations due to the formation of dipoles and junctions:

$$\dot{\rho}_{m3}^s = -\alpha_3 \rho_m^s v_g^s / \bar{l} \quad (2.10)$$

where  $\alpha_3$  is the immobilization parameter. The fourth rate equation refers to the mobilization of the immobile dislocations due to the breakup of junctions, dipoles, pinning parts, etc., when a critical stress is reached.

$$\dot{\rho}_{m4}^s = \alpha_4 (|\tau^s| / \tau_{th}^s)^\zeta \rho_i^s v_g^s / \bar{l} \quad (2.11)$$

where  $\tau_{th}^s$  is the threshold stress,  $\rho_i^s$  represents the immobile dislocation density,  $\alpha_4$  is the mobilization parameter, and  $\zeta$  is a constant set to 0.5. The cross slip contribution is considered in the fifth rate equation. Cross slip takes place when a screw dislocation in a specific slip system jumps to another slip system during plastic deformation. The change in dislocation density can be written as follows:

$$\dot{\rho}_{m5}^s = \alpha_5 \sum_{\beta=1}^{N_{cs}} P^{s\beta} \rho_m^\beta v_g^s / \bar{l} \quad (2.12)$$

where  $\alpha_5$  is the fraction of the screw dislocations that cross-slip from one-slip plane into another glide plane during plastic deformation,  $N_{cs}$  is the number of cross-slip planes (e.g., in FCC metals  $N_{cs}=2$ ) and  $P^{s\beta}$  is the probability matrix that describes whether cross-slip would occur or not. The components of the matrix  $P^{s\beta}$  are obtained from Monte Carlo analysis. This matrix assumes values of 0, -1, or +1 corresponding to no cross slip, dislocation transition to the slip plane “s”, and dislocation transition from the slip plane “s”, respectively. The sixth rate equation corresponds to the trapping of mobile dislocations due to the interaction with immobile dislocations, thus reducing

mobile dislocation density:

$$\dot{\rho}_{m6}^s = -\alpha_6 R_c \rho_m^s \rho_i^s v_g^s \quad (2.13)$$

The material parameters ( $\alpha_1 - \alpha_6$ ) can be obtained from discrete dislocation dynamics analysis as outlined by Li et al. (2014) [171] or by fitting the model with the experimental data as presented in section 2.3.1. The evolution equations of both mobile and immobile dislocation densities can be expressed by adding the effect of the above six rate equations:

$$\begin{aligned} \dot{\rho}_m^s = & \alpha_1 \rho_m^s v_g^s / \bar{l} - 2\alpha_2 R_c (\rho_m^s)^2 v_g^s - \alpha_3 \rho_m^s v_g^s / \bar{l} + \alpha_4 (|\tau^s| / \tau_{th}^s)^\zeta \rho_i^s v_g^s / \bar{l} \\ & + \alpha_5 \sum_{\beta=1}^{N_{cs}} P^{s\beta} \rho_m^\beta v_g^s / \bar{l} - \alpha_6 R_c \rho_m^s \rho_i^s v_g^s \end{aligned} \quad (2.14)$$

The evolution of the immobile dislocation density is expressed as

$$\dot{\rho}_i^s = \alpha_3 \rho_m^s v_g^s / \bar{l} - \alpha_4 (|\tau^s| / \tau_{th}^s)^\zeta \rho_i^s v_g^s / \bar{l} - \alpha_6 R_c \rho_m^s \rho_i^s v_g^s \quad (2.15)$$

### 2.2.3 Geometrically Necessary Dislocations

Geometrically necessary dislocations (GNDs) are dislocations corresponding to the additional storage of material defects required to accommodate the lattice curvature during plastic deformation [173]. In other words, GNDs are indispensable for the compatibility of the grain deformation that can be perturbed by the lattice mismatch at the grain boundaries [174]. In this context, GNDs act as obstacles to the movement of mobile dislocations and hence contribute to the hardening of the material [173]. The relation between GND densities and plastic strain gradients is described by Nye's dislocation density tensor [155]. The effect of GNDs is implemented in the mean free path of the moving dislocations  $\bar{l}$ . GNDs accumulate near the grain boundary, resulting in the reduction of the mean free path by hindering the movement of the mobile dislocations [158]. Thus, the mean free path can be written as:

$$\bar{l}^s = \frac{c^*}{\sqrt{\sum_{j=1}^{N_{si}} w^{js} (\rho_{TS}^j + \|\rho_{GND}^j\|)}} \quad (2.16)$$

where  $c^*$  is a numerical constant,  $N_{si}$  is the number of slip systems that interact with slip system “s”,  $w^{js}$  is the weight matrix that controls the contribution of statistically stored and geometrically necessary dislocations to the mean free path of the moving dislocations on slip system “s”, and  $\|\rho_{GND}^j\|$  denotes the density norm of GNDs on slip system “j.” The GND density can be expressed as

$$\|\rho_{GND}^j\| = \frac{1}{b} \sqrt{\alpha_{nm}^j \alpha_{nm}^j} \quad (2.17)$$

in which  $\alpha_{ij}$  is the Nye’s tensor [155]. Shizawa and Zbib (1999) proposed a tensor notation describing the evolution of the Nye’s tensor for large deformations [175]:

$$\dot{\alpha} = curl(L^p) \text{ or } \dot{\alpha}_{ij} = e_{jkl} L_{il,k}^p \quad (2.18)$$

where  $e_{jkl}$  denotes the permutation tensor and  $L_{il,k}^p$  is the derivative of the velocity gradient with respect to the third index “k.” In this work, the derivative of the velocity gradient  $L_{il,k}^p$  is determined numerically using the central difference method proposed by Lyu et al. (2015) [159]. The components of the tensor can be obtained by assuming an (n x m) grid, where each element in the grid represents a grain of length L. The grid is assumed to be in 2D, as described in Figure 2.4, while it could be easily extended to 3D. In the grid, each grain is defined by its position with coordinates (x, y), and each grain has four neighboring grains. Hence, the derivative of the velocity gradient tensor can be obtained following the method below:

$$\left. \frac{\partial L_{ij}^p}{\partial x} \right|_{grain_i} = \frac{L_{ij}^p(grainA) - L_{ij}^p(grainC)}{x_A - x_C} \quad (2.19)$$



$$\left. \frac{\partial L_{ij}^p}{\partial y} \right|_{\text{grain}_i} = \frac{L_{ij}^p(\text{grainB}) - L_{ij}^p(\text{grainD})}{y_B - y_D}$$

A schematic representation of the polycrystalline is shown in Figure 2.4, where each grain has a specific orientation with respect to the global coordinate system. The problem is simplified by assuming that the grains have a cubic shape, represented by squares in 2-D of pre-defined grain size (Figure 2.4(c)). Therefore, a grid can be constructed by assuming initially a uniform grain size distribution. By using the described framework, the mechanical response of each grain is influenced by the behavior of its neighboring grains (i.e. grains A, B, C, and D). Nye's tensor components can be determined for each grain as follows:

$$\dot{\alpha} = \begin{pmatrix} \dot{\alpha}_{11} & \dot{\alpha}_{12} & \dot{\alpha}_{13} \\ \dot{\alpha}_{21} & \dot{\alpha}_{22} & \dot{\alpha}_{23} \\ \dot{\alpha}_{31} & \dot{\alpha}_{32} & \dot{\alpha}_{33} \end{pmatrix} \quad (2.20)$$

$$\text{with } \dot{\alpha}_{11} = \frac{\partial L_{12}^p}{\partial z} - \frac{\partial L_{13}^p}{\partial y}, \dot{\alpha}_{12} = \frac{\partial L_{13}^p}{\partial x} - \frac{\partial L_{11}^p}{\partial z}, \dot{\alpha}_{13} = \frac{\partial L_{11}^p}{\partial y} - \frac{\partial L_{12}^p}{\partial x}, \dot{\alpha}_{21} = \frac{\partial L_{22}^p}{\partial z} - \frac{\partial L_{23}^p}{\partial y},$$

$$\dot{\alpha}_{22} = \frac{\partial L_{23}^p}{\partial x} - \frac{\partial L_{21}^p}{\partial z}, \dot{\alpha}_{23} = \frac{\partial L_{21}^p}{\partial y} - \frac{\partial L_{22}^p}{\partial x}, \dot{\alpha}_{31} = \frac{\partial L_{32}^p}{\partial z} - \frac{\partial L_{33}^p}{\partial y}, \dot{\alpha}_{32} = \frac{\partial L_{33}^p}{\partial x} - \frac{\partial L_{31}^p}{\partial z}, \dot{\alpha}_{33} =$$

$$\frac{\partial L_{31}^p}{\partial y} - \frac{\partial L_{32}^p}{\partial x}$$

#### 2.2.4 Grain Fragmentation Model

As previously stated, based on the Tóth et al. (2010) lattice curvature approach, the grain fragmentation process is assumed to be the result of a higher accumulation of dislocations near the grain boundary inducing different crystallographic reorientation rates within the crystal. The ECAP process induces a refinement of the average grain size, alters the texture, and hardens the material as a result of an evolution of the dislocation density. In the following section, a fragmentation model based on the Tóth et al. (2010) lattice curvature approach is proposed. In our attempt to simulate the lattice curvature,

we estimate the crystallographic orientation rates by combining the Taylor-Lin polycrystalline plasticity with the CDD theory that accounts for GNDs to estimate the dislocation densities at the center of the grain and near the grain boundary. Therefore, a grain fragmentation model that monitors the development of misorientation between subgrains is proposed. Each grain is defined by its initial size (constant for all the grains), orientation, and position. However, during deformation, a misorientation between different areas of the grain may lead to the fragmentation of the grain into several new ones. As described in the previous section, the hardening behavior of the material is captured by the dislocation density evolution that is controlled by a set of rate equations. The majority of the accumulated dislocations on the grain boundaries are stored as geometrically necessary dislocations. Under large plastic deformation, GNDs hinder the movement of dislocations around the grain boundaries. Consequently, a deformation gradient develops between the center of a grain and its boundary that results in a misorientation development, leading to the subdivision of the grain when a threshold value of misorientation is attained.

To determine whether a grain may undergo fragmentation, the plastic velocity gradient is calculated in two steps. In the first calculation step, the plastic velocity gradient is computed for the center of the grain, which is not influenced by the neighboring grains, i.e., the GND effect is deactivated (Figure 2.5(a)). Thus, each grain deforms as a bulk, independently from the other grains since the grain boundary effects are not considered in this step. In the second calculation step, the plastic velocity gradient is computed by considering the grain-grain interaction effect, i.e., with active GND effect (Figure 2.5(b)).

The misorientation of each grain boundary is determined from the relative misorientation angles between each grain and its neighboring grains, calculated from the

first and second calculation steps. In the following section, the details of the calculation are provided. The relative misorientation between each grain and its four neighboring grains is calculated. The relative misorientation matrix  $\Delta Q^{i\_neigh}$  can be calculated for each boundary as follows [176]:

$$\Delta Q^{i\_neigh} = Q^{neigh} \cdot (Q^i)^T \quad (2.21)$$

where  $Q^i$  is the transformation matrix of grain “i” and  $Q^{neigh}$  is the transformation matrix of one of the four neighboring grains. Hence, the relative misorientation angle is calculated as follows:

$$\theta_{i\_neigh} = \text{acos} \left( \frac{\text{tr}(\Delta Q^{i\_neigh}) - 1}{2} \right) \quad (2.22)$$

From the first calculation step, a transformation matrix  $Q_1$  describing the crystallographic orientation of the center of each grain is determined. The relative misorientation angles between grain “i” and each of the four neighboring grains A, B, C, and D are noted as  $\theta_{i-A}$ ,  $\theta_{i-B}$ ,  $\theta_{i-C}$ ,  $\theta_{i-D}$ , respectively (Figure 2.5(a)). Additionally, from the second calculation step where the interaction between grains is considered, the transformation matrix of each grain  $Q_2$  can be determined. Using the same definitions given by Eqs. (21) and (22), the relative misorientation angles  $\theta'_{i\_neigh}$  between a grain “i” and one of the four neighboring grains is calculated. Similarly,  $\theta'_{i-A}$ ,  $\theta'_{i-B}$ ,  $\theta'_{i-C}$ , and  $\theta'_{i-D}$  are the relative misorientation angles between grain “i” and each of the neighboring grains A, B, C and D, respectively (Figure 2.5(b)). The smallest misorientation of the applied 24 symmetry operations of cubic crystals is selected for the misorientation calculation [148].

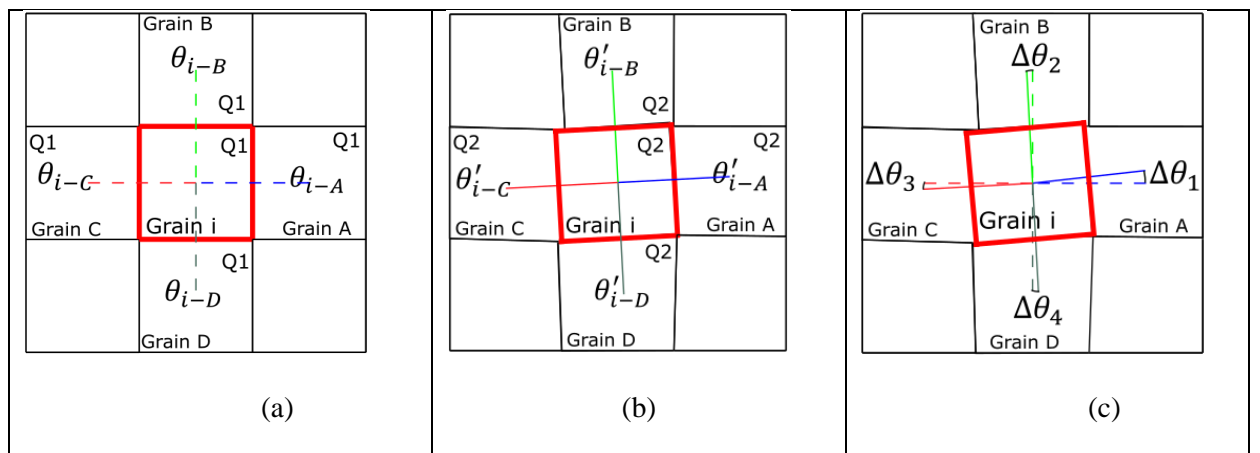
It was reported in several investigations that the misorientation evolution between two neighboring grains and between subgrains (within the grain) is mainly due

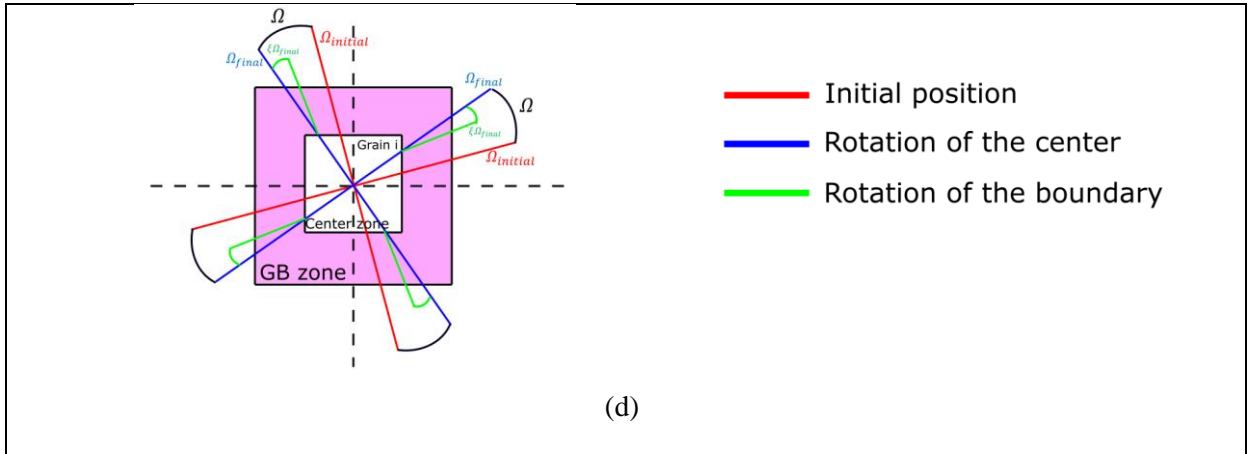
to the contribution of GNDs [177–181]. The curvature-induced grain rotation, which is the difference in rotation between the center and the boundary of the grain, is mainly influenced by the lattice orientation of the neighboring grains [177,178]. The microstructural data of severely deformed polycrystalline materials were investigated using the electron backscattered diffraction (EBSD) method to study the orientation gradient between the grain boundary and the center of the crystal. It was reported that the maximum misorientation is found at the grain boundary and that it decreases while moving toward the center of the grain [182,183]. Following the arguments presented above, one can assume, as proposed by Tóth et al. (2010), that the concomitant rotation of the crystallographic planes of the crystal near the grain boundary rotates more slowly than the center of the grain. To illustrate this assumption, our square-shaped grain is divided into two zones: grain boundary zone and the grain center zone (Figure 2.5(d)).

The difference in the rate of rotation between the center of the grain and the boundary is proposed to be considered in the model by using a parameter  $\xi$  ( $0 < \xi < 1$ ) representing the grain boundary retardation coefficient. To illustrate the rotation retardation process, the initial position  $\Omega_{initial}$  of the crystallographic plane is represented in Figure 2.5(d) as a straight line. Large plastic deformation induces a rotation of the crystallographic lattice by an angle  $\Omega$ . After deformation, the center of the grain has  $\Omega_{final}$  as its final orientation. However, the grain boundary retardation mechanism will induce a rotation of the grain boundary zone lattice by an angle  $(\Omega_{final} - \xi\Omega_{final})$ . For simplicity, it is assumed in the current work that each grain boundary slows down by the same retardation factor  $\xi$ . Finally, the misorientation angle  $\Delta\theta$  between the center and the boundary of the grain is calculated by subtracting the two previously calculated misorientation angles ( $\theta_i$  and  $\theta'_i$ ), as illustrated in Figure 2.5(c). Since the lattice rotation

of the grain “i” is influenced by four different grains (A, B, C, and D), different boundary retardation rates on each grain boundary may occur. Thus, the misorientation between the center and the boundary of the grain “i” is calculated as follows:  $\Delta\theta = \Delta\theta_1 + \Delta\theta_2 + \Delta\theta_3 + \Delta\theta_4$ , where  $\Delta\theta_1 = \theta_{i-A} - \theta'_{i-A}$ ,  $\Delta\theta_2 = \theta_{i-B} - \theta'_{i-B}$ ,  $\Delta\theta_3 = \theta_{i-C} - \theta'_{i-C}$ , and  $\Delta\theta_4 = \theta_{i-D} - \theta'_{i-D}$ .  $\Delta\theta_1$ ,  $\Delta\theta_2$ ,  $\Delta\theta_3$ , and  $\Delta\theta_4$  are the misorientation angles between the center of the grain and the grain boundary influenced by grains A, B, C, and D, respectively.

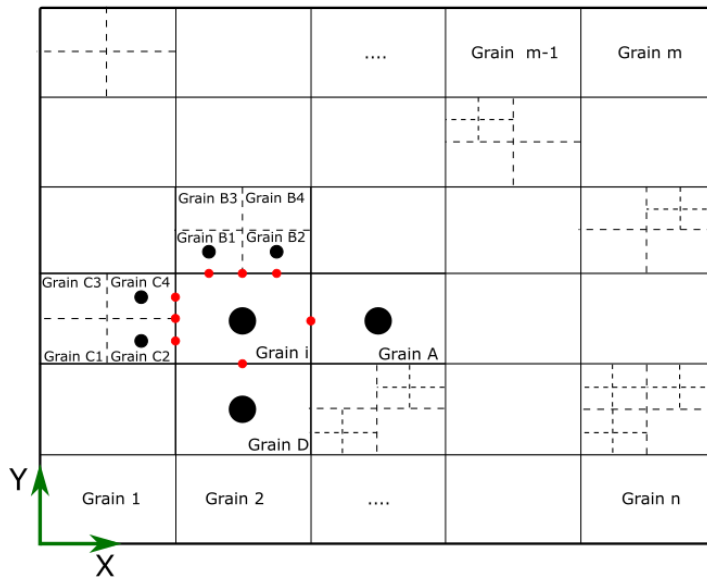
Per our assumption, the fragmentation occurs if the calculated misorientation angle between the grain center and the grain boundary exceeds  $5^\circ$ . When the fragmentation process is active, the parent grain splits into four new grains. An example of how the grain refinement process takes place based on the previously presented assumptions is depicted in Figure 2.6. For instance, let us assume that each of the grains “B” and “C” have split into four new grains, grain “i” is now surrounded by 6 grains, leading to an increase of the GND density at the boundary. Therefore, as the GND density is proportional to the Nye’s tensor and the latest is inversely proportional to the distance between the centers of two grains, the GND density increases.





**Figure 2.5 (a) Strain state without the effect of neighboring grains, (b) strain state accounting for grain-grain interaction effect, (c) misorientation evolution between the center and the boundary of the grain, (d) effect of GND on the rotation of the grain boundary.**

In our approach, the numerical complexity is reduced by allowing each grain to undergo a maximum of five levels of splitting, which means that each grain can be divided into a maximum of  $4 \times 4 \times 4 \times 4 \times 4 = 1,024$  grains. The fragmented grains' size is considered half the size of their parent grain size, and their crystallographic orientation will depend on the calculated plastic velocity gradient. As an approximation, the two opposite grains (e.g., grain "C1" and grain "C4" in Figure 2.6) are assigned the crystallographic orientation of their parent grain after deformation but without including the GND effect, while the other two grains (e.g., grain "C2" and grain "C3") are assigned the crystallographic orientation of their parent grain after deformation with activated GND effect. Moreover, the alteration of the grain distribution in the grid microstructure can affect the fragmentation process. For instance, by considering two different distributions of grains (i.e., the same grain orientations but different positions in the grid), we obtain two different final grid microstructures. Depending on the position of the grain, grain fragmentation will be active in one grid microstructure configuration and not in another configuration.



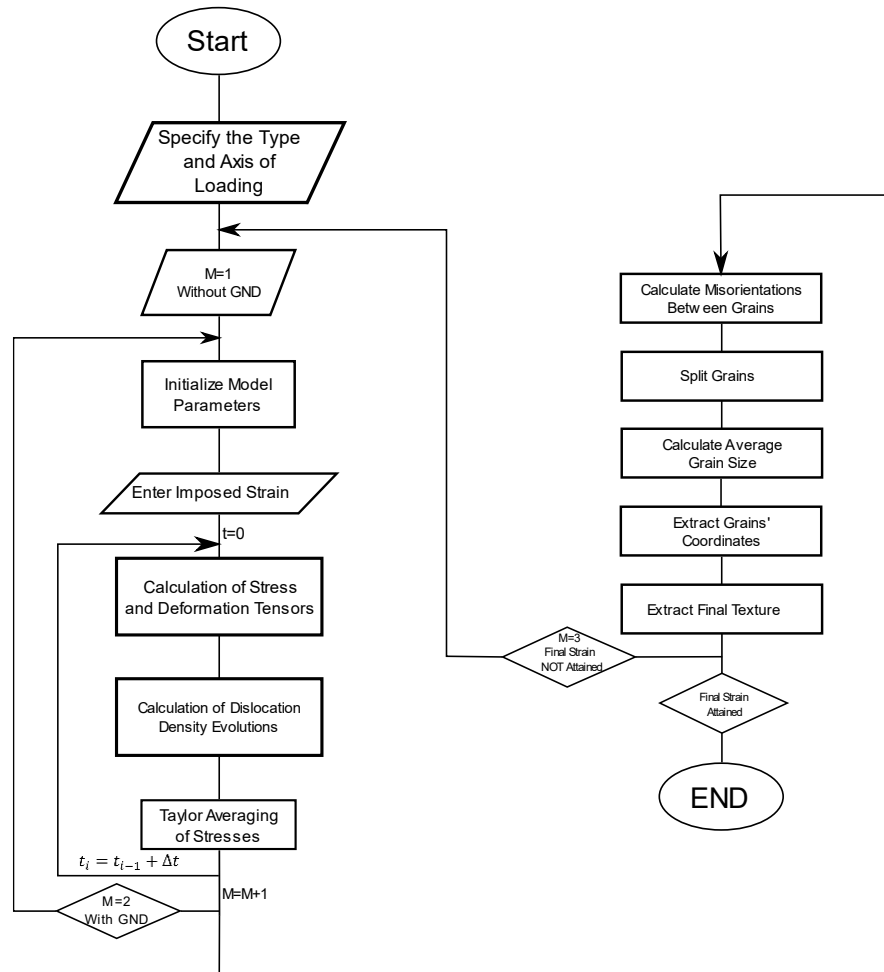
**Figure 2.6 Example of fragmentation for several grains after reaching a certain strain level.**

### **2.2.5 Numerical Implementation**

The Taylor-Lin CP-CDD model and the proposed grain fragmentation criterion are implemented into a Fortran program. In this work, the model efficiency to predict the texture and microstructure of an ECAP-processed material is validated on a commercially pure copper. The properties of the initial texture and microstructure are provided by Tóth et al. (1992) [184]. The initial texture of the polycrystal is represented by 64 grain orientations, where each orientation is described by the three Euler angles  $(\varphi_1, \varphi, \varphi_2)$ . For computational efficiency, the simulation box is represented as a 2D mesh with fixed boundaries where the grains at the boundaries of the simulation box are allowed to split (initially, each grain is affected with 5 calculation points, one in the middle and one on the middle of each boundary). The implemented Taylor-Lin CP-CDD model is summarized by the Fortran flowchart presented in Figure 2.7. In our model, each grain is assigned a position and a crystallographic orientation, and its neighbors are determined automatically according to their location on the grid. As a first step, the loading condition

(e.g., shear, tension, or compression) and the appropriate loading direction are specified. Two successive calculation loops are performed. In the first loop ( $M=1$ ), the plastic velocity gradient of the center of each grain is calculated by neglecting the presence of GND. In the second loop ( $M=2$ ), the plastic velocity gradient of the boundary of each grain is calculated assuming the presence of the GNDs. During each loop, the stress tensors and dislocation densities are computed using the Taylor-Lin CP-CDD model for each crystal at each time increment  $t_i$ . The overall stress at each calculation increment is computed according to the Taylor-Lin scheme (section 2.2.2). The gradient of the plastic velocity gradient is then determined using the finite difference method (section 2.2.3). After the two strain loops ( $M$  loops) are finished, the misorientation angle developed within each grain is calculated. When the critical value of the misorientation angle is attained, the grain fragmentation approach is activated. Therefore, the new grains are assigned with a new grain size, crystallographic orientation, and position. The strain loops continue their calculations and check whether fragmentation occurs or not until the final strain is attained. The strain increment used in the calculations is 0.1. Finally, the average grain size is calculated, and the final texture is extracted.



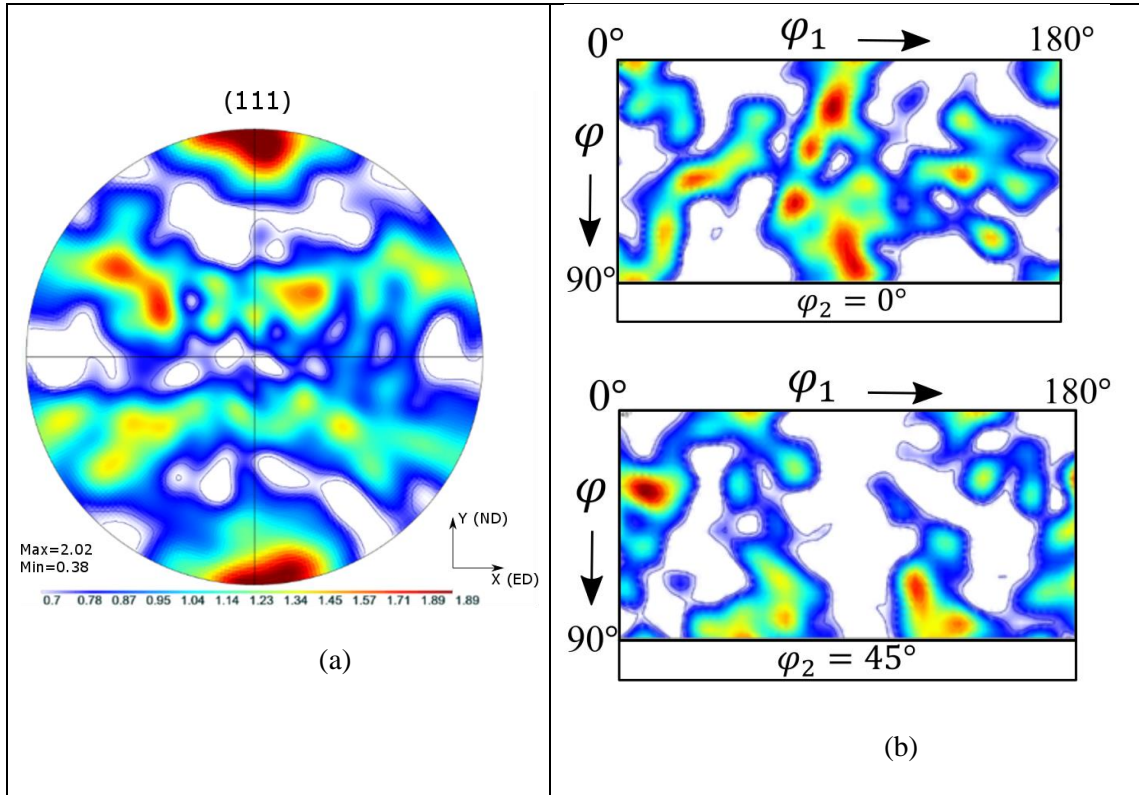


**Figure 2.7 Flowchart of the Taylor crystal plasticity model in the Fortran program**

### 2.3 Results and Discussions

The parameters of the presented Taylor-Lin CP-CDD model were first calibrated on torsion experiments. The torsion experiments, presented by Tóth et al. (1992), were performed on commercially pure copper. Then, the predictive capability of the proposed model was validated through ECAP-processed copper experiments via routes A and Bc. ECAP experimental results were presented by Tóth et al. (2010), where the same material was used in both the Tóth et al. (2010) and the Tóth et al. (1992) investigations [148,184]. The studied copper polycrystal texture was constructed from the orientation of 500 grains, as described in Tóth et al. (1992). The initial texture is presented in Figure 2.8 by the

(111) pole figure and the orientation distribution functions (ODFs). The initial microstructure has a normal distribution of grain sizes that range between  $14 \mu\text{m}$  and  $35 \mu\text{m}$  [148].



**Figure 2.8 Initial texture of the copper represented by (a) (111) pole figure, (b) ODFs at  $\varphi_2 = 0$  and  $45^\circ$  sections**

### 2.3.1 Experiments and Model Parameters Identification

The proposed approach was used to model the mechanical behavior and the texture development in commercially pure copper subjected to free-end torsion. According to the experiments, the shear mode develops in the  $xy$  plane (Figure 2.1), and hence the deformation gradient tensor is written as:

$$\mathbf{F} = \begin{pmatrix} 1 & \dot{\epsilon}t & 0 \\ 0 & 1 & 0 \\ 0 & 0 & 1 \end{pmatrix} \quad (2.23)$$

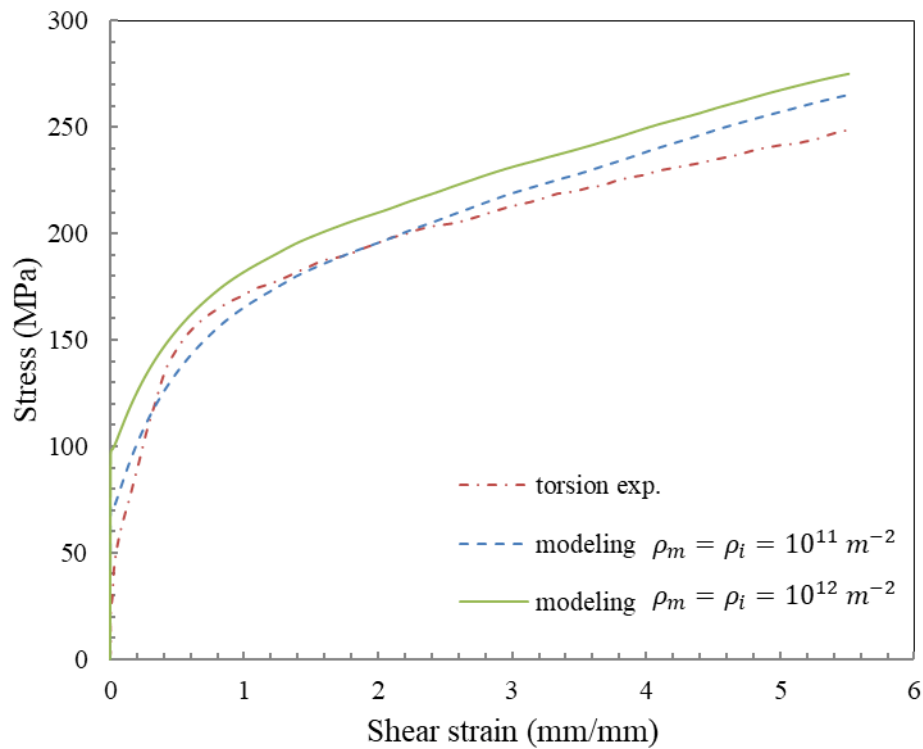
The shear stress-strain diagram, shown in Figure 2.9 and presented by Tóth et

al. (1992) [184], refers to the commercially pure copper sample subjected to free-end torsion. On the same plot, we show the simulated shear stress-strain diagram of copper samples with two different initial dislocation density values ( $10^{11} \text{ m}^{-2}$  and  $10^{12} \text{ m}^{-2}$ ). It can be seen that the initial dislocation density can considerably affect the overall mechanical response. It is clear that better fitting of the experimental results is achieved when using an initial density of  $10^{11} \text{ m}^{-2}$ .

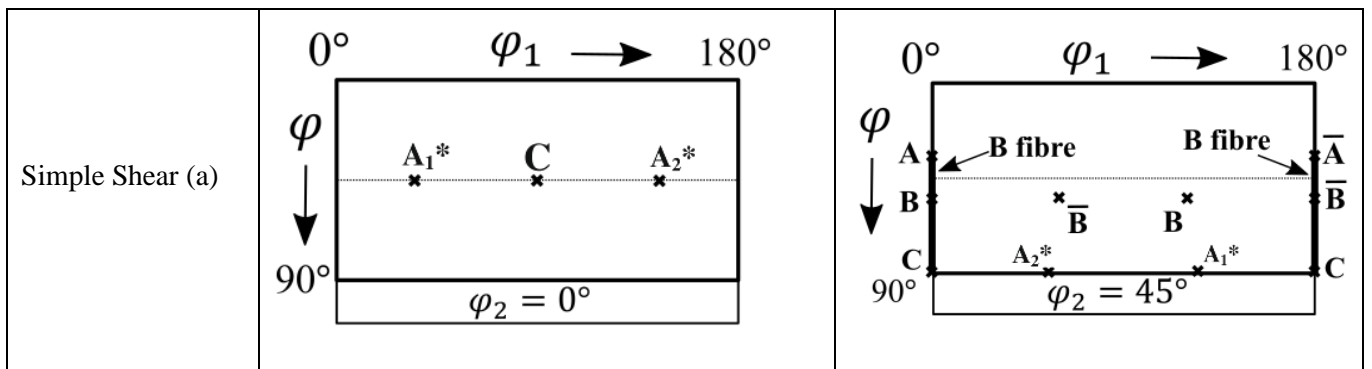
The predicted texture was extracted at a shear strain  $\gamma$  of 5.5 and at an intermediate shear strain  $\gamma$  of 2.0 and was compared with the reported experimental findings. The predicted textures are represented using ODFs with constant  $\varphi_2$ . These ODFs are constructed from the crystallographic orientation of 500 grains and are presented for sections at  $\varphi_2 = 0^\circ$  and  $45^\circ$ . Figure 2.10 shows a comparison between the experimental and predicted textures. A key figure representing the ideal positions of the simple shear components is shown in Figure 2.10(a) to help compare the predicted and experimental shear textures. The comparison between the experimental texture and the ideal components of shear shows clearly that the developed texture after the free-end torsion test exhibits pure shear components. Figure 2.10 also shows a good agreement between the predicted textures and the reported experimental findings [184] for  $\gamma = 2$ . The Taylor-Lin CP-CDD model captured the  $A_1^*$ , C, and  $A_2^*$  components of the ideal shear orientations in the  $\varphi_2 = 0^\circ$  ODF section and shows similarity with the experimental texture.

For  $\varphi_2 = 45^\circ$  ODF section, the model mimicked the experimental texture perfectly, with some disturbance in the B component (Figure 2.10 (b) and (c)). For the higher strain ( $\gamma = 5.5$ ), the texture components are captured accurately; however, we observe some weakness in capturing the intensity of the  $A_1^*$  component in the  $\varphi_2 = 0^\circ$

section in the Taylor-Lin CP-CDD model. Furthermore, the distribution of the grain orientations becomes more concentrated at the ideal positions at the higher strain, demonstrating the higher strength of the C and  $A_2^*$  components. Table 2-1 lists the optimized parameters that resulted in a satisfactory agreement between the model and the experimental mechanical and texture results (the results of the selected parameters are presented in Figure 2.9 and Figure 2.10).



**Figure 2.9 Comparison of the stress-strain behavior of copper between experimental [184] and crystal plasticity modeling at different initial dislocation densities**



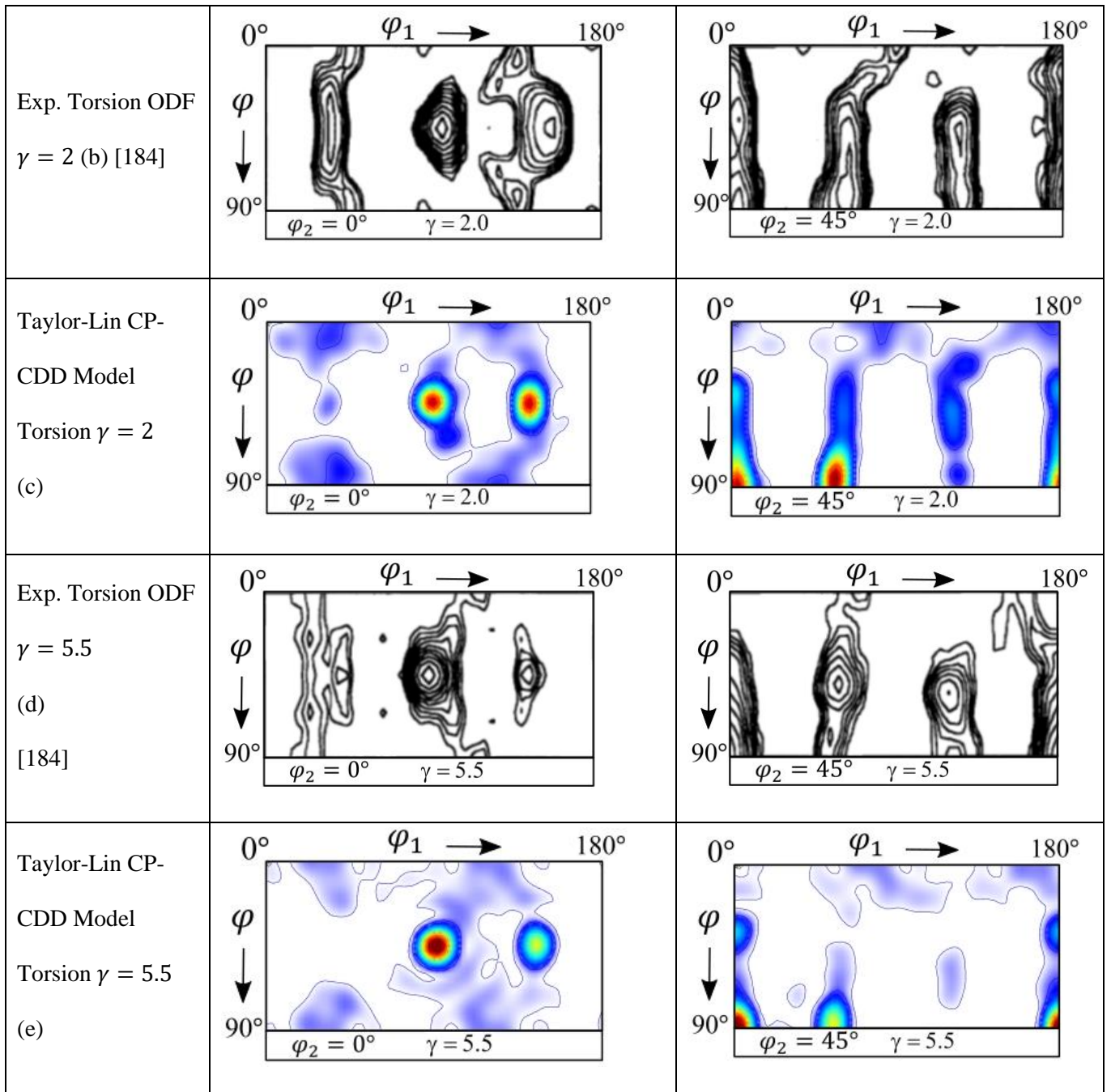


Figure 2.10 ODF  $\varphi_2 = 0, 45^\circ$  sections for (a) ideal orientations, (b) and (d) experimental textures, (c) and (e) Taylor-Lin CP-CDD model

Table 2-1 Model parameters of copper	
PARAMETER	VALUE (UNIT)
$C_{11}$	168400 MPa
$C_{12}$	121400 MPa
$C_{44}$	75400 MPa
$\mu$	44700 MPa
<b>K (H-P PARAMETER)</b>	4.43 MPa. mm <sup>1/2</sup>
<b>B (BURGERS MAGNITUDE)</b>	2.56. 10 <sup>-10</sup> m

<b>STRAIN RATE ( <math>\dot{\epsilon}</math> )</b>	0.0038 s <sup>-1</sup> for torsion 0.01 s <sup>-1</sup> for ECAP
$\tau_0$ *	12 MPa
<b>STRAIN RATE SENSITIVITY ( <math>\eta</math> ) *</b>	0.08
$c^*$ *	0.8
<b>Q *</b>	1.4
$v_0$ * (REFERENCE STRAIN RATE)	0.001 m/s
$\alpha_{BH}$ *	0.16
$\alpha_1$ *	0.002
$\alpha_2$ *	1.0
$\alpha_3$ *	0.002
$\alpha_4$ *	0.002
$\alpha_5$ *	0.011
$\alpha_6$ *	1.0
$\rho_{m\ initial}$ *	10 <sup>11</sup> m <sup>-2</sup>
$\rho_{i\ initial}$ *	10 <sup>11</sup> m <sup>-2</sup>
$\rho_{GND\ initial}$ *	10 <sup>13</sup> m <sup>-2</sup>
<b>* : MODEL PARAMETERS</b>	

### 2.3.2 ECAP Predictions and Experimental Validation

The experimental texture and microstructural characterization of ECAP-processed copper are used to validate the predictive capability of the model incorporating grain refinement criteria. The deformation mode developed by the samples during ECAP is simple shear as proposed by Segal (1999, 1995) [185,186]. The shear deformation mode is developed at the two channels' intersection plane (x'y' plane shown in Figure 2.1). The global deformation gradient is then obtained with an axis transformation as

follows:  $\mathbf{F}_{x,y,z} = \mathbf{P} \cdot \mathbf{F}_{x',y',z'} \cdot \mathbf{P}^T$ , where  $\mathbf{P} = \begin{pmatrix} \cos(\phi/2) & -\sin(\phi/2) & 0 \\ \sin(\phi/2) & \cos(\phi/2) & 0 \\ 0 & 0 & 1 \end{pmatrix}$ ,  $\phi$  is the

die angle, and  $\mathbf{P}^T$  is the transpose of  $\mathbf{P}$  in the transformation matrix. The calibrated model parameters of copper are used to simulate both passes of the ECAP process. According to the discussion in section 2.2.4, accounting for the grain-grain interaction effect leads to the slow-down of the grain boundary rotation with respect to the grain center. Thus, the grain boundary retardation parameter  $\xi$  represents a main model

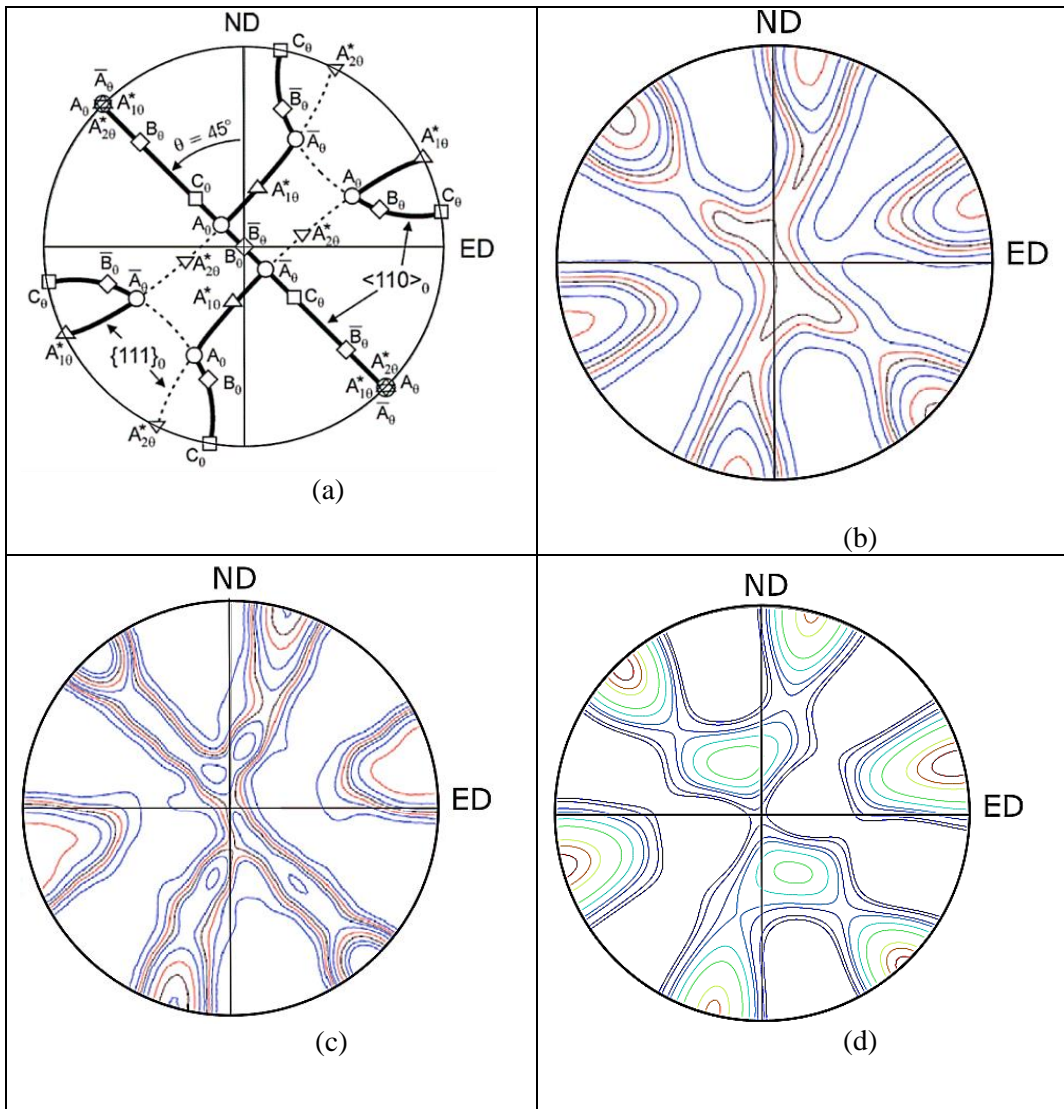
parameter that controls the rate of grain refinement. Actually, it was found by tuning the value of the retardation parameter that  $\xi = 0.1$  led to the best results of texture and grain refinement.

### 2.3.2.1 Texture Prediction

Several factors can affect the evolution of the texture, such as the die angle, deformation mechanisms, and the initial texture. Generally, knowing the effects of these factors provides a clear perspective on the predicted texture. For instance, the ideal positions of the shear texture components are influenced by the die angle, which rotates the shear plane and in consequence rotates the texture components [30].

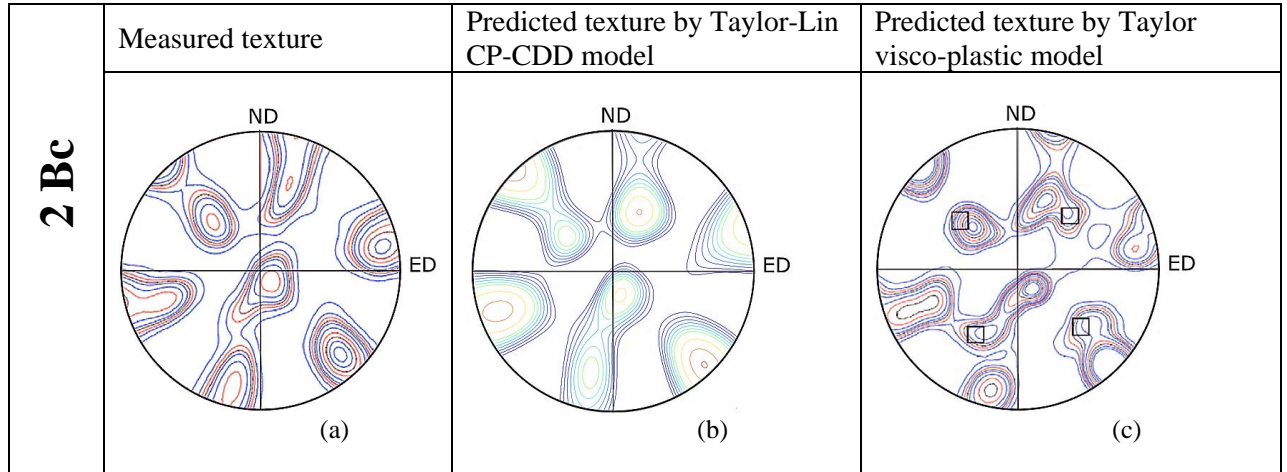
The measured and simulated textures of the ECAP-processed copper are presented in Figure 2.11. The measured texture components after ECAP 1A (Figure 2.11(b)) are well aligned with the ideal orientations presented in Figure 2.11(a), with a strong B component shifted slightly from its ideal position. The predicted textures obtained by the proposed Taylor-Lin CP-CDD model and the Taylor VP model [148] are displayed in Figure 2.11. They were calculated using a Gaussian distribution of  $7^\circ$  around each grain orientation. Both models captured the main texture components of the experimental ECAP texture and their relative intensity levels.

The measured textures, and the predicted textures by the Taylor VP model, after 2Bc [148] are compared with the proposed Taylor-Lin CP-CDD model predictions in Figure 2.12. In route Bc, after two passes, all main texture components are reproduced in the right positions (Figure 2.12(b) and (c)). However, a small discrepancy appears in both texture predictions, which is related to the use of the Taylor model as illustrated in Molinari and Toth (1994) and Tóth et al. (2010) [148,188].



**Figure 2.11 (a) (111) Ideal orientations of FCC metal texture subjected to one pass ECAP with die angle=90, (b) measured (111) pole figure (PF) after 1A [148], (c) predicted (111) PF texture by Taylor visco-plastic model after 1A [148], and (d) predicted (111) PF texture by Taylor-Lin CP-CDD model after 1A. Isolevels: 0.7, 1, 1.2, 1.4, 1.6, 2, 2.5, 3, 3.5, 4**





**Figure 2.12 (111) pole figures for the (a) measured texture [148], (b) predicted textures by Taylor-Lin CP-CDD model, and (c) predicted textures by Taylor VP model of ECAP 2Bc [148]. Isolevels: 0.7, 1, 1.2, 1.4, 1.6, 2, 2.5, 3, 3.5, 4**

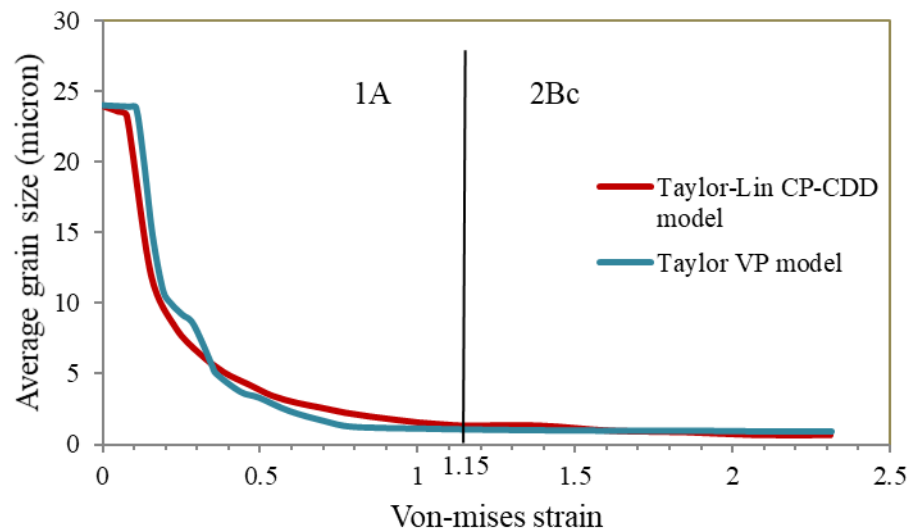
### 2.3.2.2 Grain Size

During ECAP, grain fragmentation is a dominant deformation mechanism induced by the grains' need to reduce their high internal energy. Consequently, subgrain microstructures develop and affect the texture evolution by reorienting a portion of the parent grain and by constituting obstacles for dislocation motion. Increasing the misorientation angle results in an increase of the accumulated defects at the subgrain boundaries, leading to the formation of new grains with distinct microstructure [30].

In the proposed Taylor-Lin CP-CDD model, the misorientation angle between the subgrains is assumed initially to be zero. During deformation, the evolution of the misorientation between subgrains depends on the developed plastic velocity gradient, the position of the grain, and the texture of the neighboring grains. Furthermore, the suggested modeling framework relates the hardening of the material with the neighboring grains' size and the crystallographic orientation, which consecutively affect the evolution of the misorientation and the fragmentation process. When the misorientation angle reaches a threshold value of  $5^\circ$ , the subgrains are considered as new grains and assigned half of their parent grain size. As the deformation continues, each new grain can subdivide

into smaller grains, leading to high rate of refinement. The fragmentation process continues until the final imposed shear strain is reached.

The plot of the grain size variation with the von Mises (VM) strain is displayed in Figure 2.13 for both models. The average grain size after one-pass ECAP reaches a final grain size of  $1.2 \mu\text{m}$  experimentally,  $1.35 \mu\text{m}$  as predicted by the Taylor-Lin CP-CDD model, and  $1.5 \mu\text{m}$  as predicted by the Taylor VP model. In the second pass 2Bc, the rate of grain refinement has decreased, and a final average grain size has been attained of  $1.15 \mu\text{m}$  experimentally,  $0.8 \mu\text{m}$  by the Taylor-Lin CP-CDD model, and  $0.9 \mu\text{m}$  by the Taylor VP model.

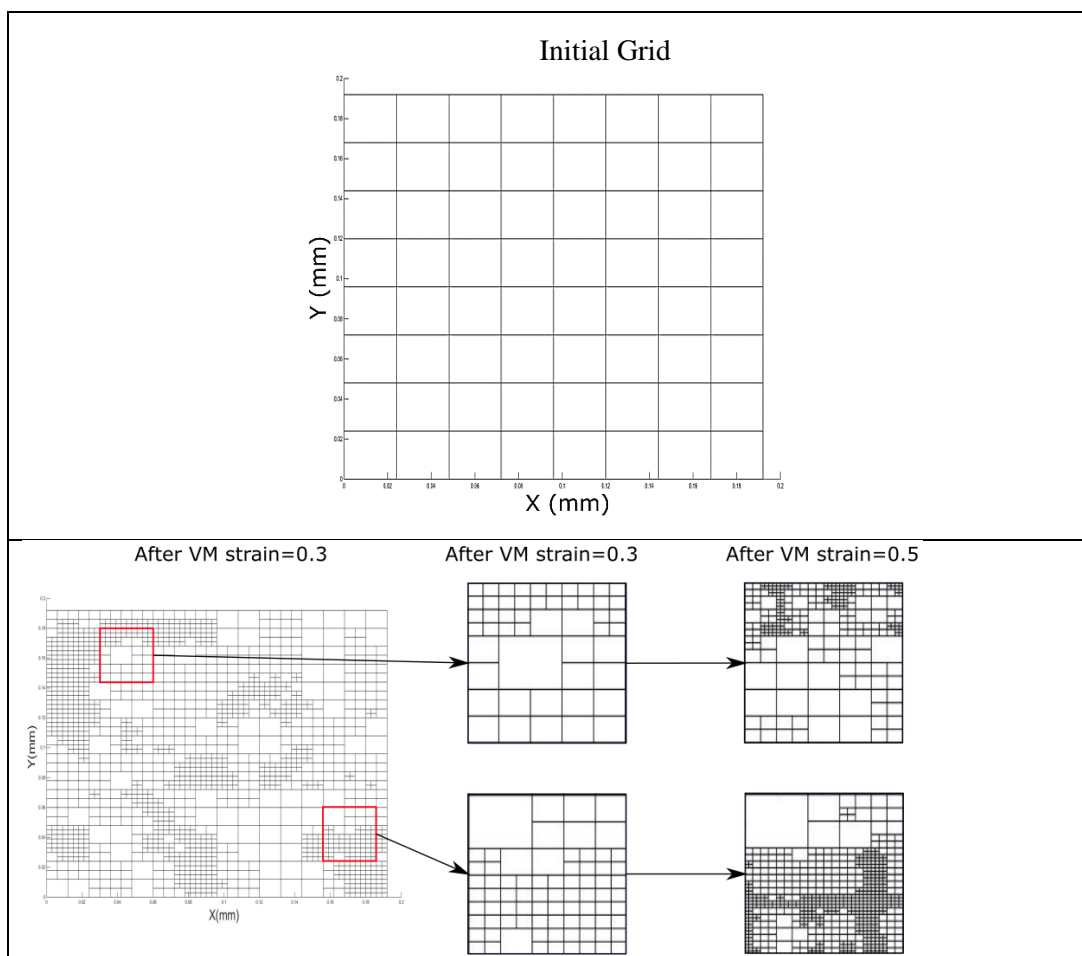


**Figure 2.13 Evolution of grain size after two passes of ECAP**

### 2.3.2.3 Grain Distribution

Grain shape evolution is studied in the Taylor-Lin CP-CDD model using a two-dimensional analysis of the grain size distribution. Figure 2.14 represents the distribution of grains at different VM strains. Since ECAP introduces large grain-shape change, the grid will be extremely distorted. Figure 2.14 shows that, after the grains do split, each grain boundary is affected by multiple neighboring grains. Thus, more geometrically

necessary dislocations will be induced at the grain boundary, leading to a higher misorientation angle and subsequently a high probability of fragmentation. During simulation, the subgrains' information is updated after each strain increment of 0.1. When subgrains exceed their threshold misorientation value, they are treated as new grains having information associated with their parent grains. The population of grains with different crystallographic orientation has increased from 64 initially to about 50000 at the end of one route-A ECAP pass.



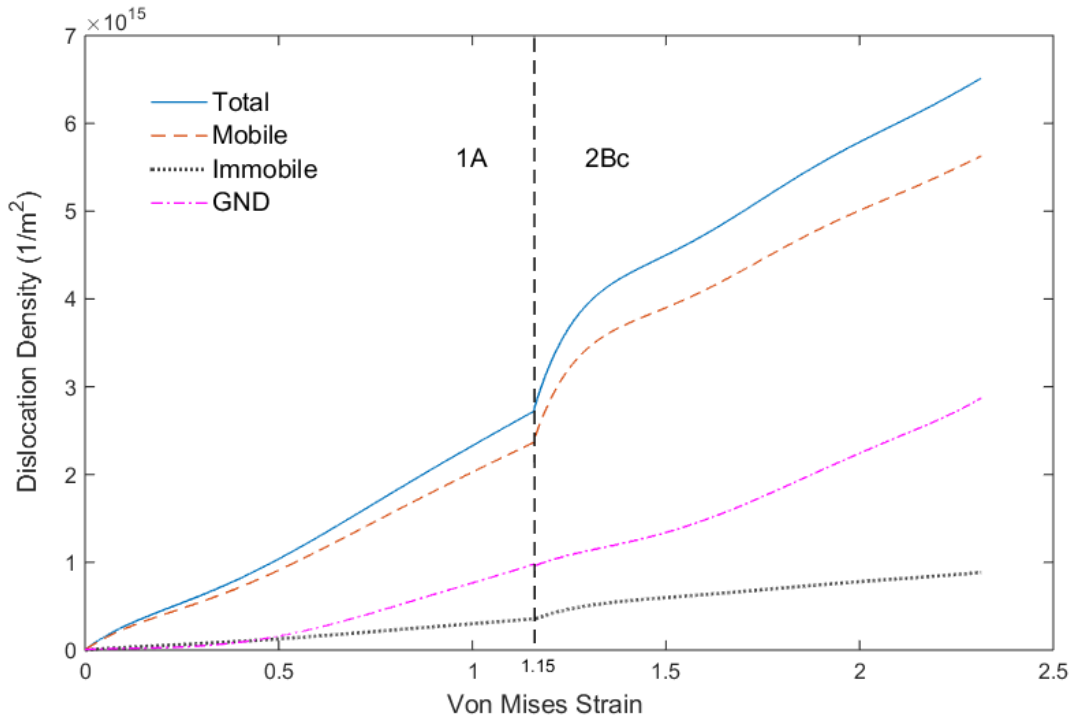
**Figure 2.14 Grain refinement at different strains during ECAP 1A**

#### 2.3.2.4 Dislocation Density Evolution

As mentioned in section 2.2.3, the geometrically necessary dislocations act as obstacles for the mobile dislocations at the grain boundaries. The effect of GNDs is

implemented in the mean free path of moving dislocations in equation (2.16), which affects directly the dislocation density evolutions. As estimated in section 2.3.1, the initial dislocation density is found to be equal to  $10^{11} m^{-2}$  for both mobile and immobile dislocations and to  $10^{13} m^{-2}$  for the GND.

Figure 2.15 shows the evolutions of the dislocation densities with strain. It is noticed that higher values for the mobile dislocations are reached when compared to the immobile dislocations and GNDs. During ECAP, the mobile dislocations as well as the immobile dislocations are responsible for the hardening of the bulk of the grains. However, the GNDs cause the accumulation of dislocations at the grain boundaries, which also contribute to the total dislocation density as explained in section 2.2.4. The GND density is found to be one-third of the total dislocation density in both passes. With increasing deformation, the mechanisms of multiplication, annihilation, and transition of dislocations occur, resulting in an increase of the dislocation densities. During the first pass, the dislocation densities increase in a nearly linear manner. In the second pass, the mobile and the total dislocation densities increase parabolically for around 20% of strain, then the rate of evolving slows down and continues increasing linearly.



**Figure 2.15 Prediction of dislocation densities evolution after two ECAP passes**

## 2.4 Conclusions

A grain fragmentation modeling approach was proposed in which a continuum dislocation dynamics model is coupled with a crystal plasticity framework. The proposed model predicted the mechanical and microstructural features of FCC metals subjected to severe plastic deformation (SPD) processes. The proposed grain refinement model was developed by accounting for the effect of the geometrically necessary dislocations (GNDs) that accumulate in the grain boundary zone. The proposed approach assumed that initially, each grain consisted of a number of subgrains with similar microstructural properties. The refinement process was activated when a threshold misorientation angle between different areas of the grain was attained. The fragmentation model was implemented in a Taylor-Lin CP-CDD model. The problem was simplified by assuming that the grains have cubic shape of pre-defined grain size and orientation. Furthermore, it was assumed that each grain can be divided into a maximum of  $4 \times 4 \times 4 \times 4 \times 4 = 1,024$  grains. The influence of the neighboring grains and the position of the grain in the microstructure

was considered, and the GND density was estimated by the influence of the neighboring grains on the parent grain. The model predictive capability was validated on experimental results available in the literature [148,184,188]. The model parameters were calibrated by fitting the mechanical response and texture evolution on torsion test on pure copper [184]. The model was able to capture with good accuracy the texture grain size and dislocation density evolutions after 1A and 2Bc ECAP paths.

Although ECAP experiments were used for validating the model's predictive capability, the model can be used to predict the texture and the mechanical properties of a wide range of deformation processes involving grain refinement mechanisms. The model parameters were optimized on torsion experiments performed on commercially pure copper. The predictive capability of the proposed model was validated on ECAP experiments in routes A and Bc of the same commercially pure copper material (all the experimental results presented in this work are extracted from the literature). Satisfactory predictions of the texture development and microstructural evolution are found.

The presented model has proved its efficiency as a useful tool to model severe plastic deformations, a few limitations are still present. The grain shape was assumed to be square-shaped in 2D; however, in reality, grains could have random 3D shapes and therefore, could be surrounded by more than eight grains, with common boundary located in a 3D space. In addition, the proposed model is limited to modeling FCC crystal structures. This model can be extended to account for different crystal structures (such as HCP and BCC materials), which will be the focus of future studies. Furthermore, the model can be extended to account for high-temperature deformation mechanisms such as grain boundary sliding and dynamic recrystallization.

## CHAPTER 3

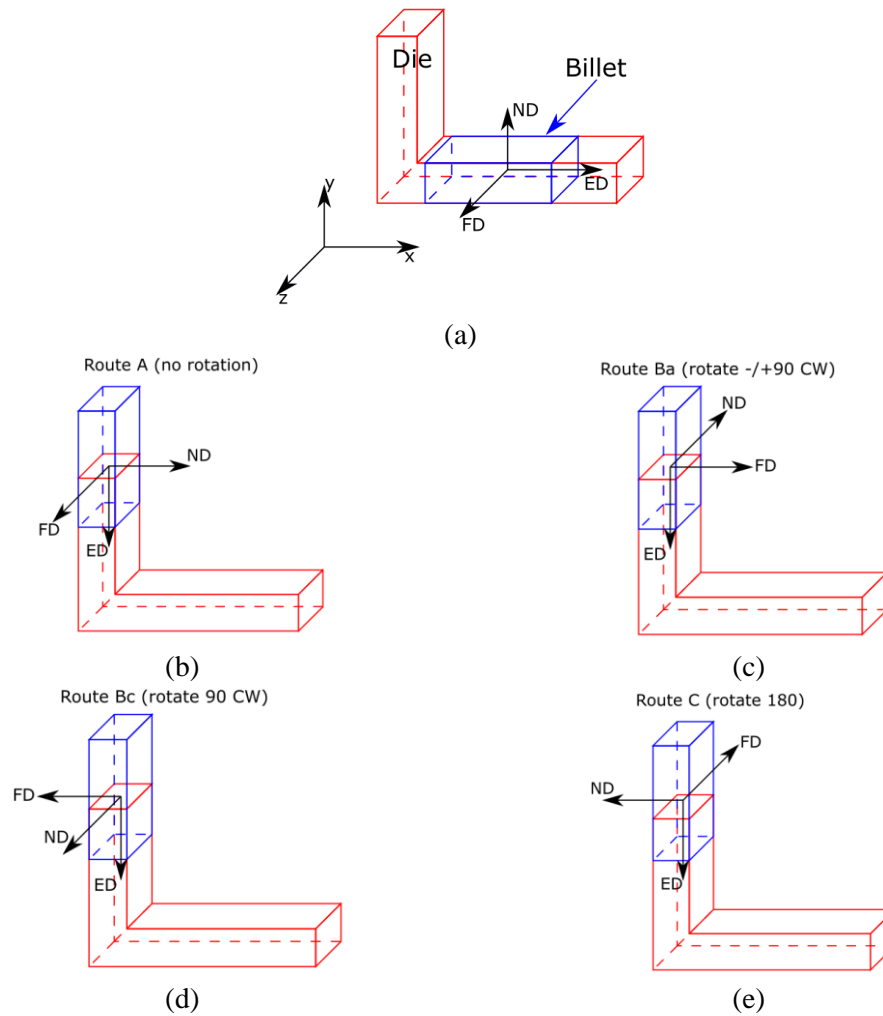
# MODELING OF THE ECAP INDUCED STRAIN HARDENING BEHAVIOR IN FCC METALS

### 3.1 Introduction

Ultrafine-grained microstructure in metallic materials is manufactured by using severe plastic deformation methods, which consecutively result in mechanical properties alteration. The most common severe plastic deformation grain refinement techniques are equal channel angular pressing (ECAP), high-pressure torsion, and accumulated roll bonding [125]. ECAP is an effective method that was first introduced by Segal in the 1970s [189] and is used to enhance the mechanical properties by achieving exceptional grain refinement [22,185,186]. ECAP is a metal flow process in which a billet is pressed through a die consisting of two channels with equal cross-sections intersecting at an angle  $\Phi$ . As the billet is pushed through the die, it deforms severely in simple shear mode [185]. ECAP presents the advantage of processing large samples while maintaining an unchanged cross-sectional area. Numerous studies on ECAP were conducted to uncover the mechanisms of texture and microstructure alteration induced by grain refinement [22,130,132,150,190]. ECAP process parameters such as die angle  $\Phi$ , number of passes, deformation routes, and the back-pressure considerably affect the grain refinement process and hence the texture and the microstructure [22,30]. The effect of the die angle was studied experimentally at room temperature (RT) on pure aluminum using four different die angles ranging from  $90^\circ$  to  $157.5^\circ$  [191]. For each die angle, the aluminum sample was processed by using several passes while maintaining the final imposed strain at  $\sim 4$ . Ultrafine equiaxed

grains microstructure was achieved only with  $\Phi=90^\circ$ . There are four basic types of routes in ECAP, namely, A, B<sub>a</sub>, B<sub>c</sub>, and C, as illustrated in Figure 3.1. Li and Mishin [192] reported that different deformation routes significantly affect the texture components intensity, which consecutively influences the anisotropic plastic response of aluminum billets. Ferrasse et al. [193] showed that the strength of ECAPed copper samples saturates as the grain refinement is slowed down after four passes. In addition, for copper and aluminum billets ECAPed via routes A and B, ultra-fine subgrain shear bands are observed within the parent grains. Another work by Shaeri et al. [194] reported that after 4 passes via routes A and B<sub>c</sub>, the ECAPed aluminum presents a very fine microstructure with an average grain size of about 1  $\mu\text{m}$  and 0.7  $\mu\text{m}$ , respectively. Moreover, the first ECAP pass results in strong texture components that weaken after four processing passes. Finally, back-pressure is reported to considerably improve the workability of metallic alloys during ECAP [195,196]. Stolyarov and Lapovok [195] reported that the strength and microhardness of aluminum alloy 5083 were significantly improved when ECAP processing with a back-pressure. Krasil'nikov [196] reported that a pure copper processed by 16 ECAP passes with a back-pressure of 450 MPa resulted in a homogeneous microstructure with a grain size of 0.19  $\mu\text{m}$  and exhibiting an ultimate tensile strength of 470 MPa.





**Figure 3.1 (a) Simple schematic of the ECAP process, (b) reinsertion of the billet in route A with no rotations between passes, (c) reinsertion of the billet in route B<sub>a</sub> with a rotation of 90° in alternative directions between consecutive passes, (d) reinsertion of the billet in route B<sub>c</sub> with a rotation of 90 ° in the same sense between each pass, (e) reinsertion of the billet in route C with a rotation of 180 ° between passes.**

Metals are ECAPed at either low or high temperatures, yet, since most cubic metals exhibit good ductility, they are ECAPed at room or warm temperatures. The effect of ECAP temperature was investigated extensively in order to study its influence on microstructural and mechanical development in metals [197–201]. Chen et al. [197] investigated the effect of different ECAP extrusion temperatures on the evolution of some metallographic parameters of aluminum alloy, such as grain size, grain aspect ratio, and grain boundary misorientation. It was reported that with increasing extrusion temperature, the average grain size gradually increases for temperatures between 50 and 250 °C and

then a sudden increase is reported for 300 °C, attributed to the significant boundary migration. Additionally, the proportion of low-angle boundaries increases while the proportion of high-angle boundaries decreases with an increase of the extrusion temperature. The grain shape aspect ratio decreases from 2.7 to 1.5 when the processing temperature changes from 50 to 300 °C, resulting in a more equiaxed grain structure. Chang et al. [200] studied the mechanical properties of 5083 aluminum alloy ECAPed at 200 °C through 8 passes using route C and then tensile tested at room temperature and at 250 °C. At room temperature, the yield strength showed a substantial increase from 129 MPa for the as-received sample to 249 MPa after the first pass and to 290 MPa after 8 passes, while no remarkable variation of the total elongation was observed. However, the Vickers microhardness increased drastically after the first pass, followed by an insignificant variation with an increasing number of passes. The increase of the microhardness after the first pass was attributed to the work hardening associated with the drastic dislocation density increase and the formation of subgrain bands. On the other hand, at high temperature (250 °C), the extruded aluminum alloy showed a decrease in the yield strength from 72 MPa for the as-received sample to 52 MPa after 8 passes, while a considerable increase in elongation (220%) was noted after 8 passes. Another study by Prados et al. [201] showed that at room temperature, the yield strength of an ECAPed aluminum alloy through 4 passes increases by up to 3 times the yield strength of the unprocessed specimens. Moreover, the ductility is observed to decrease considerably after the first pass; however, with an increasing number of passes the ductility is recovered and reaches its maximum after the fourth pass. For all tensile samples after ECAP, no work hardening effect was observed. This observation is attributed to two mechanisms, the mutual annihilation and the absorption of the mobile dislocations by the

grain boundaries. These mechanisms result in the reduction of mobile dislocation density. They can occur easily in ECAPed materials due to the small diffusion distances [202] or due to dynamic recovery, which is expected to occur in aluminum at room temperature (30% of the homologous temperature) [203]. Although we can find in the literature some experimental characterization of the mechanical properties of ECAPed materials, there is a lack of modeling approaches predicting the mechanical, microstructural, and textural properties of ECAPed materials. Hence, developing physics-based models that predict the properties of ECAPed materials is essential in order to provide insights on the underlying deformation mechanisms.

In the literature, phenomenological- based, dislocation- based or crystal-plasticity-based models were proposed for predicting grain refinement and texture evolution of ECAP-processed materials [109,140–150,204]. A phenomenological grain refinement model assuming the self-similarity of the grain refinement process was proposed by Beygelzimer [140]. The activation of the grain refinement mechanism was initiated when sufficient pressure and strain. A quantitative grain fragmentation process influenced by the strain path complexity was proposed by Petryk and Stupkiewicz [143]. The proposed model predicted the microstructural changes, grain refinement and strain hardening of FCC metals deformed by ECAP, however the texture evolution was neglected. A volume averaged number of dislocations generated based model was proposed by Starink et al, [204] for predicting the grain refinement during SPD. The formation of new grain boundaries induced by the multiplication of geometrically necessary dislocations (GNDs) and local bond energies dislocations resulting from the effective dislocation-free path and solute–solute nearest-neighbour interactions were predicted.

A disclination-based model describing the grain subdivision mechanism was proposed by Seefeldt et al. [205]. Disclinations, by definition, are line defects separating rotated (with slip activity) from unrotated (no slip activity) crystal areas. The microstructure development is described through the disclination model at two different scales, mesoscopic scale (cell block or subgrain level) and microscopic scale (cell or grain level). On the mesoscopic scale, partial disclinations describe nuclei of misorientation resulting from mobile dislocations of the same sign or character being trapped at cell block boundary or cell walls [206]. On the microscopic scale, parallel dislocation-dislocation interactions lead to the formation of dislocation sheets which in turn lead to the formation of cell walls and thus the formation of new grains [205]. Nazarov et al. [145,146] implemented the disclination criterion into a viscoplastic self-consistent model to describe the grain subdivision mechanism. The combination of these two approaches provides information on the formation of disclinations at the grain boundary junctions resulting from the strain incompatibilities between the homogenous effective medium and the grain. Junctions are then transformed into low angle dislocation boundaries and with further straining they split into new smaller grains [146].

Crystal plasticity models were developed also to understand the microstructural and texture development and to evaluate the mechanical response of ECAPed materials [141,147,148,207–209]. Several aspects were considered in these models, such as the grain size reduction, texture evolution, work hardening, grain shape effect, and grain neighboring effect. Beyerlein et al. [141] proposed a grain fragmentation model based on a visco-plastic self-consistent (VPSC) scheme. Although the proposed model considered the grain shape effect in the fragmentation criteria, it disregarded the influence of the intragranular microstructure. Another physically based approach to model grain

fragmentation was proposed by Tóth et al. [148]. The proposed model assumed that the grain is divided into two zones: the grain center and the grain boundary. The grain boundary, unlike the grain center, was assumed to be slowed down by a friction factor during deformation, leading to lattice curvature development. However, the grain-grain interaction effect was neglected in this model. Inspired by the lattice curvature approach, a recent physically based model was proposed by Kobaissy et al. [207] where the influence of the neighboring grains was taken into account. In this model, the grain-grain interaction effect was described by the accumulation of the geometrically necessary dislocations (GNDs) that were considered as additional material defects accumulated near the grain boundary to accommodate the lattice curvature [178–181]. In addition, several aspects, including texture evolution, dislocation densities evolutions, and grain fragmentation, were considered. This model was validated on pure copper processed through two passes of ECAP and showed a very good agreement with the experimental results. Even though some research efforts were devoted to modeling grain fragmentation, rather less attention was paid to the modeling of the post-mechanical properties of the ECAPed materials. In this work, the post-ECAP mechanical properties of aluminum are predicted by using a modified continuum dislocation dynamics-based model. This paper is organized as follows. The experimental procedure used to ECAP-process and characterize the mechanical, microstructural, and texture properties of an aluminum alloy and the experimental results are described in section 3.2. Section 3.3 describes briefly the grain fragmentation model and the grain neighboring effect. In section 03.4, the modeling predictions are analyzed and compared with the experiments. Conclusions are provided in section 3.5.

## **3.2 Experimental Procedure and Results**

A commercial Al Al-1100 O-tempered plate with an average grain size of  $80\ \mu\text{m}$  and initially low dislocation density is used as the starting material. Texture measurements are conducted on the starting material to confirm the typical rolled texture. A composition of 99 at. % Al purity is utilized to eliminate the occurrence of dynamic precipitation that could occur during ECAP. The plates are machined to 6" long billets with a 1" x 1" area cross section for the ECAP process.

### ***3.2.1 Equal Channel Angular Pressing (ECAP)***

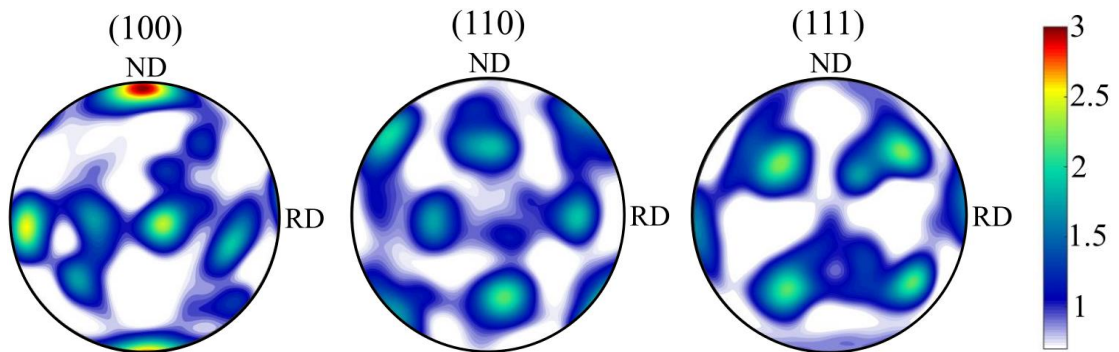
All ECAP passes are conducted at room temperature along a  $90^\circ$  angled die with a pressing speed of 10 mm/min (strain rate of  $10^{-2}\ \text{s}^{-1}$ ) with an applied back pressure from 2–4 KSI incremented with each pass. Each pass is approximately determined to apply 95% strain per pass. ECAP under Route C, with  $180^\circ$  clockwise rotation along the extrusion direction after each pass, is conducted for each billet. Single ECAP passes under the 2C and 4C routes are conducted on separate billets to study the evolution of texture, grain size, and mechanical properties.

### ***3.2.2 Electron Back Scatter Diffraction (ESBD)***

EBSB specimens are cut from the flow plane of the as-received and ECAP-processed billets using electrical discharge machining (EDM). Samples are cut from the middle section of the billet where uniform elongation is normally observed. Samples are mechanically ground on the flow plane surface using SiC paper down to a 1000 grit size. Mechanical polishing is conducted using polycrystalline diamond paste at  $3\ \mu\text{m}$  and  $1\ \mu\text{m}$  grit size, followed by a final polish of  $0.06\ \mu\text{m}$  colloidal silica. Samples are cleaned

using a felt pad and deionized water. EBSD is conducted on a TESCAN FERA-3 SEM under a 15-keV beam voltage. For the rolled condition, a 3 x 3 mm<sup>2</sup> area is scanned with a 10 μm step size, while for all ECAP samples a 25 x 25 μm<sup>2</sup> area is scanned with a 0.1 μm step size. EBSD scans are acquired using Oxford Instruments Aztec software, and post processing, including grain size determination and texture, are conducted on *Oxford Instruments HKL Channel 5 software*. A minimum of 10,000 grains are used to calculate the pole figures and to represent the texture of the as-received and ECAP-processed billets. It is argued that to accurately represent the macrotexture of medium- to moderately textured materials, the orientation data from approximately 10,000 grains generated from EBSD are necessary.

### 3.2.3 Experimental Results



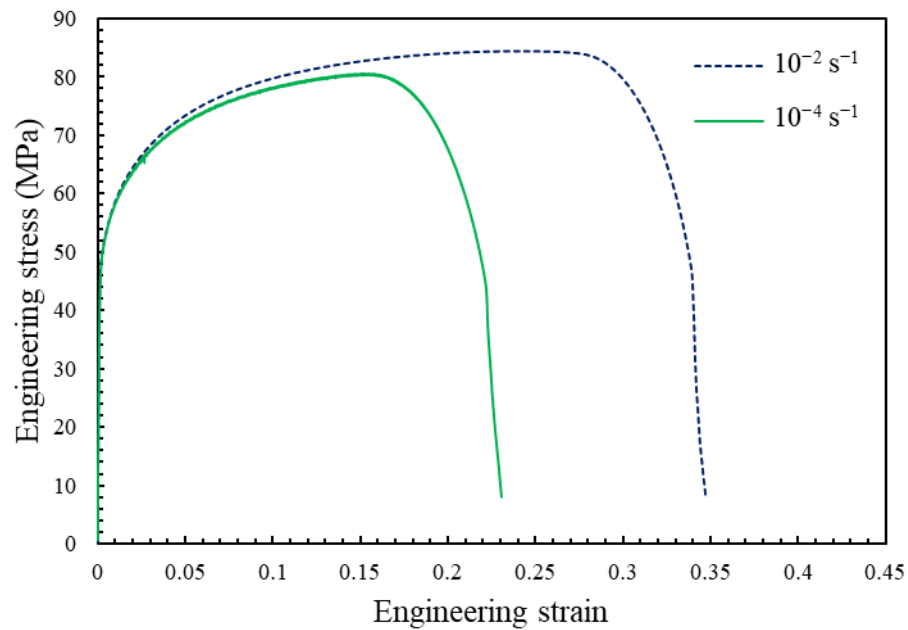
**Figure 3.2 Pole figures representing the initial texture of Aluminum alloy AA-1100.**

Figure 3.2 shows the (100), (110), and (111) pole figures of the initial Al 1100 alloy. The (111) pole figure shows a typical cube  $\{001\} \langle 100 \rangle$  texture commonly observed in hot-rolled FCC alloys formed due to dynamically recrystallized grains during high-temperature rolling [210,211]. Some diffuse texture densities are also observed in the (111) pole figure, suggesting that some recrystallized grains may have formed within the shear bands during the rolling process, causing some grains to misorient away from

the typical cube texture. Equiaxed grains within these shear bands could become possible nucleation sites for new recrystallized grains during ECAP with larger misorientations, which could further misorient the grains away from the typical cube texture [212].

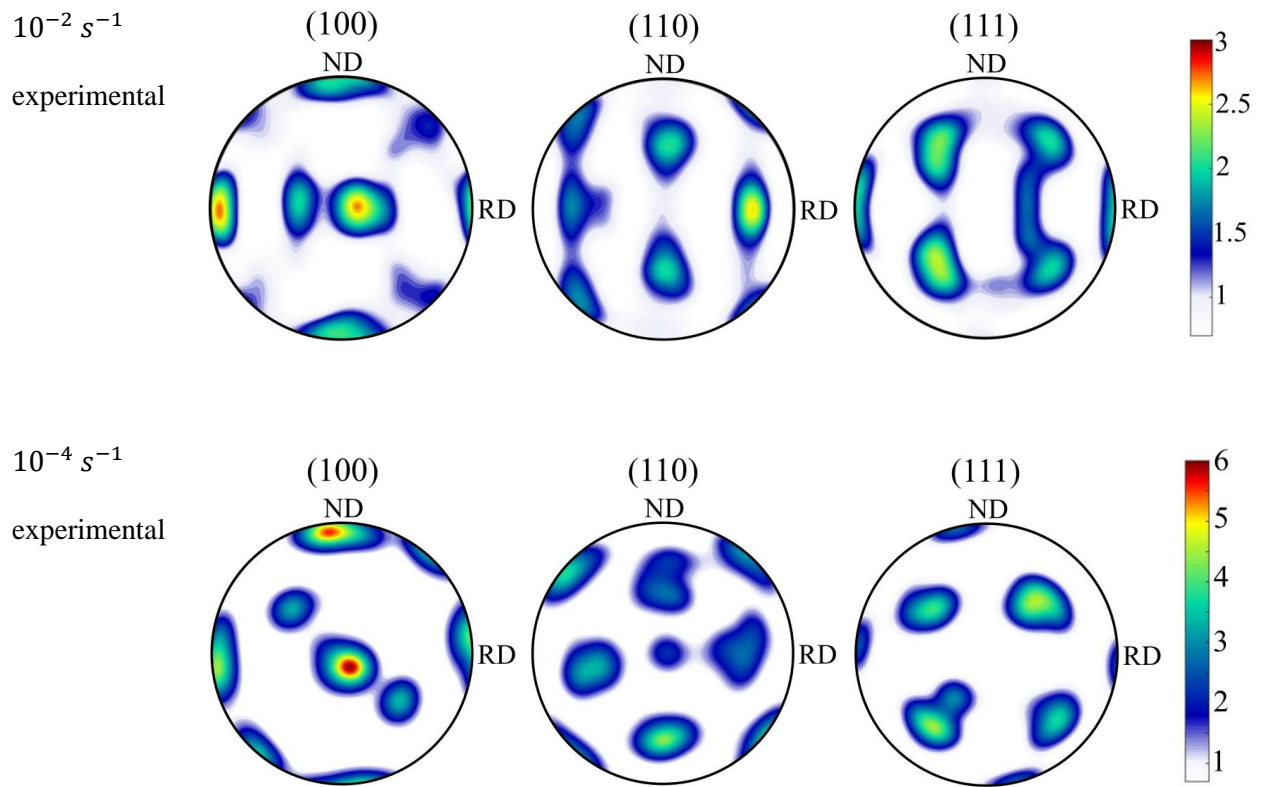
Figure 3.3 shows the tensile engineering stress-engineering strain plots at room temperature for the as-received Al-1100 under two different strain rates,  $10^{-2}$  and  $10^{-4}$   $s^{-1}$ , along the rolling direction (RD). The strain hardening response between the two strain rates does not show a significant difference in the experimental tests due to similar slip conditions. Compression tests conducted by other studies on Al1100-O alloys at  $10^{-5}$  to  $10^{-1}$   $s^{-1}$  also showed a similar lack of strain hardening difference within this strain rate window. Strain rate hardening differences were observed only under high strain impact tests with a range of 100–1000  $s^{-1}$  [213]. The uniformly elongated region for the  $10^{-4}$   $s^{-1}$  strain rate in Figure 3.3 occurs at 0.15 strain, compared to the  $10^{-2}$   $s^{-1}$  strain rate at 0.25 strain; hence, strain localization is occurring sooner for the  $10^{-4}$   $s^{-1}$  condition. Due to the symmetric cube texture observed, isotropic strain hardening responses can be assumed for the starting material. Anisotropic strain hardening responses have been observed for FCC alloys with anisotropic texture properties.



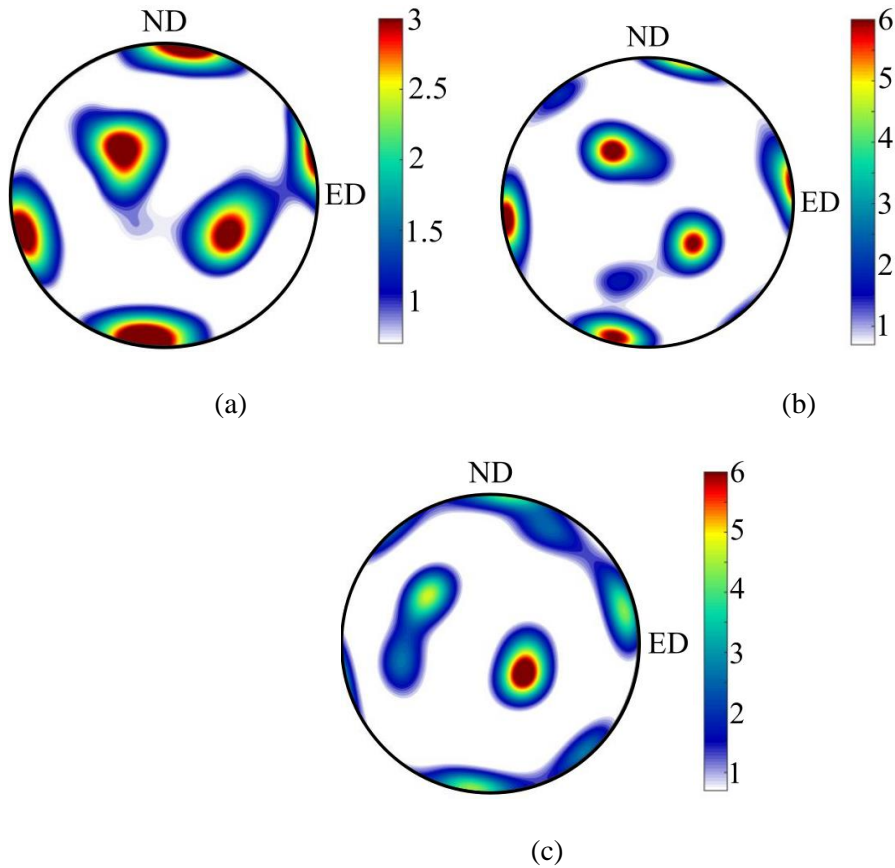


**Figure 3.3 Measured stress-strain response of the as-received Al-1100 alloy at two strain rates,  $10^{-2} \text{ s}^{-1}$  and  $10^{-4} \text{ s}^{-1}$ .**

Figure 3.4 shows the pole figures after tensile deformation at both strain rates. The texture is measured in the uniformly elongated region away from the necked region. Similar texture evolution for the two different strain rates is observed. In both textures, the initially misoriented grains are reoriented closer to the typical cube texture, allowing easy dislocation slip and providing a recovery process for deformed grains. This recovery process is normally observed during rolling deformation of FCC alloys, but this similar mechanism was observed during simple tensile deformation to accommodate higher straining [214,215].



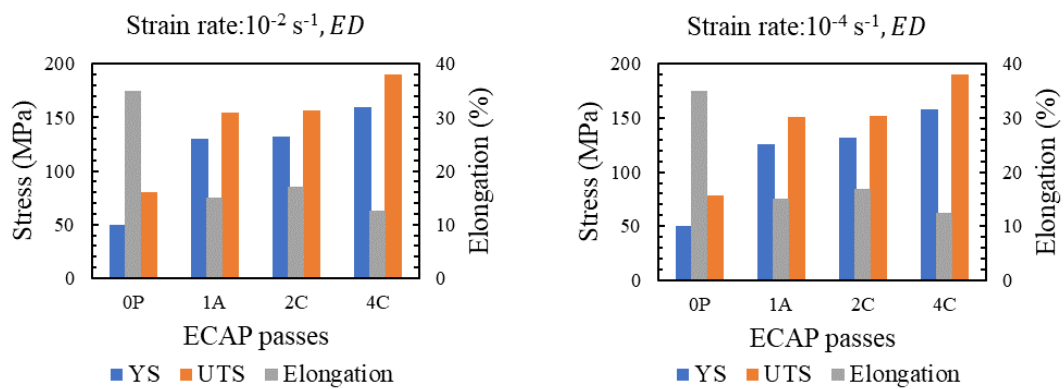
**Figure 3.4 Measured textures of the tensile as-received samples at two strain rates.**



**Figure 3.5 (111) pole figures of the measured textures after 1 (a), 2 (b), and 4 (c) passes of ECAP via route C.**

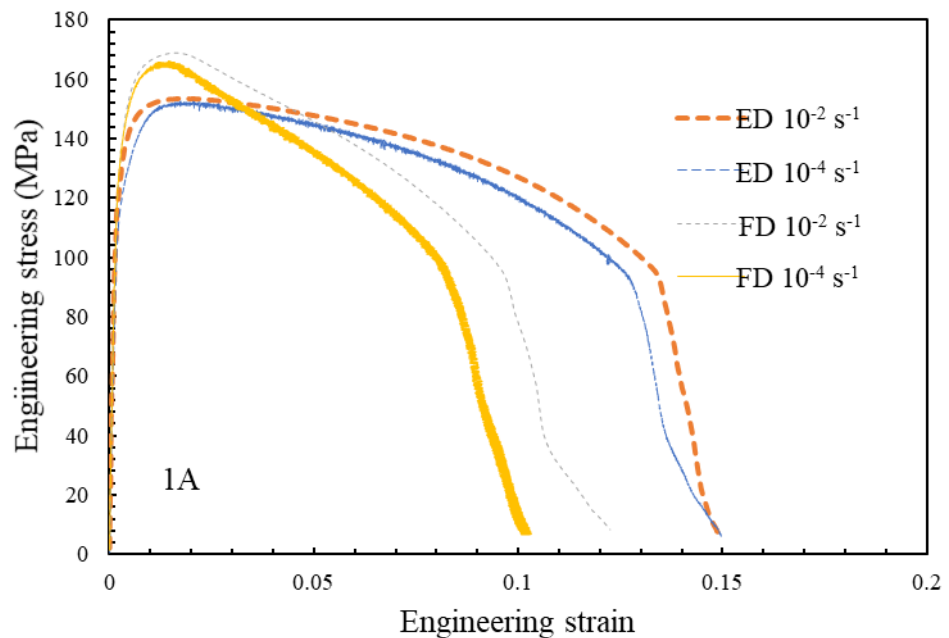
Figure 3.5 shows the ECAP texture of the flow plane for routes 1A, 2C, and 4C. The texture of the 1A ECAP route shows a rigid rotation of  $45^\circ$  around the flow direction of the center of the cube texture but maintains the typical cube texture. ECAP was conducted at room temperature; hence, strong grain refinement should be observed with the formation of subgrain and low-angle grain boundaries. The major texture densities show a slight spread in orientation from the main oriented peaks, which show subgrain formation with a misorientation of  $1^\circ$ – $2^\circ$  and the formation of low-angle grain boundaries with misorientations of  $2^\circ$ – $10^\circ$ . Route C involves rotating the billet by 180 degrees along the extrusion direction between each ECAP pass. After the first pass, a simple shear along the  $45^\circ$  angle produces elongated grains along the shearing direction. On the second pass,

due to the 180-degree rotation, an equal and opposite shear strain is applied on the billet, which readjusts the elongated grains to a more equiaxed structure. The comparison between the textures of route 2C and route 1A shows a distinct difference in the low-angle spread of the major texture points in the pole figures. Therefore, subgrain and low-angle grain boundaries are decreased, while high-angle grain ( $>10^\circ$ ) boundaries are increased. The route 4C texture shows a further increase in high-angle grain boundaries, with the development of new density peaks away from the typical cubic texture. However, the density of low-angle grain boundaries stayed very similar to route 2C. Those grain misorientation distributions are commonly observed in low-temperature ECAP of FCC alloys. Early ECAP deformation ( $\sim 1$  to 2 passes) results in subgrain boundary formation with low-angle grain boundaries. Then, with increasing number of passes, more dislocations are deposited along the subgrain, and low-angle boundaries increase the misorientation angle, leading to the development of more low-energy high-angle grain boundaries [216].

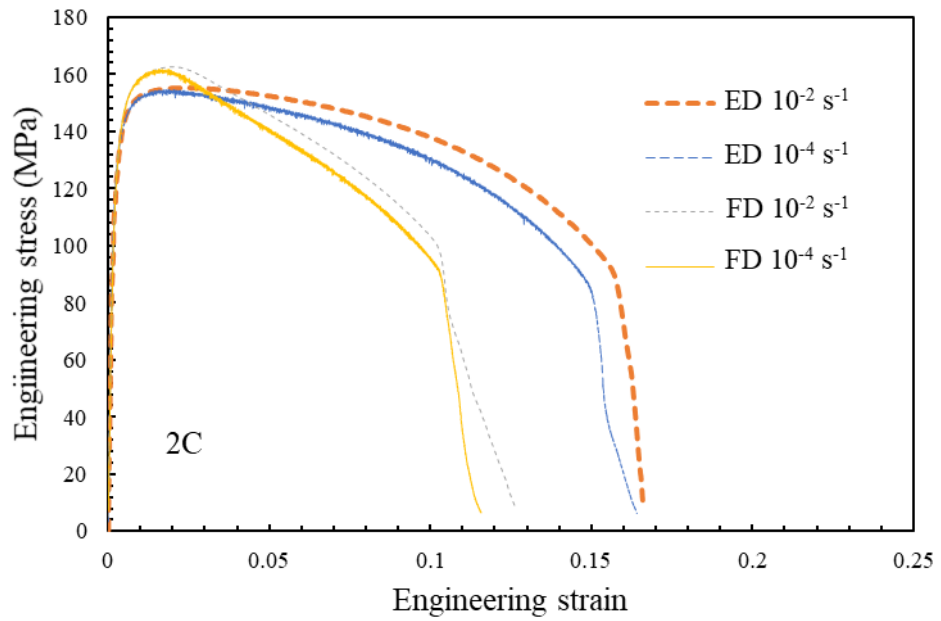


**Figure 3.6 Experimental tensile behavior data (yield strength (YS), ultimate tensile strength (UTS) and elongation) of the as-received sample (0 pass) and the ECAPed samples after 1, 2, and 4 passes via route C at two strain rates. Data values for only the ED tests are shown.**

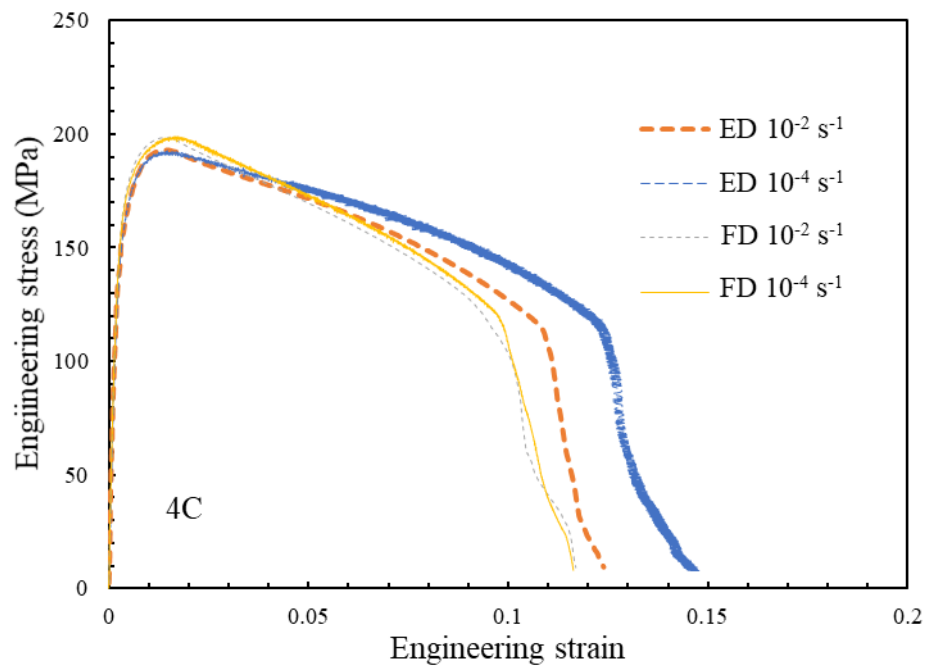
To investigate the mechanical properties of AA-1100 after ECAP, tensile tests are performed at room temperature. Tensile loading is applied on specimens with their major axes being aligned along either the extrusion direction (ED) or the flow direction (FD) at two strain rates of  $10^{-2} \text{ s}^{-1}$  and  $10^{-4} \text{ s}^{-1}$ . A summary of the yield stress (YS), ultimate tensile strength (UTS), and elongation is shown for each ECAP route at  $10^{-2} \text{ s}^{-1}$  and  $10^{-4} \text{ s}^{-1}$  strain rates in Figure 3.6. The yield and ultimate tensile strengths increased from 50 MPa and 80 MPa to 130 MPa and 150 MPa after one pressing pass and to 160 MPa and 190 MPa after 4 passes, respectively. The higher strength of the ECAPed material is attributed to the decrease in the grain size (Hall-Petch effect), where the flow stress is inversely proportional to the square root of the grain size. The elongation decreased considerably after one pass and remained almost unchanged with the increasing number of ECAP passes.



(a)



(b)



(c)

**Figure 3.7 Engineering stress vs. engineering strain plots for the ECAPed Al-1100 alloy at two different strain rates and along two directions for routes (a) 1A, (b) 2C, and (c) 4C. (ED: extrusion direction and FD: flow direction).**

Figure 3.7(a) shows the experimental tensile responses of route 1A at two different strain rates and along two different directions, extrusion and flow. Experimental results show very little strain hardening difference between the two directions and strain rates. This type of hardening behavior was observed for similar Al alloys with ultrafine grain structure. Figure 3.7(b) and (c) show the experimental tensile responses of routes 2C and 4C, respectively. An increase in the yield stress and ultimate tensile strength is observed with the increase in the number of passes, which can be attributed to the grain refinement and increase in dislocation density. In contrast, a relatively perfect plastic behavior is observed for all ECAP routes 1A, 2C, and 4C. The lack of strain hardening could be due to the increased dislocation density after ECAP, which allows more dynamic dislocation recovery in FCC alloys during tensile deformation [217].

### 3.3 Modeling Methodology

#### 3.3.1 Summary of the CP-CDD Approach

During severe plastic deformation, dislocation density increases drastically in the polycrystal, leading to an increase in the internally stored energy. As deformation continues, new grain boundaries are developed, and the internal energy is released by the fragmentation of the parent grain into smaller grains [30]. In prior work, Kobaissy et al. [207] proposed a grain fragmentation model based on a crystal plasticity (CP) scheme coupled with a continuum dislocation dynamics (CDD) model to capture the microstructural behavior during the ECAP process. The behavior of each crystal is described by crystal plasticity. The Taylor-Lin [162] [161,163] homogenization scheme is used to capture the overall response of the metallic polycrystal. The polycrystal Cauchy stress is expressed as  $\mathbf{T} = \frac{1}{N} \sum_{k=1}^N w^k \mathbf{T}^k$ , where  $w^{(k)}$  and  $\mathbf{T}^{(k)}$  correspond to the weight

factor and the Cauchy stress of the  $k^{th}$  crystal, respectively, and  $N$  is the total number of crystals. In this scheme, the addition of the elastic  $\mathbf{l}_e^{(k)}$  and the plastic  $\mathbf{l}_p^{(k)}$  velocity gradient tensors in each grain is assumed to be equal to the macroscopic velocity gradient  $\mathbf{L}$  ( $\mathbf{l}_e^{(k)} + \mathbf{l}_p^{(k)} = \mathbf{L}$ ). The stress in a metallic single crystal is defined by the second Piola-Kirchoff stress tensor, which is expressed as  $\mathbf{T}^* = \mathcal{L} \cdot \mathbf{E}^e$ , where  $\mathcal{L}$  is the fourth-order stiffness tensor of the single crystal and  $\mathbf{E}^e$  is the elastic Green-Lagrange strain tensor. The Cauchy stress in each crystal can be written then as  $\mathbf{T}^{(k)} = \frac{1}{\det \mathbf{F}^e} \mathbf{F}^e \mathbf{T}^* \mathbf{F}^{e-T}$ . In this work,  $\mathbf{F}$  represents the deformation gradient tensor, which can be decomposed multiplicatively into elastic  $\mathbf{F}^e$  and plastic  $\mathbf{F}^p$  deformation gradient tensors as  $\mathbf{F} = \mathbf{F}^e \mathbf{F}^p$  [166]. The evolution of the plastic deformation gradient  $\mathbf{F}^p$  can be expressed in terms of the plastic velocity gradient tensor  $\mathbf{L}^p$  as follows:  $\dot{\mathbf{F}}^p = \mathbf{L}^p \mathbf{F}^p$ , with  $\mathbf{L}^p = \sum_{s=1}^{12} \dot{\gamma}^s \mathbf{S}^s$  for materials deforming only by slip.  $\dot{\gamma}^s$  is the slip shear rate on the slip system “s” and  $\mathbf{S}^s = \mathbf{m}_0^s \otimes \mathbf{n}_0^s$  is the Schmid tensor, where  $\mathbf{m}_0^s$  and  $\mathbf{n}_0^s$  are the slip direction and the slip plane normal of the “s” slip system, respectively.

A continuum dislocation dynamic model is coupled with the crystal plasticity model for the purpose of capturing the evolution of dislocation densities. The Orowan relationship [169] is used to describe the effect of mobile dislocation density and glide velocity in the formulation of the plastic shear rate:  $\dot{\gamma}^s = \rho_m^s b v_g^s$ , where  $\rho_m^s$  is the mobile dislocation density in the slip system “s” and  $b$  is the magnitude of the Burger vector. The dislocation glide velocity  $v_g^s$  on system “s” can be written as  $v_g^s = v_0 \left| \frac{\tau^s}{\tau_{th}^s} \right|^{1/\eta} \text{sign}(\tau^s)$ , where  $v_0$  is the reference velocity,  $\eta$  is the strain rate sensitivity factor,  $\tau^s$  is the resolved shear stress on slip system “s,” and  $\tau_{th}^s$  is the threshold resolved stress of the slip system “s.”  $\tau_{th}^s$  can be decomposed additively into three stresses, the



initial critical resolved shear stress  $\tau_0$ , the Hall-Petch stress  $\tau_{HP}^s$ , and the shear stress responsible for the material hardening  $\tau_H^s$ . Hence, the threshold stress on each slip system “s” is expressed as  $\tau_{th}^s = \tau_0 + \tau_{HP}^s + \tau_H^s$ . The Hall-Petch stress is expressed in terms of the Hall-Petch parameter  $K$  and grain size  $D$  as  $\tau_{HP}^s = K^s D^{-0.5}$ . In addition, the hardening stress resulting from the long-range interactions between dislocations is expressed as  $\tau_H^s = \sum_{r=1}^{N_{si}} \Omega^{sr} \alpha_{BH} G b \sqrt{\rho_{TSS}^r}$ , where  $\Omega^{sr}$  is the interaction matrix,  $\alpha_{BH}$  is the Bailey-Hirsch coefficient,  $G$  is the shear modulus,  $N_{si}$  is the number of slip systems that interact with the slip system “s,” and  $\rho_{TSS}^r$  is the total statistically stored dislocation density, defined as the sum of the mobile ( $\rho_m^r$ ) and the immobile ( $\rho_i^r$ ) dislocation densities in the slip system “r” ( $\rho_{TSS}^r = (\rho_m^r + \rho_i^r)$ ). During plastic deformation, both the mobile and the immobile dislocation densities can evolve. The evolution laws for these two quantities are described by Li et al. [171] and are represented below in equations (3.1) and (3.2).

$$\dot{\rho}_m^s = \alpha_1 \rho_m^s v_g^s / \bar{l} - 2\alpha_2 R_c (\rho_m^s)^2 v_g^s - \alpha_3 \rho_m^s v_g^s / \bar{l} + \alpha_4 (|\tau^s| / \tau_{th}^s)^\zeta \rho_i^s v_g^s / \bar{l} \quad (3.1)$$

$$+ \alpha_5 \sum_{\beta=1}^{N_{cs}} P^{s\beta} \rho_m^\beta v_g^s / \bar{l} - \alpha_6 R_c \rho_m^s \rho_i^s v_g^s$$

$$\dot{\rho}_i^s = \alpha_3 \rho_m^s v_g^s / \bar{l} - \alpha_4 (|\tau^s| / \tau_{th}^s)^\zeta \rho_i^s v_g^s / \bar{l} - \alpha_6 R_c \rho_m^s \rho_i^s v_g^s \quad (3.2)$$

In these equations,  $\bar{l}$  is the mean free path of dislocations,  $R_c$  is the critical radius for dislocation annihilation,  $P^{s\beta}$  is the matrix that describes the probability for the cross-slip mechanism to occur, and  $\zeta$  is a constant set as 0.5. Six dislocation mechanisms contributing to the hardening behavior of the material are described by the rate equation (1), which depends on six material parameters ( $\alpha_1 - \alpha_6$ ). The first term captures the rate of multiplication and generation of mobile dislocations resulting from the propagation of resident dislocations and the production of new dislocations due to Frank-Read sources.

The second term describes the annihilation of two mobile dislocations of opposite signs. The immobilization of mobile dislocations due to the formation of dipoles and junctions is captured in the third term, while the mobilization of immobile dislocations due to the breakup of pinning points, junctions, and dipoles is described in the fourth term in equation (3.1). The fifth term accounts for the cross-slip mechanism that occurs when a screw dislocation on one slip plane jumps to another slip plane during plastic deformation. Finally, the annihilation of mobile and immobile dislocations due to their interaction is presented in the sixth term.

### ***3.3.2 Grain Fragmentation Modeling***

Severe plastic deformation alters the microstructural and texture properties of polycrystalline materials by evolving the dislocation density and grain size. In the proposed approach, material hardening results from the evolution of the dislocation density and reduction of the average grain size that hinder the movement of dislocations. We differentiate between two types of dislocations: the statistically stored dislocations (SSDs) and the geometrically necessary dislocations (GNDs). SSDs are dislocations that are randomly trapped within a grain, while GNDs are dislocations that accumulate near the grain boundaries. GNDs account for the effect of the neighboring grains by the additional storage of materials defects that hinder the movement of mobile dislocations and thus reduce their mean free path. SSDs give rise to homogeneous stress and strain fields [159], while GNDs contribute to an inhomogeneous state of stress and strain that accommodates the lattice curvature during the non-uniform plastic deformation [173]. The GND effect is implemented in the mean free path of the moving dislocations and written as follows [157,158]:

$$\bar{l}^s = \frac{c^*}{\sqrt{\sum_{j=1}^{N_{sl}} w^{js} (\rho_{TSS}^j + \|\rho_{GND}^j\|)}} \quad (3.3)$$

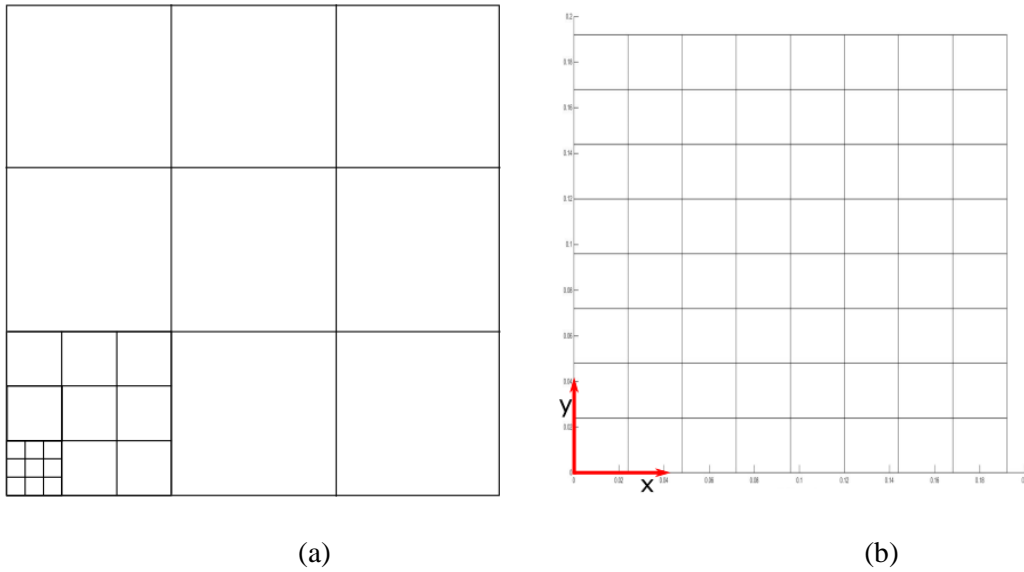
where  $c^*$  is scale factor accounting for the non-uniformity of the dislocations distribution in the crystal,  $w^{js}$  is a weight matrix fully populated by ones for simplicity, and  $\|\rho_{GND}^j\|$  denotes the density norm of GNDs on slip system “ $j$ ” and is expressed in terms of the Nye’s tensor  $\alpha_{nm}^j$  corresponding to slip system “ $j$ ” [155] as,

$$\|\rho_{GND}^j\| = \frac{1}{b} \sqrt{\alpha_{nm}^j \alpha_{nm}^j} \quad (3.4)$$

The evolution of the Nye’s tensor for large deformation is described as the gradient of the plastic velocity gradient  $\mathbf{L}^p$ :

$$\dot{\alpha} = \text{curl}(\mathbf{L}^p) \text{ or } \dot{\alpha}_{ij} = e_{jkl} L_{il,k}^p \quad (3.5)$$

where  $e_{jkl}$  denotes the permutation tensor.  $L_{il,k}^p$  is the derivative of the plastic velocity gradient and is obtained using the central difference method [159].



**Figure 3.8. (a) Subdivision of grain into 9x9 subgrains, and (b) schematic representation of the polycrystal.**

A grain fragmentation model was recently proposed by Kobaissy et al. [207] to predict the microstructural, texture, and mechanical behavior of cubic material during ECAP. The model is based on the lattice curvature approach proposed by Tóth et al. [148] and extended to account for the grain-grain interaction. This approach represents the initial microstructure by cubic grains with predefined grain size. Furthermore, with increasing plastic deformation, the Kobaissy et al. [207] approach accounts for the development of the misorientation angle between the center of a grain and its boundary. When a threshold misorientation angle is reached (i.e.  $5^\circ$ ), the subgrains are then considered as new grains with different orientations from their parent grain. The model assumes that a grain fragments into four grains of equal size. In this work, the grain fragmentation procedure is improved to better mimic the experimental observations: a grain is subdivided into nine subgrains with a grain-boundary-free central subgrain. The subgrains are assigned their parent grain orientation before deformation. The subgrains are considered as new grains when the fragmentation criterion is satisfied (misorientation

angle exceeds 5°). Each parent grain is allowed to split up to a maximum of 9x9x9=729 new grains (3 fragmentation levels) (Figure 3.8(a)). Depending on the neighboring grains, the subgrains of a parent grain can exhibit different levels of fragmentation. In our simulations, the initial polycrystal microstructure is discretized into a uniform 2D grid of squared grains, as represented in Figure 3.8(b). Each grain in the grid is assigned a grain size, orientation, initial dislocation density, and position whereby the neighboring grains are identified. It is assumed that the middle subgrains are not affected by the neighboring grains, while the neighboring grains' effect is accounted for in the deformation calculation of the remaining subgrains by adding the GND effect. It is also assumed that the accumulation of GNDs at the grain boundary is associated with the induced misorientation angle according to the relation proposed by Konijnenberg et al. (2015):

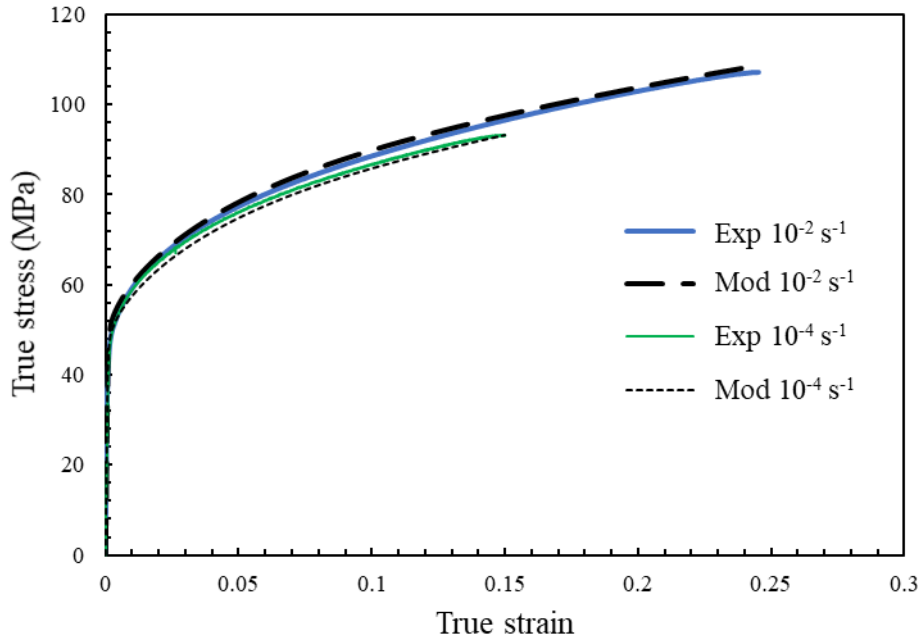
$$\theta_m = \rho_{GND} * D * b/3 \quad (3.6)$$

where D is the grain size and b is the magnitude of the Burgers vector.

### 3.4 Results and Discussions

In this section, the numerical results are presented, analyzed, and compared with the experimental ones. First, the model parameters are identified by fitting both the tensile stress-strain response and the texture results. The identified model parameters are then used to conduct ECAP simulations with route C through a different number of passes. The predicted texture evolution is then compared to the experimental results, and the strain hardening, dislocation density evolution, and slip system activity are extracted. Finally, the mechanical behavior of the ECAPed aluminum is simulated and compared to the experimental mechanical behavior results.

### 3.4.1 Calibration of Model Parameters



**Figure 3.9** Experimental and simulated true stress-true strain behaviors at two different strain rates  $10^{-2} \text{ s}^{-1}$  and  $10^{-4} \text{ s}^{-1}$ .

The initial microstructure of the polycrystal aluminum alloy presented an average grain size of  $80 \mu\text{m}$ , and its initial texture, represented by the (100), (110), and (111) pole figures, is shown in Figure 3.2. The model parameters are identified by fitting the simulated tensile true stress-true strain curves and the resulting texture to the experimental ones. As mentioned previously, the tensile tests were conducted at room temperature along the rolling direction for two different strain rates,  $10^{-2} \text{ s}^{-1}$  and  $10^{-4} \text{ s}^{-1}$ . The deformation gradient tensor can be written as:

$$F = \begin{pmatrix} e^{\dot{\epsilon}\tau} & 0 & 0 \\ 0 & e^{-\dot{\epsilon}\tau/2} & 0 \\ 0 & 0 & e^{-\dot{\epsilon}\tau/2} \end{pmatrix} \quad (3.7)$$

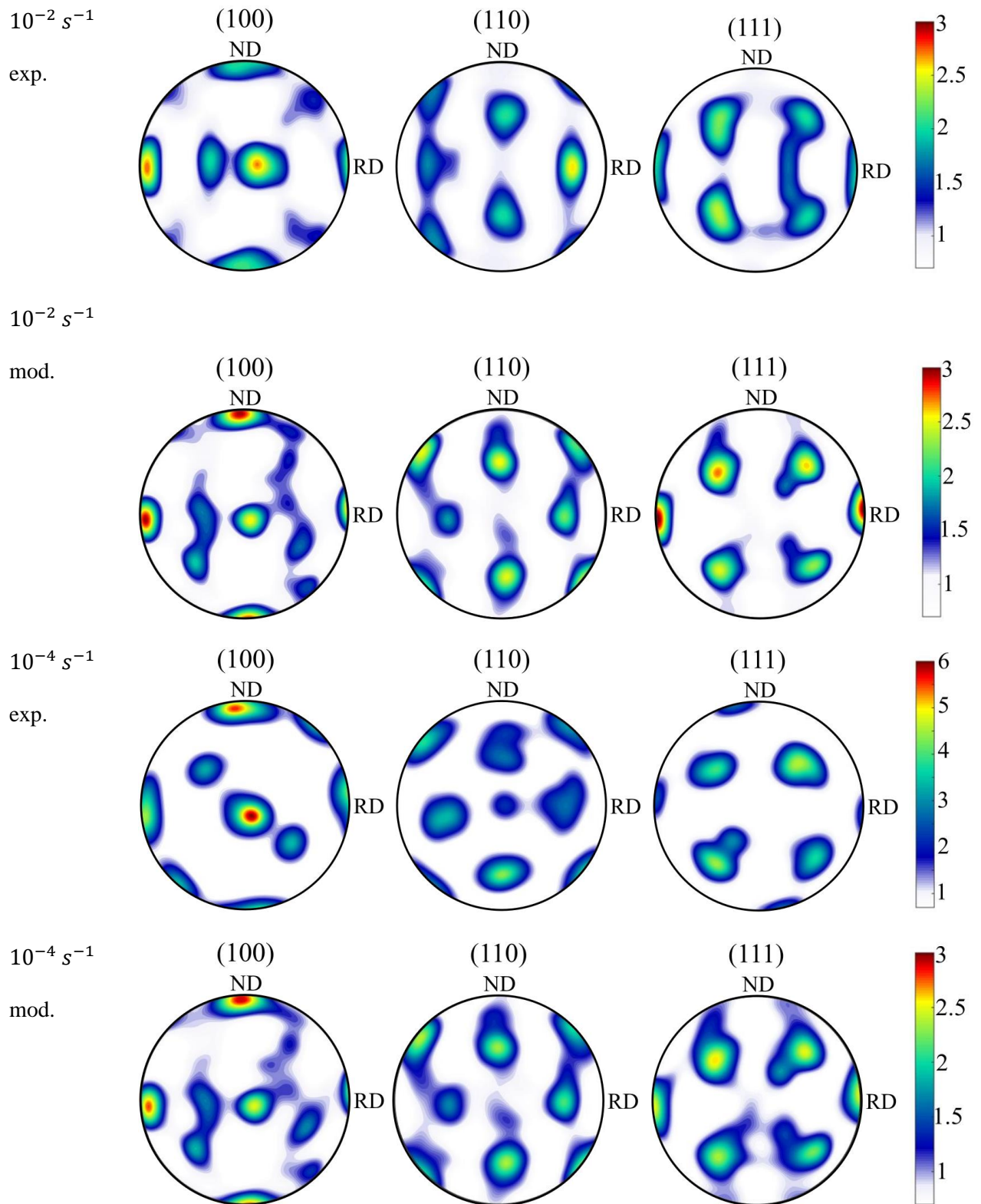
where  $\dot{\epsilon}$  is the strain rate and  $\tau$  is the time increment.

The comparison between the experimental and the numerical tensile true stress-true strain curves is presented in Figure 3.9. An excellent agreement between the

numerical and the experimental results for both strain rates is observed. It is worth mentioning that the model parameters are calibrated on the experimental results interrupted at the ultimate tensile strength (UTS), since the stress state deviates from the uniaxial loading condition with the propagation of the plastic instability. The UTS values for the  $10^{-2} \text{ s}^{-1}$  and  $10^{-4} \text{ s}^{-1}$  strain rates are equal to 93 MPa and 107 MPa, respectively.

**Table 3-1 List of properties and calibrated model parameters of aluminum alloy.**

<b>Parameter</b>	<b>Definition</b>	<b>Value (unit)</b>
$C_{11}, C_{12}, C_{44}$	Elasticity constants	106800, 60700, 28000 MPa
$\mu$	Shear modulus	26000 MPa
$K$	Hall-Petch coefficient	1.0 MPa. mm <sup>1/2</sup>
$D$	Average grain size	80 $\mu\text{m}$
$b$	Magnitude of Burgers vector	$2.86 \cdot 10^{-10} \text{ m}$
$\dot{\epsilon}$	Strain rate	0.01 s <sup>-1</sup> for ECAP
$\tau_0$	Initial critical resolved shear stress	12 MPa
$\eta$	Strain rate sensitivity	0.01
$c^*$	Numerical constant	0.8
$q$	Ratio of the latent hardening rate to the self-hardening rate	1.4
$v_0$	Reference strain rate	0.001 m/s
$\alpha_{BH}$	Bailey-Hirsch hardening coefficient	0.07
$\alpha_1$	Dislocation multiplication coefficient	0.02
$\alpha_2$	Dislocation annihilation coefficient	1.0
$\alpha_3$	Immobilization coefficient	0.002
$\alpha_4$	Mobilization coefficient	0.002
$\alpha_5$	Cross-slip coefficient	0.003
$\alpha_6$	Mobile-immobile annihilation coefficient	1.0
$\rho_{m-initial}^i$	Initial mobile dislocation density on slip system $i$	$10^{12} \text{ m}^{-2}$
$\rho_{i-initial}^i$	Initial immobile dislocation density on slip system $i$	$10^{12} \text{ m}^{-2}$
$\rho_{GND initial}$	Initial geometrically necessary dislocation density	$10^{13} \text{ m}^{-2}$



**Figure 3.10 Comparison of the measured and the simulated textures of the tensiled as-received samples at two strain rates. Note the experimental results are repeated here for the sake of visual comparison.**



The numerical texture is also compared to the experimental textures for both tensile loading conditions (the texture is measured in the gage length away from the necking area). Figure 3.10 shows the capability of the model to reproduce all the main texture components. The difference in the intensity levels may be attributed to the difference in the number of grains used to plot the pole figures. Table 3-1 lists the model parameters that are used to generate the optimal fit between the numerical and the experimental results. The initial SSD and GND densities values are taken as  $2.4 \times 10^{13} m^{-2}$  and  $1.2 \times 10^{14} m^{-2}$ , respectively.

### 3.4.2 Predictions of ECAP

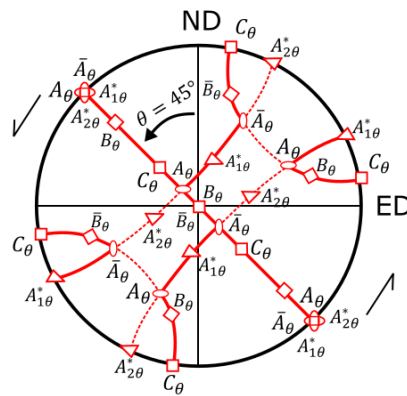
#### 3.4.2.1 Texture

**Table 3-2 Main ideal orientations, represented by their Euler angles and Miller indices, of FCC crystals in ECAP with die angle  $\Phi=90^\circ$ .**

Notation	Euler angles			Miller indices		
	$\varphi_1$	$\varnothing$	$\varphi_2$	ED	ND	FD
$A_{1\theta}^*$	80.26	45	0	$[4\ 4\ \bar{1}]$	$[\bar{1}\ \bar{1}\ \bar{8}]$	$[\bar{1}\ 1\ 0]$
	170.26	90	45			
$A_{2\theta}^*$	9.74	45	0	$[1\ 1\ 8]$	$[\bar{4}\ \bar{4}\ 1]$	$[\bar{1}\ \bar{1}\ 0]$
	99.74	90	45			
$A_\theta$	45	35.26	45	$[9\ 1\ 4]$	$[1\ 11\ \bar{5}]$	$[\bar{1}\ 1\ 2]$
$\bar{A}_\theta$	225	35.26	45	$[\bar{9}\ \bar{1}\ \bar{4}]$	$[\bar{1}\ \bar{1}\ \bar{1}\ 5]$	$[\bar{1}\ 1\ 2]$
$B_\theta$	45	54.74	45	$[15\ 4\ 11]$	$[7\ 26\ \bar{19}]$	$[\bar{1}\ 1\ 1]$
	165	54.74	45			
$\bar{B}_\theta$	105	54.74	45	$[\bar{15}\ \bar{4}\ \bar{11}]$	$[\bar{7}\ \bar{26}\ 19]$	$[\bar{1}\ 1\ 1]$

	225	54.74	45			
$C_\theta$	135	45	0	[3 3 4]	[2 2 $\bar{3}$ ]	$[\bar{1} 1 0]$
	45	90	45			

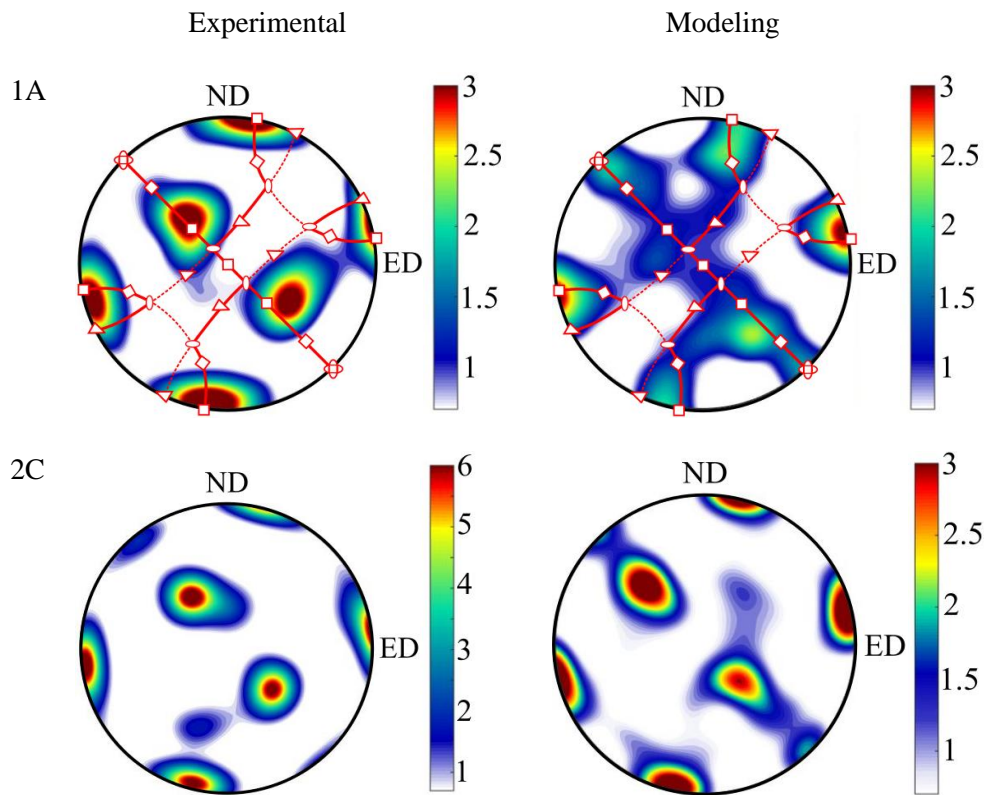
The polycrystal texture changes significantly with the severe plastic deformation induced by the ECAP process. The considerable change in the texture results in an evolution of the material's mechanical and anisotropic properties. Several processing factors, such as processing route, number of passes, die angle, etc., affect the evolution of the texture. In this work, aluminum alloy is ECAPed up to four passes through route C. A Taylor-Lin model combining crystal plasticity and continuum dislocation dynamics approaches is used to predict the texture evolution during ECAP. The predicted and the experimental texture are compared by analyzing the presence and location of the ideal orientations of the shear texture listed in Table 3-2.

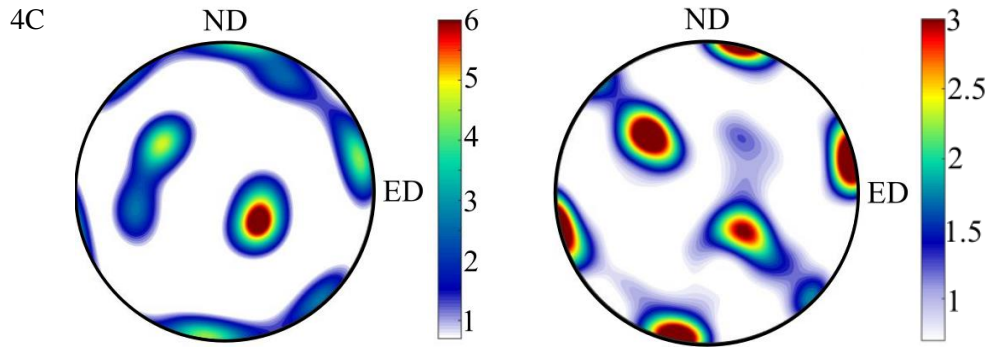


**Figure 3.11 (111) key pole figure representing the ideal orientations after one pass of ECAP.**

The ideal orientations of ECAP textures were studied by several investigations [219,220] and found to be CCW-rotated by an angle  $\theta = \Phi/2$  around the flow direction (FD) in the (111) pole figure. The main ECAP texture components, similar to simple

shear texture components, are distributed along fibers in the orientation space and are represented in the (111) pole figure in Figure 3.11 [221]. Figure 3.12 shows the experimental and the predicted textures after one pass of ECAP. The experimental texture is measured using the electron back-scattered diffraction (EBSD) method and then plotted, similarly to the predicted texture, using the MTEX software. A good agreement between the experimental and the predicted texture can be noticed; furthermore, the predicted texture exhibits all the ideal ECAP texture orientation components. All ideal components were captured by the model; however,  $A_\theta/\bar{A}_\theta$  components were missing from the measured texture. In addition, some intensity-level differences between the two textures were observed, which may be attributed to the different number of grains used to plot the pole figures.





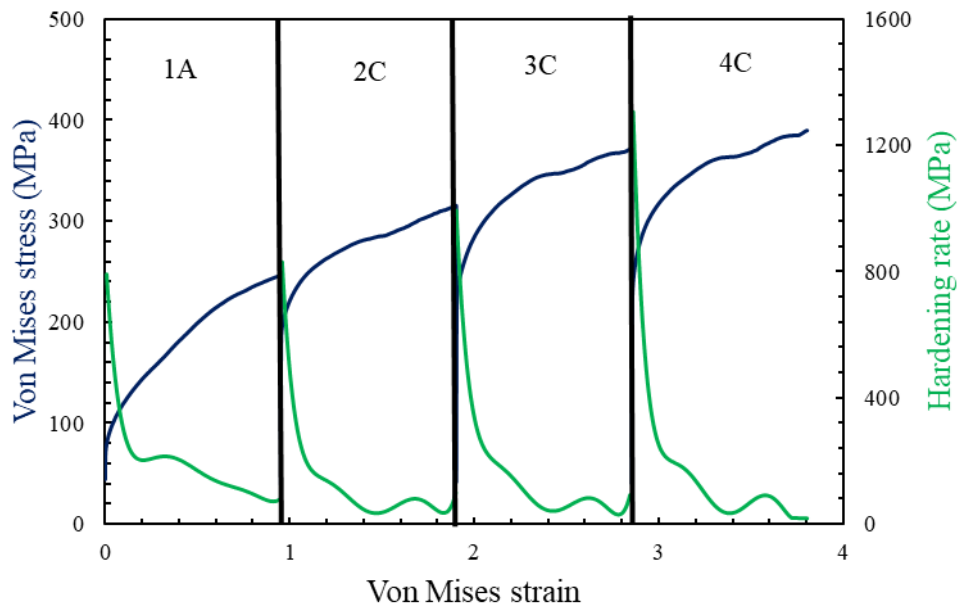
**Figure 3.12 (111) pole figures of the measured and predicted textures after 1, 2, and 4 passes of ECAP via route C. Note the experimental results are repeated here for the sake of visual comparison.**

The post-mechanical properties of aluminum ECAPed through route C after four passes is studied. Under route C, also called the reversal route, the shear direction is reversed between consecutive passes while maintaining the same plane of shearing. The texture symmetry under route C is maintained as long as the sample's deformation is kept homogeneous and the sample is rotated around the axis of symmetry (FD). This texture symmetry, also called monoclinic symmetry, exhibits a shear-like texture in which the texture after even-numbered passes is recovered and the textures after odd-numbered passes resemble the first-pass texture [30,222]. The measured and predicted textures of the aluminum ECAPed through route C after two and four passes are presented in Figure 3.12. The ideal shear texture components are observed in the measured textures of the 2C and 4C ECAPed aluminum. Furthermore, a good agreement with the predicted texture is observed, with a difference in the intensity levels of a factor of two.

#### 3.4.2.2 Strain-Hardening Behavior

In the last decade, modeling the strain-hardening behavior of materials subjected to severe plastic deformation was of interest in many investigations. Dislocation-based models were proposed for that purpose [148,223–225]. Using the continuum dislocation

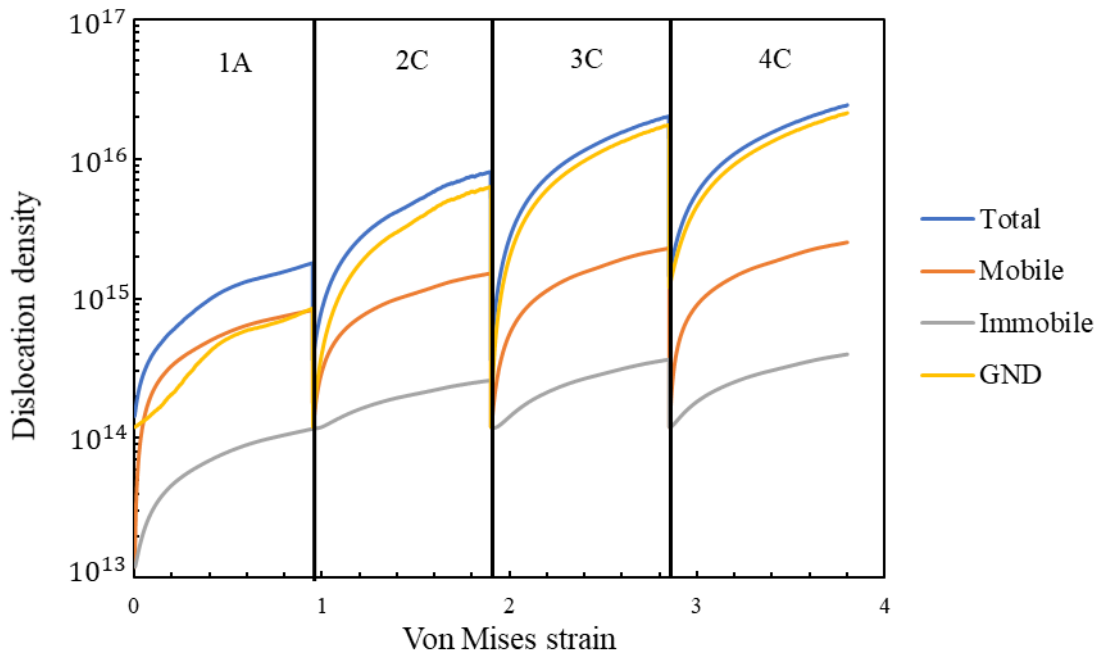
dynamics-based grain fragmentation model [207], the in-situ mechanical response of the material during the ECAP process is predicted. Figure 3.13 depicts the predicted von Mises stress-von Mises strain curve as well as the strain hardening rate versus von Mises strain for the four ECAP passes. The predicted strain-hardening behavior follows the expected behavior of a polycrystalline material as reported in the literature [148,225]. Although the elastic region (ends at a strain of 0.2%) is very small compared to the plastic region, the elastic behavior is predicted by our simulations, since the elastic deformation is accounted for by the Taylor-Lin CP-CDD model. Initially, the strain-hardening rate shows a fast linear decrease up to 20% of strain, followed by a slower continuous decrease until the end of the first pass. The decrease in the strain-hardening rate with increasing strain was suggested to be induced by the dynamic recovery process [225]. Figure 3.13 shows that the 1A aluminum exhibits a different strain-hardening behavior when ECAPed through route C, compared to the as-received material when ECAPed. The different hardening behavior is attributed to the evolution of the microstructure and texture after the 1A ECAP pass, where the majority of the grains are rotated to their ideal positions, which leads to a decrease in the Taylor factor [226]. In the 2C pass, the rate of strain hardening decreases rapidly until it reaches a plateau-like behavior after a strain of 20%. In the third ECAP pass, Figure 3.13 shows a decrease in the yield stress and a linear strain-hardening behavior due to the texture developed in the second pass, where the billet is rotated by 180° between consecutive passes. The strain-hardening behavior in the fourth pass mimics the behavior in the second pass, which can be explained by the monoclinic symmetry after even passes via route C, as illustrated in section 03.4.2.1.



**Figure 3.13 Predicted hardening behavior of aluminum alloy during four passes of ECAP**

During plastic flow, the dislocation motion is affected either by short-range barriers, such as vacancies and interstitial atoms, or by long-range barriers, such as grain/subgrain boundaries and forest dislocations. Low-angle boundaries subgrains are formed by the accumulation of dislocations. The immobilization of dislocations at the subgrain boundaries results in an increase of the misorientation angle and hence the formation of new grains. The dislocation density evolution is influenced by the microstructural change (grain size decrease) induced by the severe plastic deformation. In fact, the movement of the mobile dislocations is hindered by the increasing volume of grain boundaries [227]. Recently, several studies [228–232] characterized the microstructural evolution of aluminum alloys and measured the dislocation density for several ECAP passes via different routes. The studies reported a major increase in dislocation density after the first pass where grain fragmentation is the main deformation mechanism. However, a gradual increase was reported for the subsequent passes. Based

on the literature [228–232], the SSD density was reported to reach a value of  $2.4 \times 10^{14} \text{ m}^{-2}$  after the first pass, which is less than the value predicted by our proposed model. We can explain the difference between the experimental and predicted SSD density by the fact that the proposed model does not account for the dynamic recovery process contributing to moderate the plastic hardening during ECAP processing. A recovery factor was applied before each pass to reduce the dislocation density and hence account indirectly for the dynamic recovery process. The same recovery factor of the dislocation density between passes under route C (same as [228]) was assumed; thus, the dislocation density values are  $3 \times 10^{14} \text{ m}^{-2}$  and  $3.6 \times 10^{14} \text{ m}^{-2}$  after the second and the fourth pass of ECAP via route C.

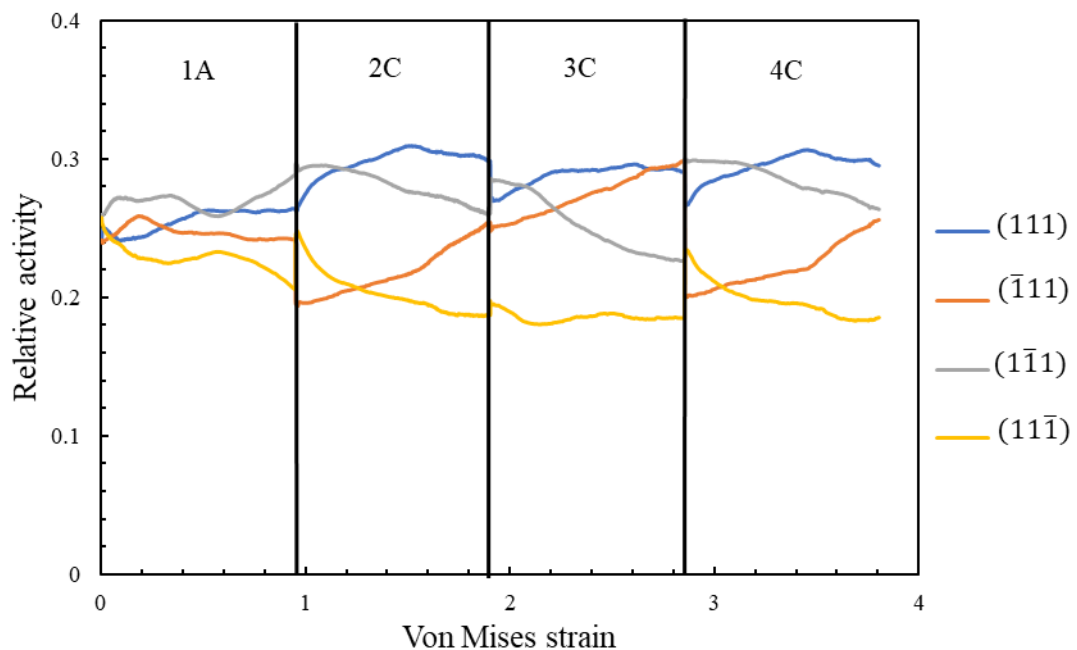


**Figure 3.14 Dislocation density evolution during the four passes of ECAP.**

Figure 3.14 shows the evolutions of mobile, immobile, and geometrically necessary dislocation densities as a function of the strain for the different ECAP passes. During the 1A pass, the densities of the mobile dislocations and the GNDs exhibit a similar evolution, although the initial value of the GND density is 10 times greater than

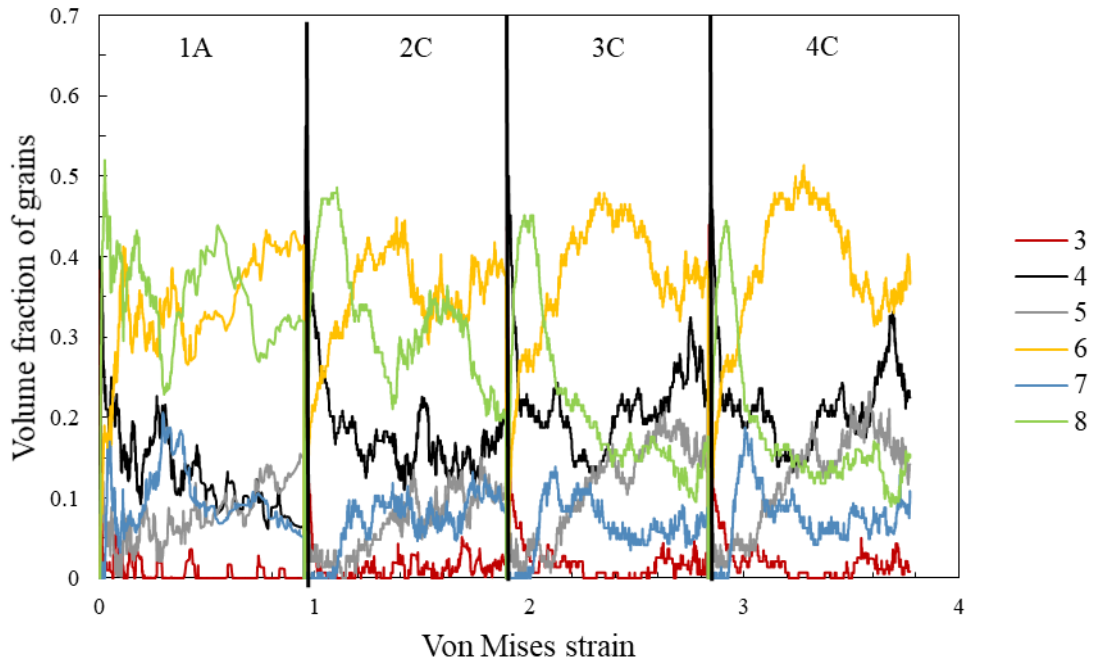
that of the mobile dislocation density. During the 1A pass, grains are subjected to severe plastic deformation, which drastically increases their internal energy, leading to grain fragmentation as a relief mechanism. Consequently, the coarse grains are fragmented into smaller grains exhibiting different dislocation densities than the parent grains. The increase in the dislocation density is predicted in Figure 3.14, where both mobile dislocations and GNDs increase similarly up to a strain of 80%. After this strain value, most of the grains are fragmented, so the mobile dislocation evolution rate decreases since the GNDs now act as obstacles at the grain boundaries. During each pass, the generation and the multiplication of dislocations will lead to an increase in the dislocation density, which is predicted by the current model in Figure 3.14.

### 3.4.2.3 Slip Activity



**Figure 3.15 Relative slip system activities during ECAP.**





**Figure 3.16 Predicted volume fraction of grains with at maximum three, four, five, six, seven or eight active slip system during four ECAP passes.**

Dislocation motion usually occurs on a specific slip system, which is a combination of slip plane and slip direction. The movement of dislocations initiates the plastic deformation, implying that several slip systems are activated. In FCC metals, twelve slip systems  $\{111\}\langle 110 \rangle$  may be activated when the resolved shear stress on a specific system exceeds the critical resolved shear stress, which is responsible for a dislocation movement. In the present work, crystallographic slip is assumed to be the main deformation mechanism that induces plasticity. The activity of slip systems affects the texture evolution and the lattice reorientation [233]. Figure 3.15 shows the relative activity of the 12 slip systems, represented by the four slip planes, obtained numerically for the four passes of ECAP. The relative activity on slip system “s,”  $RA^s$ , is calculated as the average of the slip system activity for all grains in the polycrystal [234]:

$$RA^s = \frac{\sum_{N=1,Ng} \dot{\gamma}^s(N) * w(N)}{\sum_{j=1,12} \sum_{N=1,Ng} \dot{\gamma}^j(N) * w(N)} \quad (3.8)$$

where  $N_g$  is the total number of grains and  $w$  is the weight factor of the grain.

For all passes, all of the slip systems are activated, with some slip systems dominating others. In the first pass, all slip planes have approximately similar relative activities up to 50%, after which the  $(1\bar{1}1)$  slip plane becomes more active and the  $(11\bar{1})$  slip plane becomes less active, while  $(111)$  and  $(\bar{1}11)$  remain unchanged. Other slip systems show an almost stable relative activity during the first pass. Different relative activities are shown in the second pass due to the developed texture and to the rotation of the billet by 180 between ECAP passes. We can notice that the relative activities of the  $(1\bar{1}1)$  and  $(\bar{1}11)$  slip planes exhibit an opposite evolution. The relative activity of the  $(\bar{1}11)$  slip plane shows a noticeable increase with strain, while the relative activity of  $(1\bar{1}1)$  slip plane shows a slight decrease with strain. The slip planes' activity variations could be explained by the multiplication and annihilation of dislocations on those slip systems. Figure 3.15 shows a similar relative activity evolution for the different slip planes in the 2C and 4C passes, since a similar initial texture is used for both passes due to the texture symmetry in route C after an even number of passes. In contrast, different relative activity evolutions are observed for the 3C pass since the initial texture of the billet is rotated 180°.

During ECAP, the shearing plane, defined at the two intersecting ECAP channels, are the macroscopically most stressed plane. Thus, dislocations with different Burgers vectors are developed mainly at this plane and its surrounding in which slip systems are active [235]. As mentioned previously, strain hardening is induced by the activation of different slip systems [236], and in order to accommodate for strain incompatibilities during plastic deformation, a minimum of five activated slip systems

are required [237,238]. The volume fraction of grains deforming by three, four, five, six, seven and eight slip systems are predicted in Figure 3.16. In the first pass, most of the grains deform with either six or eight slip systems which could be attributed to the high stress applied to the coarse grains in the polycrystal. However, for the second, third and fourth passes, the volume fraction of grains slipping by eight slip systems has decreased considerably while grains deforming with four slip systems has increased. This could be attributed to the presence of fine grains resulted from the fragmentation process. After the second pass, only little change is observed in the volume fraction of grains since the texture have reached its ideal ECAP components.

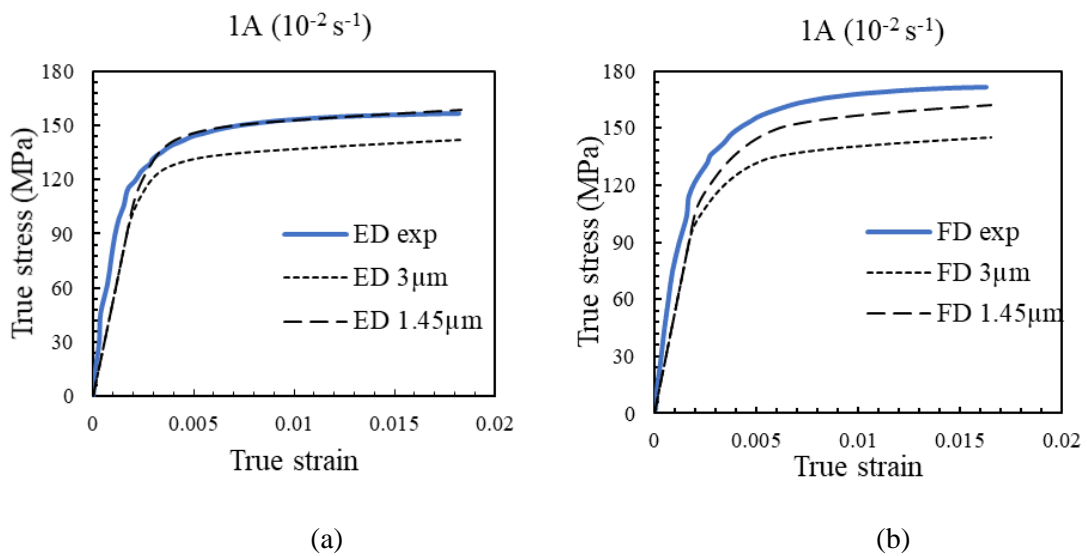
#### 3.4.2.4 Grain Size

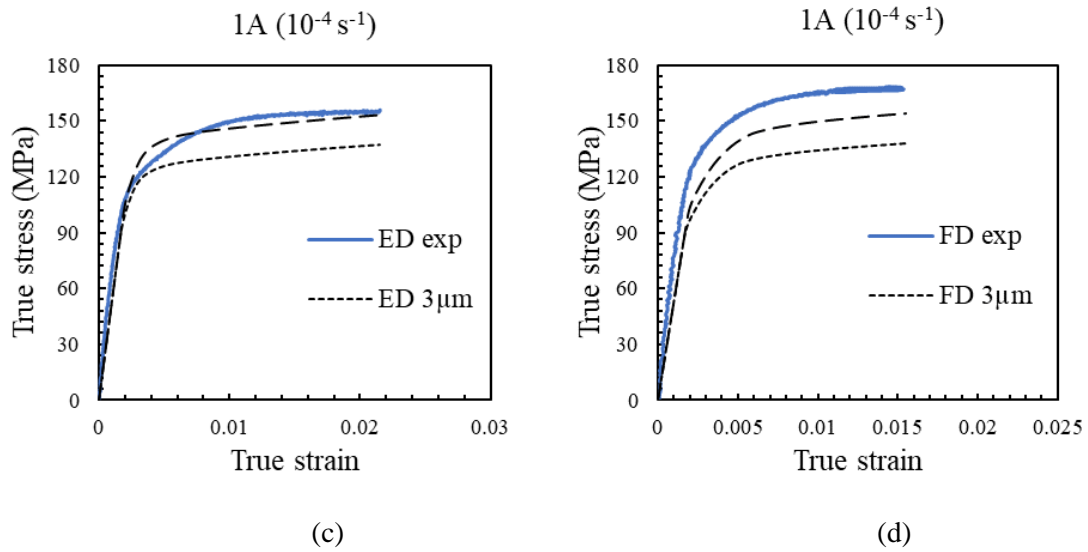
A microstructure with ultra-fine grain size varying from a few microns to submicron can be obtained from severe plastic deformation processes such as ECAP. With a high level of plastic strain, the high internal energy stored in the grains is the result of the high dislocation densities that promote the formation of obstacles (GNDs) that hinder the motion of mobile dislocations. The increase in the internal energy of the grains leads to an increase in the misorientation angle between subgrains, and grain fragmentation occurs when this angle reaches a critical value (i.e., the misorientation angle exceeds  $5^\circ$ ). The new grains are formed with a microstructure distinct from their parent grain in terms of dislocation density, grain size, and orientation.

In our grain fragmentation model, grains are subdivided initially into nine subgrains having similar microstructure and orientation to their parent grains, where each subgrain is assigned one-third of its parent grain size. As explained in section 3.3.2, each

grain is allowed to exhibit three fragmentation levels, i.e.,  $9 \times 9 \times 9 = 729$  new grains. Thus, a polycrystal with an average grain size of  $80 \mu m$  can reach  $80/27 = 2.96 \mu m$  as a minimum value after one pass of ECAP. After the 1A ECAP pass, the EBSD-measured average grain size of the aluminum alloy is found to be equal to  $1.45 \mu m$ , while the predicted value is equal to  $3 \mu m$ . An additional fragmentation level is necessary to capture the grain size after the first pass well; however, it is difficult to implement due to computational limitations. A better grain size prediction is achieved for the 2C ECAP pass. The experimental and the predicted average grain size in the 2C ECAP pass are equal to  $1.11 \mu m$  and  $1.02 \mu m$ , respectively. Furthermore, a good prediction of the average grain size is obtained at the 4C ECAP pass, with an experimental value of  $0.7 \mu m$  and a predicted value of  $0.675 \mu m$ .

### 3.4.3 Post-ECAP

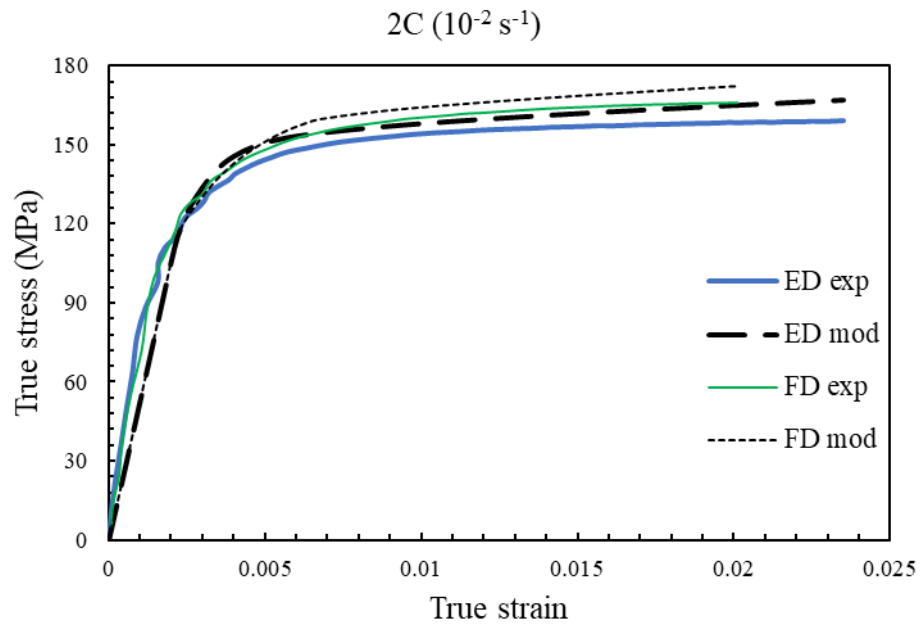




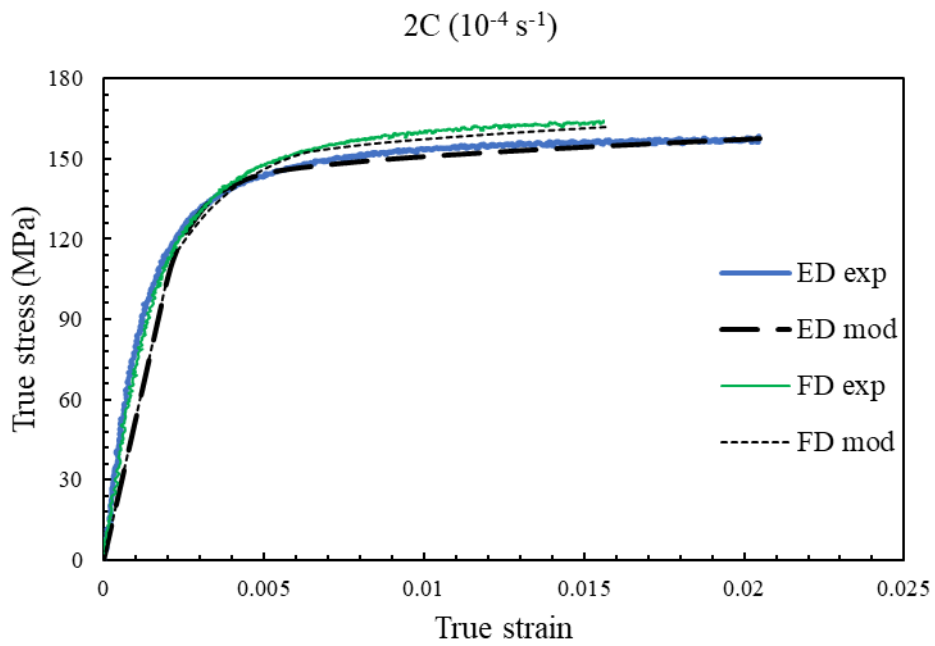
**Figure 3.17 Predictions of the stress-strain behavior of the ECAPed sample after one pass at two strain rates and along two directions (ED: extrusion direction and FD: flow direction).**

As illustrated in section 3.4.2.2, different microstructural features of the polycrystal are developed after severe plastic deformation. As the plastic strain increases, dislocations start to accumulate at the subgrain boundaries, forming low-angle grain boundaries. At higher levels of strain, the misorientation between subgrains increases and new grains are created with relatively low dislocation density. Grain fragmentation occurs in order to release the stored energy in the polycrystal during deformation. As a consequence of grain fragmentation, the new fine grain boundaries hinder the dislocation movement by pinning them at the boundaries, thus reducing the mobile dislocation density. In order to predict the mechanical properties of the ECAPed samples, several simulations were performed. Figure 3.17 shows the true stress-true strain curves of the ECAPed aluminum alloy for one pass at room temperature. The model was used to predict the flow stress up to the UTS, since no damage formulation that can predict the flow stress response after necking is included in the current model. Although the predicted grain size after one pass is  $3 \mu m$ , simulations related to the measured grain size ( $1.45 \mu m$ ) were performed for the sake of comparison with the experimental data. An excellent agreement

can be seen between the predicted ( $1.45 \mu m$ ) and the measured tensile behaviors. However, a shift of around 20 MPa is revealed between the predicted ( $3 \mu m$ ) and the measured tensile behaviors. This shift can be explained by the Hall-Petch relationship, where the flow stress is inversely proportional to the square root of the grain size, i.e., larger grains lead to smaller stress. In addition, it can be seen from Figure 3.17 that the predictions in the extrusion direction are better than the predictions in the flow direction due to the texture developed during the ECAP process. The tensile behavior of the ECAPed aluminum alloy after 2C is plotted in Figure 3.18. For both strain rates, the model-generated curves are in accordance with the experimental curves for both the extrusion direction and the flow direction. Similarly, the predictions after the fourth pass of ECAP are in excellent agreement with the experimental results for both strain rates and both directions, as shown in Figure 3.19.

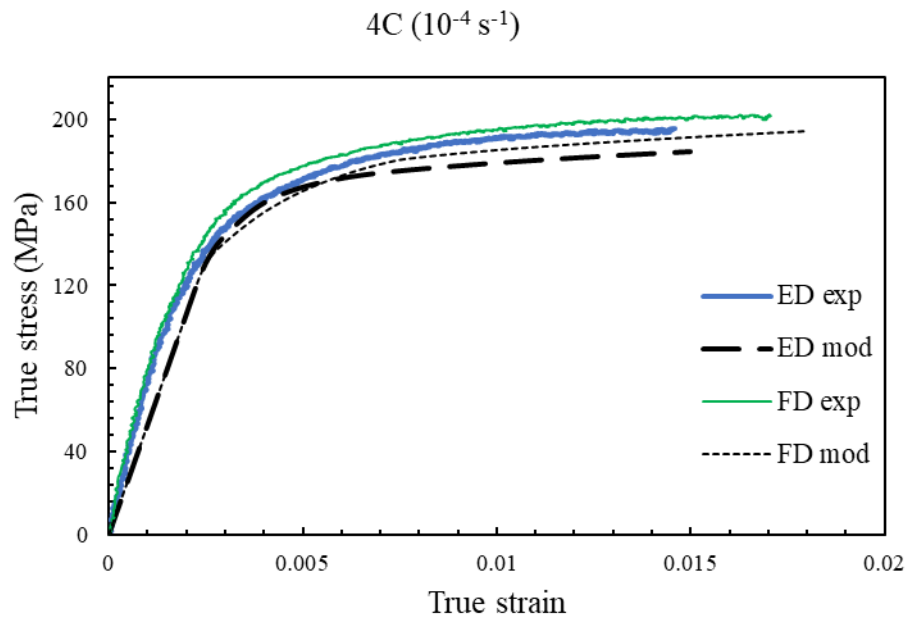
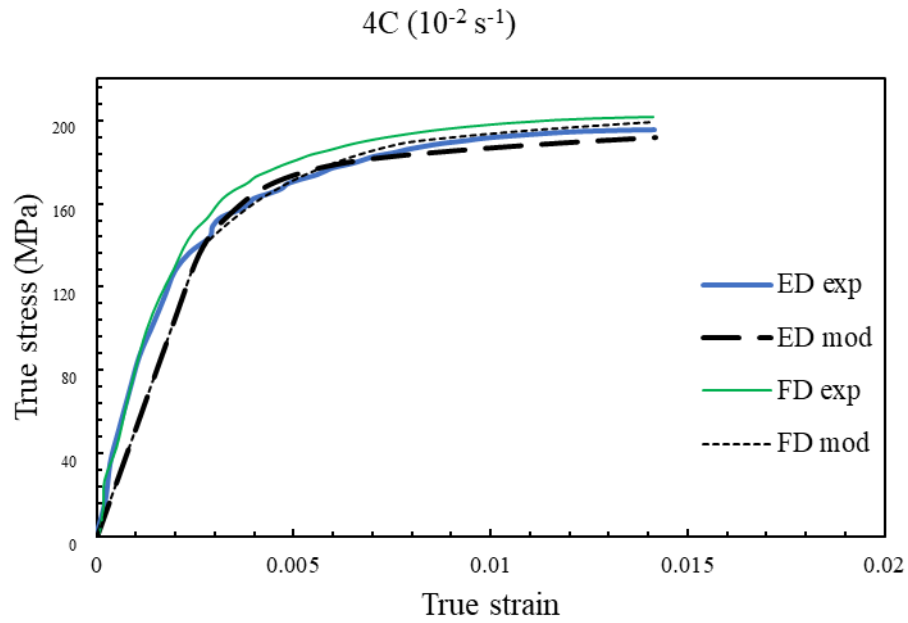


(a)



(b)

**Figure 3.18 Predictions of the stress-strain behavior of the ECAPed sample after second pass at two strain rates and along two directions (ED: extrusion direction and FD: flow direction).**



**Figure 3.19 Predictions of the stress-strain behavior of the ECAPed sample after fourth pass at two strain rates and along two directions (ED: extrusion direction and FD: flow direction).**

### 3.5 Conclusions

In this work, the material mechanical, microstructural and textural behavior during equal channel angular pressing (ECAP) processes are modeled using a multi-scale



framework that couples a crystal plasticity (CP) scheme with a continuum dislocation dynamics (CDD) model. The proposed multi-scale approach predicted the texture evolution, the statistically stored dislocations (SSDs) and the geometrically necessary dislocations (GNDs) densities evolutions, the microstructure evolution and finally the mechanical properties of the SPD processed material. The strain hardening in the model was considered to result from both the increase in the dislocation density and the grain fragmentation. The grain fragmentation process was modeled by accounting for the grain-grain interaction and incorporating the concept of the geometrically necessary dislocations (GNDs) into the mean free path of the dislocations. GNDs result from grain boundaries restricting the free deformation of a grain, causing an internal plastic deformation gradient that subsequently leads to grain fragmentation. A commercial Al 1100 billet, with rolling texture, was ECAP processed at room temperature using route C. After a single pressing, a considerable refinement of the microstructure was observed (grain size was reduced by 55 times), and the texture transformed into a shear-like texture rotated by an angle of  $45^\circ$ . The average grain size after one pass reduced from  $80 \mu\text{m}$  to  $1.45 \mu\text{m}$  and reached  $0.7 \mu\text{m}$  after four passes. The yield strength of the as-received Al alloy increased drastically from 80 MPa to 130 MPa after single pressing and to 160 MPa after four passes. The proposed model parameters were calibrated using the tensile true-stress true-strain curves of the unprocessed material at two strain rates. The ECAP-processed aluminum microstructure, texture and dislocation densities were predicted. The model predicted increase in the dislocation density during each ECAP pass, through generation and the multiplication of dislocations. Both mobile dislocations and GNDs increased similarly up to a threshold strain, beyond which the mobile dislocation evolution rate decreased. After three ECAP passes, the dislocation density increase rate

slowed down significantly. The mechanical properties of the ECAP processed materials was predicted successfully by using the predicted texture, microstructure and dislocation densities.

## CHAPTER 4

# ON THE MODELING OF THE ANISOTROPIC BEHAVIOR OF MAGNESIUM AZ31 ALLOY SUBJECTED TO ECAP

### 4.1 Introduction

The race for producing energy efficient vehicles is prompted by the need to reduce greenhouse gases and increase electric cars range per charge. Magnesium (Mg) alloys are considered as promising alternative to conventional metals and excellent candidates to save structural weight due to their low density, high specific stiffness and strength, good shock absorption capacity, and good recyclability [214,239,240]. However, the widespread application of Mg alloys is hindered by the limited understanding of their deformation behavior [214,239]. Indeed, Mg alloys processed by hot rolling or hot extrusion develop strong basal texture which leads to poor formability, low ductility and high anisotropy at room temperature (RT) [241–244]. These unfavorable properties are the result of the low number of active slip/twin systems during deformation. In general, the deformation in hexagonal close packed (HCP) metals, such as Mg, is accommodated by the following slip systems; basal  $(0001)\langle 11\bar{2}0 \rangle$ , prismatic  $\{10\bar{1}0\}\langle 11\bar{2}0 \rangle$ , pyramidal  $\langle a \rangle \{10\bar{1}1\}\langle 11\bar{2}0 \rangle$  and pyramidal  $\langle c + a \rangle \{11\bar{2}2\}\langle 11\bar{2}3 \rangle$ , and twin systems; extension twin  $\{10\bar{1}2\}\langle \bar{1}011 \rangle$  and contraction twin  $\{10\bar{1}1\}\langle 10\bar{1}\bar{2} \rangle$  [245,246].

At room temperature, the deformation of Mg is accommodated by mainly two independent  $(0001)\langle 11\bar{2}0 \rangle$  basal slip systems. The activation of additional deformation modes such as non-basal slip and twinning are needed to satisfy the Taylor criterion for homogeneous plastic deformation of a polycrystalline aggregate that requires the

activation of five independent slip systems [238,241,247]. However, the activation of the different deformation modes depends on external factors (such as loading direction, strain rate and temperature [103,248–255]) and structural parameters (such as dislocation density, crystallographic orientation and microstructure [241,252,256–258]). The plastic anisotropy exhibited by Mg alloys is the result of substantial variations in the critical resolved shear stress (CRSS) needed to activate the deformation modes via dislocation glide or twinning. Numerous studies reported estimations of the critical resolved shear stresses (CRSS) that needs to be achieved to activate dislocation movement on a specific slip system and to activate twinning [245,259–263]. The results in the literature indicate that the basal slip is the easiest system to activate, followed by extension twinning, prismatic and pyramidal  $\langle a \rangle$  and finally pyramidal  $\langle c + a \rangle$ . Accordingly, basal slip and extension twin are the main active deformation mechanisms during uniaxial tension/compression testing of randomly textured-Mg polycrystals at low temperatures and low strain rates [95,259,264–266]. Lou et al. [267] reported that the plastic deformation of Mg alloy during uniaxial tension results primarily from the activation of basal slip with secondary contributions from other non-basal slip and twinning. Furthermore, during in-plane compression twinning activity was found to be initially predominant, as strain increases basal slip to becomes the predominant deformation mode [267]. Moreover, as processing temperature increases the CRSS of the non-basal slip systems (prismatic and pyramidal) decreases which results in an increase in their activity [245,261,266,268–270]. Additionally, the ductility of Mg alloys mechanisms is enhanced at higher temperature with the activation of intergranular deformation mechanisms such as grain boundary sliding (GBS) and dynamic recrystallization (DRX) [246,249,261,271–273]. Textured-Mg polycrystals exhibit anisotropic deformation induced by deformation

twinning [10]. Extension twinning accommodates the deformation of strongly textured Mg alloys, with a parallel c-axis to the normal direction (e.g., rolled Mg sheets), at low strains during uniaxial compressive loading along the rolling direction [274–276]. Al-Samman and Gottstein [249] studied the limited formability of magnesium AZ31 alloy by compressing several samples with different initial textures at room temperature. It was reported that the strain was accommodated by the basal and prismatic slip as well as twinning with various activation rate varying from one sample to another leading to different mechanical behaviors [249]. A strain rate study, conducted by Ulacia et al. [246], reported that extension twinning in a compressed Mg alloy along the rolling direction (RD) is enhanced at high strain rates ( $\sim 10^3 \text{ s}^{-1}$ ) even at very high temperatures ( $\sim 400 \text{ }^\circ\text{C}$ ), however, this mechanism exhibits a transition into slip at low strain rates when processed above  $\sim 200 \text{ }^\circ\text{C}$ . Dogan et al. [277] reported that twin activity is highly dependent on grain size and upon grain refinement the tension–compression yield asymmetry was decreased which indicates that more slip activity is involved during deformation.

Although numerous experimental investigations helped unravel the mechanisms of deformation controlling the plasticity of HCP metals, the effect of anisotropy is still not well understood. Consequently, mathematical models can be valuable tools to gain insight into the HCP metals plasticity deformation mechanisms that are still challenging to assess experimentally. Over the past several decades, several phenomenological [278,279] and physical-based [144,260,280–283] models were proposed to allow better understandings the behavior of HCP metals under multiaxial loading conditions. A phenomenological continuum plasticity model, implemented into a finite element framework (ABAQUS), was developed by Lee et al. [278] to predict the anisotropic and

asymmetric properties of magnesium alloy sheets. The model integrated anisotropy by modifying the Drucker-Prager pressure dependent yield surface [284]. Furthermore, the general stress–strain response of metal sheets, that includes the Bauschinger effect, transient behavior and the unusual asymmetry, was modeled mathematically by adapting the two-surface hardening law model. Slip, twinning, and untwining observed when testing HCP metals in tension/compression were considered by the model with simplified relations between the state of deformation and their histories. Slip mode was reported to be the dominant deformation mechanism during uniaxial tensile loading while twinning and untwining modes were reported to be the dominant deformation mechanisms during in-plane compression and compression-tension loadings [278]. Agnew et al. [260] used an elasto-plastic self-consistent (EPSC) crystal plasticity model to investigate the effect of slip and twin activity on the anisotropic asymmetry of a commercial magnesium alloy AZ31B. It was reported that accurate simulation of the anisotropic behavior is achieved by the activation of non-basal slip and deformation twinning which local contributions dictate the development of intergranular strains. Dogan et al. [285] used a hybrid experimental and viscoplastic self-consistent (VPSC) crystal plasticity model to study the anisotropic behavior and texture evolution of twin-roll cast magnesium AZ31 alloy sheets processed with equal channel angular plate extrusion at different temperatures. Staroselsky and Anand [282] developed a crystal mechanics-based model implemented in a commercial FEM model that accounts for both slip and twinning mechanisms, to predict the anisotropic plastic deformation and texture evolution of hcp metals. The proposed model predicted that basal, prismatic, pyramidal  $\langle a \rangle$  slip and extension twinning are the dominant intragranular crystallographic mechanisms. In addition, the effect of the intergranular grain boundary accommodation was implemented into the model where it

was shown that the crystal lattice reorientation during deformation influences predominantly the strain hardening behavior of the material. The simulations also showed that the rapid crystal lattice reorientation is induced mostly by the mechanical twinning.

Severe plastic deformation (SPD) processes are being used to improve the mechanical properties of magnesium alloys [286]. Equal channel angular pressing (ECAP) induces significant microstructural changes leading to enhanced ductility and strength [22]. The ECAP process parameters used to control the levels of applied shear strains and consequently the texture and microstructure evolutions are; temperature, number of passes, and back pressure [287]. Usually, severe pressing of ductile materials such as Mg alloys is performed at elevated temperatures to prevent cracking and thus to enhance the formability of the material [288]. However, this could affect the grain refinement mechanism and consequently reduce the expected materials' strength [289]. The effect of temperature on the mechanical response and microstructure evolution in of pure Mg and Mg alloys has been investigated under various loading conditions[289–294]. Kwak et al. [290] showed that as the processing temperature is increased, both strength and fracture tendency decreased, while grain size increased due to dynamic recrystallisation. A study conducted by Tan et al. [294] concluded that ECAP processing of a rare earth magnesium alloy achieves the best comprehensive properties at a temperature of 340 °C. Yamashita et al. [289] reported that both yield strength and ductility are significantly enhancement after the first pass of ECAP, while negligible improvement was measured with further pressing passes [289]. Another ECAP experiments were conducted by Cheng et al. [295] at 300 °C to study the influence of the number of ECAP passes on grain refinement and material texture of Mg alloy. After 6 passes, the microstructure reached its finest state where the grain average size was refined

from 10  $\mu\text{m}$  to 2.49  $\mu\text{m}$ . Furthermore, the texture revealed a strong ED-tilted texture where the intensity increased with the increase of the number of ECAP passes. ECAP-processing of Mg at low temperatures requires a meticulously controlled back-pressure. Gu et al. [293] processed Mg alloy at room temperature by applying a back-pressure greater than the yield stress by a factor of three. The average grain size was reduced from 10  $\mu\text{m}$  to around 3  $\mu\text{m}$  after only one pass. In addition, extension twins  $\{10\bar{1}2\}$  were observed in the coarse grains while they were absent in small grains. Xia et al. [292] were able to deform Mg AZ31 alloy without fracture up to 8 ECAP passes at low temperatures by applying controlled back pressure. The microstructure was refined significantly and an average grain size of 1  $\mu\text{m}$  was attained after 4 passes. As a result of this refinement, the hardness of the material also increased, as expected by the Hall-Petch relationship.

Besides numerous experimental works, many authors attempted to model grain refinement mechanism [141,147,148,185,207,296–298]. Segal [185] proposed a model that links the grain refinement mechanism to the macro-mechanics of simple shear. The grain subdivision criterion is assumed to be induced mainly by shear bands, caused by the intensive applied shear strain, as well as subgrain rotation, caused by crystallographic slip during SPD. Another model, proposed by Zhu and Lowe [296], concluded that grain refinement mechanism is induced by the interaction of shearing plane with both crystal structure and deformation texture. The accumulation of shear strain played an additional role in inducing this mechanism during multiple ECAP passes and different routes. The aforementioned models neglect the effect of recovery and recrystallization processes during severe plastic deformation. A grain fragmentation model proposed by Kobaissy et al. [207,299] implemented the grain-grain interaction effect by means of the geometrically necessary dislocations accumulated at the grain boundaries. These



accumulations were assumed to restrict the free deformation of the grain inducing internal plastic deformation gradient between the grain center and its boundaries which subsequently lead to grain subdivision. Su et al. [298] proposed a grain refinement model for HCP crystalline structures at elevated temperatures and included the influence of thermal processes such as continuous recovery, dynamic recrystallization, and grain growth. Another grain refinement model based on dynamic recrystallization principles was proposed by Figueiredo and Langdon [300] where the creation of new grain sites is preferred to nucleate along the grain boundaries and along twin boundaries. Kowalczyk-Gajewska et al. [301] presented a computational procedure to model the texture evolution using visco-plastic self-consistent (VPSC) scheme and grain refinement by applying a simplified phenomenological model. Recently, Gzyl et al. [302] developed a multiscale cellular automata finite element method to model the microstructure evolution at various temperatures and strain rates during ECAP. The proposed approach assumed that the nucleation of new grain sites is triggered when a critical value of dislocation density in a certain cell is attained. While the stored energy in this cell is higher than that in another cells, nucleation is favored, and the cell transforms into a recrystallized cell (subgrain) which in turn lead to the formation of new grains.

Although it is reported that grain refinement reduces the anisotropic behavior of Mg alloys, the associated mechanism resulting from the mechanical shear and strain accumulation during severe plastic deformation such as ECAP, are not well depicted by the existing constitutive models. It remains arguable if the existing models are comprehensive and can sufficiently describe the grain refinement process and the grain size anisotropic dependency resulting from severe plastic deformation conditions. To the best of our knowledge, no grain refinement model for Mg alloys found in literature has

accounted for the grain-grain interaction which is expected to have a noticeable effect on the grain refinement mechanism. In this work, a physically based model accounting for the aforementioned effect is proposed to predict the mechanical behavior, the texture evolution, and the microstructural development. The proposed model uses the crystal plasticity (CP) model coupled with a continuum dislocation dynamics (CDD) model. Since twinning mechanism has a significant effect on the anisotropy of magnesium alloys, this effect was modeled through crystal plasticity approach with maintaining the slip modeling through the continuum dislocation dynamics approach. A grain refinement mechanism is also integrated into the model in order to predict the formation of refined grains during severe plastic deformation. Anisotropy evolution of magnesium is then examined by predicting the mechanical behavior, dislocation evolution, and the slip/twin systems activities of the ECAPed material. This study has contributed to the intricate understanding of the deformation mechanisms and the mechanical properties of Mg AZ31 subjected to ECAP process. The paper is organized as follows. A detailed description of the model combining the crystal plasticity, the continuum dislocation dynamics and the grain refinement is presented in section 4.2. Section 4.3 presents a comparison between the experimental results with the predicted ones where analysis and discussion are performed. Conclusions are drawn in section 4.4.

## 4.2 Modeling approach

### 4.2.1 Texture development

#### 4.2.1.1 Texture representation in Euler space

The mechanical properties of HCP polycrystalline metals are highly directional and dependent on the crystallographic orientation. The crystallographic orientation, or texture, is controlled through material processing to design the optimal mechanical properties. A random texture with crystals positioned in all possible orientations with equal frequency results into an isotropic polycrystalline material. Anisotropy in polycrystalline materials is associated with crystals positioned in a privileged orientation [303]. Indeed, the macroscopic properties of polycrystalline materials is an averaged behavior over all the single crystal orientations. A fixed coordinate system is associated to the crystal structure unit cell,

In principle, the crystal orientation is described by various equivalent methods of representation. Their basic concept allows mapping the fixed coordinate system associated to the crystal structure unit cell (crystal coordinates) to a global coordinate system. The most common method of representing crystal orientation is by using the Euler's angle where the orientation of each crystal is described by three elemental rotations around the reference coordinate system (Z, X, Z) (see Figure 4.1). Three elemental rotations are obtained by knowing three different angles labeled the Bunge-Euler angles  $\varphi_1$ ,  $\Phi$ , and  $\varphi_2$ . Thus, the rotation matrices associated with each elemental rotation are:

$$\mathbf{R}_{\varphi_1}^Z = \begin{bmatrix} \cos \varphi_1 & \sin \varphi_1 & 0 \\ -\sin \varphi_1 & \cos \varphi_1 & 0 \\ 0 & 0 & 1 \end{bmatrix} \quad (4.1)$$

$$\mathbf{R}_{\phi}^X = \begin{bmatrix} 1 & 0 & 0 \\ 0 & \cos \phi & \sin \phi \\ 0 & -\sin \phi & \cos \phi \end{bmatrix} \quad (4.2)$$

$$\mathbf{R}_{\varphi_2}^Z = \begin{bmatrix} \cos \varphi_2 & \sin \varphi_2 & 0 \\ -\sin \varphi_2 & \cos \varphi_2 & 0 \\ 0 & 0 & 1 \end{bmatrix} \quad (4.3)$$

The transformation matrix  $\mathbf{Q}$  that allows mapping the crystal coordinates to the global coordinates is obtained by multiplying the three elemental rotation matrices:

$$\mathbf{Q}_{(\varphi_1 \phi \varphi_2)} = \begin{bmatrix} \cos \varphi_1 \cos \varphi_2 - \sin \varphi_1 \sin \varphi_2 \cos \phi & \sin \varphi_1 \cos \varphi_2 + \cos \varphi_1 \sin \varphi_2 \cos \phi \\ -\cos \varphi_1 \sin \varphi_2 - \sin \varphi_1 \cos \varphi_2 \cos \phi & -\sin \varphi_1 \sin \varphi_2 + \cos \varphi_1 \cos \varphi_2 \cos \phi \\ \sin \varphi_1 \sin \varphi_2 & -\cos \varphi_1 \sin \varphi_2 \end{bmatrix} \quad (4.4)$$

$$\begin{bmatrix} \sin \varphi_2 \sin \phi \\ \cos \varphi_2 \sin \phi \\ \cos \phi \end{bmatrix}$$

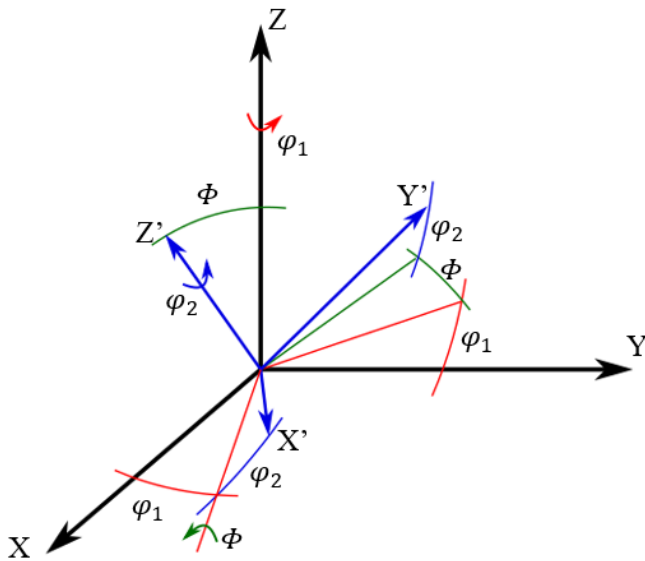


Figure 4.1. Euler angle rotation representation in space

#### 4.2.1.2 Crystallographic Rotations associated with ECAP passes

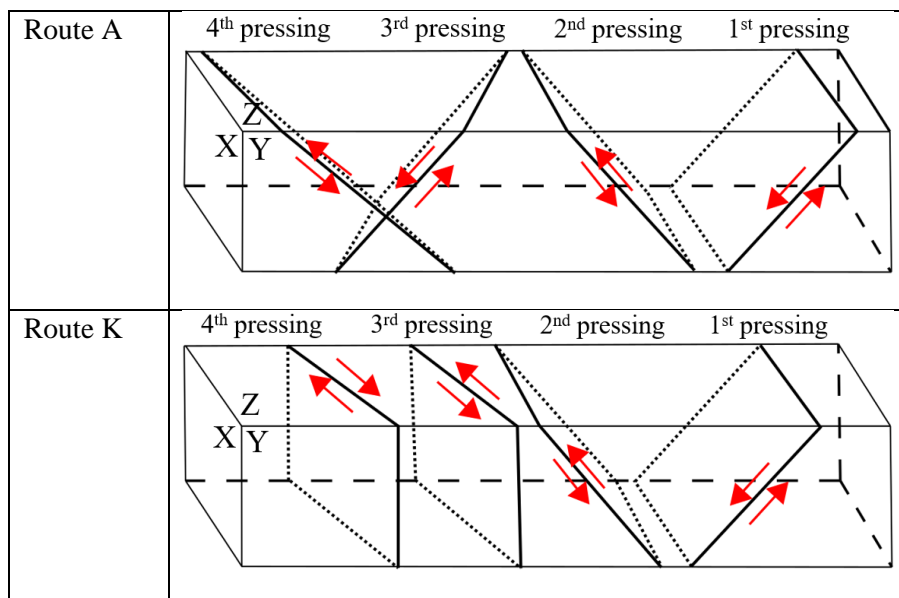
ECAP processing of polycrystalline materials induces a significant texture evolution associated with the severe plastic deformation. Additionally, the severity of the applied plastic deformation is affected by several processing factors, such as processing route, number of passes, die angle, etc. Consequently, a considerable change in the material's mechanical and anisotropic properties results from the texture evolution. In this work, ECAP routes A, and K were studied to investigate the mechanisms of deformation controlling the grain fragmentation in Magnesium AZ31 alloy. Route A consist of reinserting the billet into the ECAP channel without applying any rotation between each pass. While in route K, a 90° rotation of the ECAPed-billet is applied about the extrusion direction axis before the third pass. The shear planes associated with each route are described in Figure 4.2 where the X, Y, and Z planes denote the transverse (extrusion) plane, the flow plane, and the longitudinal plane of the billet, respectively. Routes A and K are not redundant shear strain processes since the applied shear deformation is not cancelled by consecutive passes instead it is accumulated after each pass [22]. The effect of these processing routes on the distortion of a cubic element (square sections in the three orthogonal planes) is presented in Table 4-1 and it is used to illustrate the induced deformation. After ECAP processing, the square sections are distorted, and the deformed configuration are represented schematically in Table 4-1. For instance, a billet pressed via route A in a 90° ECAP die exhibit a shear plane that is 45° inclined with respect to the X-plane. As a result, the cubic element is distorted by compressing the X-plane, shearing the Y-plane and no deformation on the Z-plane (see Figure 4.3). The illustration of the cross-sectional deformation along the three orthogonal planes are shown for routes A and K up to four passes. A close inspection for the shearing

pattern in route A, shows that cross-sections parallel to X and Y planes exhibit continuous deformation with no shape recovery with increasing number of passes, while cross-section parallel to the Z-plane exhibits no deformation and their initial square shape is maintained. On the other hand, the 90° rotation about the Z axis leads to a distortion of the Z plane, as illustrated for route K.

The accurate description of the of ECAPed material texture necessitates applying a rigid body rotation before each pass. For instance, although no billet rotation is applied in route A around the extrusion direction, a 90° rotation of the texture around the flow direction is needed to account for the re-insertion of the billet. For route K, a double rigid body rotation of the texture is necessary before the third pass, one about the extrusion direction and the other about the flow direction. Analytically, the rotation matrix  $Q$ , representing the Euler angles, should be multiplied by a rotation matrix before each ECAP pass. Thus, the new transformation matrix becomes:



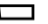









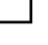



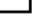
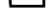








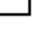



$$Q_{new} = RQR^T \quad (4.5)$$

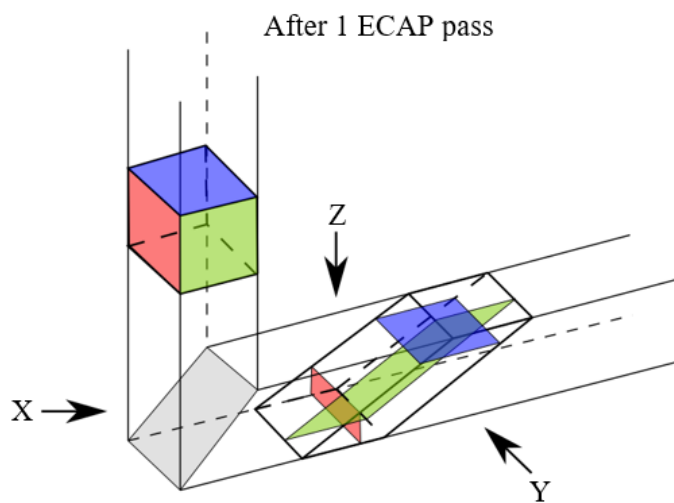
where  $R$  is the rigid body rotation matrix about desired specific axis.



**Figure 4.2** The shear planes observed on the X, Y, and Z planes for 4A and 4K processing routes

**Table 4-1 Distorted planes projected on X, Y and Z planes for routes A and K up to four passes**

Route	Plane	Number of pressings				
		0	1	2	3	4
Route A	X					
	Y					
	Z					
Route K	X					
	Y					
	Z					



**Figure 4.3. Example of the projection of the three cross-sections viewed on X, Y and Z planes**

#### **4.2.2 Summary of grain refinement modeling**

Modeling grain refinement is based on the concept that dislocation cell structures, formed due to the application of plastic strain, are transformed into finer grain structures. The increase in the misorientation between neighboring dislocation cells lead

to continuous decrease in the grain size, and thus, resulting in significant material hardening [304]. Dislocation density-based models are commonly used in modeling grain refinement mechanism since they incorporate the effect of dislocation evolution mechanisms. The dislocation density and its evolution are considered to be the main parameters affecting material hardening. We differentiate between the statistically stored dislocations (SSDs) and the geometrically necessary dislocations (GNDs). The SSDs are randomly trapped dislocations resulting from plastic strain. Its density evolution is affected by 6 factors: (1) the production of Frank-Read source dislocations, (2) the annihilation of two mobile dislocations, (3) the immobilization of mobile dislocations, (4) the mobilization of the immobile dislocations, (5) the cross-slip contribution, and finally (6) the trapping of mobile dislocations. The GNDs accommodate the plastic strain gradient resulting from the misorientation between subgrains or grains. The concept of GNDs was initially introduced by Nye (1953) and then expanded by Ashby (1970) to explain the formation of dislocations accommodating the lattice curvature during the non-uniform plastic deformations. The GNDs are accounted for in our approach using the effective dislocation mean free path proposed by Ohashi (2005) and Ohashi et al. (2007). A multiscale model is proposed to incorporate the effect of SSDs and GNDs by coupling continuum dislocation dynamics with a crystal plasticity framework [159]. Accordingly, the influence of both dislocation types is combined in a mean free path formulation as described in Kobaissy et al. [207] by the following relation,

$$\bar{l}^s = \frac{c^*}{\sqrt{\sum_{j=1}^{N_{sl}} (\rho_{TS}^j + \rho_{GND}^j)}} \quad (4.6)$$



where  $c^*$  is a constant,  $N_{si}$  is the number of slip systems interacting with the slip system “s”,  $\rho_{TS}^j$  is the total statistically stored dislocation density and  $\rho_{GND}^j$  is the density of the geometrically necessary dislocation on the slip system “j”.

Dislocations arising from statistically stored sources contribute to the stress rise within the crystal, while those trapped at the crystal boundaries such as GNDs contribute to the lattice curvature accommodation. Based on this interpretation, a grain fragmentation model was proposed by Kobaissy et al. [207]. The proposed model predicted accurately the grain size, the texture and the mechanical properties evolutions for FCC materials copper [207] and aluminum [299] subjected to ECAP via different routes. In this work, the Kobaissy et al. [207] model is extended to be used for HCP materials (Magnesium AZ31 alloy) by accounting for different HCP slip systems and twinning. In summary, the grain fragmentation model extended the lattice curvature approach proposed by Toth et al. [148] by accounting for the grain-grain interaction effect. The latter effect is considered in the computation of the GND densities using the central difference method as proposed by Lyu et al. [159]. The proposed grain fragmentation model controls the evolution of the misorientation between neighboring subgrains. Within the model, each grain is described initially by its grain size, orientation and position with respect to the entire texture. The application of plastic strain develops a deformation gradient between the center of the grain and its boundary due to the accumulation of dislocations at the grain boundaries. The majority of these dislocations are stored as GNDs which hinder the dislocation movement and thus, lead to the development of the lattice curvature of the grain. Consequently, a misorientation develops between different areas of the grain leading to grain subdivision where each area is considered as new grain when a threshold value of misorientation is reached.

### 4.2.3 Strain hardening model (Theoretical framework)

In this work, a multiscale model combining the crystal plasticity model with the continuum dislocation dynamics framework is used to capture the behavior of HCP single crystal and polycrystalline material. Dislocation slip and deformation twinning are the dominant deformation mechanisms in HCP materials. Thus, the formulation of the grain fragmentation model described in our previous studies [207,299] is extended to account for the different HCP deformation mechanisms. The essential feature of the crystal plasticity model is that metals deform plastically by means of material flow due to dislocation motion and then the materials deform elastically associated with rigid rotations (Figure 4.4(a)) [164]. Hence, the deformation gradient can be decomposed multiplicatively into elastic and plastic deformation components:

$$\mathbf{F} = \mathbf{F}^* \mathbf{F}^p \quad (4.7)$$

where  $\mathbf{F}^*$  represents the elastic deformation associated with lattice rotation and  $\mathbf{F}^p$  represents the plastic deformation. The transition from the relaxed (intermediate) to the current (loaded) configuration is accompanied by the rigid body rotation component  $\mathbf{R}^*$  of the elastic deformation gradient  $\mathbf{F}^*$  where  $\mathbf{R}^* = \mathbf{F}^* \mathbf{U}^{-1}$  and  $\mathbf{U}$  represents the elastic distortion.

Kalidindi (1998) proposed a scheme to incorporate deformation twinning in the single crystal plasticity model as shown in Figure 4.4(b) [280]. In addition to the deformation twinning, three slip modes, basal, prismatic, and pyramidal  $\langle c+a \rangle$  contribute to the plastic deformation. In the intermediate relaxed configuration, only one twin system is shown, however, multiple twin systems could occur at once. Plastic deformation accommodated by twinned region causes part of the lattice to rotate. Following the assumption described

in Figure 4.4(b), stresses in the twinned and untwinned regions of the crystals can be expressed as

$$\mathbf{T}_{untw}^* = \mathcal{L}^{untw} \mathbf{E}^e \quad (4.8)$$

$$\mathbf{T}_{tw}^* = \mathcal{L}^{tw} \mathbf{E}^e \quad (4.9)$$

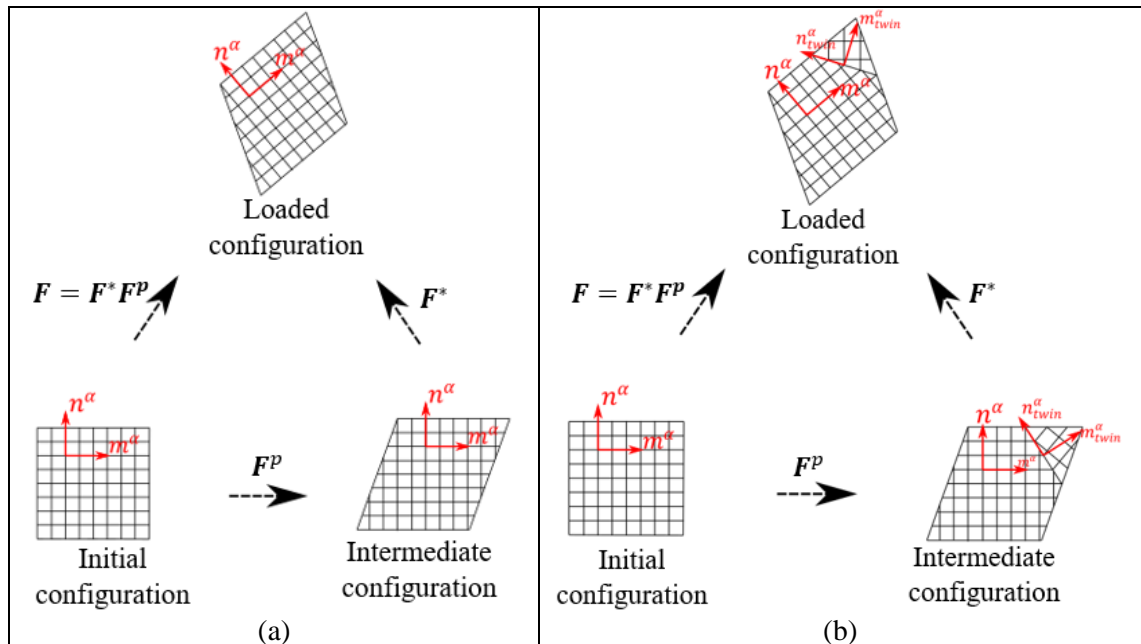
where  $\mathcal{L}$  is the fourth-order stiffness tensor expressed in the crystal coordinate system,  $\mathbf{T}^*$  is the second Piola-Kirchhoff stress and  $\mathbf{E}^e$  is the elastic Green-Lagrange strain tensors. The subscripts ‘tw’ and ‘untw’ refer to the twinned and untwinned regions, respectively.  $\mathcal{L}^{tw}$  can be obtained from the stiffness tensor  $\mathcal{L}^{untw}$  by applying the following transformation,

$$\mathcal{L}_{ijkl}^{tw} = \mathcal{L}_{pqrs}^{untw} K_{ip}^\beta K_{jq}^\beta K_{kr}^\beta K_{ls}^\beta \quad (4.10)$$

where  $\mathbf{K}^\beta$  describes the transformation matrix from the untwinned region to the twinned region and is denoted by

$$\mathbf{K}^\beta = 2\mathbf{n}^\beta \otimes \mathbf{n}^\beta - \mathbf{1} \quad (4.11)$$

where  $\mathbf{n}^\beta$  represents the twin-plane normal direction.



**Figure 4.4** (a) Schematic representation of the decomposition of the deformation gradient accounting only for slip, (b) schematic representation of the decomposition of the deformation gradient accounting for both slip and twinning mechanisms [280].

The Cauchy stress is related to the second Piola-Kirchhoff stress by the following relation:

$$\mathbf{T}^{untw} = \mathbf{F}^{*-1}[(\det \mathbf{F}^*)\mathbf{T}_{untw}^*]\mathbf{F}^{*-T} \quad (4.12)$$

$$\mathbf{T}^{tw} = \mathbf{F}^{*-1}[(\det \mathbf{F}^*)\mathbf{T}_{tw}^*]\mathbf{F}^{*-T} \quad (4.13)$$

$$\mathbf{E}^e = \frac{1}{2}[\mathbf{F}^{*T}\mathbf{F}^* - \mathbf{I}] \quad (4.14)$$

where  $\mathbf{I}$  is the identity matrix.

The effect of the stress distribution in the twinned region is incorporated into the Cauchy stress equation by the following rule of mixture,

$$\mathbf{T} = \left(1 - \sum_{\beta} f^{\beta}\right)\mathbf{T}^{untw} + \sum_{\beta} f^{\beta}\mathbf{T}^{tw} \quad (4.15)$$

The twin region volume fraction  $f$  evolution equation is expressed by:

$$\dot{f}^{\beta} = \frac{\dot{\gamma}^{\beta}}{\gamma^{twin}} \quad (4.16)$$

where  $\gamma^{twin}$  is the twin shear strain defined by  $\gamma^{twin} = \sqrt{3}/(c/a) - (c/a)/\sqrt{3}$  for HCP materials ( $\gamma^{twin} = 0.129$  for magnesium) and  $\dot{\gamma}^{\beta}$  is the plastic shear rate.

The contribution of the twinning mechanism is also implemented in the formulation of the velocity gradient where similar mathematical expressions are considered for slip and twinning:

$$\mathbf{L}_{cp}^p = \left(1 - \sum_{\beta}^{N^{twin}} f^{\beta}\right) \sum_{\alpha}^{N^{slip}} \dot{\gamma}^{\alpha} \mathbf{S}^{\alpha} + \sum_{\beta}^{N^{twin}} \dot{f}^{\beta} \gamma^{twin} \mathbf{S}^{\beta} \quad (4.17)$$

where  $\mathbf{S}^{\alpha} = \mathbf{m}^{\alpha} \otimes \mathbf{n}^{\alpha}$ ,  $\mathbf{m}^{\alpha}$  and  $\mathbf{n}^{\alpha}$  represents the slip direction and the slip plane normal respectively. To incorporate the effect of the dislocation density evolution, the slip shear

rate formulation used in this model follows the Orowan relationship [169]. Thus, one can write:

$$\dot{\gamma}^{\alpha} = \rho_m^{\alpha} b^{\alpha} v_g^{\alpha} \quad (4.18)$$

where  $b^{\alpha}$  is the burgers vector magnitude in slip system  $\alpha$  (values presented in Table 4-2),  $\rho_m^{\alpha}$  is the mobile dislocation density on slip system  $\alpha$  and  $v_g^{\alpha}$  is the dislocation glide velocity on slip system  $\alpha$  and can be expressed as:

$$\begin{cases} v_g^{\alpha} = v_0 \left| \frac{\tau^{\alpha}}{\tau_{th}^{\alpha}} \right|^{1/\eta} \text{sign}(\tau^{\alpha}) & \text{for } \tau^{\alpha} \geq \tau_{th}^{\alpha} \\ v_g^{\alpha} = 0 & \text{for } \tau^{\alpha} < \tau_{th}^{\alpha} \end{cases} \quad (4.19)$$

$v_0$  is the reference velocity,  $\eta$  is the strain rate sensitivity constant, and  $\tau_{th}^{\alpha}$  is the threshold resolved stress on slip system  $\alpha$ , which constitutes of the initial critical resolved shear stress  $\tau_0$ , the Hall-Petch stress  $\tau_{HP}^{\alpha}$ , and the material hardening stress  $\tau_H^{\alpha}$ . The Hall-Petch stress is inversely proportional to the square root of the grain size  $D$  and can be expressed as  $\tau_{HP}^{\alpha} = K^{\alpha}/\sqrt{D}$  where  $K^{\alpha}$  is the Hall-Petch parameter related for each slip system.

The evolution rate of the mobile dislocation density  $\dot{\rho}_m^s$  can be characterized by five dislocation mechanisms that contribute to the material hardening [207]. The five mechanisms are described by the five terms presented in the dislocation evolution rate equation (equation (4.20)) where the first term represents the multiplication and generation of dislocations. The annihilation of two mobile dislocations having opposite signs is depicted in the second term where  $R_c$  is the critical radius for dislocation annihilation. During deformation, mobile dislocations can immobilize due to the formation of dipoles (third term) while immobile dislocations can mobilize due to the breakup of these dipoles (fourth term). Finally, the interaction of mobile and immobile dislocations that lead to their annihilation is represented in the fifth term. Besides the

evolution rate of mobile dislocation density, immobile dislocation density evolution rate  $\dot{\rho}_i^s$  can be characterized by the last three mechanisms as described in equation (4.20).

$$\begin{aligned}\dot{\rho}_m^s &= \alpha_1 \rho_m^s v_g^s / \bar{l} - 2\alpha_2 R_c (\rho_m^s)^2 v_g^s - \alpha_3 \rho_m^s v_g^s / \bar{l} + \alpha_4 (|\tau^s| / \tau_{th}^s)^\zeta \rho_i^s v_g^s / \bar{l} - \\ &\alpha_5 R_c \rho_m^s \rho_i^s v_g^s \\ \dot{\rho}_i^s &= \alpha_3 \rho_m^s v_g^s / \bar{l} - \alpha_4 (|\tau^s| / \tau_{th}^s)^\zeta \rho_i^s v_g^s / \bar{l} - \alpha_5 R_c \rho_m^s \rho_i^s v_g^s\end{aligned}\quad (4.20)$$

**Table 4-2 Burgers vector magnitude at different slip/twin systems**

Slip/twin plane	Burgers magnitude	Burgers value
Basal planes $(0001)\langle 11\bar{2}0 \rangle \langle a \rangle$	a	3.2094 Å
Prismatic planes $(10\bar{1}0)\langle 1\bar{2}10 \rangle \langle a \rangle$	a	3.2094 Å
Pyramidal planes $(11\bar{2}2)\langle \bar{1}\bar{1}23 \rangle \langle c+a \rangle$	$\sqrt{a^2 + c^2}$	6.12 Å
Pyramidal planes tension twin $\langle c+a \rangle$	$\sqrt{a^2 + c^2}$	6.12 Å
Pyramidal planes compression twin $\langle c+a \rangle$	$\sqrt{a^2 + c^2}$	6.12 Å

Twinning, unlike slip, involves a shear displacement of several interatomic distances where it reorients the lattice abruptly [5]. The shear displacement depends on the resolved shear stress  $\tau^\alpha$  and the slip resistance  $s^\alpha$  within the grain. Thus, twin shear rate is expressed using the conventional constitutive equation described by Asaro and Needleman [164]. The plastic shear strain rate can be described by a rate sensitive equation as follows,

$$\dot{\gamma}^\alpha = \dot{\gamma}_0 \left| \frac{\tau^\alpha}{s^\alpha} \right|^{1/\lambda} \text{sign}(\tau^\alpha) \quad (4.21)$$

where  $\dot{\gamma}_0$  and  $\lambda$  represents the reference shearing rate and the rate sensitivity for twinning, respectively. The resolved shear stress  $\tau^\alpha$  and the slip resistance  $s^\alpha$  on twin system  $\alpha$  are expressed as:

$$\tau^\alpha = \mathbf{T}_{tw}^* \mathbf{S}^\alpha \quad (4.22)$$

and

$$\dot{s}^\alpha = \sum_{\beta} h^{\alpha\beta} |\dot{\gamma}^\beta| \quad (4.23)$$

where  $h^{\alpha\beta}$  is the strain hardening rate of twin system  $\alpha$  due to shear on the twin system  $\beta$ .

$$h^{\alpha\beta} = q^{\alpha\beta} h^\beta \quad (4.24)$$

$q^{\alpha\beta}$  describes the self and latent hardening behavior of slip/twin systems of a crystalline and  $h^\beta$  is the hardening rate of twin system  $\beta$  and can be written as follows,

$$h^\beta = h_0 \left[ 1 - \frac{s^\beta}{s_s} \right]^\chi \quad (4.25)$$

where  $h_0$ ,  $\chi$ , and  $s_s$  are twin hardening parameters for both extension and contraction twinning.

The overall stress of the polycrystal is then calculated beyond the computation of the crystal stress and strain information. The Taylor-Lin [162,163] homogenization method is utilized to average the Cauchy stress on the macroscopic level by assuming that all grains possess the same volume, thus,

$$\mathbf{T}_{avg} = \frac{1}{N_g} \sum_{g=1}^{N_g} \mathbf{T}^g \quad (4.26)$$

where  $\mathbf{T}^g$  is the Cauchy stress on the  $g$ -th crystal and  $N_g$  is the total number of grains in the polycrystal.

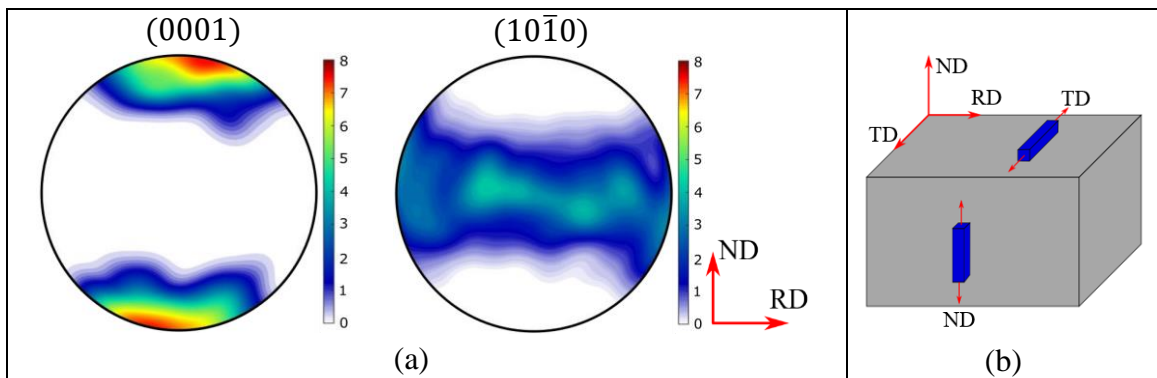
### 4.3 Results and discussions

In this work, the proposed approach is validated by experimental data generated previously by the authors [305,306]. For that purpose, we analyzed the behavior of a commercial magnesium alloy AZ31B hot-rolled plate, annealed at 350 °C for 12h. The as received material presented a basal texture (Figure 4.5(a)) with an average grain size of 25  $\mu\text{m}$ . After annealing, tensile samples were extracted from the plate and machined with their major axis being aligned with either the transverse direction (TD) or the normal direction (ND) (Figure 4.5(b)). Tensile tests were performed at two temperatures, room temperature and 200 °C at a strain rate of  $5 \times 10^{-4} \text{s}^{-1}$  [305]. The purpose of conducting tensile loading along different material's directions aimed to evaluate the material anisotropy by the activation of different plasticity deformation mechanisms. It is expected, with respect to the Schmid's law [306], that loading along ND favors extension twinning, while prismatic  $\langle a \rangle$  is favored when loading along TD. Billets machined from the hot-rolled Mg plate, were ECAP extruded at a rate of 4.57 mm/min at 200 °C with a back pressure of 20MPa. In order to achieve the same average grain size but with different texture, two ECAP routes (route A and route K) were used and samples were processed up to four passes. The ECAPed-samples exhibited refined grains with an average grain size of 1~4  $\mu\text{m}$  in both routes. To investigate the mechanical anisotropy of the ECAP materials, tensile specimens were machined from the ECAPed billets with their major axis being with the extrusion (ED) and the flow directions (FD). Tensile testing was achieved at room temperature at a strain rate of  $5 \times 10^{-4} \text{s}^{-1}$  [307].

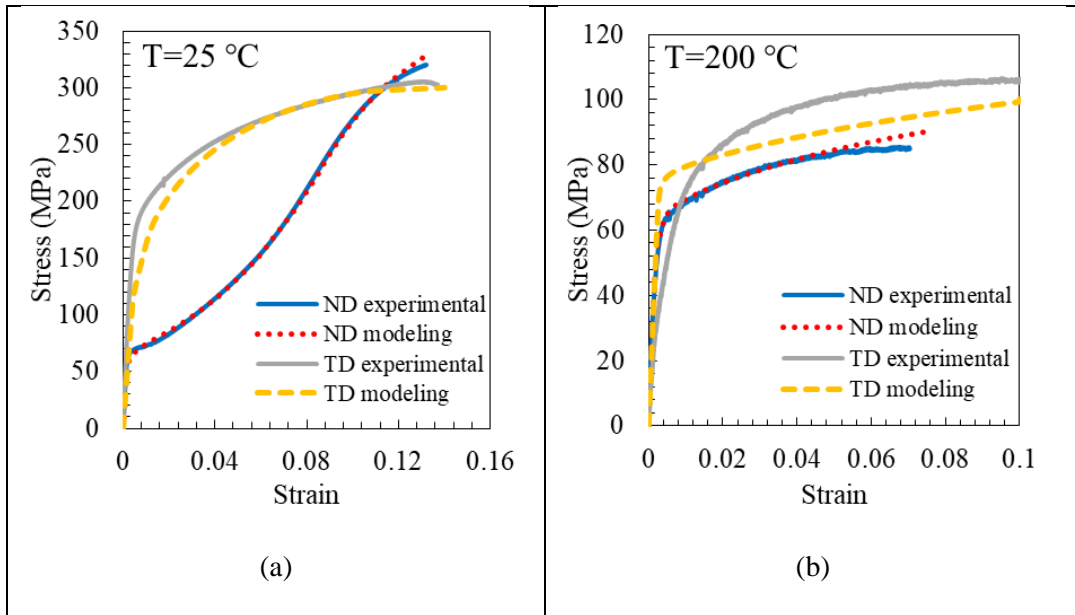


### 4.3.1 Pre-ECAP Model Parameters Calibration

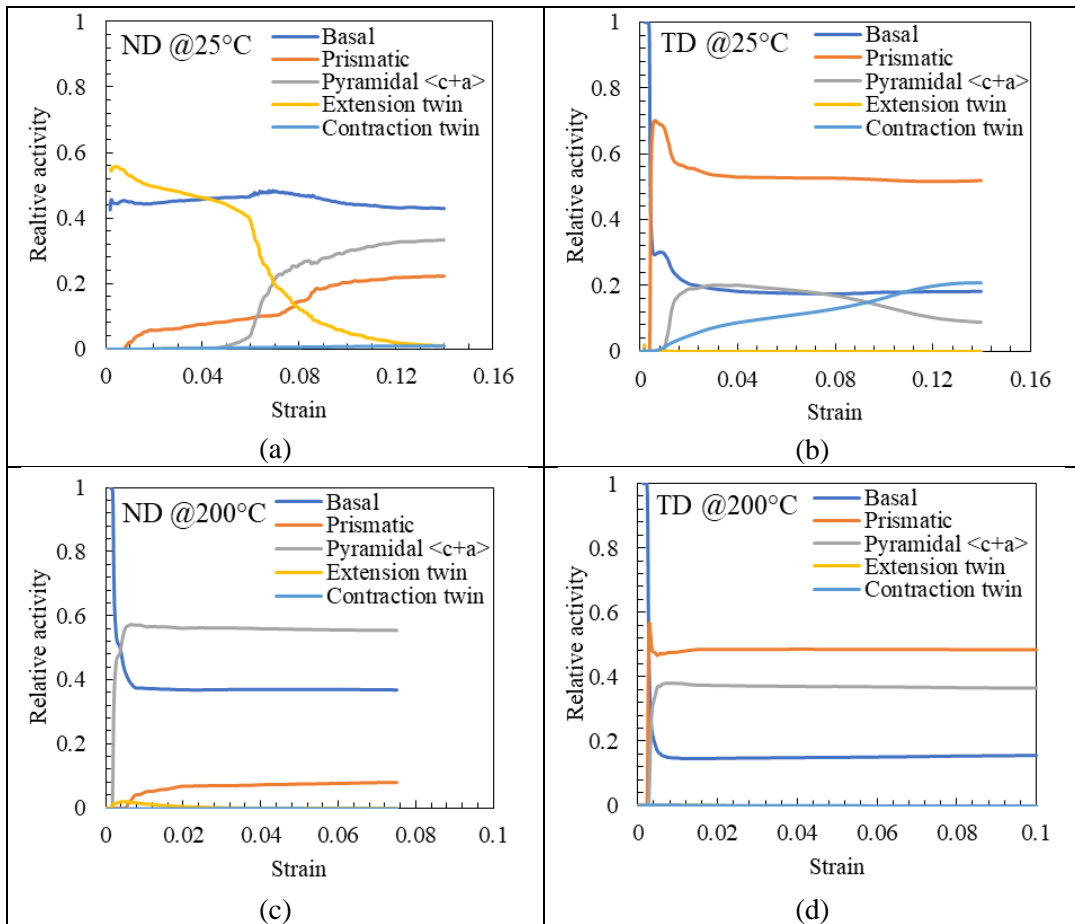
In this section, the model parameters are identified using the true stress true strain responses of tensile tests performed along TD and ND at room temperature and 200 °C. Thus, a set of true stress true strain responses of tensile tests performed on AZ31 at various temperatures are fitted in Figure 4.6 with the numerical results of the Taylor- Lin-crystal plasticity- continuum dislocation dynamics model. Since the set of model parameters is not unique and different sets could fit the same experimental results, a robust identification method is required. Thus, the model parameters of magnesium were initially extracted from literature and then modified to fit the experimental results as necessary. The initial critical resolved shear stress for slip and twin deformation modes were selected from Ayoub et al. [283]. However, the material parameters ( $\alpha_1 - \alpha_5$ ) and the self and latent hardening matrix  $q^{\alpha\beta}$  of the continuum dislocation dynamics model were obtained from Askari et al. [170] with some modifications. The Hall-Petch parameters for different slip systems of rolled magnesium were identified from Wang and Choo [308]. The calibrated model parameters are presented in Table 4-3 for different temperatures. In addition to fitting the tensile mechanical behavior, the relative activity of slip and twin systems is analyzed and compared with the reported results in the literature to confirm the reliability of the selected model parameters.



**Figure 4.5 (a) Initial texture of the as-received magnesium AZ31 material, (b) Schematic of as-received material of magnesium showing the tensile directions along ND and TD.**



**Figure 4.6** Stress strain responses of the as-received material tensile tested along normal (ND) and transverse (TD) directions at (a) room temperature and (b) 200 C.



**Figure 4.7** Slip/twin systems activities of the tensiled as-received material

In Figure 4.6, plastic anisotropy at RT is triggered by the activation of different slip/twinning mechanisms which are required to satisfy the Taylor criterion [10], however, at 200C, this effect is reduced since twinning effect vanishes with the increase of temperature. At room temperature, tensile loading along the normal direction (ND) favors the extension twinning (Figure 4.7(a)) which results in twinned grains leading to the minimization of the induced-deformation by other slip mechanisms [305]. The slip/twin activity results of the Taylor-Lin CP-CDD model are consistent with the predictions of the VPSC model [285,305] indicating that deformation by basal slip and extension twinning are the dominant. Unlike the ND sample, prismatic slip is favored for loading along the TD. However, prismatic slip could not fully accommodate the c-axis compression promoted by the tensile loading along TD. Therefore, additional slip/twin systems such as basal, pyramidal and contraction twin are necessary to accommodate this deformation (Figure 4.7(b)). The high anisotropy shown between the ND and TD cases is attributed to the suppression of extension twinning and replacing it with prismatic slip mechanism. As a general trend, increasing the processing temperature induces a decrease in the yield strength, an increase in the elongation to failure along with a thermal softening of the flow stress, and a change in slip/twin systems activations. These effects are attributed to the decrease in the critical resolved shear stress required to move dislocations along the prismatic and pyramidal  $\langle c+a \rangle$  slip systems which leads to the satisfaction of the Taylor criterion [270]. At 200C, Taylor-Lin CP-CDD model indicated that the activity of extension twin vanished and was replaced by the pyramidal slip when loading along the ND (Figure 4.7(c)). Similarly, a high pyramidal slip activity is revealed in the

predictions of the sample loaded along the TD (Figure 4.7(d)). These results are in good consistency with the VPSC predictions [305].

**Table 4-3 List of model parameters calibrated at two temperatures T=25°C and T=200°C.**

Parameter		T=25°C	T=200°C
<b>Initial shear resistance <math>\tau_0</math></b> (MPa)	Basal		0.5
	Prismatic	55	40
	Pyramidal <c+a>	70	35
	Twin extension	30	35
	Twin contraction		200
$\alpha_0$	Basal		0.1
	Prismatic	0.15	0.1
	Pyramidal <c+a>	0.8	0.1
$\alpha_1$	Basal		0.1
	Prismatic	0.1	0.05
	Pyramidal <c+a>		0.1
$\alpha_2$	Basal/Prismatic/Pyramidal		1
$\alpha_3$	Basal/Prismatic/Pyramidal		0.01
$\alpha_4$	Basal/Prismatic/Pyramidal		0.002
$\alpha_5$	Basal/Prismatic/Pyramidal		1
<b>Final saturated stress <math>s_s</math></b> (MPa)	Twin extension		38
	Twin contraction		400
<b>Initial hardening rate <math>h_0</math></b> (MPa)	Twin extension		8
	Twin contraction		20
<b>Twinning reference shearing rate <math>\dot{\gamma}_{0 \text{ twin}}</math></b> ( $s^{-1}$ )	Twin extension	$10^{-4}$	$10^{-6}$
	Twin contraction		$10^{-4}$
<b>Twinning hardening exponent <math>\chi</math></b>	Extension/ contraction twin		0.5
<b>Hall-Petch parameter <math>K</math></b>	Basal	2.61	1
	Prismatic	5.54	2.2
	Pyramidal <c+a>	9.86	3.9
<b>Twin rate sensitivity <math>\lambda</math></b>		0.2	
<b>Slip rate sensitivity <math>\eta</math></b>		0.02	
<b>Strain rate <math>\dot{\epsilon}</math></b> ( $s^{-1}$ )		$5 \times 10^{-4}$	
<b>Reference velocity <math>v_0</math></b> ( $s^{-1}$ )		$10^{-3}$	
<b>Initial SSD density</b> ( $m^{-2}$ )		$2.4 \times 10^{12}$	
<b>Initial GND density</b> ( $m^{-2}$ )		$1.2 \times 10^{13}$	
<b>Average grain size</b> ( $\mu m$ )		25	

### **4.3.2 ECAP Model Predictions**

The experimentally measured initial texture of magnesium alloy displayed in Figure 4.5(a) is used as an input to the Taylor-Lin-CP-CDD model. The modeling parameters used for ECAP modeling approach to predict the microstructural features and texture evolution are the identified parameters in section 4.3.1. The predicted results obtained from the calibrated parameters in Table 4-3 are then compared with the measured (experimental) texture for both routes A and K. In addition, the model predictions such as slip/twin activities and dislocation densities evolutions are analyzed.

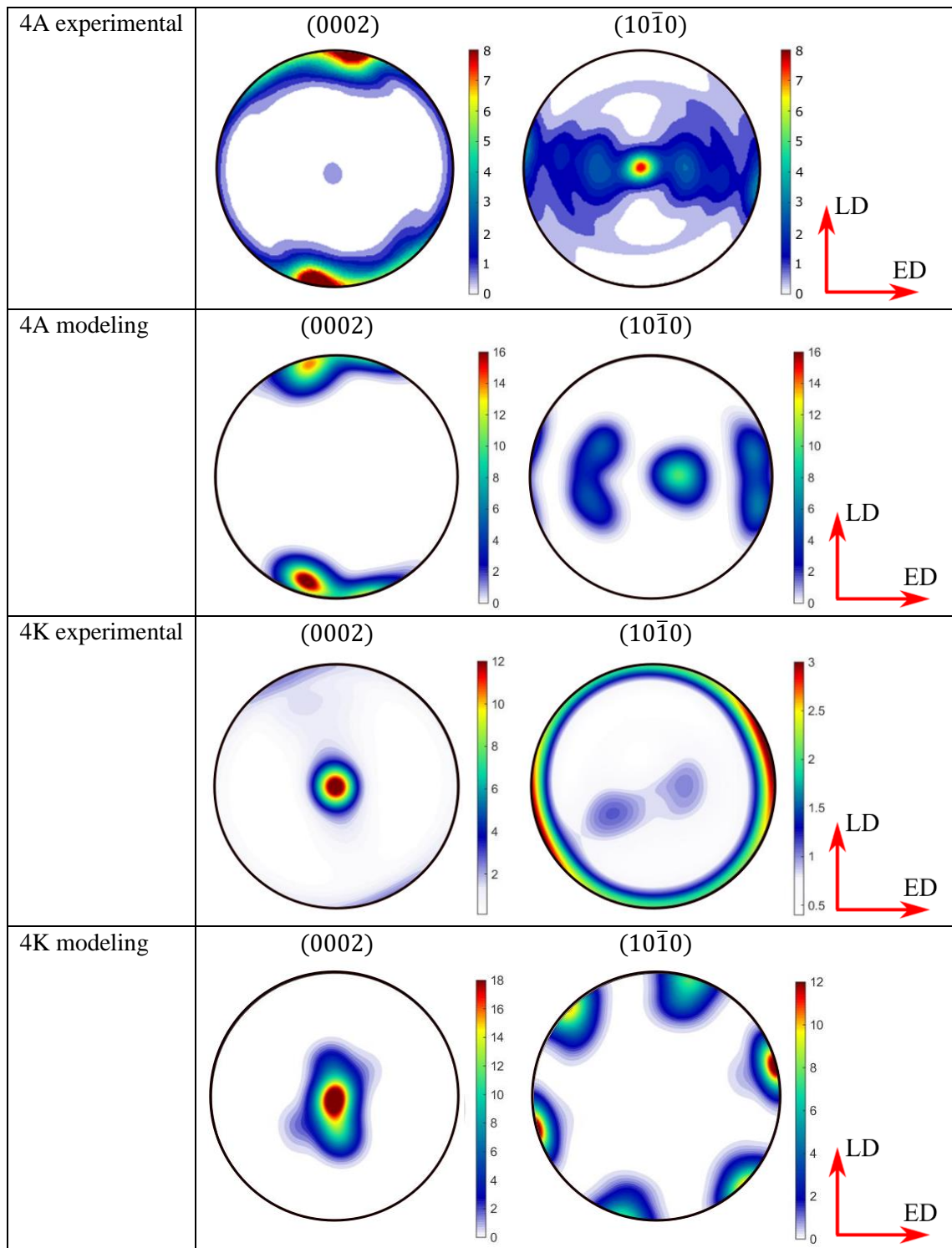
#### 4.3.2.1 Microstructural and texture predictions

Ultrafine grained metals can be produced by subjecting the material to severe plastic deformation. ECAP is considered as one of the conventional processes that has showed an effective strengthening in magnesium alloys [309]. In addition, thermo-mechanical processing with different ECAP routes of magnesium alters its microstructural and texture properties[310,311]. In this work, magnesium AZ31 alloy was ECAP-processed using routes A and K, at an extrusion rate of 4.57 mm/min and a temperature of 200°C to prevent the formation of cracks [307]. During ECAP process, grain fragmentation is considered as the dominant deformation mechanism that results into an ultrafine grain microstructure. Indeed, severe plastic deformation increases the density of dislocations that are inhomogeneously distributed within the grains resulting into a deformation gradient and lattice curvature. Accumulated dislocations at the grain boundaries hinder the movement of mobile dislocations resulting in the geometrically necessary dislocations which lead to a misorientation difference between different regions of the grain called subgrains. The evolution of the GNDs density is expressed in terms of the Nye's tensor [155] which in turn is calculated from the derivative of the

velocity gradient using the central difference method [159]. With further strain application, the misoriented regions (i.e., subgrains) split and are considered as new grains treated independently from their parent grain, with distinct microstructure and smaller grain size. When the fragmentation criterion is satisfied (i.e., misorientation between the center of the grain and its boundaries exceeds  $5^\circ$ ), the fragmented grains are assigned their parent's dislocation density and their orientation with a slight misorientation calculated based on the accumulation of the GNDs as described in [299]. To determine the density of the GNDs accumulated at the new grain's boundaries, the position of the new grains are updated and the same calculation procedure is repeated. In this model, processing via routes 4A and 4K led to grain size reduction from  $25 \mu\text{m}$  to around  $4 \mu\text{m}$  and  $2.7 \mu\text{m}$ , respectively. The predicted average grain size is in agreement with the experimentally measured average grain size which was reported to be equal to  $3.5 \mu\text{m}$  and  $2.3 \mu\text{m}$  after 4 passes via routes A and K, respectively.

The predicted ECAPed textures are compared in Figure 4.8 with the experimental (measured) textures. The measured texture of the material processed via route A showed a rolling-like texture over the four passes where subsequent passes strengthen the texture by reorienting its components into similar positions after each pass. The 4K measured texture exhibits a rigid rotation with respect to the initial rolling texture about the extrusion direction of the sample. This rotation is associated to the  $90^\circ$  rotation of the sample applied before the third pass. The results of the textures predicted by the Taylor-Lin CP-CDD model rebuilt the experimental ones where the main features are reproduced. The texture components predicted in the (0001) pole figure for both routes 4A and 4K are in good agreement with the measured texture. However, a small discrepancy appears in the (10-10) pole figures of the 4A textures which could be

associated to the misorientation evolution in the grain during the fragmentation process. In the strong peaks in the predicted (10-10) pole figure of the 4K texture precisely resemble the strong peaks in the measured texture while the weak peaks observed in the measured one are more scattered compared to the predicted one.



**Figure 4.8 Measured (experimental) textures compared with the simulated ones for four passes of route A and route K**

4.3.2.2 Microstructural behavior

For decades, SPD materials were of high interest for numerous industrial applications. Thus, internal microstructural developments were investigated using physics-based modeling frameworks [148,223–225]. Studying strain hardening behavior between ECAP passes gives a clear insight into the influence of ECAP routes and the effect of the rotations between ECAP passes. For that purpose, dislocation-based models were proposed such as the one proposed in this work. During plastic flow, dislocation movement are triggered when the resolved shear stress exceeds its critical value. Their evolution is influenced by the short-range barriers such as vacancies or by the long-range barriers such as grain boundaries. The microstructural changes of magnesium alloys due to deformation via ECAP are a direct consequence of the multiplication and rearrangement of dislocations moving over different slip systems. In the initial stage of deformation due to ECAP process, dislocations are rapidly generated and multiplied in the coarse grains. With the increase of the plastic strain, grains divide into subgrains demarcated by dislocation walls, named geometrically necessary boundaries (GNBs). Further strain results in a misorientation difference between subgrains due to the movement of the trapped dislocations along the neighboring subgrains boundaries. The increase in dislocation density due to high strain leads to the increase of the internal stored energy which induces further grain refinement. Subsequent ECAP passes result in increasing the fraction of new fine grains due to the transformation of generated dislocations within the grains into new boundaries [309].

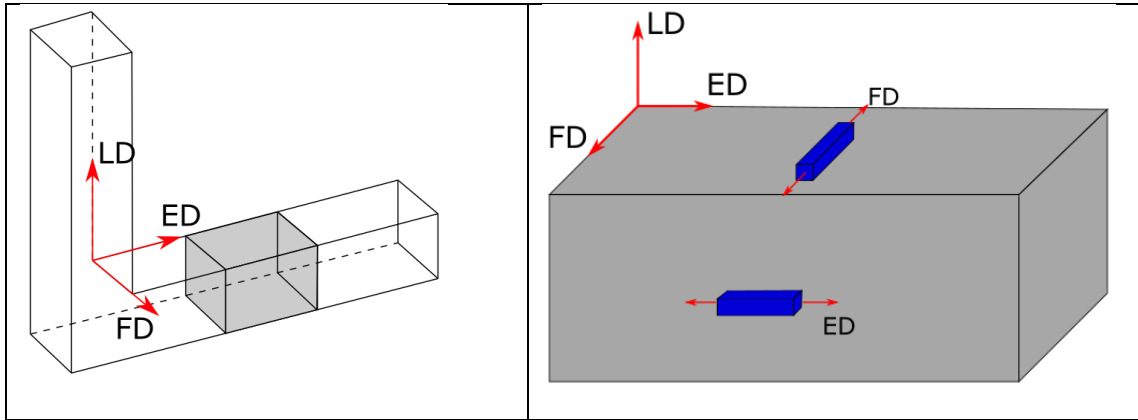
Figure 4.10 depicts the relative activity of the different slip/twin systems activity for routes A and K. In the first two passes, the same relative activity is predicted by the



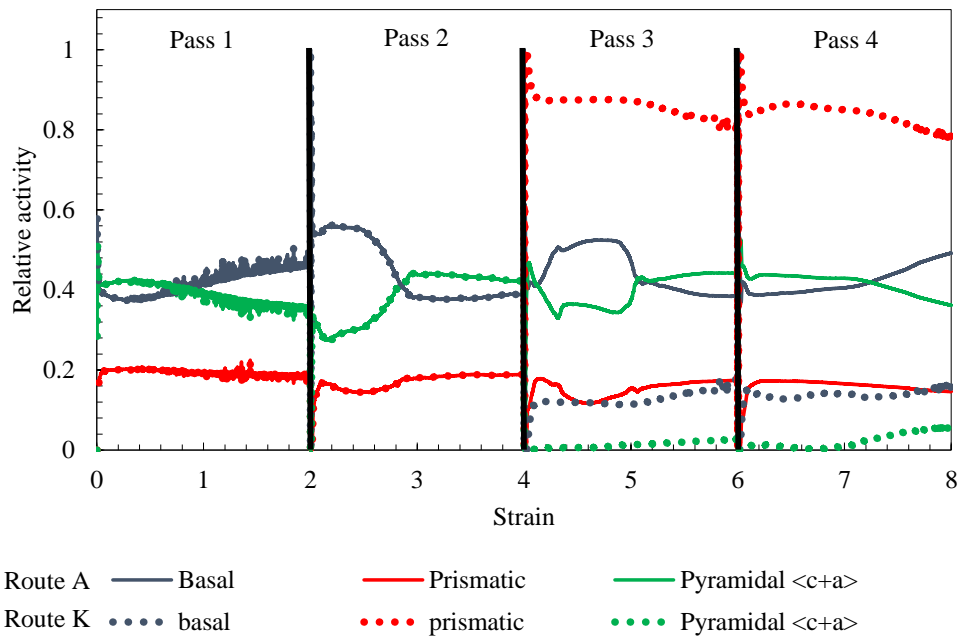
model for both routes, which is expected since the same loading path is applied to the sample. While in consecutive two passes, the differences in the relative slip/twin activities are clear, which is also expected since different loading paths are applied associate with the 90° rotation of the route K sample applied before the third pass. Twin relative activities are predicted to be almost inexistent which is also expected due to high processing temperature. Different deformation behaviors can be analyzed by applying Schmid law which dictates that a slip/twin system can be activated whenever the resolved shear stress on a slip/twin plane exceeds a CRSS value [312]. Nan et al. [313] reported the calculated Schmid factors (SFs) for different loading directions and different slip/twin systems in magnesium. The higher the value of Schmid factor, the higher activation of slip/twin system. Schmid factor can be calculated by the following relation:  $SF = \cos\Omega \times \cos\delta$  where  $\Omega$  and  $\delta$  are the angles between the slip/twin plane normal and the slip/twin direction with the loading direction, respectively. ECAP process is a shear process mechanism where the shear loading is applied at the intersection plane between the two intersecting ECAP channels (Figure 4.9). In route A, the sample is inserted to the ECAP where the c-axis is parallel to the extrusion direction, thus the shear stress direction makes a 45° with the c-axis. According to the SF values calculated in Nan et al. for different deformation modes, basal slip systems have the maximum value followed by pyramidal  $\langle c+a \rangle$  slip then prismatic slip. The predicted results by the Taylor-Lin CP-CDD model of the slip relative activities are consistent with the calculated values of the Schmid factors. Among the four passes via route A, relative activities of each slip system showed almost the same activities since subsequent passes strengthen the texture by reorienting grains' orientations to a rolling-like texture. The rigid rotation of the sample before the third K route pass leads the prismatic slip to dominate other slip systems where

pyramidal slip activity becomes negligible. Since no rotation was performed between the third and the fourth pass in route K, relative activity of each slip system has exhibited almost the same activity during the third and fourth passes

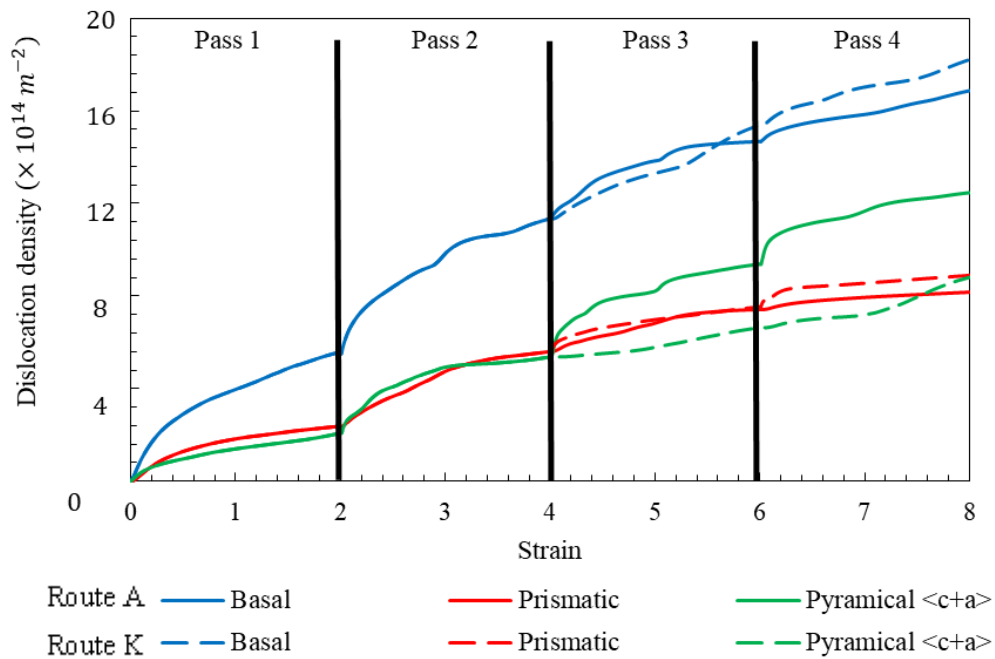
The predictions of dislocation density evolution along each slip system for both routes are depicted in Figure 4.11. The dislocation density first evolved rapidly during the first two passes; however, its evolution rate has decreased in the next two ECAP passes which can be attributed to the recovery of dislocation structure during consecutive passes [314]. In addition, the formation of new grains during the grain refinement mechanism is characterized by the transformation of dislocation clusters into boundaries resulting in a significant consumption of dislocations within the polycrystal [315], which explain the decrease in the dislocation density evolution rate with subsequent ECAP passes. Figure 4.11 shows that dislocations evolving at the basal slip system exhibit the highest density compared to prismatic and pyramidal slip systems. This can be explained by the easiness of dislocation movement and generation at the basal slip system due to its low CRSS value. In the first two passes, dislocation density evolutions are identical in both routes since route A and route K are identical. However, in the third and fourth passes, a significant drop in evolution of dislocation density along the pyramidal slip systems is revealed between both routes. This can be related to the deactivation of pyramidal slip system in route K after the second pass.



**Figure 4.9. Schematic of ECAPed samples showing the tensile loading under the extrusion direction (ED) and the flow direction (FD)**



**Figure 4.10 Relative activity of slip systems as function of strain for four passes of route A and route K**



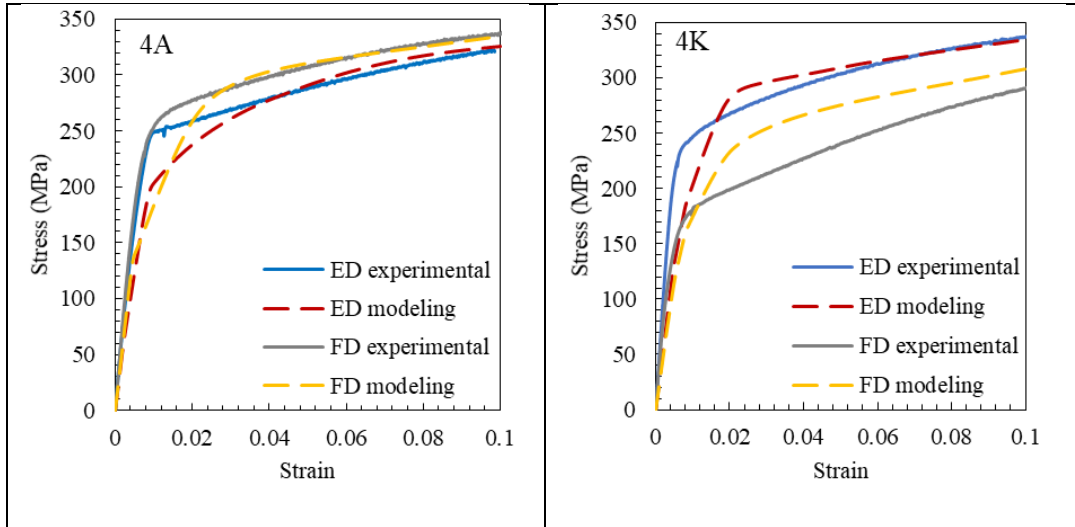
**Figure 4.11 Dislocation density evolution along slip systems for route A and route K**

#### 4.3.3 Post-ECAP mechanical behavior

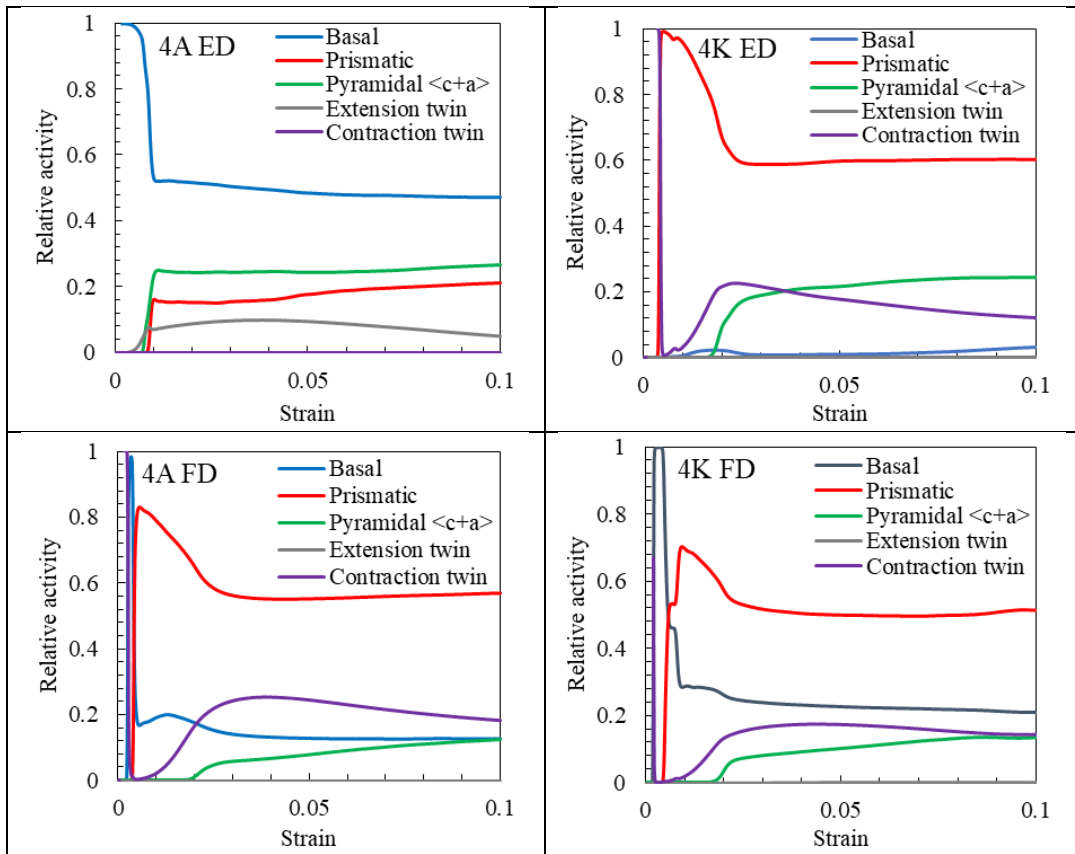
Magnesium alloys processed by ECAP exhibit a grain structure refinement which alters the mechanical properties of the material. Similar to the as-received material, ECAPed-magnesium alloy may present mechanical anisotropy where loading direction affects their stress-strain behavior and yield strength. Anisotropy has been reported for ECAPed- magnesium alloys in both tensile and compression directions [285,310,316]. Predicting the microstructural features of the processed materials can give an advantage for one ECAP route against the others in terms of strength and anisotropy. Processing magnesium via different routes lead to certainly different textures that influence their mechanical responses. Different initial textures yield to different evolution of dislocation densities and thus activation of different slip systems that lead to a distinct yield strength of the material. In polycrystalline materials, grains with different orientations are demarcated by grain boundaries which obstruct dislocations from gliding. Although the plastic deformation behavior at the micro-scale is controlled by the dislocation-based

mechanism, different grain boundary structures and different grain sizes could influence the interaction of the moving dislocations with the accommodated dislocations at the boundaries, thus affecting the overall response of the polycrystal [317]. In this work, a comparison between the experimental and predicted true tensile stress-strain curves up to the ultimate tensile strength for both routes 4A and 4K along both directions, extrusion and flow (see Figure 4.9), are depicted in Figure 4.12. The model parameters used to predict the stress-strain curves are similar to the model parameters identified at room temperature in section III.1, however, the Hall-petch (H-P) parameter is altered due to the effect of grain size reduction. It was found in literature that the reduction of grain size due to severe plastic deformation reduces the H-P parameter by a certain factor depending on the loading direction and the processing conditions[318,319]. For instance, rolling magnesium alloy AZ31 with an average grain size of between 16 and 35  $\mu\text{m}$  led to a H-P parameter of  $348 \text{ MPa}\cdot\mu\text{m}^{0.5}$  [320], while processing the Mg AZ31 alloy with an average grain size of 2-8  $\mu\text{m}$  led to a H-P parameter of  $180 \text{ MPa}\cdot\mu\text{m}^{0.5}$  [321]. A similar trend of the H-P parameter reduction related to the grain size and processing conditions is assumed in this work. Thus, the H-P parameters for basal, prismatic and pyramidal were selected to be 1, 2.2, and  $3.9 \text{ MPa}\cdot\mu\text{m}^{0.5}$ , respectively with a reduction factor of 2.5. The yield strength of the ECAPed material is significantly enhanced compared to the as-received material. The present results show also that the anisotropy effect exist in the ECAP processed billets especially in route 4K, but with low influence compared to the as-received samples. The tension asymmetry of the ED and FD flow stress curves is overturned between routes 4A and 4K. Figure 4.12 shows a good agreement between the simulated and measured (experimental) stress-strain curves with a shift of around 30MPa of the flow stress along the flow direction in route 4K. By inspecting the relative activities

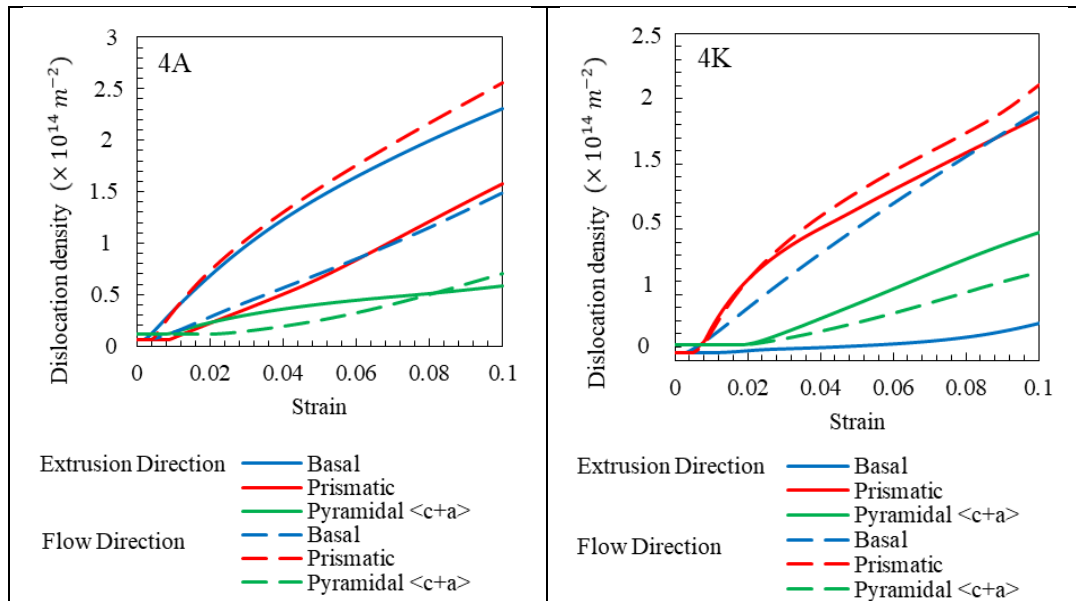
and dislocation density evolution in Figure 4.13 and Figure 4.14, one can understand better the flow curves in Figure 4.12. Although yield strength and strain hardening behavior for 4A sample are almost similar, it is predicted that dislocations have activated different slip systems. Loading along the extrusion direction has activated basal (55%), pyramidal (25%), prismatic (15%) slip and a small fraction of extension twinning (5%) which contributed to the small decrease in yield strength. On the other hand, in the samples loaded along the flow direction, about 55% of plastic strain resulted from prismatic slip, nearly 25% from contraction twinning, 15% from basal slip and a small fraction (5%) from pyramidal  $\langle c+a \rangle$  slip. These results are in good accordance with another study performed for an initially rolled texture by Graff et al. [322], in which similar relative activities to that of the current predicted 4A texture activities were predicted by crystal plasticity framework. In route 4K, the activation of basal slip system when loading along the flow direction has decreased the yield strength since dislocations requires lower CRSS to move. Figure 4.14 presents the dislocations evolutions at each slip system for both routes. By comparing Figure 4.13 and Figure 4.12 one can deduce that the increase of dislocations generation and multiplication on a certain slip system is associated to the increase in the activation of this slip system and vice versa. In addition, no dislocation evolution is recorded on slip systems that have no slip activation such as in the case of pyramidal  $\langle c+a \rangle$  in 4K below 2% strain. Comparing the dislocation evolution in both directions for the 4A sample, dislocation densities has shown a flip in their values between the basal and prismatic systems. Although both prismatic and pyramidal  $\langle c+a \rangle$  have shown an almost same dislocation density evolution in the 4K tensile-samples along both directions, a huge reduction was revealed for the basal slip due to its deactivation in the extrusion direction.



**Figure 4.12** Mechanical responses of the ECAP-samples loaded along extrusion and flow directions



**Figure 4.13** Predictions of slip/twin activities of the tensiled samples after four passes of ECAP



**Figure 4.14** Predicted dislocation density evolution of the tensiled samples after four passes of ECAP

#### 4.4 Conclusions

In this work, the microstructural, textural and anisotropic mechanical behavior evolution of equal channel angular pressed (ECAPed) Mg-3Al-1Zn rolled billet was investigated and analyzed. For that purpose, a physically based model accounting for grain to grain interaction and grain refinement mechanisms is proposed to predict the mechanical behavior, the texture evolution, and the microstructural development. The proposed model uses the crystal plasticity (CP) model coupled with a continuum dislocation dynamics (CDD) model. Since twinning mechanism has a significant effect on the anisotropy of magnesium alloys, this effect was modeled through crystal plasticity approach with maintaining the slip modeling through the continuum dislocation dynamics approach. A grain refinement mechanism is also integrated into the model in order to predict the formation of refined grains during severe plastic deformation. Anisotropy evolution of magnesium is then examined by predicting the mechanical behavior, dislocation evolution, and the slip/twin systems activities of the ECAPed material. The behavior of an annealed commercial magnesium alloy AZ31B hot-rolled plate was



initially analyzed. The model parameters were identified using the true stress true strain responses of tensile tests performed along TD and ND at room temperature and 200 °C. A robust parameter identification method was proposed which initially used critical resolved shear stresses, continuum dislocation hardening parameters and Hall-Petch from the literature than calibrated slightly to fit the mechanical behavior, texture evolution and previously predicted deformation systems relative activities.

The as received AZ31B hot-rolled plate had a basal texture with an average grain size of 25  $\mu\text{m}$ . A high anisotropy was observed from the different mechanical response exhibited by the material when loaded along ND and TD at room temperature. This high anisotropy is attributed to the suppression of extension twinning and increasing activity of prismatic slip mechanism. Tensile loading along ND favors extension twinning while along TD prismatic slip shows higher activity. At 200 °C, the plastic anisotropy is reduced since increasing temperature drastically reduces the twinning activity. This observation is attributed to the decrease in the CRSS of pyramidal  $\langle\text{c+a}\rangle$  slip which result in the disappearance of extension twin activity and its replacement by the pyramidal slip when loading along the ND. While a higher pyramidal slip activity is reported in when loading along the TD.

Billets machined from the hot-rolled Mg plate, were ECAP extruded up to four passes in route A and K at a rate of 4.57 mm/min at 200 °C with a back pressure of 20MPa. The identified model parameters were used to predict the ECAP texture and microstructure. The model predicted that processing via routes 4A and 4K resulted in a grain size reduction from 25  $\mu\text{m}$  to around 4  $\mu\text{m}$  and 2.7  $\mu\text{m}$ , respectively, which is in agreement with the experimentally measured. The Taylor-Lin CP-CDD model predicted textures were compared to the experientially measured ones, and a good agreement was

shown. The route A ECAPed material texture showed a rolling-like texture over the four passes while the route K ECAPed material texture exhibits a rigid rotation with respect to the initial rolling texture about the extrusion direction of the sample associated to the 90° rotation of the sample applied before the third pass. In the first two passes, the same relative activity is predicted by the model for both routes A and K while in the consecutive two passes, a different relative slip/twin activities are observed. Twin relative activities are predicted to be almost inexistent which is also expected due to the high processing temperature. In route A, the Taylor-Lin CP-CDD model predicted that basal slip presented the highest relative activity followed by pyramidal  $\langle c+a \rangle$  slip then prismatic slip. The rigid rotation of the sample before the third K route pass leads the prismatic slip to dominate other slip systems where pyramidal slip activity becomes negligible.

The processed AZ31B hot-rolled billets via different routes developed different textures and microstructures that influence the anisotropic mechanical response. A good agreement between the experimental and predicted true tensile stress-strain curves up to the ultimate tensile strength for both routes 4A and 4K along extrusion and flow directions is found. The yield strength of the ECAPed material is significantly increased compared to the as-received material. Furthermore, the anisotropy is reduced, although a slight difference in the yield stress between the FD and ED samples can be still observed. The ECAPed material doesn't present any tensile stress strain asymmetry between the ED and FD. The model predicts for the 4A ED sample an activity of the basal (55%), pyramidal (25%), prismatic (15%) slip and a small fraction of extension twinning (5%) which contributes to a slight decrease in yield strength. On the other hand, for the 4A FD sample the model predicts that about 55% of plastic strain results from prismatic slip, nearly 25% from contraction twinning, 15% from basal slip and a small fraction (5%) from pyramidal

$\langle c+a \rangle$  slip. The activation of basal slip when loading the 4K FD samples results into a decrease of the yield strength which is a consequence of the low basal CRSS. Although both prismatic and pyramidal  $\langle c+a \rangle$  presents almost similar dislocation density evolution for the 4K FD and ED samples, the deactivation of basal slip in the extrusion direction resulted in an important reduction in their dislocation density.

## CHAPTER 5

### CONCLUSIONS AND RECOMMENDATIONS

#### 5.1 Summary and Conclusions

In this research, we investigated the microstructural evolutions of deformed metallic materials. Following the general introduction on the theory of plasticity, and dislocation generation and movement mechanisms in the first chapter, the novel grain refinement approach has been proposed in the second chapter. The investigations were based on a numerical modeling approach proposed in this dissertation and incorporated into a crystal plasticity scheme coupled with a continuum dislocation dynamics framework. The model was validated on FCC metallic material subjected to severe plastic deformation process where it showed high predictability of the main microstructural evolutions such as grain size, dislocation density, strain hardening behavior, and texture evolution.

In chapter 3, the model was developed to increase the capability of predicting more refinement by allowing each grain to split into nine finer grains instead of four grains. The model was able to predict the mechanical properties of the ECAP-processed FCC metallic materials along different loading directions and at different strain rates.

Investigations of HCP materials were performed in chapter 4 by extending the proposed model to account for the four deformation modes (i.e., basal slip, prismatic slip, pyramidal slip, and twinning). Modeling of the ECAP process showed a good agreement with the experimental results. In addition, the predictability of the model was validated for both ECAP microstructural features evolutions and post-ECAP mechanical properties.

## 5.2 Recommendations for Future Work

### 5.2.1 Grain Boundary Sliding (GBS) model

In this thesis, the microstructural features and the mechanical properties of metallic structural materials at room temperatures were investigated. In future work, we intend to develop the current model to investigate the effect of high processing temperatures on the mechanical properties of the materials. At elevated temperatures, deformation is induced mainly by the grain boundary sliding (GBS) mechanism where it becomes more prominent than other deformation mechanisms. Integrating this deformation mechanism into our model can enhance its predictability of the processed materials' microstructures at high temperatures. Grain boundary sliding is a thermally activated deformation mechanism where its effect is assumed to be localized near the grain boundaries [282]. Staroselsky and Anand [282] considered that a portion of the grain located near the grain boundary, having a volume fraction  $\xi$ , deforms according to an isotropic plasticity flow rule while the rest of the grain deforms, having a volume fraction  $(1 - \xi)$  according to the crystal plasticity theory. The effect of the GBS deformation is integrated into the velocity gradient formulation using the rule of mixture, thus, the overall plastic velocity gradient is written  $L^p = (1 - \xi)L_{cp}^p + \xi L_{GBS}^p$  where  $L_{cp}^p$  is the plastic velocity gradient derived from the crystal plasticity scheme, and  $L_{GBS}^p$  is the plastic velocity gradient due to GBS contribution. The GBS velocity gradient can be decomposed additionally into deformation rate  $D_{GBS}^p$  and plastic spin  $W_{GBS}^p$  where  $D_{GBS}^p = \dot{\gamma}_{GBS}^p \sqrt{2} \frac{T'}{2\tau}$  and  $W_{GBS}^p = \dot{R}R^T$ .  $\dot{\gamma}_{GBS}^p$  defines the plastic shear rate,  $T'$  is the deviatoric part of the Cauchy stress  $T$ ,  $\tau$  is the resolved shear stress, and  $R$  is the transformation matrix due to grain rotation around an

axis. Integration of the GBS scheme into the proposed grain refinement model can offer significant understanding of the fragmentation process at elevated temperatures.

### ***5.2.2 Effect of neighboring grains***

Implementing the grain-grain interaction effect in the grain fragmentation model revealed an enhancement in the texture and microstructure predictions. This effect was incorporated into the model by means of the GNDs accumulated at the grain boundaries as explained in this dissertation. Thus, depending on the neighboring grains, each grain can exhibit different misorientation angle and therefore different levels of fragmentation can occur. In future work, this effect will be studied explicitly by investigating the influence of several sets of surrounding grains with different orientations on the fragmentation of a preselected grain. Distinct material textures will be studied such as Aluminum, Copper, and Magnesium to illustrate the effect of deformation mechanisms on reorienting grains differently. This study could be performed by imposing different sets of neighboring grains' orientations surrounding the same grain and simulate the texture in shear mode up to a shear strain of 2. Numerical simulations of the case where the grain-grain interaction effect is considered will then be compared with the case where no effect of neighboring grains. Comparisons may be done by plotting the pole figures, the misorientation frequency distribution using the both the correlated and the non-correlated misorientation distribution methods, and the dislocation density evolutions. These plots may provide clear implications on the effect of grain-grain interaction.

## LIST OF PUBLICATIONS

### Peer-Reviewed Journal Papers

- **Ali Al-Hadi Kobaissy**, Georges Ayoub, Wahaz Nasim, Jahanzaib Malik, Ibrahim Karaman, Mu'tasem Shehadeh, "Modeling of the ECAP Induced Strain Hardening Behavior in FCC Metals", *Metallurgical and Materials Transactions A*, August 2020
- Viet Q. Vu, Laszlo S. Toth, Yan Beygelzimer, Roman Kulagin, **Ali Al-Hadi Kobaissy**, "Modeling of crystallographic texture in plastic flow machining", *Advanced Engineering Materials*, July 2019
- **A.H. Kobaissy**, G. Ayoub, L.S. Toth, S. Mustapha, M. Shehadeh, "Continuum dislocation dynamics-based grain fragmentation modeling", *International Journal of Plasticity*, November 2018

### International-Conference Papers

- **Ali Al-Hadi Kobaissy**, *Continuum dislocation dynamic-based grain fragmentation modeling for severe plastic deformation in FCC metals*, Osaka, Japan, October 2018 (Oral presentation)

### Local-Conference Papers

- **Ali Al-Hadi Kobaissy**, *Crystal Plasticity Based Model for Severe Plastic Deformation in FCC Metals*, 16th Faculty of Engineering and Architecture Student and Alumni Conference, April 2017
- **Ali Al-Hadi Kobaissy**, *Continuum dislocation dynamic-based grain fragmentation modeling for severe plastic deformation in FCC metals*, IDEAS 2019, AUB, Lebanon, April 2019

## BIBLIOGRAPHY

- [1] W.D. Callister, D.G. Rethwisch, *Materials Science and Engineering: An Introduction*, 2009.
- [2] J.W. Morris Jr, *Dislocation-controlled Plasticity of Crystalline Materials : Overview*, *Encycl. Mater. Sci. Technol.* 1 (2001) 1–11.
- [3] D. Hull, D. Bacon, *Introduction to Dislocations (Fifth Edition)*, Oxford, 2011.
- [4] F.C. Frank, W.T. Read, *Multiplication Processes for Slow Moving Dislocations*, (1950).
- [5] G.G. Yapici, *Severe Plastic Deformation of Difficult-to-Work Alloys*, 2004.
- [6] N. Taheri-Nassaj, *A dislocation-based multiscale modeling of plasticity and controlling mechanisms*, 2016.
- [7] M.A. Shehadeh, N.K. Shatarat, W. Jaber, *Modeling the mechanical response and microstructure evolution of magnesium single crystals under c-axis compression*, *Comput. Mater. Sci.* 138 (2017) 236–245. doi:10.1016/j.commatsci.2017.06.022.
- [8] W.F. Hosford, *Mechanical Behavior of Materials (Second Edition)*, 2010.
- [9] X.L. Wu, X.Z. Liao, S.G. Srinivasan, F. Zhou, E.J. Lavernia, R.Z. Valiev, Y.T. Zhu, *New deformation twinning mechanism generates zero macroscopic strain in nanocrystalline metals*, *Phys. Rev. Lett.* 100 (2008) 5–8. doi:10.1103/PhysRevLett.100.095701.
- [10] J.W. Christian, S. Mahajan, *Deformation twinning*, *Prog. Mater. Sci.* 39 (1995) 1–157. doi:10.1016/0079-6425(94)00007-7.
- [11] A. Kelly, K.M. Knowles, *Crystallography and crystal defects (Second edition)*, 1970. doi:10.1002/9783527644131.ch10.
- [12] B. Ehrler, X. Hou, T. Zhu, K.M.Y. P'Ng, C.J. Walker, A. Bushby, D.J. Dunstan, *Grain size and sample size interact to determine strength in a soft metal*, *Philos. Mag.* 25 (2008) 3043–3050.
- [13] K. Krabbenhøft, *Basic Computational Plasticity*, Tech. Univ. Denmark. (2002) 1–40.
- [14] H. Razavi-Khosroshahi, K. Edalati, H. Emami, E. Akiba, Z. Horita, M. Fuji, *Optical Properties of Nanocrystalline Monoclinic Y2O3 Stabilized by Grain Size and Plastic Strain Effects via High-Pressure Torsion*, *Inorg. Chem.* 56 (2017) 2576–2580. doi:10.1021/acs.inorgchem.6b02725.
- [15] K. Edalati, Z. Horita, *Application of high-pressure torsion for consolidation of ceramic powders*, *Scr. Mater.* 63 (2010) 174–177. doi:10.1016/j.scriptamat.2010.03.048.
- [16] K. Edalati, M. Arimura, Y. Ikoma, T. Daio, M. Miyata, D.J. Smith, Z. Horita, *Plastic deformation of BaTiO<sub>3</sub> ceramics by high-pressure torsion and changes in phase transformations, optical and dielectric properties*, *Mater. Res. Lett.* 3 (2015) 216–221. doi:10.1080/21663831.2015.1065454.
- [17] P.L. Sun, P.W. Kao, C.P. Chang, *Effect of deformation route on microstructural development in aluminum processed by equal channel angular extrusion*, *Metall. Mater. Trans. A.* 35 (2003) 1359–1368. doi:10.1007/s11661-004-0311-5.
- [18] A.S. Khan, B. Farrokh, L. Takacs, *Effect of grain refinement on mechanical properties of ball-milled bulk aluminum*, *Mater. Sci. Eng. A.* 489 (2008) 77–84. doi:10.1016/j.msea.2008.01.045.



- [19] A.P. Zhilyaev, T.G. Langdon, Using high-pressure torsion for metal processing: Fundamentals and applications, *Prog. Mater. Sci.* 53 (2008) 893–979. doi:10.1016/j.pmatsci.2008.03.002.
- [20] M.A. Meyers, A. Mishra, D.J. Benson, Mechanical properties of nanocrystalline materials, 51 (2006) 427–556. doi:10.1016/j.pmatsci.2005.08.003.
- [21] R.Z. Valiev, R.K. Islamgaliev, I. V. Alexandrov, Bulk nanostructured materials from severe plastic deformation, 2000. doi:10.1016/S0079-6425(99)00007-9.
- [22] R.Z. Valiev, T.G. Langdon, Principles of equal-channel angular pressing as a processing tool for grain refinement, *Prog. Mater. Sci.* 51 (2006) 881–981. doi:10.1016/j.pmatsci.2006.02.003.
- [23] K. Edalati, Z. Horita, A review on high-pressure torsion (HPT) from 1935 to 1988, *Mater. Sci. Eng. A.* 652 (2016) 325–352. doi:10.1016/j.msea.2015.11.074.
- [24] Y. Saito, H. Utsunomiya, N. Tsuji, T. Sakai, NOVEL ULTRA-HIGH STRAINING PROCESS FOR BULK MATERIALS—DEVELOPMENT OF THE ACCUMULATIVE ROLL-BONDING (ARB) PROCESS, *Acta Mater.* 47 (1999).
- [25] R. Jamaati, M.R. Toroghinejad, H. Edris, Effect of stacking fault energy on nanostructure formation under accumulative roll bonding (ARB) process, *Mater. Sci. Eng. A.* 578 (2013) 191–196. doi:10.1016/j.msea.2013.04.090.
- [26] D.V. Orlov, V. V Stolyarov, H.S. Salimgareyev, E.P. Soshnikova, A. Reshetov, Y.Y. Beygelziraer, S.G. Synkov, V.N. Varyukhin, Microstructure, mechanical properties and anisotropy of pure Ti processed by twist extrusion and cold rolling, in: *Ultrafine Grained Mater. III*, 2004: p. 6.
- [27] J. Richert, M. Richert, A new method from unlimited deformation of metals and alloys, *Aluminium.* 62 (1986) 604–607.
- [28] Y.T. Zhu, H. Jiang, J. Huang, T.C. Lowe, A new route to bulk nanostructured metals, *Metall. Mater. Trans. A Phys. Metall. Mater. Sci.* 32 (2001) 1559–1562. doi:10.1007/s11661-001-0245-0.
- [29] Y.T. Zhu, R.Z. Valiev, Y. Estrin, Z. Horita, T.G. Langdon, M.J. Zehetbauer, Y.T. Zhu, Producing bulk ultrafine-grained materials by severe plastic deformation . *JOM Producing Bulk Ultrafine-Grained Materials by Severe Plastic Deformation*, (2006). doi:10.1007/s11837-006-0213-7.
- [30] I.J. Beyerlein, L.S. Tóth, Texture evolution in equal-channel angular extrusion, *Prog. Mater. Sci.* 54 (2009) 427–510. doi:10.1016/j.pmatsci.2009.01.001.
- [31] Y. Cao, S. Ni, X. Liao, M. Song, Y. Zhu, Structural evolutions of metallic materials processed by severe plastic deformation, *Mater. Sci. Eng. R Reports.* 133 (2018) 1–59. doi:10.1016/j.mser.2018.06.001.
- [32] Y.H. Zhao, X.Z. Liao, Y.T. Zhu, Z. Horita, T.G. Langdon, Influence of stacking fault energy on nanostructure formation under high pressure torsion, *Mater. Sci. Eng. A.* 410–411 (2005) 188–193. doi:10.1016/j.msea.2005.08.074.
- [33] Y.H. Zhao, Y.T. Zhu, X.Z. Liao, Z. Horita, T.G. Langdon, Tailoring stacking fault energy for high ductility and high strength in ultrafine grained Cu and its alloy, *Appl. Phys. Lett.* 89 (2006) 87–90. doi:10.1063/1.2356310.
- [34] S. Qu, X.H. An, H.J. Yang, C.X. Huang, G. Yang, Q.S. Zang, Z.G. Wang, S.D. Wu, Z.F. Zhang, Microstructural evolution and mechanical properties of Cu-Al alloys subjected to equal channel angular pressing, *Acta Mater.* 57 (2009) 1586–1601. doi:10.1016/j.actamat.2008.12.002.
- [35] Z.W. Wang, Y.B. Wang, X.Z. Liao, Y.H. Zhao, E.J. Lavernia, Y.T. Zhu, Z.

- Horita, T.G. Langdon, Influence of stacking fault energy on deformation mechanism and dislocation storage capacity in ultrafine-grained materials, *Scr. Mater.* 60 (2009) 52–55. doi:10.1016/j.scriptamat.2008.08.032.
- [36] T. Ungár, L. Balogh, Y.T. Zhu, Z. Horita, C. Xu, T.G. Langdon, Using X-ray microdiffraction to determine grain sizes at selected positions in disks processed by high-pressure torsion, *Mater. Sci. Eng. A.* 444 (2007) 153–156. doi:10.1016/j.msea.2006.08.059.
- [37] N. Hansen, C.Y. Barlow, *Plastic Deformation of Metals and Alloys*, Fifth Edit, Elsevier, 2014. doi:10.1016/B978-0-444-53770-6.00017-4.
- [38] W. D.Kuhlmann, Theory of Plastic Deformation : -Properties of low energy dislocation structures, *Mater. Sci. Eng. A.* 3 (1989) 1–41.
- [39] B. Bay, N. Hansen, D.A. Hughes, D. Kuhlmann-Wilsdorf, Overview no. 96 evolution of f.c.c. deformation structures in polyslip, *Acta Metall. Mater.* 40 (1992) 205–219. doi:10.1016/0956-7151(92)90296-Q.
- [40] D. Kuhlmann-Wilsdorf, N. Hansen, Geometrically necessary, incidental and subgrain boundaries, *Scr. Metall. Mater.* 25 (1991) 1557–1562. doi:10.1016/0956-716X(91)90451-6.
- [41] A. Mishra, B.K. Kad, F. Gregori, M.A. Meyers, Microstructural evolution in copper subjected to severe plastic deformation: Experiments and analysis, *Acta Mater.* 55 (2007) 13–28. doi:10.1016/j.actamat.2006.07.008.
- [42] M. Muzyk, Z. Pakiela, K.J. Kurzydowski, Ab initio calculations of the generalized stacking fault energy in aluminium alloys, *Scr. Mater.* 64 (2011) 916–918. doi:10.1016/j.scriptamat.2011.01.034.
- [43] Y.L. Wei, A. Godfrey, W. Liu, Q. Liu, X. Huang, N. Hansen, G. Winther, Dislocations, boundaries and slip systems in cube grains of rolled aluminium, *Scr. Mater.* 65 (2011) 355–358. doi:10.1016/j.scriptamat.2011.05.005.
- [44] D. Kuhlmann-Wilsdorf, High-strain dislocation patterning, texture formation and shear banding of wavy glide materials in the LEDS theory, *Scr. Mater.* 36 (1997) 173–181. doi:10.1016/S1359-6462(96)00347-8.
- [45] H.W. Zhang, X. Huang, N. Hansen, Evolution of microstructural parameters and flow stresses toward limits in nickel deformed to ultra-high strains, *Acta Mater.* 56 (2008) 5451–5465. doi:10.1016/j.actamat.2008.07.040.
- [46] N.Q. Chinh, T. Csanádi, J. Gubicza, T.G. Langdon, Plastic behavior of face-centered-cubic metals over a wide range of strain, *Acta Mater.* 58 (2010) 5015–5021. doi:10.1016/j.actamat.2010.05.036.
- [47] N. Hansen, X. Huang, D.A. Hughes, Microstructural evolution and hardening parameters, *Mater. Sci. Eng. A.* 317 (2001) 3–11. doi:10.1016/S0921-5093(01)01191-1.
- [48] D.A. Hughes, N. Hansen, Microstructure and strength of nickel at large strains, *Acta Mater.* 48 (2000) 2985–3004. doi:10.1016/S1359-6454(00)00082-3.
- [49] Y. Chen, Y. Li, L. He, C. Lu, H. Ding, Q. Li, The influence of cryoECAP on microstructure and property of commercial pure aluminum, *Mater. Lett.* 62 (2008) 2821–2824. doi:10.1016/j.matlet.2008.01.091.
- [50] M. Zehetbauer, V. Seumer, Cold work hardening in stages IV and V of F.C.C. metals-I. Experiments and interpretation, *Acta Metall. Mater.* 41 (1993) 577–588. doi:10.1016/0956-7151(93)90088-A.
- [51] M. Zehetbauer, Cold work hardening in stages IV and V of F.C.C. metals-II. Model fits and physical results, *Acta Metall. Mater.* 41 (1993) 589–599.

- doi:10.1016/0956-7151(93)90089-B.
- [52] T. Sakai, A. Belyakov, R. Kaibyshev, H. Miura, J.J. Jonas, Dynamic and post-dynamic recrystallization under hot, cold and severe plastic deformation conditions, *Prog. Mater. Sci.* 60 (2014) 130–207. doi:10.1016/j.pmatsci.2013.09.002.
- [53] N.Q. Chinh, G. Horváth, Z. Horita, T.G. Langdon, A new constitutive relationship for the homogeneous deformation of metals over a wide range of strain, *Acta Mater.* 52 (2004) 3555–3563. doi:10.1016/j.actamat.2004.04.009.
- [54] D. Moldovan, D. Wolf, S.R. Phillpot, A.J. Haslam, Role of grain rotation during grain growth in a columnar microstructure by mesoscale simulation, *Acta Mater.* 50 (2002) 3397–3414. doi:10.1016/S1359-6454(02)00153-2.
- [55] D. Farkas, S. Mohanty, J. Monk, Strain-driven grain boundary motion in nanocrystalline materials, *Mater. Sci. Eng. A.* 493 (2008) 33–40. doi:10.1016/j.msea.2007.06.095.
- [56] N. Hansen, Hall-petch relation and boundary strengthening, *Scr. Mater.* 51 (2004) 801–806. doi:10.1016/j.scriptamat.2004.06.002.
- [57] X.Z. Liao, Y.H. Zhao, Y.T. Zhu, R.Z. Valiev, D. V Gunderov, Grain-size effect on the deformation mechanisms of nanostructured copper processed by high-pressure torsion, *J. Appl. Phys.* 96 (2004) 636–640. doi:10.1063/1.1757035.
- [58] M.A. Meyers, O. Vöhringer, V.A. Lubarda, The onset of twinning in metals: A constitutive description, *Acta Mater.* 49 (2001) 4025–4039. doi:10.1016/S1359-6454(01)00300-7.
- [59] F. Zhao, L. Wang, D. Fan, B.X. Bie, X.M. Zhou, T. Suo, Y.L. Li, M.W. Chen, C.L. Liu, M.L. Qi, M.H. Zhu, S.N. Luo, Macrodeformation Twins in Single-Crystal Aluminum, *Phys. Rev. Lett.* 116 (2016) 1–5. doi:10.1103/PhysRevLett.116.075501.
- [60] Y.S. Li, N.R. Tao, K. Lu, Microstructural evolution and nanostructure formation in copper during dynamic plastic deformation at cryogenic temperatures, *Acta Mater.* 56 (2008) 230–241. doi:10.1016/j.actamat.2007.09.020.
- [61] G.H. Xiao, N.R. Tao, K. Lu, Effects of strain, strain rate and temperature on deformation twinning in a Cu-Zn alloy, *Scr. Mater.* 59 (2008) 975–978. doi:10.1016/j.scriptamat.2008.06.060.
- [62] Y. Zhang, N.R. Tao, K. Lu, Effects of stacking fault energy, strain rate and temperature on microstructure and strength of nanostructured Cu-Al alloys subjected to plastic deformation, *Acta Mater.* 59 (2011) 6048–6058. doi:10.1016/j.actamat.2011.06.013.
- [63] Y. Cao, Y.B. Wang, X.Z. Liao, M. Kawasaki, S.P. Ringer, T.G. Langdon, Y.T. Zhu, Applied stress controls the production of nano-twins in coarse-grained metals, *Appl. Phys. Lett.* 101 (2012). doi:10.1063/1.4769216.
- [64] Y.B. Wang, X.Z. Liao, Y.H. Zhao, E.J. Lavernia, S.P. Ringer, Z. Horita, T.G. Langdon, Y.T. Zhu, The role of stacking faults and twin boundaries in grain refinement of a Cu-Zn alloy processed by high-pressure torsion, *Mater. Sci. Eng. A.* 527 (2010) 4959–4966. doi:10.1016/j.msea.2010.04.036.
- [65] N.R. Tao, K. Lu, Nanoscale structural refinement via deformation twinning in face-centered cubic metals, *Scr. Mater.* 60 (2009) 1039–1043. doi:10.1016/j.scriptamat.2009.02.008.
- [66] N. Maury, N.X. Zhang, Y. Huang, A.P. Zhilyaev, T.G. Langdon, A critical examination of pure tantalum processed by high-pressure torsion, *Mater. Sci.*

- Eng. A. 638 (2015) 174–182. doi:10.1016/j.msea.2015.04.053.
- [67] Q. Wei, Z.L. Pan, X.L. Wu, B.E. Schuster, L.J. Kecskes, R.Z. Valiev, Microstructure and mechanical properties at different length scales and strain rates of nanocrystalline tantalum produced by high-pressure torsion, *Acta Mater.* 59 (2011) 2423–2436. doi:10.1016/j.actamat.2010.12.042.
- [68] P. Li, X. Wang, K.M. Xue, Y. Tian, Y.C. Wu, Microstructure and recrystallization behavior of pure W powder processed by high-pressure torsion, *Int. J. Refract. Met. Hard Mater.* 54 (2016) 439–444. doi:10.1016/j.ijrmhm.2015.10.004.
- [69] L.J. Kecskes, K.C. Cho, R.J. Dowding, B.E. Schuster, R.Z. Valiev, Q. Wei, Grain size engineering of bcc refractory metals: Top-down and bottom-up-Application to tungsten, *Mater. Sci. Eng. A.* 467 (2007) 33–43. doi:10.1016/j.msea.2007.02.099.
- [70] Q. Wei, H.T. Zhang, B.E. Schuster, K.T. Ramesh, R.Z. Valiev, L.J. Kecskes, R.J. Dowding, L. Magness, K. Cho, Microstructure and mechanical properties of super-strong nanocrystalline tungsten processed by high-pressure torsion, *Acta Mater.* 54 (2006) 4079–4089. doi:10.1016/j.actamat.2006.05.005.
- [71] V.P. Pilyugin, L.M. Voronova, T.M. Gapontseva, T.I. Chashchukhina, M. V. Degtyarev, Structure and hardness of molybdenum upon deformation under pressure at room and cryogenic temperatures, *Int. J. Refract. Met. Hard Mater.* 43 (2014) 59–63. doi:10.1016/j.ijrmhm.2013.10.022.
- [72] G.M. Cheng, H. Yuan, W.W. Jian, W.Z. Xu, P.C. Millett, Y.T. Zhu, Deformation-induced  $\omega$  phase in nanocrystalline Mo, *Scr. Mater.* 68 (2013) 130–133. doi:10.1016/j.scriptamat.2012.09.033.
- [73] K. Edalati, T. Fujioka, Z. Horita, Evolution of mechanical properties and microstructures with equivalent strain in Pure Fe processed by High Pressure Torsion, *Mater. Trans.* 50 (2009) 44–50. doi:10.2320/matertrans.MD200812.
- [74] D. Jia, K.T. Ramesh, E. Ma, Effects of nanocrystalline and ultrafine grain sizes on constitutive behavior and shear bands in iron, *Acta Mater.* 51 (2003) 3495–3509. doi:10.1016/S1359-6454(03)00169-1.
- [75] R.Z. Valiev, Y. V. Ivanisenko, E.F. Rauch, B. Baudelet, Structure and deformation behaviour of Armco iron subjected to severe plastic deformation, *Acta Mater.* 44 (1996) 4705–4712. doi:10.1016/S1359-6454(96)00156-5.
- [76] S. Lee, Z. Horita, High-pressure torsion for pure chromium and niobium, *Mater. Trans.* 53 (2012) 38–45. doi:10.2320/matertrans.MD201131.
- [77] Y. Cao, Y.B. Wang, X.H. An, X.Z. Liao, M. Kawasaki, S.P. Ringer, T.G. Langdon, Y.T. Zhu, Concurrent microstructural evolution of ferrite and austenite in a duplex stainless steel processed by high-pressure torsion, *Acta Mater.* 63 (2014) 16–29. doi:10.1016/j.actamat.2013.09.030.
- [78] K. Edalati, Z. Horita, High-pressure torsion of pure metals: Influence of atomic bond parameters and stacking fault energy on grain size and correlation with hardness, *Acta Mater.* 59 (2011) 6831–6836. doi:10.1016/j.actamat.2011.07.046.
- [79] J. Wang, Z. Zeng, C.R. Weinberger, Z. Zhang, T. Zhu, S.X. Mao, In situ atomic-scale observation of twinning-dominated deformation in nanoscale body-centred cubic tungsten, *Nat. Mater.* 14 (2015) 594–600. doi:10.1038/nmat4228.
- [80] D. Caillard, Kinetics of dislocations in pure Fe. Part II. In situ straining experiments at low temperature, *Acta Mater.* 58 (2010) 3504–3515. doi:10.1016/j.actamat.2010.02.024.

- [81] S.S. Lau, J.E. Dorn, Asymmetric slip in Mo single crystals, *Phys. Stat Sol.* 825 (1970) 825–836.
- [82] Q. Wei, B.E. Schuster, S.N. Mathaudhu, K.T. Hartwig, L.J. Kecskes, R.J. Dowding, K.T. Ramesh, Dynamic behaviors of body-centered cubic metals with ultrafine grained and nanocrystalline microstructures, *Mater. Sci. Eng. A.* 493 (2008) 58–64. doi:10.1016/j.msea.2007.05.126.
- [83] Z. Pan, F. Xu, S.N. Mathaudhu, L.J. Kecskes, W.H. Yin, X.Y. Zhang, K.T. Hartwig, Q. Wei, Microstructural evolution and mechanical properties of niobium processed by equal channel angular extrusion up to 24 passes, *Acta Mater.* 60 (2012) 2310–2323. doi:10.1016/j.actamat.2011.12.019.
- [84] H.R.Z. Sandim, H.H. Bernardi, B. Verlinden, D. Raabe, Equal channel angular extrusion of niobium single crystals, *Mater. Sci. Eng. A.* 467 (2007) 44–52. doi:10.1016/j.msea.2007.02.086.
- [85] Y. Fukuda, K. Oh-ishi, M. Furukawa, Z. Horita, T.G. Langdon, The application of equal-channel angular pressing to an aluminum single crystal, *Acta Mater.* 52 (2004) 1387–1395. doi:10.1016/j.actamat.2003.11.028.
- [86] L. Zhu, M. Seefeldt, B. Verlinden, Three Nb single crystals processed by equal-channel angular pressing - Part I: Dislocation substructure, *Acta Mater.* 61 (2013) 4490–4503. doi:10.1016/j.actamat.2013.04.018.
- [87] L. Zhu, M. Seefeldt, B. Verlinden, Three Nb single crystals processed by equal-channel angular pressing - Part II: Mesoscopic bands, *Acta Mater.* 61 (2013) 4504–4511. doi:10.1016/j.actamat.2013.04.019.
- [88] Q. Wei, T. Jiao, S.N. Mathaudhu, E. Ma, K.T. Hartwig, K.T. Ramesh, Microstructure and mechanical properties of tantalum after equal channel angular extrusion (ECAE), *Mater. Sci. Eng. A.* 358 (2003) 266–272. doi:10.1016/S0921-5093(03)00305-8.
- [89] D. Goran, J.J. Fundenberger, E. Bouzy, W. Skrotzki, S. Suwas, T. Grosdidier, L.S. Toth, Local texture and microstructure in cube-oriented nickel single crystal deformed by equal channel angular extrusion, *Philos. Mag.* 91 (2011) 291–309. doi:10.1080/14786435.2010.519352.
- [90] Q. Wei, T. Jiao, K.T. Ramesh, E. Ma, L.J. Kecskes, L. Magness, R. Dowding, V.U. Kazykhanov, R.Z. Valiev, Mechanical behavior and dynamic failure of high-strength ultrafine grained tungsten under uniaxial compression, *Acta Mater.* 54 (2006) 77–87. doi:10.1016/j.actamat.2005.08.031.
- [91] Y. Ivanisenko, R.Z. Valiev, H.J. Fecht, Grain boundary statistics in nanostructured iron produced by high pressure torsion, *Mater. Sci. Eng. A.* 390 (2005) 159–165. doi:10.1016/j.msea.2004.08.071.
- [92] B.Q. Han, E.J. Lavernia, F.A. Mohamed, Dislocation structure and deformation in iron processed by equal-channel-angular pressing, *Metall. Mater. Trans. A Phys. Metall. Mater. Sci.* 35 A (2004) 1343–1350. doi:10.1007/s11661-004-0309-z.
- [93] K. Edalati, Z. Horita, Universal plot for hardness variation in pure metals processed by high-pressure Torsion, *Mater. Trans.* 51 (2010) 1051–1054. doi:10.2320/matertrans.M2009431.
- [94] G.W. Groves, A. Kelly, Independent slip systems in crystals, *Philos. Mag.* 8 (1963) 877–887. doi:10.1080/14786436308213843.
- [95] M.H. Yoo, Slip, twinning, and fracture in hexagonal close-packed metals, *Metall. Trans. A.* 12 (1981) 409–418. doi:10.1007/BF02648537.

- [96] G.G. Yapici, I. Karaman, H.J. Maier, Mechanical flow anisotropy in severely deformed pure titanium, *Mater. Sci. Eng. A.* 434 (2006) 294–302. doi:10.1016/j.msea.2006.06.082.
- [97] Z. Zeng, S. Jonsson, H.J. Roven, The effects of deformation conditions on microstructure and texture of commercially pure Ti, *Acta Mater.* 57 (2009) 5822–5833. doi:10.1016/j.actamat.2009.08.016.
- [98] Y.J. Chen, Y.J. Li, J.C. Walmsley, S. Dumoulin, P.C. Skaret, H.J. Roven, Microstructure evolution of commercial pure titanium during equal channel angular pressing, *Mater. Sci. Eng. A.* 527 (2010) 789–796. doi:10.1016/j.msea.2009.09.005.
- [99] Z. Horita, K. Matsubara, K. Makii, T.G. Langdon, A two-step processing route for achieving a superplastic forming capability in dilute magnesium alloys, *Scr. Mater.* 47 (2002) 255–260. doi:10.1016/S1359-6462(02)00135-5.
- [100] X. Zhao, X. Yang, X. Liu, X. Wang, T.G. Langdon, The processing of pure titanium through multiple passes of ECAP at room temperature, *Mater. Sci. Eng. A.* 527 (2010) 6335–6339. doi:10.1016/j.msea.2010.06.049.
- [101] M. Arul Kumar, I.J. Beyerlein, R.J. McCabe, C.N. Tomé, Grain neighbour effects on twin transmission in hexagonal close-packed materials, *Nat. Commun.* 7 (2016) 1–9. doi:10.1038/ncomms13826.
- [102] P. Gao, S.Q. Zhu, X.H. An, S.Q. Xu, D. Ruan, C. Chen, H.G. Yan, S.P. Ringer, X.Z. Liao, Effect of sample orientation and initial microstructures on the dynamic recrystallization of a Magnesium alloy, *Mater. Sci. Eng. A.* 691 (2017) 150–154. doi:10.1016/j.msea.2017.03.047.
- [103] A. Chapuis, J.H. Driver, Temperature dependency of slip and twinning in plane strain compressed magnesium single crystals, *Acta Mater.* 59 (2011) 1986–1994. doi:10.1016/j.actamat.2010.11.064.
- [104] H. Li, D.E. Mason, T.R. Bieler, C.J. Boehlert, M.A. Crimp, Methodology for estimating the critical resolved shear stress ratios of  $\alpha$ -phase Ti using EBSD-based trace analysis, *Acta Mater.* 61 (2013) 7555–7567. doi:10.1016/j.actamat.2013.08.042.
- [105] L. Wang, Z. Zheng, H. Phukan, P. Kenesei, J.S. Park, J. Lind, R.M. Suter, T.R. Bieler, Direct measurement of critical resolved shear stress of prismatic and basal slip in polycrystalline Ti using high energy X-ray diffraction microscopy, *Acta Mater.* 132 (2017) 598–610. doi:10.1016/j.actamat.2017.05.015.
- [106] A.A. Salem, S.R. Kalidindi, S.L. Semiatin, Strain hardening due to deformation twinning in  $\alpha$ -titanium: Constitutive relations and crystal-plasticity modeling, *Acta Mater.* 53 (2005) 3495–3502. doi:10.1016/j.actamat.2005.04.014.
- [107] X. Wu, S.R. Kalidindi, C. Necker, A.A. Salem, Prediction of crystallographic texture evolution and anisotropic stress-strain curves during large plastic strains in high purity  $\alpha$ -titanium using a Taylor-type crystal plasticity model, *Acta Mater.* 55 (2007) 423–432. doi:10.1016/j.actamat.2006.08.034.
- [108] M. Knezevic, R.A. Lebensohn, O. Cazacu, B. Revil-Baudard, G. Proust, S.C. Vogel, M.E. Nixon, Modeling bending of  $\alpha$ -titanium with embedded polycrystal plasticity in implicit finite elements, *Mater. Sci. Eng. A.* 564 (2013) 116–126. doi:10.1016/j.msea.2012.11.037.
- [109] K.H. Jung, D.K. Kim, Y.T. Im, Y.S. Lee, Prediction of the effects of hardening and texture heterogeneities by finite element analysis based on the Taylor model, *Int. J. Plast.* 42 (2013) 120–140. doi:10.1016/j.ijplas.2012.10.006.

- [110] D.H. Shin, I. Kim, J. Kim, Y.S. Kim, S.L. Semiatin, Microstructure development during equal-channel angular pressing of titanium, *Acta Mater.* 51 (2003) 983–996. doi:10.1016/S1359-6454(02)00501-3.
- [111] D.H. Shin, I. Kim, J. Kim, Y.T. Zhu, Shear strain accommodation during severe plastic deformation of titanium using equal channel angular pressing, *Mater. Sci. Eng. A.* 334 (2002) 239–245. doi:10.1016/S0921-5093(01)01813-5.
- [112] I. Kim, J. Kim, D.H. Shin, C.S. Lee, S.K. Hwang, Effects of equal channel angular pressing temperature on deformation structures of pure Ti, *Mater. Sci. Eng. A.* 342 (2003) 302–310. doi:10.1016/S0921-5093(02)00318-0.
- [113] G. Proust, C.N. Tomé, G.C. Kaschner, Modeling texture, twinning and hardening evolution during deformation of hexagonal materials, *Acta Mater.* 55 (2007) 2137–2148. doi:10.1016/j.actamat.2006.11.017.
- [114] Y.B. Chun, S.H. Yu, S.L. Semiatin, S.K. Hwang, Effect of deformation twinning on microstructure and texture evolution during cold rolling of CP-titanium, *Mater. Sci. Eng. A.* 398 (2005) 209–219. doi:10.1016/j.msea.2005.03.019.
- [115] J.L. Sun, P.W. Trimby, X. Si, X.Z. Liao, N.R. Tao, J.T. Wang, Nano twins in ultrafine-grained Ti processed by dynamic plastic deformation, *Scr. Mater.* 68 (2013) 475–478. doi:10.1016/j.scriptamat.2012.11.025.
- [116] M.H. Yoo, J.K. Lee, Deformation twinning in h.c.p. metals and alloys, *Philos. Mag. A Phys. Condens. Matter, Struct. Defects Mech. Prop.* 63 (1991) 987–1000. doi:10.1080/01418619108213931.
- [117] X. Zhao, W. Fu, X. Yang, T.G. Langdon, Microstructure and properties of pure titanium processed by equal-channel angular pressing at room temperature, *Scr. Mater.* 59 (2008) 542–545. doi:10.1016/j.scriptamat.2008.05.001.
- [118] I. Kim, J. Kim, D.H. Shin, X.Z. Liao, Y.T. Zhu, Deformation twins in pure titanium processed by equal channel angular pressing, *Scr. Mater.* 48 (2003) 813–817. doi:10.1016/S1359-6462(02)00513-4.
- [119] Q. Yu, J. Wang, Y. Jiang, R.J. McCabe, N. Li, C.N. Tomé, Twin-twin interactions in magnesium, *Acta Mater.* 77 (2014) 28–42. doi:10.1016/j.actamat.2014.05.030.
- [120] Q. Yu, R.K. Mishra, A.M. Minor, The effect of size on the deformation twinning behavior in hexagonal close-packed Ti and Mg, *Jom.* 64 (2012) 1235–1240. doi:10.1007/s11837-012-0437-7.
- [121] Q. Yu, Z.W. Shan, J. Li, X. Huang, L. Xiao, J. Sun, E. Ma, Strong crystal size effect on deformation twinning, *Nature.* 463 (2010) 335–338. doi:10.1038/nature08692.
- [122] J. Li, W. Xu, X. Wu, H. Ding, K. Xia, Effects of grain size on compressive behaviour in ultrafine grained pure Mg processed by equal channel angular pressing at room temperature, *Mater. Sci. Eng. A.* 528 (2011) 5993–5998. doi:10.1016/j.msea.2011.04.045.
- [123] X.L. Wu, K.M. Youssef, C.C. Koch, S.N. Mathaudhu, L.J. Kecskés, Y.T. Zhu, Deformation twinning in a nanocrystalline hcp Mg alloy, *Scr. Mater.* 64 (2011) 213–216. doi:10.1016/j.scriptamat.2010.10.024.
- [124] P.W. Bridgman, On torsion combined with compression, *J. Appl. Phys.* 14 (1943) 273–283. doi:10.1063/1.1714987.
- [125] A. Azushima, R. Kopp, A. Korhonen, D.Y. Yang, F. Micari, G.D. Lahoti, P. Groche, J. Yanagimoto, N. Tsuji, A. Rosochowski, A. Yanagida, Severe plastic deformation (SPD) processes for metals, *CIRP Ann. - Manuf. Technol.* 57 (2008)

- 716–735. doi:10.1016/j.cirp.2008.09.005.
- [126] R.Z. Valiev, a. V. V Korznikov, R.R.R. Mulyukov, Structure and properties of ultrafine-grained materials produced by severe plastic deformation, *Mater. Sci. Eng. A.* 168 (1993) 141–148. doi:10.1016/0921-5093(93)90717-S.
- [127] Y. Iwahashi, Z. Horita, M. Nemoto, T.G. Langdon, The process of grain refinement in equal-channel angular pressing, *Acta Mater.* 46 (1997) 3317–3331. doi:10.1016/S1359-6454(97)00494-1.
- [128] L.S. Toth, C. Gu, Ultrafine-grain metals by severe plastic deformation, *Mater. Charact.* 92 (2014) 1–14. doi:10.1016/j.matchar.2014.02.003.
- [129] E.A. El-Danaf, Texture evolution and fraction of favorably oriented fibers in commercially pure aluminum processed to 16 ECAP passes, *Mater. Sci. Eng. A.* 492 (2008) 141–152. doi:10.1016/j.msea.2008.03.008.
- [130] A.S. Khan, C.S. Meredith, Thermo-mechanical response of Al 6061 with and without equal channel angular pressing (ECAP), *Int. J. Plast.* 26 (2010) 189–203. doi:10.1016/j.ijplas.2009.07.002.
- [131] C.S. Meredith, A.S. Khan, Texture evolution and anisotropy in the thermo-mechanical response of UFG Ti processed via equal channel angular pressing, *Int. J. Plast.* 30–31 (2012) 202–217. doi:10.1016/j.ijplas.2011.10.006.
- [132] Z. Horita, T. Fujinami, T.G. Langdon, The potential for scaling ECAP: Effect of sample size on grain refinement and mechanical properties, *Mater. Sci. Eng. A.* 318 (2001) 34–41. doi:10.1016/S0921-5093(01)01339-9.
- [133] S. Li, I.J. Beyerlein, D.J. Alexander, S.C. Vogel, Texture evolution during multi-pass equal channel angular extrusion of copper: Neutron diffraction characterization and polycrystal modeling, *Acta Mater.* 53 (2005) 2111–2125. doi:10.1016/j.actamat.2005.01.023.
- [134] A. Gholinia, P.B. Prangnell, M. V. Markushev, Effect of strain path on the development of deformation structures in severely deformed aluminium alloys processed by ECAE, *Acta Mater.* 48 (2000) 1115–1130. doi:10.1016/S1359-6454(99)00388-2.
- [135] S. Suwas, R. Arruffat-Massion, L.S. Toth, J.J. Fundenberger, A. Eberhardt, W. Skrotzki, Evolution of crystallographic texture during equal channel angular extrusion of copper: The role of material variables, *Metall. Mater. Trans. A Phys. Metall. Mater. Sci.* 37 (2006) 739–753. doi:10.1007/s11661-006-0046-6.
- [136] R. Lapovok, I. Timokhina, P.W.J. McKenzie, R. O'Donnell, Processing and properties of ultrafine-grain aluminium alloy 6111 sheet, *J. Mater. Process. Technol.* 200 (2008) 441–450. doi:10.1016/j.jmatprotec.2007.08.083.
- [137] D.J. Alexander, I.J. Beyerlein, Anisotropy in mechanical properties of high-purity copper processed by equal channel angular extrusion, *Mater. Sci. Eng. A.* 410–411 (2005) 480–484. doi:10.1016/j.msea.2005.08.149.
- [138] M. Reihanian, R. Ebrahimi, N. Tsuji, M.M. Moshksar, Analysis of the mechanical properties and deformation behavior of nanostructured commercially pure Al processed by equal channel angular pressing (ECAP), *Mater. Sci. Eng. A.* 473 (2008) 189–194. doi:10.1016/j.msea.2007.04.075.
- [139] M.C.V.. Vega, R.E.. Bolmaro, M.. Ferrante, V.L.. Sordi, A.M.. Kliauga, The influence of deformation path on strain characteristics of AA1050 aluminium processed by equal-channel angular pressing followed by rolling, *Mater. Sci. Eng. A.* 646 (2015) 154–162. doi:10.1016/j.msea.2015.07.083.
- [140] Y. Beygelzimer, Grain refinement versus voids accumulation during severe



- plastic deformations of polycrystals: Mathematical simulation, *Mech. Mater.* 37 (2005) 753–767. doi:10.1016/j.mechmat.2004.07.006.
- [141] I.J. Beyerlein, R.A. Lebensohn, C.N. Tomé, Modeling texture and microstructural evolution in the equal channel angular extrusion process, *Mater. Sci. Eng. A.* 345 (2003) 122–138. doi:10.1016/S0921-5093(02)00457-4.
- [142] A. Ostapovets, P. Šedá, A. Jäger, P. Lejček, New misorientation scheme for a visco-plastic self-consistent model: Equal channel angular pressing of magnesium single crystals, *Int. J. Plast.* 29 (2012) 1–12. doi:10.1016/j.ijplas.2011.07.006.
- [143] H. Petryk, S. Stupkiewicz, A quantitative model of grain refinement and strain hardening during severe plastic deformation, *Mater. Sci. Eng. A.* 444 (2007) 214–219. doi:10.1016/j.msea.2006.08.076.
- [144] R.A. Lebensohn, C.N. Tomé, A self-consistent anisotropic approach for the simulation of plastic deformation and texture development of polycrystals: Application to zirconium alloys, *Acta Metall. Mater.* 41 (1993) 2611–2624. doi:10.1016/0956-7151(93)90130-K.
- [145] N.A. Enikeev, M.F. Abdullin, A.A. Nazarov, I.J. Beyerlein, Modelling grain refinement in fcc metals during equal-channel angular pressing by route “C,” *Int. J. Mater. Res.* 98 (2007) 167–171. doi:10.3139/146.101451.
- [146] A.A. Nazarov, N.A. Enikeev, A.E. Romanov, T.S. Orlova, I. V. Alexandrov, I.J. Beyerlein, R.Z. Valiev, Analysis of substructure evolution during simple shear of polycrystals by means of a combined viscoplastic self-consistent and disclination modeling approach, 54 (2006) 985–995. doi:10.1016/j.actamat.2005.10.025.
- [147] K. Frydrych, K. Kowalczyk-Gajewska, A three-scale crystal plasticity model accounting for grain refinement in fcc metals subjected to severe plastic deformations, *Mater. Sci. Eng. A.* 658 (2016) 490–502. doi:10.1016/j.msea.2016.01.101.
- [148] L.S. Tóth, Y. Estrin, R. Lapovok, C. Gu, A model of grain fragmentation based on lattice curvature, *Acta Mater.* 58 (2010) 1782–1794. doi:10.1016/j.actamat.2009.11.020.
- [149] S.R. Kalidindi, B.R. Donohue, S. Li, Modeling texture evolution in equal channel angular extrusion using crystal plasticity finite element models, *Int. J. Plast.* 25 (2009) 768–779. doi:10.1016/j.ijplas.2008.06.008.
- [150] I.J. Beyerlein, C.N. Tomé, Modeling transients in the mechanical response of copper due to strain path changes, *Int. J. Plast.* 23 (2007) 640–664. doi:10.1016/j.ijplas.2006.08.001.
- [151] H. Lim, M.G. Lee, J.H. Kim, B.L. Adams, R.H. Wagoner, Simulation of polycrystal deformation with grain and grain boundary effects, *Int. J. Plast.* 27 (2011) 1328–1354. doi:10.1016/j.ijplas.2011.03.001.
- [152] H.M. Zbib, E.C. Aifantis, On the gradient-dependent theory of plasticity and shear banding, *Acta Mech.* 92 (1992) 209–225. doi:10.1007/BF01174177.
- [153] N.A. Fleck, J.W. Hutchinson, *Strain Gradient Plasticity*, Elsevier Masson SAS, 1997. doi:10.1016/S0065-2156(08)70388-0.
- [154] R.K. Abu Al-Rub, G.Z. Voyiadjis, A physically based gradient plasticity theory, *Int. J. Plast.* 22 (2006) 654–684. doi:10.1016/j.ijplas.2005.04.010.
- [155] F. Nye, 2 . Single Glide : Two-Dimensional Case, *Acta Metall.* 1 (1953).
- [156] M.F. Ashby, The deformation of plastically non-homogeneous materials, *Philos. Mag.* 21 (1970) 399–424. doi:10.1080/14786437008238426.

- [157] T. Ohashi, Crystal plasticity analysis of dislocation emission from micro voids, *Int. J. Plast.* 21 (2005) 2071–2088. doi:10.1016/j.ijplas.2005.03.018.
- [158] T. Ohashi, M. Kawamukai, H. Zbib, A multiscale approach for modeling scale-dependent yield stress in polycrystalline metals, *Int. J. Plast.* 23 (2007) 897–914. doi:10.1016/j.ijplas.2006.10.002.
- [159] H. Lyu, A. Ruimi, H.M. Zbib, A dislocation-based model for deformation and size effect in multi-phase steels, *Int. J. Plast.* 72 (2015) 44–59. doi:10.1016/j.ijplas.2015.05.005.
- [160] S.R. Kalidindi, C.A. Bronkhorst, L. Anand, Crystallographic Deformation Texture Processing Evolution in Bulk, *J. Mech. Phys. Solids.* 40 (1992) 537–569.
- [161] N. Zouhal, A. Molinari, T.S. Toth, Elastic-plastic effects during cyclic loading as predicted by the Taylor-Lin model of polycrystal elasto-viscoplasticity, 12 (1996) 343–360.
- [162] G.I. Taylor, Plastic strain in metals, *J. Inst. Met.* 62 (1938) 307–325.
- [163] T.H. Lin, Analysis of elastic and plastic strains of a face-centred cubic crystal, *J. Mech. Phys. Solids.* 5 (1957) 143–149. doi:10.1016/0022-5096(57)90058-3.
- [164] R.J. Asaro, A. Needleman, Overview no. 42 Texture development and strain hardening in rate dependent polycrystals, *Acta Metall.* 33 (1985) 923–953. doi:10.1016/0001-6160(85)90188-9.
- [165] H. Askari, M.R. Maughan, N. Abdolrahim, D. Sagapuram, D.F. Bahr, H.M. Zbib, A stochastic crystal plasticity framework for deformation of micro-scale polycrystalline materials, *Int. J. Plast.* 68 (2015) 21–33. doi:10.1016/j.ijplas.2014.11.001.
- [166] E.H. Lee, Elastic-Plastic Deformation at Finite Strains, *J. Appl. Mech.* 36 (1969) 1. doi:10.1115/1.3564580.
- [167] A. Needleman, R.J. Asaro, J. Lemonds, D. Peirce, Finite element analysis of crystalline solids, *Comput. Methods Appl. Mech. Eng.* 52 (1985) 689–708. doi:10.1016/0045-7825(85)90014-3.
- [168] L. Anand, A constitutive model for interface friction, *Comput. Mech.* 12 (1993) 197–213. doi:10.1007/BF00369962.
- [169] E. Orowan, Problems of plastic gliding, *Proc. Phys. Soc.* 52 (1940) 8. doi:10.1088/0959-5309/52/1/303.
- [170] H. Askari, J. Young, D. Field, G. Kridli, D. Li, H. Zbib, A study of the hot and cold deformation of twin-roll cast magnesium alloy AZ31, *Philos. Mag.* 94 (2014) 381–403. doi:10.1080/14786435.2013.853884.
- [171] D. Li, H. Zbib, X. Sun, M. Khaleel, Predicting plastic flow and irradiation hardening of iron single crystal with mechanism-based continuum dislocation dynamics, *Int. J. Plast.* 52 (2014) 3–17. doi:10.1016/j.ijplas.2013.01.015.
- [172] A. Alankar, I.N. Mastorakos, D.P. Field, H.M. Zbib, Determination of Dislocation Interaction Strengths Using Discrete Dislocation Dynamics of Curved Dislocations, 134 (2012) 1–4. doi:10.1115/1.4005917.
- [173] H. Gao, Y. Huang, Geometrically necessary dislocation and size dependent plasticity, *Scr. Mater.* 48 (2003) 113–118.
- [174] D.A. Hughes, N. Hansen, High angle boundaries formed by grain subdivision mechanisms, *Acta Mater.* 45 (1997) 3871–3886. doi:10.1016/S1359-6454(97)00027-X.
- [175] K. Shizawa, H.M. Zbib, A thermodynamical theory of gradient elastoplasticity with dislocation density tensor. I: Fundamentals, *Int. J. Plast.* 15 (1999) 899–938.

- doi:10.1016/S0749-6419(99)00018-2.
- [176] M. Miodownik, A.W. Godfrey, E.A. Holm, D.A. Hughes, On boundary misorientation distribution functions and how to incorporate them into three-dimensional models of microstructural evolution, *Acta Mater.* 47 (1999) 2661–2668. doi:10.1016/S1359-6454(99)00137-8.
  - [177] J.G. Tang, X.M. Zhang, Z.Y. Chen, Y.L. Deng, Finite element simulation of influences of grain interaction on rolling textures of fcc metals, *J. Cent. South Univ. Technol. (English Ed.)* 13 (2006) 117–121. doi:10.1007/s11771-006-0141-2.
  - [178] N.C. Admal, G. Po, J. Marian, A unified framework for polycrystal plasticity with grain boundary evolution, *Int. J. Plast.* 106 (2018) 1–30. doi:10.1016/j.ijplas.2018.01.014.
  - [179] M.E. Gurtin, A finite-deformation, gradient theory of single-crystal plasticity with free energy dependent on the accumulation of geometrically necessary dislocations, *Int. J. Plast.* 26 (2008) 1073–1096. doi:10.1016/j.ijplas.2010.02.002.
  - [180] S. Wulfinghoff, E. Bayerschen, T. Böhlke, A gradient plasticity grain boundary yield theory, *Int. J. Plast.* 51 (2013) 33–46. doi:10.1016/j.ijplas.2013.07.001.
  - [181] C.F.O. Dahlberg, J. Faleskog, C.F. Niordson, B.N. Legarth, A deformation mechanism map for polycrystals modeled using strain gradient plasticity and interfaces that slide and separate, *Int. J. Plast.* 43 (2013) 177–195. doi:10.1016/j.ijplas.2012.11.010.
  - [182] S.R. Skjervold, N. Ryum, Characterization of local texture in a moderately deformed polycrystalline AlSi-alloy, *Acta Met. Mater.* 43 (1995) 3159–3176.
  - [183] S.K. Mishra, P. Pant, K. Narasimhan, A.D. Rollett, I. Samajdar, On the widths of orientation gradient zones adjacent to grain boundaries, *Scr. Mater.* 61 (2009) 273–276. doi:10.1016/j.scriptamat.2009.03.062.
  - [184] L.S. Tóth, J.J. Jonas, D. Daniel, J. a. Bailey, Texture Development and Length Changes in Copper Bars Subjected to Free End Torsion, *Textures Microstruct.* 19 (1992) 245–262. doi:10.1155/TSM.19.245.
  - [185] V.M. Segal, Equal channel angular extrusion : from macromechanics to structure formation, *Mater. Sci. Eng. A271* (1999) 322–333.
  - [186] V.M. Segal, Materials processing by simple shear, *Mater. Sci. Eng. A.* 197 (1995) 157–164. doi:10.1016/0921-5093(95)09705-8.
  - [187] A. Molinari, L.S. Toth, Tuning a self consistent viscoplastic model by finite element results - I. Modeling, *Acta Met. Mater.* 42 (1994) 2453.
  - [188] A. Molinari, L.S. Tóth, Tuning a self consistent viscoplastic model by finite element results-I. Modeling, *Acta Metall. Mater.* 42 (1994) 2453–2458. doi:10.1016/0956-7151(94)90324-7.
  - [189] V.M. Segal, Methods of Stress-Strain Analysis in Metal forming, *Phys. Tech. Inst. Acad. Sci. Buelorussia.* (1974).
  - [190] L.S. Toth, C. Gu, Ultrafine-grain metals by severe plastic deformation, *Mater. Charact.* 92 (2014) 1–14. doi:10.1016/j.matchar.2014.02.003.
  - [191] K. Nakashima, Z. Horita, M. Nemoto, T.G. Langdon, Influence of channel angle on the development of ultrafine grains in equal-channel angular pressing, *Acta Mater.* 46 (1998) 1589–1599. doi:10.1016/S1359-6454(97)00355-8.
  - [192] S. Li, O. V. Mishin, Analysis of crystallographic textures in aluminum plates processed by equal channel angular extrusion, *Metall. Mater. Trans. A Phys. Metall. Mater. Sci.* 45 (2014) 1689–1692. doi:10.1007/s11661-014-2195-3.

- [193] S. Ferrasse, V.M. Segal, K.T. Hartwig, R.E. Goforth, Microstructure and properties of copper and aluminum alloy 3003 heavily worked by equal channel angular extrusion, *Metall. Mater. Trans. a-Physical Metall. Mater. Sci.* 28 (1997) 1047–1057. doi:10.1007/s11661-997-0234-z.
- [194] M.H. Shaeri, M. Shaeri, M.T. Salehi, S.H. Seyyedein, F. Djavanroodi, Microstructure and texture evolution of Al-7075 alloy processed by equal channel angular pressing, *Trans. Nonferrous Met. Soc. China (English Ed.)* 25 (2015) 1367–1375. doi:10.1016/S1003-6326(15)63735-9.
- [195] V. V Stolyarov, R. Lapovok, Effect of backpressure on structure and properties of AA5083 alloy processed by ECAP, *378 (2004) 233–236.* doi:10.1016/j.jallcom.2003.10.084.
- [196] N.A. Krasil'nikov, Strength and ductility of copper subjected to equal-channel angular pressing with backpressure, *Russ. Metall.* 2005 (2005) 220–226.
- [197] Y.C. Chen, Y.Y. Huang, C.P. Chang, P.W. Kao, The effect of extrusion temperature on the development of deformation microstructures in 5052 aluminium alloy processed by equal channel angular extrusion, *Acta Mater.* 51 (2003) 2005–2015. doi:10.1016/S1359-6454(02)00607-9.
- [198] W.H. Huang, C.Y. Yu, P.W. Kao, C.P. Chang, The effect of strain path and temperature on the microstructure developed in copper processed by ECAE, *Mater. Sci. Eng. A.* 366 (2004) 221–228. doi:10.1016/j.msea.2003.08.033.
- [199] I. Nikulin, R. Kaibyshev, The Effect of Temperature on Microstructure Evolution in a 7055 Aluminum Alloy Subjected to ECAP, *Mater. Sci. Forum.* 715–716 (2012) 317–322. doi:10.4028/www.scientific.net/MSF.715-716.317.
- [200] S.-Y. Chang, J.G. Lee, K.-T. Park, D.H. Shin, Microstructures and mechanical properties of equal channel angular pressed 5083 Al alloy, *Mater. Trans.* 42 (2001) 1074–1080.
- [201] É.F. Prados, V.L. Sordi, M. Ferrante, Microstructural Development and Tensile Strength of an ECAP - Deformed Al-4 wt . (%) Cu Alloy, *Mater. Res.* 11 (2008) 199–205.
- [202] J.H. Park, K.-T. Park, Y.S. Lee, W.J. Nam, Comparison of compressive deformation of ultrafine-grained 5083 Al alloy at 77 and 298 K, *Metall. Mater. Trans. A.* 36 (2005) 1365–1368. doi:10.1007/s11661-005-0227-8.
- [203] Y.M. Wang, E. Ma, Strain hardening, strain rate sensitivity, and ductility of nanostructured metals, *Mater. Sci. Eng. A.* 375–377 (2004) 46–52. doi:10.1016/j.msea.2003.10.214.
- [204] M.J. Starink, X.G. Qiao, J. Zhang, N. Gao, Predicting grain refinement by cold severe plastic deformation in alloys using volume averaged dislocation generation, *Acta Mater.* 57 (2009) 5796–5811. doi:https://doi.org/10.1016/j.actamat.2009.08.006.
- [205] M. Seefeldt, L. Delannay, B. Peeters, S.R. Kalidindi, P. Van Houtte, A disclination-based model for grain subdivision, *Mater. Sci. Eng. A.* 319 (2001) 192–196. doi:10.1016/S0921-5093(01)00994-7.
- [206] A.E. Romanov, V.I. Vladimirov, *Dislocations in Solids*, North Holland, Amsterdam. 9 (1992) 191–422.
- [207] A.H. Kobaissy, G. Ayoub, L.S. Toth, S. Mustapha, M. Shehadeh, Continuum dislocation dynamics-based grain fragmentation modeling, *Int. J. Plast.* 114 (2019) 252–271. doi:10.1016/j.ijplas.2018.11.006.
- [208] A.S. Khan, J. Liu, A deformation mechanism based crystal plasticity model of

- ultrafine-grained/nanocrystalline FCC polycrystals, *Int. J. Plast.* 86 (2016) 56–69. doi:10.1016/j.ijplas.2016.08.001.
- [209] Y. Aoyagi, R. Kobayashi, Y. Kaji, K. Shizawa, Modeling and simulation on ultrafine-graining based on multiscale crystal plasticity considering dislocation patterning, *Int. J. Plast.* 47 (2013) 13–28. doi:10.1016/j.ijplas.2012.12.007.
- [210] O. Daaland, E. Nes, Origin of cube texture during hot rolling of commercial Al-Mn-Mg alloys, *Acta Mater.* 44 (1996) 1389–1411. doi:10.1016/1359-6454(95)00289-8.
- [211] M. Zecevic, R.A. Lebensohn, R.J. McCabe, M. Knezevic, Modeling of intragranular misorientation and grain fragmentation in polycrystalline materials using the viscoplastic self-consistent formulation, *Int. J. Plast.* 109 (2018) 193–211. doi:10.1016/j.ijplas.2018.06.004.
- [212] A.A. Ridha, W.B. Hutchinson, Recrystallisation mechanisms and the origin of cube texture in copper, *Acta Metall.* 30 (1982) 1929–1939. doi:10.1016/0001-6160(82)90033-5.
- [213] S. Huang, A.S. Khan, Modeling the mechanical behaviour of 1100-0 aluminum at different strain rates by the bodner-partom model, *Int. J. Plast.* 8 (1992) 501–517. doi:10.1016/0749-6419(92)90028-B.
- [214] J. Hirsch, T. Al-Samman, Superior light metals by texture engineering: Optimized aluminum and magnesium alloys for automotive applications, *Acta Mater.* 61 (2013) 818–843. doi:10.1016/j.actamat.2012.10.044.
- [215] B. Poorganji, P. Sepehrband, H. Jin, S. Esmaeili, Effect of cold work and non-isothermal annealing on the recrystallization behavior and texture evolution of a precipitation-hardenable aluminum alloy, *Scr. Mater.* 63 (2010) 1157–1160. doi:10.1016/j.scriptamat.2010.08.014.
- [216] E.A. El-Danaf, M.S. Soliman, A.A. Almajid, M.M. El-Rayes, Enhancement of mechanical properties and grain size refinement of commercial purity aluminum 1050 processed by ECAP, *Mater. Sci. Eng. A.* 458 (2007) 226–234. doi:10.1016/j.msea.2006.12.077.
- [217] J.K. Kim, H.K. Kim, J.W. Park, W.J. Kim, Large enhancement in mechanical properties of the 6061 Al alloys after a single pressing by ECAP, *Scr. Mater.* 53 (2005) 1207–1211. doi:10.1016/j.scriptamat.2005.06.014.
- [218] P.J. Konijnenberg, S. Zaeferrer, D. Raabe, Assessment of geometrically necessary dislocation levels derived by 3D EBSD, *Acta Mater.* 99 (2015) 402–414. doi:10.1016/j.actamat.2015.06.051.
- [219] L.S. Tóth, R.A. Massion, L. Germain, S.C. Baik, S. Suwas, Analysis of texture evolution in equal channel angular extrusion of copper using a new flow field, *Acta Mater.* 52 (2004) 1885–1898. doi:10.1016/j.actamat.2003.12.027.
- [220] S. Li, I.J. Beyerlein, M.A.M. Bourke, Texture formation during equal channel angular extrusion of fcc and bcc materials: Comparison with simple shear, *Mater. Sci. Eng. A.* 394 (2005) 66–77. doi:10.1016/j.msea.2004.11.032.
- [221] S. LI, Application of crystal plasticity modeling in equal channel angular extrusion, *Trans. Nonferrous Met. Soc. China.* 23 (2013) 170–179. doi:http://dx.doi.org/10.1016/S1003-6326(13)62444-9.
- [222] C.F. Gu, L.S. Tóth, C.H.J. Davies, Effect of strain reversal on texture and grain refinement in route C equal channel angular pressed copper, *Scr. Mater.* 65 (2011) 167–170. doi:10.1016/j.scriptamat.2011.04.009.
- [223] Y. Estrin, H. Mecking, A unified phenomenological description of work

- hardening and creep based on one-parameter models, *Acta Metall.* 32 (1984) 57–70. doi:10.1016/0001-6160(84)90202-5.
- [224] H. Mecking, U.F. Kocks, Kinetics of flow and strain-hardening, *Acta Metall.* 29 (1981) 1865–1875. doi:10.1016/0001-6160(81)90112-7.
- [225] Y. Estrin, L.S. Tóth, A. Molinari, Y. Bréchet, A dislocation-based model for all hardening stages in large strain deformation, *Acta Mater.* 46 (1998) 5509–5522. doi:10.1016/S1359-6454(98)00196-7.
- [226] L.S. Toth, P. Gilormini, J.J. Jonas, Effect of rate sensitivity on the stability of torsion textures, *Acta Metall.* 36 (1988) 3077–3091. doi:10.1016/0001-6160(88)90045-4.
- [227] H. Hallberg, M. Wallin, M. Ristinmaa, Modeling of continuous dynamic recrystallization in commercial-purity aluminum, *Mater. Sci. Eng. A.* 527 (2010) 1126–1134. doi:10.1016/j.msea.2009.09.043.
- [228] M.H. Shaeri, M. Shaeri, M. Ebrahimi, M.T. Salehi, S.H. Seyyedain, Effect of ECAP temperature on microstructure and mechanical properties of Al-Zn-Mg-Cu alloy, *Prog. Nat. Sci. Mater. Int.* 26 (2016) 182–191. doi:10.1016/j.pnsc.2016.03.003.
- [229] M. Howeyze, H. Arabi, A.R. Eivani, H.R. Jafarian, Strengthening of AA5052 aluminum alloy by equal channel angular pressing followed by softening at room temperature, *Mater. Sci. Eng. A.* 720 (2018) 160–168. doi:10.1016/j.msea.2018.02.054.
- [230] M. Howeyze, A.R. Eivani, H. Arabi, H.R. Jafarian, Effects of deformation routes on the evolution of microstructure, texture and tensile properties of AA5052 aluminum alloy, *Mater. Sci. Eng. A.* 732 (2018) 120–128. doi:10.1016/j.msea.2018.06.081.
- [231] S.E. Mousavi, M.H. Khaleghifar, M. Meratian, B. Sadeghi, P. Cavaliere, Effect of the equal channel angular pressing route on the microstructural and mechanical behavior of Al-5086 alloy, *Materialia.* 4 (2018) 310–322. doi:10.1016/j.mtla.2018.10.007.
- [232] C. V. Venkatesh, S.G.S. Raman, U. Chakkingal, Characterization of AA6061 alloy processed by equal channel angular pressing and subjected to low cycle fatigue, *Trans. Indian Inst. Met.* 66 (2013) 147–154. doi:10.1007/s12666-012-0236-4.
- [233] M. Miraglia, P. Dawson, T. Leffers, On the influence of mechanical environment on the emergence of brass textures in FCC metals, *Acta Mater.* 55 (2007) 799–812. doi:10.1016/j.actamat.2006.07.017.
- [234] T. Hama, H. Takuda, Crystal-plasticity finite-element analysis of inelastic behavior during unloading in a magnesium alloy sheet, *Int. J. Plast.* 27 (2011) 1072–1092. doi:10.1016/j.ijplas.2010.11.004.
- [235] G. Winther, Slip patterns and preferred dislocation boundary planes, *Acta Mater.* 51 (2003) 417–429. doi:10.1016/S1359-6454(02)00423-8.
- [236] G. Gottstein, *Physikalische Grundlagen der Materialkunde*, Springer-Verlag, Berlin- Heidelberg, Germany, 1998.
- [237] G.I. Taylor, Plastic Strain in Metals, *J. Inst. Met.* 62 (1938) 307–324.
- [238] R. Von Mises, Mechanics of the ductile form changes of crystals, *Zeitschrift Fur Angew. Math. Und Mech.* 8 (1928) 161–185.
- [239] S.R. Agnew, J.F. Nie, Preface to the viewpoint set on: The current state of magnesium alloy science and technology, *Scr. Mater.* 63 (2010) 671–673.

- doi:10.1016/j.scriptamat.2010.06.029.
- [240] M. Lentz, M. Risse, N. Schaefer, W. Reimers, I.J. Beyerlein, Strength and ductility with {10 11}-{1012} double twinning in a magnesium alloy, *Nat. Commun.* 7 (2016) 1–7. doi:10.1038/ncomms11068.
- [241] A. Jäger, P. Lukáč, V. Gärtnerová, J. Haloda, M. Dopita, Influence of annealing on the microstructure of commercial Mg alloy AZ31 after mechanical forming, *Mater. Sci. Eng. A.* 432 (2006) 20–25. doi:10.1016/j.msea.2006.06.070.
- [242] Y.V.R.K. Prasad, K.P. Rao, Effect of crystallographic texture on the kinetics of hot deformation of rolled Mg-3Al-1Zn alloy plate, *Mater. Sci. Eng. A.* 432 (2006) 170–177. doi:10.1016/j.msea.2006.05.159.
- [243] S. Yi, J. Bohlen, F. Heinemann, D. Letzig, Mechanical anisotropy and deep drawing behaviour of AZ31 and ZE10 magnesium alloy sheets, *Acta Mater.* 58 (2010) 592–605. doi:10.1016/j.actamat.2009.09.038.
- [244] Q. Huo, X. Yang, J. Ma, H. Sun, J. Wang, L. Zhang, Texture weakening of AZ31 magnesium alloy sheet obtained by a combination of bidirectional cyclic bending at low temperature and static recrystallization, *J. Mater. Sci.* 48 (2013) 913–919. doi:10.1007/s10853-012-6814-3.
- [245] S.R. Agnew, Ö. Duygulu, Plastic anisotropy and the role of non-basal slip in magnesium alloy AZ31B, *Int. J. Plast.* 21 (2005) 1161–1193. doi:10.1016/j.ijplas.2004.05.018.
- [246] I. Ulacia, N. V. Dudamell, F. Gálvez, S. Yi, M.T. Pérez-Prado, I. Hurtado, Mechanical behavior and microstructural evolution of a Mg AZ31 sheet at dynamic strain rates, *Acta Mater.* 58 (2010) 2988–2998. doi:10.1016/j.actamat.2010.01.029.
- [247] Y.N. Wang, J.C. Huang, The role of twinning and untwinning in yielding behavior in hot-extruded Mg-Al-Zn alloy, *Acta Mater.* 55 (2007) 897–905. doi:10.1016/j.actamat.2006.09.010.
- [248] D.L. Yin, K.F. Zhang, G.F. Wang, W.B. Han, Warm deformation behavior of hot-rolled AZ31 Mg alloy, *Mater. Sci. Eng. A.* 392 (2005) 320–325. doi:10.1016/j.msea.2004.09.039.
- [249] T. Al-Samman, G. Gottstein, Room temperature formability of a magnesium AZ31 alloy: Examining the role of texture on the deformation mechanisms, *Mater. Sci. Eng. A.* 488 (2008) 406–414. doi:10.1016/j.msea.2007.11.056.
- [250] M. Ardeljan, I.J. Beyerlein, B.A. McWilliams, M. Knezevic, Strain rate and temperature sensitive multi-level crystal plasticity model for large plastic deformation behavior: Application to AZ31 magnesium alloy, *Int. J. Plast.* 83 (2016) 90–109. doi:10.1016/j.ijplas.2016.04.005.
- [251] T. Al-Samman, G. Gottstein, Dynamic recrystallization during high temperature deformation of magnesium, *Mater. Sci. Eng. A.* 490 (2008) 411–420. doi:10.1016/j.msea.2008.02.004.
- [252] B.S. Wang, R.L. Xin, G.J. Huang, Q. Liu, Strain rate and texture effects on microstructural characteristics of Mg-3Al-1Zn alloy during compression, *Scr. Mater.* 66 (2012) 239–242. doi:10.1016/j.scriptamat.2011.10.046.
- [253] M.G. Jiang, H. Yan, R.S. Chen, Twinning, recrystallization and texture development during multi-directional impact forging in an AZ61 Mg alloy, *J. Alloys Compd.* 650 (2015) 399–409. doi:10.1016/j.jallcom.2015.07.281.
- [254] M. Sanjari, S.A. Farzadfar, I.H. Jung, E. Essadiqi, S. Yue, Influence of strain rate on hot deformation behaviour and texture evolution of AZ31B, *Mater. Sci.*

- Technol. 28 (2012) 437–447. doi:10.1179/1743284711Y.0000000080.
- [255] A.K. Rodriguez, G.A. Ayoub, B. Mansoor, A.A. Benzerga, Effect of strain rate and temperature on fracture of magnesium alloy AZ31B, *Acta Mater.* 112 (2016) 194–208. doi:10.1016/j.actamat.2016.03.061.
- [256] L. Jiang, J.J. Jonas, R.K. Mishra, A.A. Luo, A.K. Sachdev, S. Godet, Twinning and texture development in two Mg alloys subjected to loading along three different strain paths, *Acta Mater.* 55 (2007) 3899–3910. doi:10.1016/j.actamat.2007.03.006.
- [257] N. V. Dudamell, I. Ulacia, F. Gálvez, S. Yi, J. Bohlen, D. Letzig, I. Hurtado, M.T. Pérez-Prado, Influence of texture on the recrystallization mechanisms in an AZ31 Mg sheet alloy at dynamic rates, *Mater. Sci. Eng. A.* 532 (2012) 528–535. doi:10.1016/j.msea.2011.11.018.
- [258] H. Zhang, G. Huang, D. Kong, G. Sang, B. Song, Influence of initial texture on formability of AZ31B magnesium alloy sheets at different temperatures, *J. Mater. Process. Technol.* 211 (2011) 1575–1580. doi:10.1016/j.jmatprotec.2011.04.009.
- [259] G.Y. Chin, W.L. Mammel, Competition among basal, prism, and pyramidal slip modes in hcp metals, *Metall. Mater. Trans. B.* 1 (1970) 357–361. doi:10.1007/BF02811542.
- [260] S.R. Agnew, C.N. Tomé, D.W. Brown, T.M. Holden, S.C. Vogel, Study of slip mechanisms in a magnesium alloy by neutron diffraction and modeling, *Scr. Mater.* 48 (2003) 1003–1008. doi:10.1016/S1359-6462(02)00591-2.
- [261] J.A. Del Valle, M.T. Pérez-Prado, O.A. Ruano, Deformation mechanisms responsible for the high ductility in a Mg AZ31 alloy analyzed by electron backscattered diffraction, *Metall. Mater. Trans. A Phys. Metall. Mater. Sci.* 36 (2005) 1427–1438. doi:10.1007/s11661-005-0235-8.
- [262] M.R. Barnett, A Taylor model based description of the proof stress of magnesium AZ31 during hot working, *Metall. Mater. Trans. A Phys. Metall. Mater. Sci.* 34 A (2003) 1799–1806. doi:10.1007/s11661-003-0146-5.
- [263] S.R. Agnew, M.H. Yoo, C.N. Tomé, Application of texture simulation to understanding mechanical behavior of Mg and solid solution alloys containing Li or Y, *Acta Mater.* 49 (2001) 4277–4289. doi:10.1016/S1359-6454(01)00297-X.
- [264] S. Couling, J. Pashak, L. Sturkey, Unique deformation and aging characteristics of certain magnesium-base alloys, *Trans. ASM.* 51 (1959) 94.
- [265] U.F. Kocks, D. Westlake, The importance of twinning for the ductility of cph polycrystals, *Trans Met. Soc. AIME.* 239 (1967) 1107–1109.
- [266] A. Couret, D. Caillard, An in situ study of prismatic glide in magnesium-II. Microscopic activation parameters, *Acta Metall.* 33 (1985) 1455–1462. doi:10.1016/0001-6160(85)90046-X.
- [267] X.Y. Lou, M. Li, R.K. Boger, S.R. Agnew, R.H. Wagoner, Hardening evolution of AZ31B Mg sheet, *Int. J. Plast.* 23 (2007) 44–86. doi:10.1016/j.ijplas.2006.03.005.
- [268] S. Vagarali, L. TG, Deformation Mechanisms in h.c.p. Metals at Elevated Temperatures I. Creep Behavior of a Magnesium, *Acta Metall.* 29 (1981) 1969.
- [269] E. Meza-García, P. Dobroň, J. Bohlen, D. Letzig, F. Chmelík, P. Lukáč, K.U. Kainer, Deformation mechanisms in an AZ31 cast magnesium alloy as investigated by the acoustic emission technique, *Mater. Sci. Eng. A.* 462 (2007) 297–301. doi:10.1016/j.msea.2006.02.469.



- [270] B. Hutchinson, M.R. Barnett, A. Ghaderi, P. Cizek, I. Sabirov, Deformation modes and anisotropy in magnesium alloy AZ31, *Int. J. Mater. Res.* 100 (2009) 556–563. doi:10.3139/146.110070.
- [271] J.A. del Valle, O.A. Ruano, Separate contributions of texture and grain size on the creep mechanisms in a fine-grained magnesium alloy, *Acta Mater.* 55 (2007) 455–466. doi:10.1016/j.actamat.2006.08.039.
- [272] A. Galiyev, R. Kaibyshev, G. Gottstein, Correlation of plastic deformation and dynamic recrystallization in magnesium alloy ZK60, *Acta Mater.* 49 (2001) 1199–1207. doi:10.1016/S1359-6454(01)00020-9.
- [273] M.M. Myshlyayev, H.J. McQueen, A. Mwembela, E. Konopleva, Twinning, dynamic recovery and recrystallization in hot worked Mg-Al-Zn alloy, *Mater. Sci. Eng. A.* 337 (2002) 121–133. doi:10.1016/S0921-5093(02)00007-2.
- [274] M.R. Barnett, Twinning and the ductility of magnesium alloys. Part I: “Tension” twins, *Mater. Sci. Eng. A.* 464 (2007) 1–7. doi:10.1016/j.msea.2006.12.037.
- [275] M.R. Barnett, Twinning and the ductility of magnesium alloys. Part II. “Contraction” twins, *Mater. Sci. Eng. A.* 464 (2007) 8–16. doi:10.1016/j.msea.2007.02.109.
- [276] N. V. Dudamell, I. Ulacia, F. Gálvez, S. Yi, J. Bohlen, D. Letzig, I. Hurtado, M.T. Pérez-Prado, Twinning and grain subdivision during dynamic deformation of a Mg AZ31 sheet alloy at room temperature, *Acta Mater.* 59 (2011) 6949–6962. doi:10.1016/j.actamat.2011.07.047.
- [277] E. Dogan, I. Karaman, G. Ayoub, G. Kridli, Reduction in tension-compression asymmetry via grain refinement and texture design in Mg-3Al-1Zn sheets, *Mater. Sci. Eng. A.* 610 (2014) 220–227. doi:10.1016/j.msea.2014.04.112.
- [278] M.G. Lee, R.H. Wagoner, J.K. Lee, K. Chung, H.Y. Kim, Constitutive modeling for anisotropic/asymmetric hardening behavior of magnesium alloy sheets, *Int. J. Plast.* 24 (2008) 545–582. doi:10.1016/j.ijplas.2007.05.004.
- [279] M. Li, Constitutive modeling of slip, twinning, and untwinning in AZ31B magnesium, 2006.
- [280] S.R. Kalidindi, Incorporation of Deformation Twinning in Models, *Int. J. Plast.* 46 (1998) 267–290.
- [281] A. Fernández, M.T. Pérez Prado, Y. Wei, A. Jérusalem, Continuum modeling of the response of a Mg alloy AZ31 rolled sheet during uniaxial deformation, *Int. J. Plast.* 27 (2011) 1739–1757. doi:10.1016/j.ijplas.2011.05.002.
- [282] A. Staroselsky, L. Anand, A constitutive model for hcp materials deforming by slip and twinning: Application to magnesium alloy AZ31B, *Int. J. Plast.* 19 (2003) 1843–1864. doi:10.1016/S0749-6419(03)00039-1.
- [283] G. Ayoub, A.K. Rodrigez, M. Shehadeh, G. Kridli, J.P. Young, H. Zbib, Modelling the rate and temperature-dependent behaviour and texture evolution of the Mg AZ31B alloy TRC sheets, *Philos. Mag.* 98 (2018) 262–294. doi:10.1080/14786435.2017.1403054.
- [284] D.C. Drucker, Relation of experiments to mathematical theories of plasticity, *J. Appl. Mech.* 16 (1949) 349–357.
- [285] E. Dogan, I. Karaman, G. Ayoub, G. Kridli, Reduction in tension–compression asymmetry via grain refinement and texture design in Mg–3Al–1Zn sheets, *Mater. Sci. Eng. A.* 610 (2014) 220–227. doi:10.1016/J.MSEA.2014.04.112.
- [286] R. Lapovok, Y. Estrin, Superplasticity in magnesium alloys by severe plastic deformation, Woodhead Publishing Limited, 2012.

- doi:10.1533/9780857093844.1.144.
- [287] S.X. Ding, C.P. Chang, P.W. Kao, Effects of processing parameters on the grain refinement of magnesium alloy by equal-channel angular extrusion, *Metall. Mater. Trans. A Phys. Metall. Mater. Sci.* 40 (2009) 415–425. doi:10.1007/s11661-008-9747-3.
- [288] S.L. Semiatin, V.M. Segal, R.E. Goforth, N.D. Frey, D.P. DeLo, Workability of commercial-purity titanium and 4340 steel during equal channel angular extrusion at cold-working temperatures, *Metall. Mater. Trans. A Phys. Metall. Mater. Sci.* 30 (1999) 1425–1435. doi:10.1007/s11661-999-0290-7.
- [289] A. Yamashita, Z. Horita, T.G. Langdon, Improving the mechanical properties of magnesium and a magnesium alloy through severe plastic deformation, *Mater. Sci. Eng. A.* 300 (2001) 142–147. doi:10.1016/S0921-5093(00)01660-9.
- [290] E.J. Kwak, C.H. Bok, M.H. Seo, T.-S. Kim, H.S. Kim, Processing and Mechanical Properties of Fine Grained Magnesium by Equal Channel Angular Pressing, *Mater. Trans.* 49 (2008) 1006–1010. doi:10.2320/matertrans.MC200725.
- [291] M. Mabuchi, K. Ameyama, K. Higashi, H. Iwasaki, Low temperature superplasticity of AZ91 magnesium alloy with non-equilibrium grain boundaries, *Acta Mater.* 47 (1999) 2047–2057.
- [292] K. Xia, J.T. Wang, X. Wu, G. Chen, M. Gurvan, Equal channel angular pressing of magnesium alloy AZ31, *Mater. Sci. Eng. A.* 410–411 (2005) 324–327. doi:10.1016/j.msea.2005.08.123.
- [293] C.F. Gu, L.S. Tóth, D.P. Field, J.J. Fundenberger, Y.D. Zhang, Room temperature equal-channel angular pressing of a magnesium alloy, *Acta Mater.* 61 (2013) 3027–3036. doi:10.1016/j.actamat.2013.01.063.
- [294] Y. Tan, W. Li, W. Hu, X. Shi, L. Tian, The effect of ECAP temperature on the microstructure and properties of a rolled rare earth magnesium alloy, *Materials (Basel)*. 12 (2019). doi:10.3390/ma12091554.
- [295] W. Cheng, L. Tian, S. Ma, Y. Bai, H. Wang, Influence of equal channel angular pressing passes on the microstructures and tensile properties of Mg-8Sn-6Zn-2Al alloy, *Materials (Basel)*. 10 (2017). doi:10.3390/ma10070708.
- [296] Y.T. Zhu, T.C. Lowe, Observations and issues on mechanisms of grain refinement during ECAP process, *Mater. Sci. Eng. A.* 291 (2000) 46–53. doi:10.1016/S0921-5093(00)00978-3.
- [297] C. Xu, M. Furukawa, Z. Horita, T.G. Langdon, The evolution of homogeneity and grain refinement during equal-channel angular pressing: A model for grain refinement in ECAP, *Mater. Sci. Eng. A.* 398 (2005) 66–76. doi:10.1016/j.msea.2005.03.083.
- [298] C.W. Su, L. Lu, M.O. Lai, A model for the grain refinement mechanism in equal channel angular pressing of Mg alloy from microstructural studies, *Mater. Sci. Eng. A.* 434 (2006) 227–236. doi:10.1016/j.msea.2006.06.103.
- [299] A.A.H. Kobaiassy, G. Ayoub, W. Nasim, J. Malik, I. Karaman, M. Shehadeh, Modeling of the ECAP Induced Strain Hardening Behavior in FCC Metals, *Metall. Mater. Trans. A Phys. Metall. Mater. Sci.* 51 (2020) 5453–5474. doi:10.1007/s11661-020-05971-2.
- [300] R.B. Figueiredo, T.G. Langdon, Grain refinement and mechanical behavior of a magnesium alloy processed by ECAP, *J. Mater. Sci.* 45 (2010) 4827–4836. doi:10.1007/s10853-010-4589-y.

- [301] K. Kowalczyk-Gajewska, S. Stupkiewicz, K. Frydrych, H. Petryk, Modelling of texture evolution and grain refinement on complex SPD paths, *IOP Conf. Ser. Mater. Sci. Eng.* 63 (2014). doi:10.1088/1757-899X/63/1/012040.
- [302] M. Gzyl, A. Rosochowski, A. Milenin, L. Olejnik, Modelling microstructure evolution during equal channel angular pressing (ECAP) of Mg alloys using cellular automata finite element (CAFE) method, *Comput. Methods Mater. Sci.* 13 (2013) 357–363.
- [303] H. Bunge, *Texture Analysis in Materials Science*, 1982.
- [304] Y. Estrin, A. Vinogradov, Extreme grain refinement by severe plastic deformation: A wealth of challenging science, *Acta Mater.* 61 (2013) 782–817. doi:10.1016/j.actamat.2012.10.038.
- [305] M.W. Vaughan, W. Nasim, E. Dogan, J.S. Herrington, G. Proust, A.A. Benzerga, I. Karaman, Interplay between the effects of deformation mechanisms and dynamic recrystallization on the failure of Mg-3Al-1Zn, *Acta Mater.* 168 (2019) 448–472. doi:10.1016/j.actamat.2019.02.010.
- [306] E. Schmid, W. Boas, *Kristallplastizität*, 1st ed., Springer Berlin Heidelberg, 1935. doi:https://doi.org/10.1007/978-3-662-34532-0.
- [307] S. Basu, E. Dogan, B. Kondori, I. Karaman, A.A. Benzerga, Towards designing anisotropy for ductility enhancement: A theory-driven investigation in Mg-alloys, *Acta Mater.* 131 (2017) 349–362. doi:10.1016/j.actamat.2017.02.046.
- [308] Y. Wang, H. Choo, Influence of texture on Hall-Petch relationships in an Mg alloy, *Acta Mater.* 81 (2014) 83–97. doi:10.1016/j.actamat.2014.08.023.
- [309] M. Janeček, M. Popov, M.G. Krieger, R.J. Hellmig, Y. Estrin, Mechanical properties and microstructure of a Mg alloy AZ31 prepared by equal-channel angular pressing, *Mater. Sci. Eng. A.* 462 (2007) 116–120. doi:10.1016/j.msea.2006.01.174.
- [310] S. Seipp, M.F.X. Wagner, K. Hockauf, I. Schneider, L.W. Meyer, M. Hockauf, Microstructure, crystallographic texture and mechanical properties of the magnesium alloy AZ31B after different routes of thermo-mechanical processing, *Int. J. Plast.* 35 (2012) 155–166. doi:10.1016/j.ijplas.2012.03.007.
- [311] S.R. Agnew, P. Mehrotra, T.M. Lillo, G.M. Stoica, P.K. Liaw, Crystallographic texture evolution of three wrought magnesium alloys during equal channel angular extrusion, *Mater. Sci. Eng. A.* 408 (2005) 72–78. doi:10.1016/j.msea.2005.07.052.
- [312] E. Schmid, W. Boas, *Plasticity of Crystals*, FA Hughes Co. (1950) 112–117.
- [313] X.L. Nan, H.Y. Wang, L. Zhang, J.B. Li, Q.C. Jiang, Calculation of Schmid factors in magnesium: Analysis of deformation behaviors, *Scr. Mater.* 67 (2012) 443–446. doi:10.1016/j.scriptamat.2012.05.042.
- [314] M. Janeček, J. Čížek, J. Gubicza, J. Vrátná, Microstructure and dislocation density evolutions in MgAlZn alloy processed by severe plastic deformation, *J. Mater. Sci.* 47 (2012) 7860–7869. doi:10.1007/s10853-012-6538-4.
- [315] L. Balogh, R.B. Figueiredo, T. Ungár, T.G. Langdon, The contributions of grain size, dislocation density and twinning to the strength of a magnesium alloy processed by ECAP, *Mater. Sci. Eng. A.* 528 (2010) 533–538. doi:10.1016/j.msea.2010.09.048.
- [316] F.S.J. Poggiali, J. Poggiali, L.C.P. Silva, P.H.R. Pereira, B.R. Figueirado, P.R. Cetlin, Determination of mechanical anisotropy of magnesium processed by ECAP &, *Integr. Med. Res.* 3 (2014) 331–337. doi:10.1016/j.jmrt.2014.09.002.

- [317] Z. Li, C. Hou, M. Huang, C. Ouyang, Strengthening mechanism in micro-polycrystals with penetrable grain boundaries by discrete dislocation dynamics simulation and Hall-Petch effect, *Comput. Mater. Sci.* 46 (2009) 1124–1134. doi:10.1016/j.commatsci.2009.05.021.
- [318] H. Yu, Y. Xin, M. Wang, Q. Liu, Hall-Petch relationship in Mg alloys: A review, *J. Mater. Sci. Technol.* 34 (2018) 248–256. doi:10.1016/j.jmst.2017.07.022.
- [319] W. Yuan, S.K. Panigrahi, J.Q. Su, R.S. Mishra, Influence of grain size and texture on Hall-Petch relationship for a magnesium alloy, *Scr. Mater.* 65 (2011) 994–997. doi:10.1016/j.scriptamat.2011.08.028.
- [320] N. Ono, K. Nakamura, S. Miura, Influence of grain boundaries on plastic deformation in pure Mg and AZ31 Mg alloy polycrystals, *Mater. Sci. Forum.* 419–4 (2003) 195–200.  
<https://www.cheric.org/research/tech/periodicals/view.php?seq=1254063>.
- [321] W.J. Kim, H.T. Jeong, Grain-size strengthening in equal-channel-angular-pressing processed AZ31 Mg alloys with a constant texture, *Mater. Trans.* 46 (2005) 251–258. doi:10.2320/matertrans.46.251.
- [322] S. Graff, W. Brocks, D. Steglich, Yielding of magnesium : From single crystal to polycrystalline aggregates, 23 (2007) 1957–1978. doi:10.1016/j.ijplas.2007.07.009.